



T.C.  
MANİSA CELAL BAYAR ÜNİVERSİTESİ  
FEN BİLİMLERİ ENSTİTÜSÜ

MANİSA CELAL BAYAR UNIVERSITY  
INSTITUTE OF NATURAL&APPLIED  
SCIENCE

CİLT:19 SAYI:4 YIL:2023  
VOLUME:19 ISSUE:4 YEAR:2023

ISSN: 1305-130X  
e-ISSN: 1305-1385

**CELAL BAYAR ÜNİVERSİTESİ  
FEN BİLİMLERİ DERGİSİ**

**CELAL BAYAR UNIVERSITY  
JOURNAL OF SCIENCE**

**CELAL BAYAR  
ÜNİVERSİTESİ**



# Journal of Science

Volume: 19, Issue: 4, Year: 2023

## Contact

Manisa Celal Bayar University  
Institute of Natural and Applied Sciences  
Campus of Şehit Prof Dr İlhan Varank 45140 Yunussemre – MANİSA, TÜRKİYE  
Tel: (00 90) 236 201 27 05  
Fax: (00 90) 236 241 21 49  
e-mail: cbujos@gmail.com  
Web: <https://dergipark.org.tr/tr/pub/cbayarfb>

“CBU Journal of Science is indexed by ULAKBIM-TUBITAK TR-DIZIN”



ISSN 1305-130X

E-ISSN 1305-1385

CBUJOS is published quarterly at Manisa Celal Bayar University Printing House

“CBU Journal of Science is a refereed scientific journal”



## Celal Bayar University Journal of Science

**Owner** Manisa Celal Bayar University,

**Editor** : Prof. Dr. Kamil ŞİRİN

**Layout Editor & Secretary**

Assoc. Prof. Dr. İlker Çetin KESKİN

### Subject Editors

Prof. Dr. Abdullah AKDOĞAN, Pamukkale University, Chemical Engineering  
Prof. Dr. Ali DEMİR, Manisa Celal Bayar University, Civil Engineering  
Prof. Dr. Ali KONURALP, Manisa Celal Bayar University, Mathematics  
Prof. Dr. Fatih KALYONCU, Manisa Celal Bayar University, Biology  
Prof. Dr. Mehmet ÇEVİK, Katip Çelebi University, Mechanical Engineering  
Prof. Dr. Mustafa CAN, Katip Çelebi University, Bioengineering  
Prof. Dr. Oğuz GÜRSOY; Mehmet Akif Ersoy University, Food Engineering  
Prof. Dr. Sezai TAŞKIN, Manisa Celal Bayar University, Electrical and Electronic Engineering  
Prof. Dr. Şerafettin DEMİÇ, Katip Çelebi University, Materials Engineering  
Assoc. Prof. Dr. Sermin ÇAM KAYNAR, Manisa Celal Bayar University, Physics  
Assoc. Prof. Dr. İbrahim Fadıl SOYKÖK, Manisa Celal Bayar University, Mechatronics Engineering  
Assoc. Prof. Dr. İzzet YÜKSEK, Manisa Celal Bayar University, Architecture  
Assoc. Prof. Dr. Mehmet Ali ILGIN, Manisa Celal Bayar University, Industrial Engineering  
Assoc. Prof. Dr. Tuğba ÖZACAR ÖZTÜRK, Manisa Celal Bayar University, Computer Engineering

### International Scientific Advisory Board

Prof. Dr. Arianit REKA; State University of Tetova, Macedonia  
Prof. Dr. Tomasz NIEMIEC; Warsaw University of Life Sciences, Poland  
Prof. Dr. Alyani ISMAIL; Universiti Putra, Malaysia  
Prof. Dr. Iuliana APRODU; Dunarea de Jos University, Romania  
Assoc. Prof. Can BAYRAM; University of Illinois, USA  
Assoc. Prof. Dr. Johanan Christian PRASANNA; Madras Christian College, South India  
Assoc. Prof. Dr. Noureddine ISSAOUI; Université de Monastir, Tunisie.  
Assoc. Dr. Edward Albert UECKERMANN; North-West University, South Africa  
Assoc. Dr. Zhi-Qiang ZHANG; The University of Auckland, Holland  
Assist. Prof. Dr. Young Ki KIM; Pohang University of Science and Technology, South Korea  
Assist. Prof. Dr. Mona MIRHEYDARI; Rutgers University, USA  
Assist. Prof. Dr. Donatella ALBANESE; Università Degli Studi Di Salerno, Italy  
Assist. Prof. Dr. Jinghua JIANG; The University of Memphis, USA  
Assist. Prof. Dr. Jens OLDELAND; University of Hamburg, Germany  
Dr. Cheng CHENG; Apple Inc., USA  
Dr. Sajedeh AFGHAH; Microsoft Corporation, USA  
Dr. Jinghua JIANG; The University of Memphis

### National Scientific Advisory Board

Prof. Dr. Mustafa Ersöz; Selçuk University  
Prof. Dr. Oğuz Gürsoy; Mehmet Akif University  
Prof. Dr. Mehmet Çevik; İzmir Katip Çelebi University  
Prof. Dr. Sezgin Çelik; Yıldız Teknik University  
Prof. Dr. Osman Dayan; Çanakkale Onsekiz Mart University  
Prof. Dr. Serdar İplikçi; Pamukkale University  
Prof. Dr. Yasin Üst; Yıldız Teknik University  
Prof. Dr. Mahmut Kuş; Konya Teknik University  
Prof. Dr. Ertunç Gündüz; Hacettepe University  
Prof. Dr. Tülin Aydemir; Manisa Celal Bayar University  
Prof. Dr. Sezai Taşkın; Manisa Celal Bayar University  
Prof. Dr. Fatma Şaşmaz Ören; Manisa Celal Bayar University  
Prof. Dr. Fatih Selimefendioğlu; Manisa Celal Bayar University  
Prof. Dr. Osman Çulha; Manisa Celal Bayar University  
Prof. Dr. Ali Konuralp; Manisa Celal Bayar University  
Prof. Dr. Erol Akpınar; Abant İzzet Baysal University  
Prof. Dr. Ali Demir; Manisa Celal Bayar University  
Prof. Dr. Serap Derman; Yıldız Teknik University  
Assoc. Prof. Dr. Fatih Doğan; Çanakkale Onsekiz Mart University  
Assoc. Prof. Dr. Yeliz Yıldırım; Ege University  
Assoc. Prof. Dr. Hayati Mamur; Manisa Celal Bayar University  
Assoc. Prof. Dr. Özlem Çağındı; Manisa Celal Bayar University  
Assoc. Prof. Dr. Mehmet Söylemez; Adıyaman University  
Assoc. Prof. Dr. Nil Mansuroğlu; Ahi Evran University  
Assist. Prof. Dr. Zeynep Çipiloğlu Yıldız; Manisa Celal Bayar University



---

## **CBU Journal of Science**

Celal Bayar University Journal of Science (CBUJOS) covers scientific studies in the fields of Engineering and Science and publishes accounts of original research articles concerned with all aspects of experimental and theoretical studies. CBU Journal of Science is a refereed scientific journal published four times annually (March, June, September and December) by Institute of Natural and Applied Sciences of Manisa Celal Bayar University. CBU Journal of Science considers the original research articles written in English for evaluation.

CBU Journal of Science is indexed by TUBİTAK ULAKBİM TR-DİZİN, and also is included in DOAJ, Cite Factor, Journal TOCS, Advanced Science Index and OAJI databases. Digital Object Identifier (DOI) number will be assigned for all the articles being published in CBU Journal of Science.

Instructions for Authors and Article Template can be found on the main page of MCBU Institute of Natural and Applied Sciences (<http://fbe.cbu.edu.tr>)







**Vol: 19, Issue: 4, Year: 2023**

**Contents**

**Research Article**

**Pages**

Building and Experimenting Solar Chimney Power Plant

DOI: 10.18466/cbayarfbe.1258484

301-307

Sohayb Abdulkerim , Mohammed Qaddoori Hammoodi, Mussaab Alshbib

Determination of Phytochemical and Antibacterial Properties of *Momordica charantia* Seed Extracts

DOI: 10.18466/cbayarfbe.1292919

309-313

Mehzat Altun, Zerife Orhan

Effects of Forces and Material Types on Fatigue Analysis of Beams

DOI: 10.18466/cbayarfbe.1324800

315-321

Savaş Evran

Microwave-Assisted Fabrication of Pd, Co and Ni Nanoparticles Modified-SiO<sub>2</sub>; as Catalysts in the Reduction Reaction of Organic Pollutants

DOI: 10.18466/cbayarfbe.1327271

323-332

Sevtap Çağlar Yavuz, Emre Yavuz, Serkan Dayan

Recombinant Adeno-Associated Viral Vector Transduction of Human Prostate Cancer Cell Lines

DOI: 10.18466/cbayarfbe.1336250

333-341

Muhammet Burak Batır

On 7-Dimensional Nilpotent Leibniz Algebras with 1-Dimensional Leib Ideal

DOI: 10.18466/cbayarfbe.1339702

343-349

İsmail Demir

Green Biosynthesis of Silver Nanoparticles were Obtained from the Extract of Pomegranate (*Punica granatum* L.) Leaves by Supercritical Extraction Using Microwave Method

DOI: 10.18466/cbayarfbe.1338606

351-358

Gönül Serdar

*Helianthus Annuus* L. Comparison of The Properties of Fibers Obtained From The Plant By Methods of Decortication and Retting

DOI: 10.18466/cbayarfbe.1366612

359-366

Nilsu Ataman, Levent Şık

A New Record of Genus *Parastigmaeus* (Acariformes: Stigmaeidae) from Türkiye

DOI: 10.18466/cbayarfbe.1367147

367-371

Mustafa Akyol

Investigation of the Relationship Between the Structural Properties and Air, Water Drop and Particle Permeability of Different Masks Available in the Market

DOI: 10.18466/cbayarfbe.1371598

373-380

Candan Akça, Mehmet İsmail Katı



Dose Determination of Fluvial Sediments in Manisa

DOI: 10.18466/cbayarfbe.1381567

Müjde Durukan Gültepe, Arzu Ege

381-388




Investigation of Effect of Air Gap between Surface and Bolus on Dose Distribution for 6 MV Photon Beam

DOI: 10.18466/cbayarfbe.1391876

Osman Vefa Gül

389-393

## Building and Experimenting Solar Chimney Power Plant

Sohayb Abdulkerim<sup>1\*</sup>  Mohammed Qaddoori Hammoodi<sup>1</sup> , Mussaab Alshbib<sup>2</sup> 

<sup>1\*</sup> Gaziantep University, Şehitkamil, Gaziantep, Türkiye

<sup>2</sup> Shaam University, Ezaz, Syria

\*[karim@gantep.edu.tr](mailto:karim@gantep.edu.tr)

\*Orcid No: 0000-0002-3448-9129

Received: 1 March 2023

Accepted: 22 November 2023

DOI: 10.18466/cbayarfbe.1258484

### Abstract

Recently several resources of sustainable and clean energy have been developed, such as solar panels, wind turbines, and others. The Solar Chimney Power Plant (SCPP), which is among those harnessing solar power where a stream of air is induced by adding heat through solar irradiation using the greenhouse effect, is rarely utilized for generating power. The hot air flows through the chimney under the effect of buoyancy force which in turn drives a vertical axis wind turbine. Although this technique is investigated by many reports, unfortunately, it is still in the laboratory phase. However, it might be an optimal solution for zones where operating other techniques is not efficient for various reasons. In this project, an SCPP prototype was built and tested in Anbar, a central province in Iraq. The impact of various design parameters on power generation was assessed. The experimental results prove the feasibility of SCPPs for generating electricity at low costs and the suitability of building SCPPs in countries technologically less developed with specific weather conditions and scarcity in water resources that are normally needed for cleaning solar panels, for example.

**Keywords:** Clean Energy, Renewable, Solar Chimney, Sustainability, Solar Collector.

### 1. Introduction

The working principle of Solar Chimney (SC) relies on heating up the air inside a vertical tower, due to the rising temperature, the air becomes lighter generating a buoyancy force which, in turn, induces airflow through the tower and fresh air is drawn from a room causing passive ventilation [1–4]. The history of SC for natural ventilation dates back to several centuries ago [5].

Researchers found an additional application for this machine which is producing electricity by installing a turbine at the base of the chimney. This application was exploited when the Germany Ministry of Research and Technology built the first prototype of a Solar Chimney Power Plant (SCPP) in Spain in 1982 [6]. Since then, the SCPP has not been commercialized and is still at the investigation stage. Even in diverse regions, the acceptance and transition to solar energy practices reveal socio-spatial inequalities, as observed in the Hague, The Netherlands [7]. Similarly, studies have highlighted the key role of developers in advancing solar energy acceptance in areas like the Golestan province in Iran [8]. The heat in SCPPs is added to the system through a collector which has a conical shape and is made of a

transparent material allowing the solar irradiation to heat up the air using the greenhouse effect. The top of the collector is connected to a tower where the hot air flows under the effect of buoyancy force due to the fact that hot air has lower density compared to the ambient density.

At the base of the tower, a vertical axis turbine is installed which is driven by the airflow, which in turn drives an electrical power generator [1,9–11].

A great deal of research has focused on SCs for natural ventilation such as [12–15] while other reports were focused on it being a subsystem of SCPPs such as [9–11,16–21].

Other studies investigated the dual purposes of the SC such as generating power and ventilating at the same time such as [22], generating power in addition to cooling solar panels [3], power generation and water desalination [23], or a solar updraft tower combined with solar panels [24]. Most researchers relied on a numerical simulation to analyse the flow inside the chimney using sophisticated finite element packages such as [3,9–13,22,23,25].

Furthermore, novel techniques have been introduced to improve the efficiency of solar energy systems. For instance, a three-dimensional model was developed to study solar energy reflection from mirrors in circular orbits, presenting a unique perspective on optimizing solar energy capture [26]. Another significant stride is the utilization of machine learning algorithms to forecast solar energy production, emphasizing the intersection of technology and renewable energy [27].

A smaller number of studies relied on analytical modelling in order to analyse the performance of the SC and seek major designing parameters such as [18–20,28]. Other research adopted mixed-approach, for example, a numerical and analytical method was used in [16], and [11], while analytical results were compared with experimental ones in [29]. The analytical iterative procedure with field measurements was found in [17]. While others relied only on an experimental analysis such as [14,15,24]. In spite of the large number of experimental evaluations of SCPP, the investigations were not enough to convince firms or institutions to invest in the commercialization of this machine.

However, in those studies, the investigations were focused partially on the effect of some parameters on the overall performance. For example, static pressure, driving force, power output, efficiency, airflow velocity, height, chimney radius, and the ratio of collector radius to gap height, were among those parameters studied separately using analytical and/or numerical approaches, with very few using experimental measurements.

For example, geometric parameters and ambient conditions on the performance were studied by [28], while geometrical parameters and thermal boundary condition using 3D CFD simulation were conducted by [9].

While, solar radiation and ambient temperature on pressure drop were investigated by [11]. Some studies focused on evaluating the performance of the SC in certain countries, such as in Algeria [19,30], Nigeria [2], and Spain [31]. Nevertheless, this literature review reveals that experimental investigations on the effect of major parameters such as structural dimension, solar irradiation, and atmospheric conditions on the performance of an SCPP at the middle of Anbar, Iraq, have not been conducted yet. This zone of the world was selected due to the lack of electricity in spite of abundant sunlight and meeting many other conditions outlined by [6]. This choice of using SCPP in Iraq, and in particular in Al-Anbar, is highly recommended since Iraq suffers from water scarcity and, unlike other mechanisms, water is not necessary for SCPP. Additionally, this selection is beneficial due to the availability of cheap building material for the chimneys [6].

To assess the performance of SCPPs in this region and the effect of major parameters on the overall performance, a small-scale SCPP prototype was built using locally available materials and devices, and then measured using a customized configuration of an Arduino circuit. Additionally, the effect of using a thermal isolator at the bottom of the collector was evaluated. The results of the investigation, as shown later in this report, demonstrate SCPPs can contribute to solving the present power problem in Iraq by relying on this sustainable, clean, and economical source of energy.

## 2. Theoretical Background

The power generated through a turbine is proportional to the pressure drop of the flow stream. The experiment and the analytical analysis shows that the value of the pressure drop functions to the densities difference, which can be approximated by the following integration [16]:

$$\Delta P = g \int_0^H (\rho_{o,z} - \rho_{i,z}) dz, \quad (1)$$

where,  $\rho_{o,z}$  and  $\rho_{i,z}$  are the ambient and internal air density, respectively,  $H$ , is the chimney height,  $g$  is the acceleration of gravity.

Assuming constant density for small chimney, the integration can be approximated as follows:

$$\Delta P = g(\rho_o - \rho_i).H \quad (2)$$

The density difference is created by the effect of heat difference, therefore, it can be approximated [16] as

$$(\rho_o - \rho_i) = \beta \cdot \rho \Delta T, \quad (3)$$

where,  $\Delta T$  is the air temperature difference due to the added heat can be approximated by heat balance equation:

$$\Delta T = \pi \cdot \frac{q}{c_p \cdot \dot{m}} (R_{coll}^2 - r^2), \quad (4)$$

where,  $q$  is the added heat to the air flow,  $C_p$  Specific Heat for air as an ideal gas at constant pressure, and  $\dot{m}$  is mass flow rate of air. The added heat is proportional to the solar irradiation.

Part of the total pressure drop is subject to pressure loss due to friction inside the chimney which can be evaluated as [16]

$$\delta P_{loss} = f \frac{H}{D} g \cdot \frac{\rho_i}{2} v^2, \quad (5)$$

where,  $D$  is the chimney radius,  $v$  is flow velocity,  $f$  is friction factor which depends on the Reynold's number of the flow and the material nature internal surface of the chimney.

The amount of absorbed power by turbine can be evaluated using

$$Power = \delta P_{turbine} \cdot Q, \quad (6)$$

where,  $\delta P_{turbine}$  is pressure drop over the turbine [N/m<sup>2</sup>], and  $Q$  is the flow rate in [kg/s].

Clearly, the equations show that the power increases as the cross-section, and the driving pressure drop increase. Equation [2] shows that the driving force increases as the density difference increases. The density difference increases as the radius of the collector, the heat flux, and the temperature difference increase. Thus, increasing the power output of SCPP requires bigger volume of chimney and larger area of collector and higher intensity of solar irradiation.

### 3. Methodology

To evaluate the performance of the SCPP, several prototypes with different sizes and configurations were designed, fabricated, and experimented at the same ambient conditions in Anbar, the largest province in Iraq, which is located in western Iraq, with longitude 44,39 E and latitude 35,36N, during the month of May 2020. This zone was selected because it suffers from a lack of electricity in spite of the abundance of solar irradiance. The SCPP was built using affordable locally available materials. The machine was built for investigation purposes only, and was pictured as shown in Figure 1.



Figure 1. In-house- built a prototype of a SCPP.

The bottom part was made of a transparent film from Nylon of 1mm thick with an open periphery. The height of the inlet was 30 [cm] above the ground. The chimney part was made from a Polyvinyl Chloride (PVC) tube of 4-inch diameter and a wall thickness of 1.5 mm. in order to study the effect of structural geometry, the height of the chimney, and the diameter of the collector were changed several times as it will be detailed in the experiment section. A simple turbine was installed inside the tower at the base section, the turbine was also connected to DC-generator. The load was a simple Ohm's resistance allowing to measure the applied voltage and the consumed ampere.

The used instruments and rigs:

The following devices and tools were used to perform various measurements

1- To measure the intensity of solar irradiation at the location of experiments, Lutron SPM-1116SD Solar Energy Meter with data logger capabilities had been used. The recorded data could be logged to a SD-cart or to a pc through RS232 or USB PC computer interface; the measurement resolution of the meter was 0.1 mW/m<sup>2</sup> for intensities less than 1000 W/m<sup>2</sup> and 1 mW/m<sup>2</sup> for intensities bigger than or equal to 1000 W/m<sup>2</sup> [32].

2- To log the temperature at various locations, a dedicated Arduino circuit was configured and connected to five thermal sensors. All thermal sensors were LM35 which has an accuracy of 0.5°C and suitable for remote application and has a linearity of +10.0 mV/°C scale factor [33]. The Arduino circuit was connected to a PC through a USB cable which was sending the readings of temperatures in real-time.

3- The speed of the air flow through the tower was measured using an anemometer device, the handheld anemometer was HP-817A Digital Anemometer 30m/s LCD from HoldPeak; wind speed ranges from 0.3 to 30m/s with an accuracy of ±5% and Resolution of 0.1m/s.

4- In order to measure the output electrical power, a simple device capable of measuring the voltage and ampere simultaneously was used. The volts and amperes were recorded manually.

Four different experiments were conducted as follows.

## 4. The Experiment Results

### 4.1. The First Experiment

This experiment investigated the effect of ambient temperature and the intensity of solar irradiation on the amount of electricity produced. The collector diameter was 2m, while the tower height was 3m.

The measured parameters were solar irradiation, ambient temperature, and the produced electricity. Figure 3 shows the power in milliwatt plotted against the ambient temperature in Celsius for three different cases of solar irradiance (800, 100, and 1200 W/m<sup>2</sup>). The chart shows that the amount of produced electricity depends on two factors; solar irradiation and ambient temperature.

At a solar irradiance of 1200 w/m<sup>2</sup>, the generated power is at its highest, and it increases as the temperature increases and reaches the highest value of 142 mw at a temperature of 32°C.

Conversely, the generated power at solar irradiance of 800 and 1000 w/m<sup>2</sup> reduces as the temperature increases. Furthermore, regardless of the ambient temperature, the amount of produced electricity increases as the solar irradiance increases.

#### 4.2. The Second Experiments

This experiment aimed to investigate the effect of adding thermal insulation to the collector of the SCPP on the productivity of the machine. Therefore, two experiments were carried out.

In the first experiment, the measurements were made without installing any insulator, while in the second experiment, a layer of thermal insulation of polystyrene of the thickness of 15mm and heat load coefficient of 0.03 W/(m.K) was installed on the ground beneath the collector in order to prevent any heat loss through the ground.

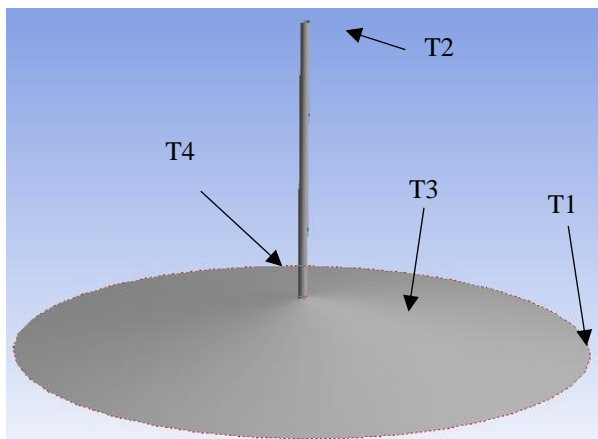


**Figure 2.** Schematic diagram of the machine and thermal sensors distribution.

In both experiments, the collector diameter was 2m. the tower height was 3m. the temperatures were measured at four different locations on the SCPP as shown in Figure 2. The first location, T1, was at the inlet of the collector while the second location, T3, was at the central point of the collector. The last two locations, T4 and T2 were at the bottom and the top ends of the tower, respectively.

The temperature was measured every hour by the Arduino circuit using the thermal sensors LM35, over 24 hours for several days.

The average values of the temperatures over seven days were calculated. The results of the first case, non-isolated, were plotted as shown in Figure 4; while the results for the insulated case were plotted as shown in Figure 5.

In the both cases, the trendline of the temperature is changing according to the time period of the day. In the period from 05:00 to 10:00 O'clock, there was a sharp increase in temperature at the four locations. Almost all locations reached maximum values in the period from 10:00 to 15:00 O'clock. The highest value was recorded at the centre of the chimney as high as 44 C° at 13:00 O'clock for the non-isolated case while it recorded 67 C° at the same period of time. Noticeably, all-temperature degrees of the isolated case are higher than those for the non-isolated case indicating the feasibility of using the thermal insulator. Furthermore, to quantify the impact of using a thermal isolator on power productivity one more experiment was conducted by measuring the resulting power for the isolated and non-isolated cases.

#### 4.3. The Third Experiments

This experiment investigated the effect of thermal insulation on electricity production by comparing the produced power for two cases, in the first case, the isolator was not installed while in the second case the insulator was installed. The experiment conditions were the same, the solar irradiation was 1200 w/m<sup>2</sup>. The used insulator was made from polystyrene with a heat load of 0.03W/(m.K). In this experiment the measured produced power, and ambient temperatures were recorded. The results were plotted as shown in Figure 6.

The chart in Figure 6 shows that the produced power decreases as the ambient temperature increases this is due to the fact that the SCPP relies on temperature differences between inner and ambient air. Furthermore, it shows that the thermal insulation increases the produced electricity. The highest power's increment was reached to 3.5% when the ambient temperature was 7°C. All in all, clearly the insulation improves the power productivity and increases the temperature differences between inside and outside of the chimney.

#### 4.4. The Fourth Experiment

This experiment investigates the effect of the dimension of the SCPP on power production. Therefore, the tower's height was altered regularly six times from 0.5 m to 3.0 m by a step of 0.5m; the diameter of the collector was also changed three times 0.5, 1.0, and 2.0 m allowing to test 18 different cases. Under the same ambient conditions and the same solar irradiation of 1200 w/m<sup>2</sup>, all measurements were recorded and plotted as shown in Figure 7.



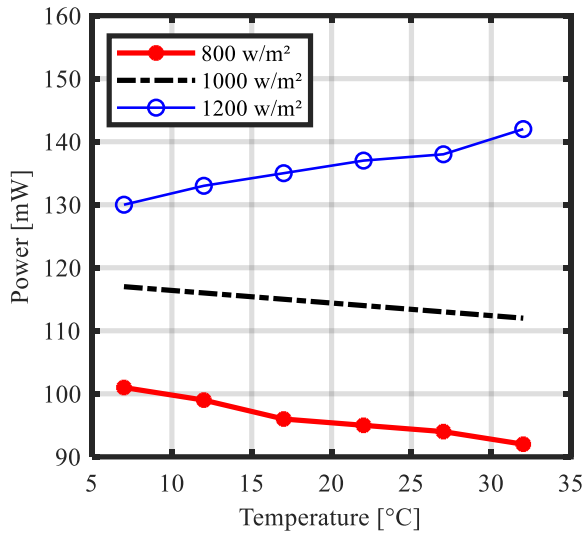


**Figure 3.** Power production versus ambient conditions.

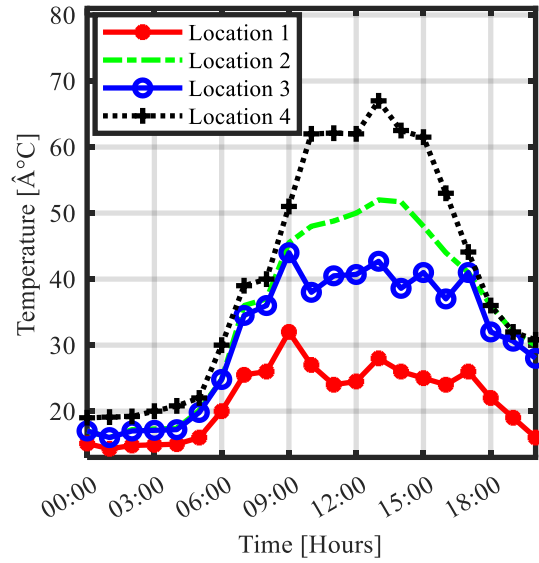


**Figure 5.** The variation of average temperature over 24 hours.

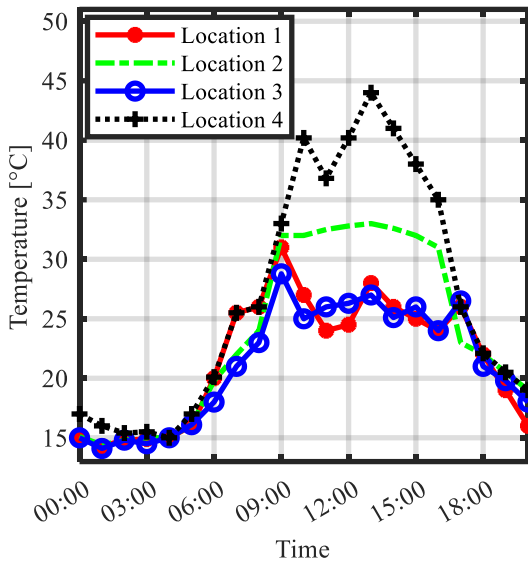


**Figure 4.** The variation of average temperature over 24 hours.

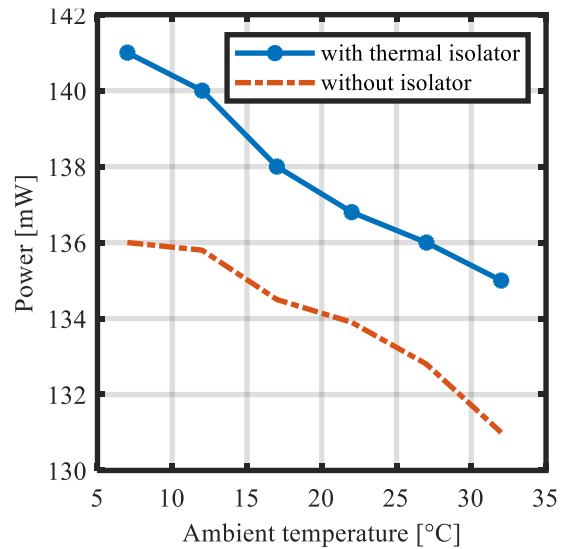


**Figure 6.** The effect of the thermal insulator on electricity production.

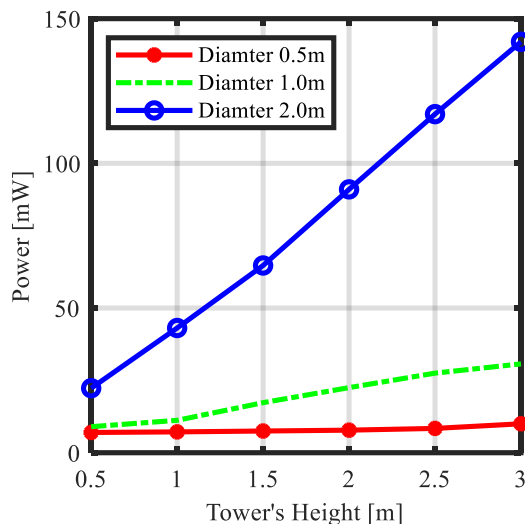


**Figure 7.** The effect of chimney's size on the generated power

The chart in Figure 7 shows that the power productivity increases as the tower's height and the collector diameter increase. This is in agreement with the analytical equation in the theoretical background section and the results of many researchers [2,6,34,35]. At a very small collector, the produced power is almost zero and the height of the tower has no impact. The impact of the height becomes more significant as the collector diameter increases. These results agree with the fact that the received energy is proportional to the area of the collector, and the pressure difference between the internal and the external of the tower is directly proportional to the elevation according to the hydrostatic pressure principle.

## 5. Conclusion

This project aimed to investigate the feasibility of SCPPs in producing electricity power in Al-Anbar, Iraq. For this purpose, an SCPP was built from locally available materials, the tower was made of a PVC tube of 4inch diameter and multiple heights from 0.5 to 3.0 meters. The base is connected to the collector which is made from transparent Nylon film, which is responsible for collecting the solar irradiation using the greenhouse effect, which was formed conically at multiple diameters 1.0, 1.5, and 2.0 meters. In some experiments, a thermal insulator of polystyrene was also installed at the bottom of the collector. In order to measure the generated power, a small system of a turbine-DC-generator, which was connected to an Ohm's resistance, was installed inside the tower allowing to measure the output power. By inspecting the experimental results, the following conclusion can be drawn:

The investigated zone of Iraq shows high intensity of solar irradiance ensuring that renewable solar energy is an appropriate choice, and harnessing solar irradiance by SCPPs is a feasible project and due to other factors, it is also low costs and low complexity.

The amount of produced electricity is directly proportional to the size of the SCPP, the chimney height, chimney and collector radius, the intensity of solar irradiance. The larger size the higher amount of produced electricity agrees others researches.

Producing energy using SCPP allows avoiding the drawback of other technologies. Specifically, it requires no water for cleaning, unlike the solar panel technology; besides, it does not affect the perspective and does not kill flying birds as the wind turbine does. In the SCPP technique, the power is collected at a low cost for a long period of the day even at night in addition to its relatively long lifespan.

## Author's Contributions

### Sohayb Abdulkerim:

Led the study's conceptualization, design, and data analysis, drafted the manuscript, and managed the literature review, playing a pivotal role in theoretical framework development.

### Mohammed Qaddoori Hammoodi:

Responsible for manufacturing the testing machine, conducting the primary experiments, and contributing to data interpretation and experimental process refinement.

### Mussaab Alshbib:

Focused on report preparation and revisions, ensuring clarity and coherence in documentation, and provided essential administrative support for the project.

## Ethics

The research conducted in this study adhered to ethical guidelines and principles. All experiments and data collection were conducted in accordance with relevant laws, regulations, and institutional guidelines. Any potential ethical concerns related to human or animal subjects, data privacy, or other ethical considerations were carefully addressed and mitigated during the course of the research.

## 6. References

- [1]. S. Pradhan, R. Chakraborty, D.K.K. Mandal, A. Barman, P. Bose, Design and performance analysis of solar chimney power plant (SCPP): A review | Elsevier Enhanced Reader, Sustain. Energy Technol. Assessments. 47 (2021) 101411. <https://doi.org/10.1016/J.SETA.2021.101411>.
- [2]. A.T. Layeni, M.A. Waheed, B.A. Adewumi, C.N. Nwaokocha, M. Sharifpur, S.O. Tongo, R.C. Okeze, C.A. Mboreha, Computational and sensitivity analysis of a dual purpose solar chimney for buildings | Elsevier Enhanced Reader, Mater. Today Proc. (2021). <https://doi.org/10.1016/J.MATPR.2021.07.292>.
- [3]. A.P. Singh, Akshayveer, A. Kumar, O.P. Singh, Strategies for effective cooling of photovoltaic panels integrated with solar chimney, Mater. Today Proc. 39 (2019) 1950–1954. <https://doi.org/10.1016/j.matpr.2020.08.440>.
- [4]. H. Dahire, S.R. Kannan, S.K. Saw, Effect of humidity on the performance of rooftop solar chimney, Therm. Sci. Eng. Prog. (2021) 101026. <https://doi.org/10.1016/j.tsep.2021.101026>.



- [5]. A. Soto, P.J. Martínez, P. Martínez, J.A. Tudela, Simulation and experimental study of residential building with north side wind tower assisted by solar chimneys, *J. Build. Eng.* 43 (2021). <https://doi.org/10.1016/j.jobe.2021.102562>.
- [6]. (5) (PDF) The Solar Chimney Electricity from the sun, (n.d.). [https://www.researchgate.net/publication/282859303\\_The\\_Solar\\_Chimney\\_Electricity\\_from\\_the\\_sun](https://www.researchgate.net/publication/282859303_The_Solar_Chimney_Electricity_from_the_sun) (accessed August 26, 2021).
- [7]. C.W. Kraaijvanger, T. Verma, N. Doorn, J.E. Goncalves, Does the sun shine for all? Revealing socio-spatial inequalities in the transition to solar energy in The Hague, The Netherlands, *Energy Res. Soc. Sci.* 104 (2023) 103245. <https://doi.org/10.1016/j.erss.2023.103245>.
- [8]. S. Salehi, The role of developers in accepting solar energy in Iran: A case study in Golestan province, *Sol. Energy.* 264 (2023) 111967. <https://doi.org/10.1016/j.solener.2023.111967>.
- [9]. M.R. Torabi, M. Hosseini, O.A. Akbari, H.H. Afrouzi, D. Toghraie, A. Kashani, A. Alizadeh, Investigation the performance of solar chimney power plant for improving the efficiency and increasing the outlet power of turbines using computational fluid dynamics, *Energy Reports.* 7 (2021) 4555–4565. <https://doi.org/10.1016/j.egyr.2021.07.044>.
- [10]. S. Hu, D.Y.C. Leung, J.C.Y. Chan, Impact of the geometry of divergent chimneys on the power output of a solar chimney power plant, *Energy.* 120 (2017) 1–11. <https://doi.org/10.1016/j.energy.2016.12.098>.
- [11]. P. Guo, J. Li, Y.Y. Wang, Y.Y. Wang, Evaluation of the optimal turbine pressure drop ratio for a solar chimney power plant, *Energy Convers. Manag.* 108 (2016) 14–22. <https://doi.org/10.1016/j.enconman.2015.10.076>.
- [12]. Y. Cao, F. Aldawi, N. Sinaga, H. Moria, H.S. Dizaji, M. Wae-hayee, Single solar chimney technology as a natural free ventilator; energy-environmental case study for Hong Kong, *Case Stud. Therm. Eng.* 26 (2021) 101173. <https://doi.org/10.1016/j.csite.2021.101173>.
- [13]. R.B. Weli, S.A. Atrooshi, R. Schwarze, Investigation of the performance parameters of a sloped collector solar chimney model – An adaptation for the North of Iraq, *Renew. Energy.* 176 (2021) 504–519. <https://doi.org/10.1016/j.renene.2021.05.075>.
- [14]. G. He, Q. Wu, Z. Li, W. Ge, D. Lv, L. Cong, Ventilation performance of solar chimney in a test house: Field measurement and validation of plume model, *Build. Environ.* 193 (2021). <https://doi.org/10.1016/j.buildenv.2021.107648>.
- [15]. B. Belfegas, S. Larbi, T. Tayebi, Experimental and Theoretical Investigation on a Solar Chimney System for Ventilation of a Living Room, *Math. Model. Eng. Probl.* 8 (2021) 259–266. <https://doi.org/10.18280/MMEP.080213>.
- [16]. T. Ming, W. Liu, G. Xu, Analytical and numerical investigation of the solar chimney power plant systems, *Int. J. Energy Res.* 30 (2006) 861–873. <https://doi.org/10.1002/ER.1191>.
- [17]. A. Koonsrisuk, T. Chitsomboon, Mathematical modeling of solar chimney power plants, *Energy.* 51 (2013) 314–322. <https://doi.org/10.1016/j.energy.2012.10.038>.
- [18]. J. Yin Li, P. Hua Guo, Y. Wang, Effects of collector radius and chimney height on power output of a solar chimney power plant with turbines, *Renew. Energy.* 47 (2012) 21–28. <https://doi.org/10.1016/j.renene.2012.03.018>.
- [19]. S. Larbi, A. Bouhdjar, T. Chergui, Performance analysis of a solar chimney power plant in the southwestern region of Algeria, *Renew. Sustain. Energy Rev.* 14 (2010) 470–477. <https://doi.org/10.1016/j.rser.2009.07.031>.
- [20]. T.W. von Backström, A.J. Gannon, Solar chimney turbine characteristics, *Sol. Energy.* 76 (2004) 235–241. <https://doi.org/10.1016/j.solener.2003.08.009>.
- [21]. M.T. Chaichan, K.I. Abass, H.A. Kazem, (3) (PDF) Dust and Pollution Deposition Impact on a Solar Chimney Performance, (2018). [https://www.researchgate.net/publication/323105920\\_Dust\\_and\\_Pollution\\_Deposition\\_Impact\\_on\\_a\\_Solar\\_Chimney\\_Performance/figures?i=1](https://www.researchgate.net/publication/323105920_Dust_and_Pollution_Deposition_Impact_on_a_Solar_Chimney_Performance/figures?i=1) (accessed August 24, 2021).
- [22]. A.T. Layeni, M.A. Waheed, B.A. Adewumi, B.O. Bolaji, C.N. Nwaokocha, S.O. Giwa, Computational modelling and simulation of the feasibility of a novel dual purpose solar chimney for power generation and passive ventilation in buildings, *Sci. African.* 8 (2020) e00298. <https://doi.org/10.1016/j.sciaf.2020.e00298>.
- [23]. P. Rahdan, A. Kasaeian, W.M. Yan, Simulation and geometric optimization of a hybrid system of solar chimney and water desalination, *Energy Convers. Manag.* 243 (2021) 114291. <https://doi.org/10.1016/j.enconman.2021.114291>.
- [24]. A.J. Jubear, Experimental study of hybrid solar updraft tower with PV panel (s), (2021).
- [25]. F. V Stojkovski, M. Chekerovska, R. V Filkoski, V. Stojkovski, Numerical Modelling of a Solar Chimney Power Plant, *Int. J. Contemp. ENERGY.* 2 (2016). <https://doi.org/10.14621/ce.20160102>.
- [26]. Onur Celik, Colin R. McInnes, A generic three-dimensional model for solar energy reflected from mirrors in circular orbits, *Adv. Sp. Res. (under Rev.)* (2023). <https://doi.org/10.1016/j.asr.2023.09.046>.
- [27]. Y. Ledmaoui, A. El Maghraoui, M. El Aroussi, R. Saadane, A. Chebak, A. Chehri, Forecasting solar energy production: A comparative study of machine learning algorithms, *Energy Reports.* 10 (2023) 1004–1012. <https://doi.org/10.1016/j.egyr.2023.07.042>.
- [28]. C. Khelifi, F. Ferroudji, M. Ouali, Analytical modeling and optimization of a solar chimney power plant, *Int. J. Eng. Res. Africa.* 25 (2016) 78–88. <https://doi.org/10.4028/www.scientific.net/JERA.25.78>.
- [29]. Z. Lipnicki, M. Gortych, A. Staszczuk, T. Kuczyński, P. Grabas, Analytical and experimental investigation of the solar chimney system, *Energies.* 12 (2019). <https://doi.org/10.3390/en12112060>.
- [30]. A. Bouchair, Solar chimney for promoting cooling ventilation in southern Algeria, *Build. Serv. Eng. Res. Technol.* 15 (1994) 81–93. <https://doi.org/10.1177/014362449401500203>.
- [31]. J. Schlaich, R. Bergermann, W. Schiel, G. Weinrebe, Design of Commercial Solar Updraft Tower Systems-Utilization of Solar Induced Convective Flows for Power Generation, n.d. <http://www.mretreview.gov.au> (accessed October 23, 2019).
- [32]. Lutron SPM-1116SD Solar Energy Meter - Netes Engineering, (n.d.). <https://www.netes.com.tr/urun/lutron-spm-1116sd-gunes-enerjisi-olcer#teknik> (accessed August 13, 2021).
- [33]. LM35 datasheet(2/15 Pages) TI1 | LM35 Precision Centigrade Temperature Sensors, (n.d.). <https://html.alldatasheet.com/html-pdf/517588/TI1/LM35/108/2/LM35.html> (accessed August 13, 2021).
- [34]. J.P. Pretorius, D.G. Kröger, Sensitivity Analysis of the Operating and Technical Specifications of a Solar Chimney Power Plant, *J. Sol. Energy Eng.* 129 (2007) 171–178. <https://doi.org/10.1115/1.2711473>.
- [35]. X. Zhou, F. Wang, R.M. Ochieng, A review of solar chimney power technology, *Renew. Sustain. Energy Rev.* 14 (2010) 2315–2338. <https://doi.org/10.1016/j.rser.2010.04.018>.

## Determination of Phytochemical and Antibacterial Properties of *Momordica charantia* Seed Extracts

Mehzat Altun<sup>1\*</sup> , Zerife Orhan<sup>2</sup> 

<sup>1</sup>Canakkale Onsekiz Mart University, Vocational School of Health Services, Çanakkale, Türkiye  
<sup>2</sup>Kahramanmaraş Sutcu Imam University, Vocational School of Health Services, Kahramanmaraş, Türkiye

\*[mehzatalun@comu.edu.tr](mailto:mehzatalun@comu.edu.tr)

\*0000-0001-7363-5056

Received: 5 May 2023

Accepted: 22 November 2023

DOI: 10.18466/cbayarfbe.1292919

### Abstract

In recent years, it has been essential to discover safe and effective antibacterial drugs because of rising antibiotic-resistant bacteria. In traditional medicine, plant extracts including biological active components have been used for therapeutic purposes. We aimed to evaluate the antimicrobial properties of the aqueous seed extract of *Momordica charantia* (*M. charantia*) on 9 pathogenic bacteria. The antibacterial activity of the extract was assessed against strains using disc diffusion and broth microdilution tests. A total of 21 constituents were identified from *M.charantia* seeds. Alcohols, esters, aldehydes, monoterpenes, and monoterpenoids were found as the prevalent groups. The seed extract showed the greatest antimicrobial activity on *Bacillus subtilis* (*B. subtilis*) and *Staphylococcus aureus* (*S. aureus*) with an inhibition zone diameter (IZD) value of 15.75±0.50 mm and 15.25±0.957 mm, respectively. The minimum inhibitory concentration (MIC) and the minimum bactericidal concentration (MBC) test results ranged from 12.5 to 100 (mg/mL). The seed extract of *M.charantia* could be used for the cure of bacterial infections as a new natural drug.

**Keywords:** Antibacterial activity, *Momordica charantia*, Phytochemical components

### 1. Introduction

Several classes of antibiotics are used for the treatment of bacterial diseases and reduced morbidity and mortality [1]. Bacteria have acquired resistance to antibiotics via biochemical and genetic mechanisms [2]. According to the World Health Organization (WHO), the failure of antibiotic treatment is due to multi-drug-resistant bacteria and their toxic effects [3]. Researchers have been focused to discover new plant-derived antimicrobials against resistant bacteria [4,5].

Since ancient times, botanical drugs have been used for the cure of bacterial diseases [6]. Any plant that has therapeutic properties or can be used as a precursor of drugs is named a medicinal plant by the WHO [7]. Plant extracts containing various phytochemicals (tannins, alkaloids, flavonoids, and phenolic compounds) are responsible for their therapeutic properties such as antimicrobial, antioxidant, and anticancer [8]. *M. charantia* (*Cucurbitaceae* family) is considered a medicinal plant [9] and has been used for the cure of toothache, diarrhea, cancer, pneumonia, and bacterial infections in traditional medicine [10-12] due to

containing bioactive components like phenolic compounds, triterpenes, and carotenoids [13,14]. The purpose of our study was to determine the phytochemical components and antibacterial properties of an aqueous extract of *M. charantia* against human pathogens.

### 2. Materials and Methods

#### 2.1. Preparation of Seed Extracts

Seeds of *M. charantia* were purchased from the local market in Turkey and identified by a taxonomist in Canakkale Onsekiz Mart University, Herbarium of the Department of Biology, and the voucher specimen was 003081.

Seeds were washed, dried, and finally powdered. Seed extracts were obtained using the maceration method. Briefly, 10 gr *M. charantia* seeds were milled into powder and dissolved in distilled water (100 mL) in a sterile Erlenmeyer flask using a magnetic stirrer at 70°C for 1 hour. The solution was filtered (Whatman-No 1) and evaporated in an incubator at 50 °C for 3 days. Then, the extract was stored at 4 °C in the dark until antibacterial assays. Aqueous extract was sterilized using a syringe filter (0.45 µm).

## 2.2. GCMS

The sample was prepared by SPME technique. The components of the seed of *M. charantia* were isolated using divinylbenzene/carboxen on polydimethylsiloxane (DVB/CAR on PDMS) 50-/30-mm fibers. After each fiber was exposed for 45 min at 50 °C, they were injected to the port of the GC-MS. Shimadzu GCMS QP 2010 ULTRA (USA) ) equipped with an RXI-5MS capillary column (30 m; 0.25 mm; 0.25 μm) was used with helium as the carrier gas (flow rate: 1.0 ml/min). The inlet temperature was set at 250°C. The split ratio was 1:30. Column oven temperature was 50 C. The oven temperature was programmed from 50 to 270 °C at 5 °C/min. All components were identified by comparison of their retention indices with Wiley 9 (Wiley, New York, NY, USA) and NIST 11 (National Institute of Standards and Technology) (Gaithersburg, MD, USA) libraries.

## 2.3. In Vitro Antibacterial Activity Assays

### 2.3.1. Microorganisms and Cultures

*Escherichia coli* ATCC 25922, *Streptococcus agalactiae* ATCC 12386, *Proteus vulgaris* ATCC 13315, *Bacillus subtilis* ATCC 6633, *Pseudomonas aeruginosa* ATCC 10145, *Streptococcus epidermidis* ATCC 12228, *Enterococcus faecalis* ATCC 29212, *Streptococcus pyogenes* ATCC 19615, and *Staphylococcus aureus* ATCC 25923 bacterial strains were used as test microorganisms and obtained from American Type Culture Collection (ATCC). All strains were stored at -20 °C in brain heart infusion broth (BHI) with 20 % glycerol. The turbidity of the bacterial suspensions was equalized to 0.5 Mc Farland standard.

### 2.3.2. Agar Disc Diffusion Method

The method was used to detect the antibacterial properties of *M. charantia* seed extracts against 9 human pathogens according to the Clinical & Laboratory Standards Institute (CLSI). 100 μL of each inoculum was spread on brain heart agar (BHA) (Biokar, France) plates. 25 μL of 100 mg/mL concentration of the seed extract were pipetted onto steril blank paper discs (Oxoid, Bioanalyse) under aseptic conditions. After incubation at 37 °C for 18-24 h, the IZDs were recorded. The negative control was distilled water; positive controls were gentamicin (10 μg/disc, Bioanalyse), ampicillin (10 μg/disc, Bioanalyse), and vancomycin (30 μg/disc, Bioanalyse). Experiments were repeated three times.

### 2.3.3. Determination of MIC and MBC

The microdilution broth method was used to detect MIC using sterile 96 well plates. Firstly, 100 μl of BHI was pipetted into each well. Two-fold serial dilutions (200-12.5 mg/mL) of seed extract were prepared in BHI. Then, 20 μl of inoculum was put into each well except for

sterility control. Growth control was put into 12th wells. After incubation, 10 μL of suspension from four negative wells was transferred to BHA plates. After the same incubation as MIC, the lowest extract concentration at which bacterial strains did not grow, was determined MBC.

### 2.3.4. Statistical Analysis

IZD results of seed extract were compared with antibiotics using one-way ANOVA and post-hoc-Turkey tests (SPSS 19 version).

## 3. Results

SPME-GC/MS identified 21 compounds in *M. charantia* seed as presented in Table 1 and the GC chromatogram is seen in Figure 1. The seed extract exhibited an antimicrobial effect on 9 pathogens. The IZD and MIC results are displayed in Table 2. The extract exhibited the greatest antibacterial effect on *B. subtilis* and *S. aureus* with the IZDs being 15.75±0.50 mm and 15.25±0.957 mm, respectively. No significant antibacterial activity was detected against *S. pyogenes* (IZD: 9.00 mm) compared to the antibiotics (p<0.05). The MIC/MBC values of the seed extract were between 12.5-100 (mg/mL).

**Table 1.** Compounds of *M. charantia* seeds using SPME/GC/MS

Peak#	Retention Time	Area %	Name
1	1.942	1.35	Acetic acid
2	2.333	1.40	1-Butanol
3	2.728	14.49	Pentanal (CAS)
4	4.194	36.28	1-Pentanol
5	4.915	0.94	Hexanal (CAS)
6	6.553	1.30	Hex-2(E)-enal
7	7.094	2.66	p-Xylene
8	7.181	2.26	Hexanol <n->
9	7.926	1.35	o-Xylene
10	9.017	7.06	Oxime-, methoxy-phenyl-
11	10.403	4.63	Hept-2(E)-enal
12	10.969	3.34	2-Hepten-1-ol, (E)-
13	11.894	1.34	2-Furanmethanol, tetrahydro- (CAS)
14	13.072	1.54	o-Cymene
15	13.238	4.47	D-Limonene
16	13.332	3.11	Eucalyptol (1,8-CINEOLE)
17	15.066	2.75	3-Heptanol, 2-methyl- (CAS)
18	19.993	2.48	Dodecane
19	20.456	4.67	Acetic acid, octyl ester
20	23.645	1.47	Tridecane (CAS)
21	32.354	1.11	Nerolidol
		100.00	



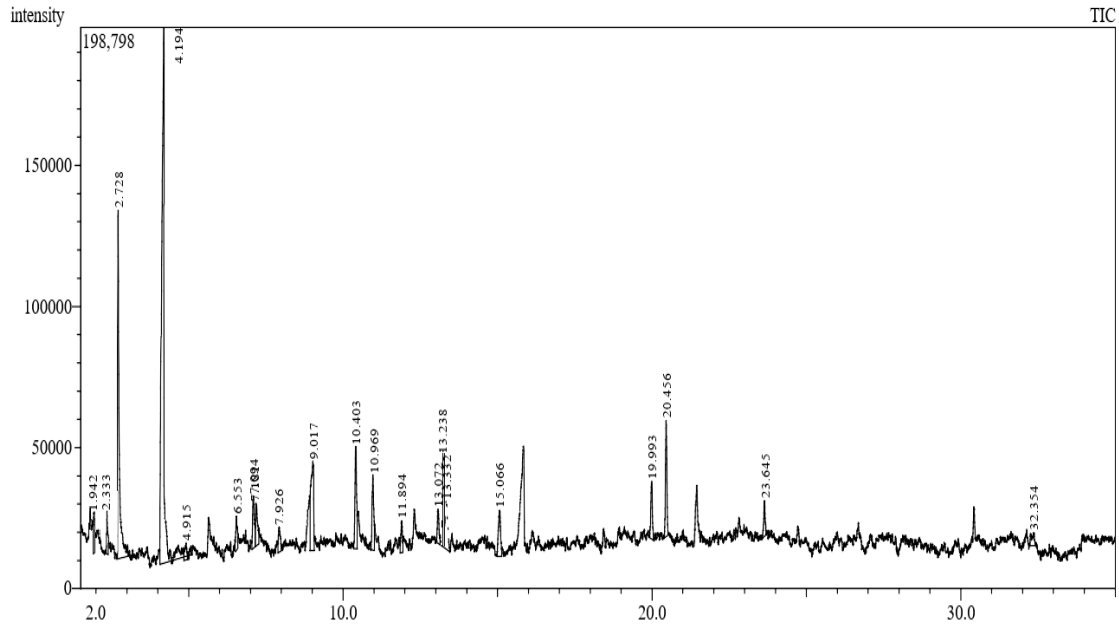


Figure 1. GC chromatograph for the *M. charantia* seeds

Table 2. IZD and MIC values of *M. charantia* seed extract on 9 standard strains

Bacterial strains	IZD (mm)			MIC (mg/mL)	MBC (mg/mL)	
	Extract (100 mg/mL)	G	A			V
<i>E. faecalis</i> ATCC 29212	13.00±0.816	14.75±0.50 (p:0.008)	11.75±0.50 (p:0.058)	11.50±0.577 (p<0.05)	25	50
<i>E. coli</i> ATCC 25922	11.50±0.577	16.75±0.957 (p<0.05)	16.00±0.816 (p<0.05)	-	50	100
<i>P. vulgaris</i> ATCC 13315	13.00±0.816	12.25±0.957 (p:0.432)	9.75±0.50 (p<0.05)	-	25	50
<i>B. subtilis</i> ATCC 6633	15.75±0.50	15.25±0.50 (p:0.515)	8.75±0.50 (p<0.05)	8.25±0.50 (p<0.05)	12.5	25
<i>S. agalactiae</i> ATCC 12386	9.75±0.50	21.75±0.50 (p<0.05)	15.50±0.577 (p<0.05)	14.25±0.50 (p<0.05)	100	100
<i>P. aeruginosa</i> ATCC 10145	12.00±0.816	14.25±0.50 (p<0.05)	9.75±0.50 (p<0.05)	-	50	50
<i>S. epidermidis</i> ATCC 12228	9.75±0.50	25.50±0.577 (p<0.05)	19.25±0.957 (p<0.05)	13.75±0.50 (p<0.05)	100	100
<i>S. pyogenes</i> ATCC 19615	9.00±0.816	20.25±0.50 (p<0.05)	25.50±1.290 (p<0.05)	15.75±0.50 (p<0.05)	100	100
<i>S. aureus</i> ATCC 25923	15.25±0.957	-	-	-	12.5	12.5

IZD in mm (Mean±SD: Standard Deviation) G: Gentamicin, A: Ampicillin, V: Vancomycin, -: ≤6 (disc zone diameter 6mm)



#### 4. Discussion

*M. charantia* has been used in medicine as an herbal drug for the cure of disorders like hemorrhoids, gastrointestinal systems, skin, bones, and blood cancer [15]. Pharmacologically active components such as flavonoids, phenols, terpenes, and triterpenoids of *M. charantia* extracts are responsible for their antibacterial activity [16,17].

Salinas-Sánchez et al. (2021) reported that linalool oxide and limonene oxide were found the major components of the hexane extract of *M. charantia* seeds [18]. In this study, GC-MS revealed five main compounds: alcohols, aldehydes, esters, monoterpenes, and monoterpenoids. The antibacterial properties of *M. charantia* is related to its bioactive components like seed oil, tannins, proteins, terpenoids, alkaloids, and steroids [19-27]. Furthermore, research suggests that polysaccharides are the primary bioactive agents in *M. charantia* responsible for its antimicrobial effects [28]. Polysaccharides extracted from *M. charantia* have demonstrated significant bactericidal activity against various bacterial strains, including *B. subtilis*, *S. aureus*, *S. typhimurium*, and *E. coli* [29].

Previous studies have reported that *M. charantia* had antibacterial potential. In a study, IZD values of aqueous seed extract of *M. charantia* on *S. aureus*, *E. coli*, and *P. aeruginosa* were 20 mm±0.51, 13 mm±0.51, and 16±0.51 mm, respectively [30]. A study by Ibisanni et al. (2022) demonstrated that the IZD of water extracts of *M. charantia* was 16±0.29 mm against *E. coli*, 20±0.29 mm against *B. cereus*; 18±0.29 mm against *S. aureus*, 14±0.17 mm against *P. aeruginosa* at a concentration of 100 mg/mL [31]. In another study reported by Top et al. (2018), the antibacterial activity of *M. charantia* plant extract on *E. coli*, *S. aureus*, *E. faecalis*, *K. pneumoniae*, and *P. aeruginosa* was investigated and the highest IZD at 100 mg/mL concentration was *E. faecalis* (8.00 mm) [32]. In our study, the antibacterial activities of the aqueous seed extract of *M. charantia* were assessed with IZD. The significant antibacterial effect was detected against *S. aureus* (IZD: 15.25±0.957 mm), and *B. subtilis* (15.75±0.50mm).

A study conducted by Khalid et al. in 2021 found that the aqueous methanolic extract obtained from the leaves exhibited the highest effectiveness with a 30 mm diameter of the IZD against *P. multocida*. In contrast, the absolute alcoholic leaf extracts showed no discernible impact on *S. aureus*. The aqueous methanolic seed extract demonstrated significant antibacterial activity, displaying a IZD of 22 mm against *E. coli* [9].

The ethanolic leaf extract of *M. charantia* exhibited low antimicrobial activity against *Proteus mirabilis* and *Klebsiella pneumoniae* with MIC values of 312.5 and 625 µg/mL, respectively [33]. The MIC/MBC value of

the acetone extract of *M. charantia* was 0.31/0.62 mg/mL against *Acinetobacter baumannii* [34]. In our experiment data, the seed extract was the most effective on the *S. aureus* strain (MIC/MBC:12.5 mg/mL).

According to the studies, the chemical composition of the *M. charantia* seed, IZD, and MIC/MBC results of its extract against bacteria are varied. The differences between the results are related to the type of solvent, extraction method, and harvest season [35].

#### 5. Conclusion

Alcohols, aldehydes, esters, monoterpenes, and monoterpenoids have found as the principal components of *M. charantia* seeds. Based on our results, the aqueous seed extract of *M. charantia* has antibacterial activity against human pathogens. After toxicity assays, the seed extracts of *M. charantia* alone or combined with antibiotics could be utilized to cure bacterial infections in the pharmacological industry.

#### Author's Contributions

**Mehzat Altun:** Conducted the experiment, performed statistical analysis, evaluated the results, and wrote the manuscript.

**Zerife Orhan:** Contributed to the experiment's advancement, manuscript preparation interpreted findings.

#### Ethics

There are no ethical issues after the publication of this manuscript.

#### References

- [1]. Huemer, M, Mairpady Shambat, S, Brugger, SD, Zinkernagel, AS. 2020. Antibiotic resistance and persistence-Implications for human health and treatment perspectives. *EMBO Reports*; 21: e51034.
- [2]. Ghosh, D, Veeraraghavan, B, Elangovan, R, Vivekanandan, P. 2020. Antibiotic Resistance and Epigenetics: More to It than Meets the Eye. *Antimicrobial agents and chemotherapy*; 27:64: e02225-19.
- [3]. Medina, E, Pieper, DH. 2016. Tackling threats and future problems of multidrug-resistant bacteria. How to overcome the antibiotic crisis; *Frontiers in Pharmacology*; 13:972935.
- [4]. Ali Mirza, S, Afzaal, M, Begum, S, Arooj, T, Almas, M, Ahmed, S, Younus, M. Chapter 11-Uptake Mechanism of Antibiotics in Plants. In: Hashmi M.Z., editor. *Antibiotics and Antimicrobial Resistance Genes in the Environment*. Volume 1. Elsevier; Amsterdam, The Netherlands, 2020, pp. 183–188.
- [5]. Michelin, DC, Moreschi, PE, Lima, AC, Nascimento, GGF, Paganelli, MO, Chaud, MV. 2005. Avaliação da atividade antimicrobiana de extratos vegetais. *Revista Brasileira de Farmacognosia*; 15: 316–320.
- [6]. Hussain, MS, Hasan, I, Millat, MS, Sen, N, Rahmad, MA, Rahman, MA, Islam, S, Moghal, MMR. 2018. Ascertainment of pharmacological activities of *Allamanda nerifolia* Hook and *Aegialitis rotundifolia* Roxb

- used in Bangladesh: An in vitro study. *Journal of Traditional and Complementary Medicine*; 8: 107-112.
- [7]. Awuchi, CG. 2019. Medicinal Plants: the medical, food, nutritional biochemistry, and uses. *International Journal of Advanced Academic Research*; 5: 220-241.
- [8]. Manandhar, S, Luitel, S, Dahal, RK. 2019. In vitro antimicrobial activity of some medicinal plants against human pathogenic bacteria. *Journal of Tropical Medicine*; 1895340.
- [9]. Khalid, Z, Hassan, S, Shahzad, S, Khurram, H. 2021. A Review on Biological Attributes of *Momordica charantia*. *Advances in Bioscience, Bioengineering*; 9: 8-12.
- [10]. Chen, J, Tian, R, Qiu, M, Lu, L, Zheng, Y, Zhang, Z. 2008. Trinorcucurbitane and cucurbitane triterpenoids from the roots of *Momordica charantia*. *Phytochemistry*; 69: 1043-1048.
- [11]. Polito, L, Djemil, A, Bortolotti, M. 2016. Plant Toxin-Based Immunotoxins for Cancer Therapy: A Short Overview. *Biomedicines*; 4: 12.
- [12]. Grover, JK, Yadav, SP. 2004. Pharmacological actions and potential uses of *Momordica charantia*: A Review. *Journal of Ethnopharmacology*; 93: 123-132.
- [13]. Cuong, DM, Kwon, SJ, Jeon, J, Park, YJ, Park, JS, Park, SU. 2018. Identification and characterization of phenylpropanoid biosynthetic genes and their accumulation in bitter melon (*Momordica charantia*). *Molecules*; 23: 469.
- [14]. Saeed, MK, Shahzadi, I, Ahmad, I, Ahma, R, Shahzad, K, Ashraf, M, Nisa V. 2010. Nutritional analysis and antioxidant activity of bitter melon (*Momordica charantia*) from Pakistan. *Pharmacologyonline*; 1: 252-260.
- [15]. Kumar, DS, Sharathnath, KV, Yogeswaran, P, Harani, A, Sudhakar, K, Sudha, P, Banji D. 2010. A medicinal potency of *Momordica charantia*. *International Journal of Pharmaceutical Sciences Review and Research*; 1: 95-100.
- [16]. Lee, YH, Yoon, SY, Baek, J, Kim, SJ, Yu, JS, Kang, H, Kim, KH. 2021. Metabolite profile of cucurbitane-type triterpenoids of bitter melon (fruit of *Momordica charantia*) and their inhibitory activity against protein tyrosine phosphatases relevant to insulin resistance. *Journal of Agricultural and Food Chemistry*; 69: 1816-1830.
- [17]. Shimada, T, Kato, F, Dwijayanti, DR, Nagata, T, Kinoshita, A, Okuyama, T, Mukai, E. 2021. Bitter melon fruit extract enhances intracellular ATP production and insulin secretion from rat pancreatic beta cells. *British Journal of Nutrition*; 127: 377-383.
- [18]. Salinas-Sánchez, DO, Ramírez-Rodríguez, R, Rivas-González, JM, Figueroa-Brito, R, Peña-Chora, G, Toledo-Hernández, E. 2021. Chemical composition of *Ricinus communis* and *Momordica charantia* seeds extracts and its bioactivity against the sugarcane aphid, *Melanaphis sacchari* (Zehntner). *International Journal of Tropical Insect Science*; 41: 2991-2996.
- [19]. Wang, S, Li, Z, Yang, G, Ho, CT, Li, S. 2017. *Momordica charantia*: A popular health-promoting vegetable with multifunctionality. *Food & Function*; 8: 1749-1762.
- [20]. Upadhyay, A, Agrahari, P, Singh, DK. 2015. A review on salient pharmacological features of *Momordica charantia*. *International Journal of Pharmacology*; 11: 405-413.
- [21]. Guarniz, W, Canuto, K, Ribeiro, P, Dodou, H, Magalhaes, K, Sa, K. 2019. *Momordica charantia* L. variety from Northeastern Brazil: Analysis of Antimicrobial Activity and Phytochemical Components. *Pharmacognosy Journal*; 11: 1312-24.
- [22]. Saini, RK, Keum, YS. 2017. Characterization of nutritionally important phytoconstituents in bitter melon (*Momordica charantia* L.) fruits by HPLC-DAD and GC-MS. *Journal of Food Measurement and Characterization*; 11: 119-125.
- [23]. Ghaffar, F, Kainatm, B, Shah, HU, Rahman, IU. 2017. DPPH Radical Scavenging Assay, Biological Activities, Nutritional Composition and Quality Parameters of *Momordica charantia* Seeds Grown in District CHarsadda, KPK, Pakistan. *Pakistan Journal of Scientific and Industrial Research Series B Biological Sciences*; 60: 80-86.
- [24]. Braca, A, Siciliano, T, D'Arrigo, M, Germanò, MP. 2008. Chemical composition and antimicrobial activity of *Momordica charantia* seed essential oil. *Fitoterapia*; 79: 123-125.
- [25]. Lu, YL, Liu, YH, Chyuan, JH, Cheng, KT, Liang, WL, Hou, WC. 2011. Antibacterial and cytotoxic activities of different wild bitter melon cultivars (*Momordica charantia* L. var. *abbreviata* Seringe). *Botanical Studies*; 52: 427-434.
- [26]. Leelaprakash, G, Rose, J, Gowtham, B, Javvaji, PK, Prasad, S. 2011. In vitro Antimicrobial and Antioxidant Activity of *Momordica charantia* Leaves. *Pharmacophore*; 2: 244-252.
- [27]. Santos, KKA, Matias, EFF, Sobral-Souza, CE, Tintino, SR, Morais-Braga, MB, Guedes, GM, Coutinho, HD. 2012. Trypanocide, cytotoxic, and antifungal activities of *Momordica charantia*. *Pharmaceutical Biology*; 50: 162-166.
- [28]. Zhang, F, Lin, L, Xie, JA. 2016. A mini-review of chemical and biological properties of polysaccharides from *M. charantia*. *International journal of biological macromolecules*; 92: 246-253.
- [29]. Wu, L, Ke, L, Huang, X, Liu, S, Chen, H, Rao, P. 2006. Separation and characterization of the active ingredients of *M. charantia* L. and their protective and repairing effect on HIT-T15 cells damaged by alloxan in vitro. *Journal of Chinese Institute of Food Science and Technology*, 6: 24-28.
- [30]. Makhija, M, Ahuja, D, Nandy, BC, Gautam, S, Tiwari, K, Awasthi, A, Saxena, P. 2011. Evaluation and comparison of antibacterial activity of leaves, seeds, and fruit extract of *Momordica charantia*. *Research Journal of Pharmaceutical, Biological and Chemical Sciences*; 2: 185-192.
- [31]. Ibisanni, TA, Aribisala, JO. 2022. Evaluation of antioxidant, phytochemicals, and antibacterial potential of *Momordica charantia* (Linn) against pathogenic bacteria isolated from ready-to-eat food sold in Akure Metropolis, Nigeria. *Bulletin of the National Research Centre*; 46: 72.
- [32]. Top, R. 2018. Bazı Önemli Tıbbi Bitkilerin Antioksidan, Antimikrobiyal ve Antikanser Etkilerinin Araştırılması. Yüksek Lisans Tezi, Bartın Üniversitesi, Fen Bilimleri Enstitüsü, Biyoloji Anabilim Dalı, Bartın, 62.
- [33]. Muribeca, AJB, Gomes, PWP, Paes, SS, da Costa, APA, Gomes, PWP, Viana, JS, Reis, JDE, Pamplona, SDGSR, Silva, C, Bauermeister, A, Santos, LDS, da Silva, MN. 2022. Antibacterial Activity from *Momordica charantia* L. Leaves and Flavones Enriched Phase. *Pharmaceutics*; 14: 1796.
- [34]. Valizadeh, M, Beigomi, M, Fazeli-Nasap, B. 2020. Antibacterial and Antibiofilm Effects of Ethanol and Aceton Leaf Extract of *Momordica charantia* and *Tecomella undulata* against *Acinetobacter baumannii*. *International Journal of Advanced Biological and Biomedical Research*; 8: 403-418.
- [35]. Ghazanfar, SA. 2007. Plant of Oman. *Indigenous Flora*; 14-18.

## Effects of Forces and Material Types on Fatigue Analysis of Beams

Savaş Evran<sup>1\*</sup> 

<sup>1</sup>Department of Jewelry and Jewelry Design, Faculty of Applied Sciences, Marmara University, İstanbul, Türkiye  
[\\*sevran@marmara.edu.tr](mailto:sevran@marmara.edu.tr)

\*Orcid No: 0000-0002-7512-5997

Received: 9 July 2023

Accepted: 6 November 2023

DOI: 10.18466/cbayarfbe.1324800

### Abstract

This numerical and statistical study deals with the evaluate the effects of forces and material types on safety factor and equivalent alternating stress of beams made of metal materials. Numerical calculations were performed by using ANSYS Workbench software. Design of analyzes based on different determining factors was determined utilizing Taguchi L9 orthogonal array design consisting of two determining factors consisting of three levels. The first and second determining factors were chosen as applied force and material type, respectively. In the finite element modeling, beams with clamped-free boundary conditions were considered. Determination of optimal levels of all factors was found using signal-to-noise ratio analysis. The contribution rate and significance level of all determining factors on the safety factor and equivalent alternating stress were calculated utilizing analysis of variance. According to the results calculated from this study, the optimum results for safety factor and equivalent alternating stress of beams were obtained by using the first levels of all determining factors. While the increase in the applied force values causes a decrease in the safety factor, it leads to an increase in the equivalent alternating stress.

**Keywords:** Safety factor, Material, Beam, ANSYS, Taguchi method.

### 1. Introduction

Fatigue may occur in the material under continuous loads. Depending on the number of applied loads, small cracks in the material may grow and then the small cracks can cause major damage. Metal materials can exhibit different fatigue life depending on their geometric structures and the magnitude of the applied force. Therefore, it is significant to determine the fatigue life of metal materials used in many sectors, especially in the field of mechanical engineering. Fatigue analysis, which has a very important in the field of engineering, has been examined in many studies [1-7] depending on different sectors. Many theories and models were offered to estimate the fatigue life and damage [8-18]. In this literature review, a lot of studies have been carried out on fatigue analysis. The effects of the methods used in the production of the bellows used in air suspension systems on the product quality were evaluated and their mechanical properties were examined [19]. A review study on the fatigue life of crankshafts under different loads is presented and the application areas of finite elements and experimental methods are discussed [20]. The fatigue analysis of the wheels designed according to aluminum material was evaluated and they benefited

from ANSYS software in their studies. They also used different radial loads [21]. The fatigue analysis of the rail connecting rods was investigated using ANSYS software, which includes the finite element method [22]. Fatigue analysis of spur gears under different loadings was performed and finite element method was used. In addition, different analyzes were examined using the finite element method [23]. In another study, the fatigue life analysis for steam turbine blades was investigated using linear and elastic finite element methods [24]. In this study, unlike the existing studies in the literature, finite element and Taguchi methods were used to safety factor and equivalent alternating stress of beams made of metal materials. This study focuses on evaluating the impact of forces and material types on the safety factor and equivalent alternating stress of metal beams. The numerical approaches were determined by the ANSYS Workbench software. The analysis design was determined using the Taguchi L9 orthogonal array design, which involved two determining factors with three levels each. The first determining factor represents the applied force, while the second determining factor represents the material type. The finite element modeling was considered for beams with clamped-free boundary conditions.

## 2. Materials and Methods

In the study, three different metal materials were used. These materials were chosen as Structural Steel, Aluminum Alloy, and Magnesium (AM100A, cast, T6), respectively. Each metal material has various mechanical properties and density. The general properties of the metal materials were demonstrated in Table 2.

**Table 1.** Common Material Properties [25]

Properties	Structural Steel	Aluminum Alloy	Magnesium, AM100A, T6
Density	7850 kg/m <sup>3</sup>	2770 kg/m <sup>3</sup>	1802 kg/m <sup>3</sup>
Young's Modulus	200 GPa	71 GPa	46.14 GPa
Tensile Strength	250 MPa	280 MPa	118.4 MPa
Tensile Ultimate Strength	460 MPa	310 MPa	175.1 MPa

Finite element calculations were performed using the L9 orthogonal array. This array was used based on the Taguchi method. In this design, there are two determining factors and each determining factor consists of three different levels. The first determining factor selected was the force applied at the free end of the beams, followed by the material type, which was chosen as the second factor. The determining factors used in the analyzes and levels of these factors are given in Table 2.

**Table 2.** Determining factors and levels

Factor	Code	Levels		
		Level 1	Level 2	Level 3
Force	A	1N	2N	3N
Material Type	B	Structural Steel	Aluminum Alloy	Magnesium, AM100A, T6

In this study, safety factor and equivalent alternating stress were preferred as the responses. The optimum value for the safety factor and equivalent alternating stress was considered as the maximum and minimum

result, respectively. In this context, “the smaller is better” and “the larger is better” quality characteristics in the Taguchi method were utilized. These quality characteristics for “the smaller is better” and “the larger is better” were given in Equation 1 and Equation 2 [26], respectively.

$$(S/N)_{SB} \text{ for } \sigma = -10 \cdot \log \left( n^{-1} \sum_{i=1}^n (y_i)^2 \right) \quad (1)$$

$$(S/N)_{HB} \text{ for } \mu = -10 \cdot \log \left( n^{-1} \sum_{i=1}^n (y_i^2)^{-1} \right) \quad (2)$$

In these equations, n signifies the number of numerical calculations for a trial and y<sub>i</sub> is i<sup>th</sup> result identified. Signal to Noise (S/N) ratios based on numerical repossess were calculated using Equation 1 and Equation 2. Statistical analysis, graphics and figures based on this analysis were obtained using Minitab R15 program. Besides of that, analysis of variance was performed at 95 % confidence level.

## 3. Finite Element Analysis

Finite element examines were completed utilizing ANSYS Workbench software. The cross-sectional dimensions of beams were chosen as 2 mm x 20 mm. In addition, the beam length was determined as 200 mm. Each beam was examined under the clamped-free (C-F) boundary conditions. In mesh operation, element order was determined as quadratic. Element size was determined as 0.5. Thus, 64000 elements and 310169 nodes were used in the numerical analyses. Equivalent (von-Mises) was utilized as stress component. The forces were applied to the free end of the beams. Stress life was determined as analysis type. Design life was used as 10<sup>9</sup> and all bodies of beams were assumed as geometry. Also, scale factor was utilized as 1. Mean stress correction theory for safety factor and equivalent alternating stress of beams were performed in accordance with Soderberg. Constant amplitude load fully reversed and means stress correction theory were illustrated in Figure 1.

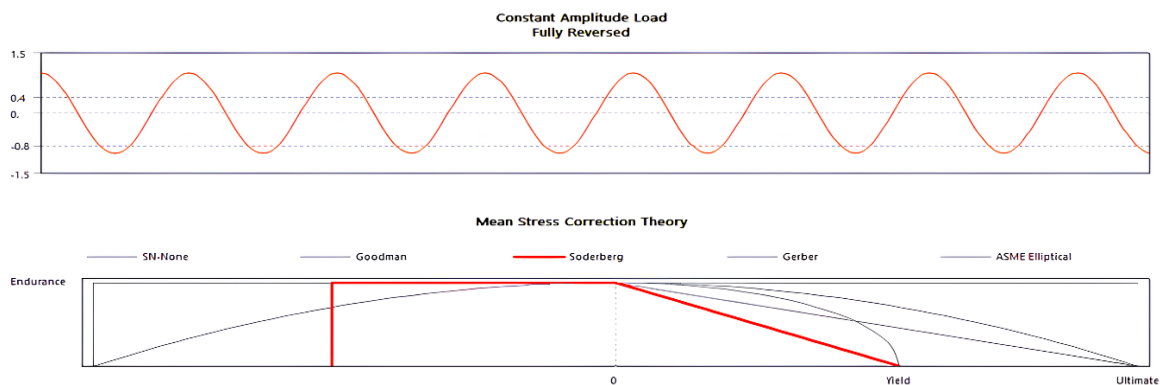


**Figure 1.** Constant amplitude load fully reversed and means stress correction theory [25]



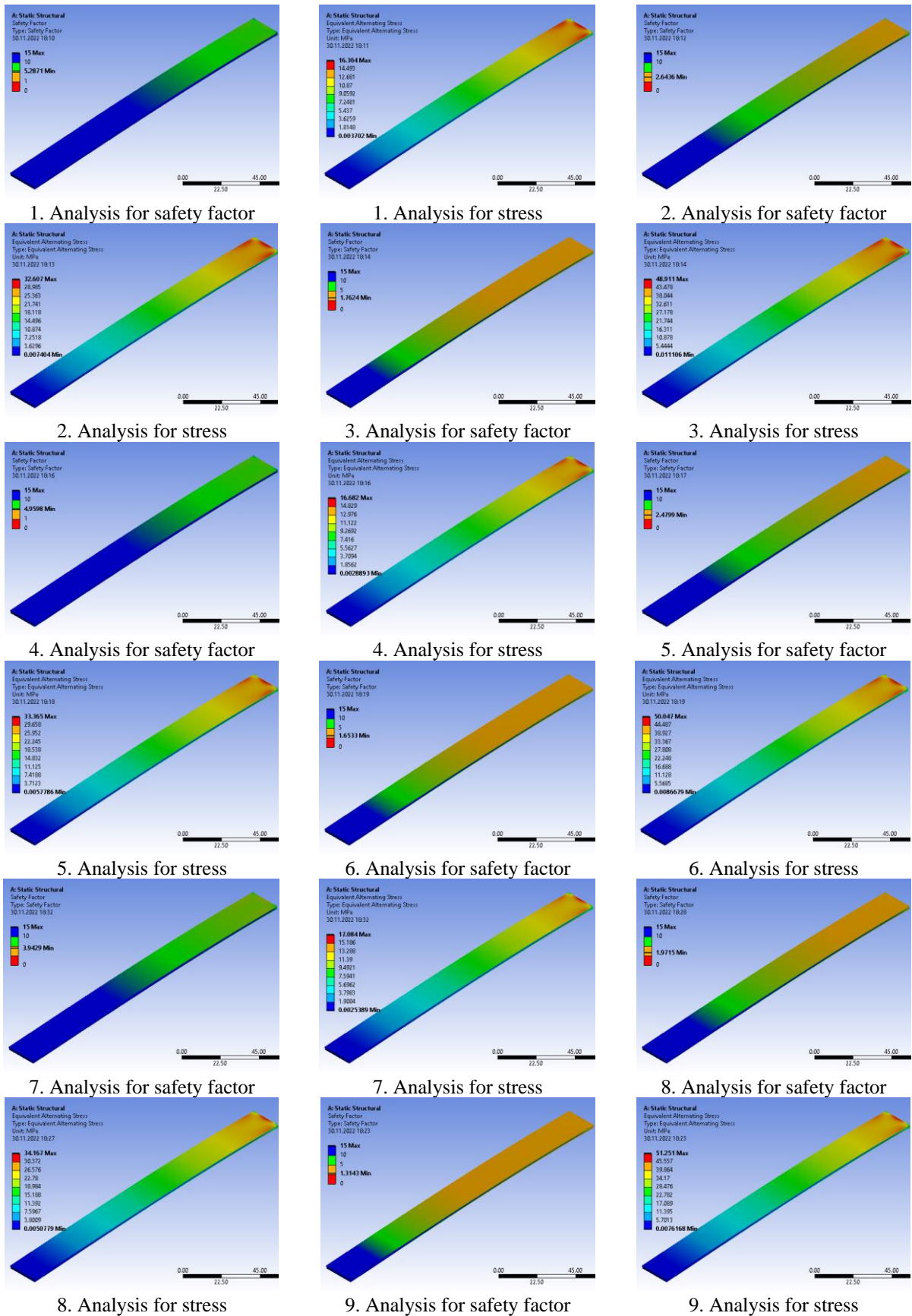


Figure 2. Numerical results for L9 orthogonal array

#### 4. Results and Discussions

This numerical and statistical research paper deals with the evaluate the effect of forces and material types on safety factor ( $\mu$ ) and equivalent alternating stress ( $\sigma$ ) of beams under clamped-free boundary conditions utilizing finite element and Taguchi approaches. Finite element and S/N ratio results were indicated in Table 3. It shows that overall means for safety factor and equivalent alternating stress in accordance with Taguchi L9 orthogonal array were found as  $\bar{T}_\mu = 2.8905$  and  $\bar{T}_\sigma = 33.3798$  MPa, respectively.

As seen in Figure 2, while the red regions are the most affected parts, the least affected parts are the blue regions.

To select the significance of force and material type towards on safety factor and equivalent alternating stress, analysis of variance (ANOVA) was implemented in accordance with 95 % confidence level. The results were tabled in Table 4.

**Table 3.** Finite element and S/N results

No	Variables		Results			
	A	B	Safety Factor $\mu$ (-)	S/N $\eta$ (dB)	Equivalent Alternating Stress $\sigma$ (MPa)	S/N $\eta$ (dB)
1	A <sub>1</sub>	B <sub>1</sub>	5.2871	14.4644	16.3040	-24.2459
2	A <sub>1</sub>	B <sub>2</sub>	2.6436	8.4439	32.6070	-30.2662
3	A <sub>1</sub>	B <sub>3</sub>	1.7624	4.9221	48.9110	-33.7881
4	A <sub>2</sub>	B <sub>1</sub>	4.9598	13.9093	16.6820	-24.4450
5	A <sub>2</sub>	B <sub>2</sub>	2.4799	7.8887	33.3650	-30.4658
6	A <sub>2</sub>	B <sub>3</sub>	1.6533	4.3670	50.0470	-33.9876
7	A <sub>3</sub>	B <sub>1</sub>	3.9429	11.9163	17.0840	-24.6518
8	A <sub>3</sub>	B <sub>2</sub>	1.9715	5.8959	34.1670	-30.6721
9	A <sub>3</sub>	B <sub>3</sub>	1.3143	2.3739	51.2510	-34.1940
Overall Means			2.8905	-	33.3798	-

#### 4.1. Determination of Optimal Levels

**Table 4.** ANOVA outcomes

Source	DF	Safety Factor					Equivalent Alternating Stress				
		Seq SS	Adj MS	F	P	% Effect	Seq SS	Adj MS	F	P	% Effect
A	2	1.101	0.551	9.31	0.03	6.29	3.65	1.83	12	0.02	0.22
B	2	16.158	8.079	136.6	0	92.35	1671.30	835.65	5492.63	0	99.75
Error	4	0.237	0.059			1.35	0.61	0.15			0.04
Total	8	17.495				100	1675.56				100
R-Sq = 98.65% and R-Sq(adj) = 97.30%						R-Sq = 99.96% and R-Sq(adj) = 99.93%					

It was found that force and material type are significant determining parameters for responses since p values are less than 0.05 value. The best effective determining factors on safety factor were determined to be material type with 92.35% effect and force with 6.29 % effect, respectively. Error data was found as 1.35 for safety factor. In addition, the most meaningful determining parameters on equivalent alternating stress of beam were detected as material type with 99.75 % effect and force

with 0.22 % effect, respectively. Error data for equivalent alternating stress was calculated as 0.04. To decide the determining factors consisting of optimal levels on safety factor and equivalent alternating stress of beams, the overall of each response characteristic (S/N ratios and numerical data) for all determining factors at each level were calculated. The response table was presented in Table 5.



**Table 5.** Response table for S/N ratios and means

Level	Safety Factor				Equivalent Alternating Stress			
	S/N data (dB)		Means (-)		S/N data (dB)		Means (MPa)	
	A	B	A	B	A	B	A	B
1	9.277	13.430	3.231	4.730	-29.43	-24.45	32.61	16.69
2	8.722	7.410	3.031	2.365	-29.63	-30.47	33.36	33.38
3	6.729	3.888	2.410	1.577	-29.84	-33.99	34.17	50.07
<b>Delta</b>	2.548	9.542	0.821	3.153	0.41	9.54	1.56	33.38
<b>Rank</b>	2	1	2	1	2	1	2	1

From Table 5, the determining factors with the optimal levels for safety factor were selected as force and material type at the first levels. Also, the optimal levels of the determining factors for equivalent alternating stress were determined as the first levels of force and material type. Thus, designations for safety factor and equivalent alternating stress were calculated as  $A_1B_1$  and  $A_1B_1$ , respectively.

#### 4.2. Effects of Determining Factors

To evaluate the impact of force and material type on safety factor and equivalent alternating stress of beams, the numerical calculations were executed utilizing L9 orthogonal array. The average data of safety factor and equivalent alternating stress in accordance with all variable determining factor at level 1, 2, and 3 depending on finite element data and S/N ratio values were plotted in Figure 3a and Figure 3b, respectively.

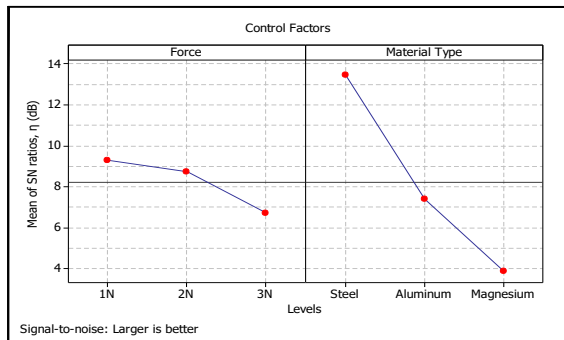


**Figure 3.** Influence of force and material type on safety factor

Figure 3 indicates that safety factor decreases with the increase of levels of force values and material types. As can be understood from Figure 4, the increase of levels of force values and material types causes the increase of equivalent alternating stress.

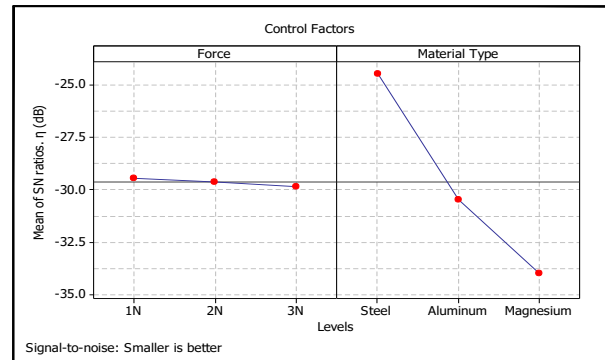


**Figure 4.** Influence of force and material type on equivalent alternating stress

These findings are due to the increase in the mechanical properties of the materials and the increase in the applied force value. The increase in the mechanical properties of the material can cause a decrease in the stress value. In this context, the mechanical properties of structural steel are higher than other materials. In addition, the increased force value can cause a decrease in the fatigue of the material. Increased fatigue can affect the safety factor of materials. Therefore, beams made of materials with high mechanical properties for high safety factor can be used under low force applications. This determination can be used in fatigue analysis.

#### 4.3. Estimation of Optimum Responses

The optimum data of safety factor and equivalent alternating stress for the optimal levels of important variables which have already been chosen as force and material type at the first levels. The estimated numerical data of the responses may be considered using Equation 3 [26].

$$\mu_i = \bar{A}_1 + \bar{B}_1 - \bar{T}_i \quad (3)$$

In Equation 3, the overall means of responses in agreement with Taguchi L9 orthogonal array were expressed as  $\bar{T}_i$  and the overall means for safety factor and equivalent alternating stress were calculated as  $\bar{T}_\mu = 2.8905$  and  $\bar{T}_\sigma = 33.3798$ , respectively.  $\bar{A}_1$  and  $\bar{B}_1$  show average data of responses at the first levels of force and material type.  $\bar{A}_1 = 3.231$  and  $\bar{B}_1 = 4.730$  was calculated for safety factor and  $\bar{A}_1 = 32.61$  and  $\bar{B}_1 = 16.69$  were determined for equivalent alternating stress. Substituting the data calculated for different terms,  $\mu_\mu = 5.0705$  for safety factor and  $\mu_\sigma = 15.9202$  MPa for equivalent alternating stress were obtained. Numerical and estimated results were demonstrated in Table 6.

Biaxiality indication, damage, and life for optimal designation were illustrated in Figure 4. From Figure 4, beam life and damage were calculated as  $10^6$  cycles and 1000, respectively. Also, the most affected part of beam for biaxiality indication was monitored as clamped end of beam.

**Table 6.** Numerical and estimated results

Test	Response	Numerical Result	Estimated Result	% Diff.
A <sub>1</sub> B <sub>1</sub>	Safety Factor	5.2871	5.0705	4.097
	Stress (MPa)	16.3040	15.9202	2.354

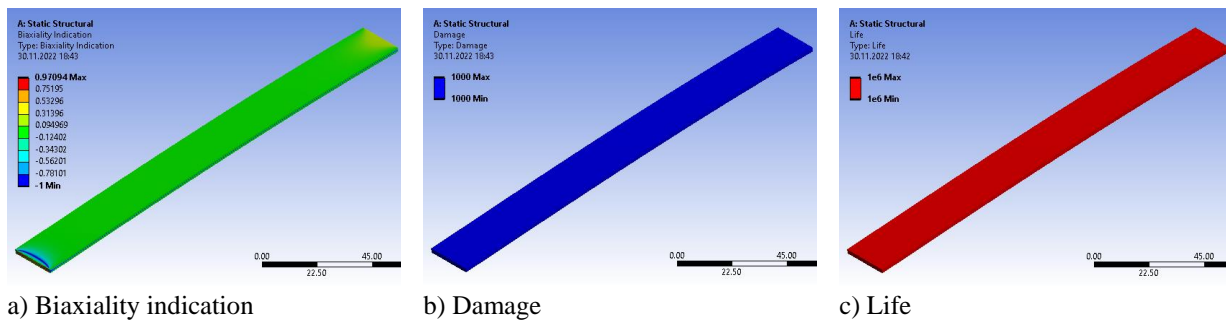


**Figure 4.** Fatigue result of beams with optimal levels: a) biaxiality indication , b) damage, and c) life

## 5. Conclusions

In this study, effect of force and material type on safety factor and equivalent alternating stress of beams with clamped-free boundary conditions was investigated utilizing numerical and Taguchi approaches. ANSYS Workbench software was implemented as numerical approach. Numerical solutions were achieved utilizing Taguchi L9 orthogonal array consisting of two determining factors, which have three levels. Force and material type were assumed as determining factors. Determining factors with optimum levels and their effects were selected utilizing analysis of signal-to-noise ratio. In addition, % effect and significant level of each determining factor on safety factor and equivalent alternating stress were obtained by ANOVA.

The conclusions of the mathematical paper may be presented as follows:

- Increase of forces applied at the free end of beams causes a decreasing in safety factor and an increase in equivalent alternating stress.
- The optimum material for safety factor and equivalent alternating stress was chosen as structure steel compared to aluminum and magnesium materials.
- The most meaningful determining parameters on safety factor were found as material type with 92.35% impact and force with 6.29 % impact, respectively.

- The most efficient determining parameters on equivalent alternating stress were noticed as material type with 99.75 % impact and force with 0.22 % impact, respectively.
- Differences between numerical and estimated results obtained using determining factors with optimum levels were calculated as 4.097 % for safety factor and 2.354 % for equivalent alternating stress.

## Author's Contributions

**Savaş Evran:** Created and composed the manuscript, conducted the result analysis.

## Ethics

There are no ethical issues after the publication of this manuscript.

## References

- [1]. Pamuk, Ö., Durgutlu, A. 2018. Patlama kaynağı yöntemi ile birleştirilen östenitik paslanmaz çelik (AISI 316L)-S235JR kompozit malzemelerde patlayıcı oranının mikroyapı ve yorulma özelliklerine etkisi. *Politeknik Dergisi*, 21: 527-34.
- [2]. Aydın, Ş. 2006. Sürtünme karıştırma kaynağı ile yapılan alüminyumun kaynağında kaynak bölgesinin eğmeli yorulma dayanımının incelenmesi. *Politeknik Dergisi*, 9: 125-30.
- [3]. Cakiroglu, R., Günay, M. 2021. Elektro erozyonla tornalama yöntemiyle işlenen soğuk iş takım çeliğinin yorulma ömrünün tahmini. *Politeknik Dergisi*, 24: 495-502.



- [4]. Shetye, N., Karlsson, M.H., Wennhage, P., Barsoum, Z. 2022. Life-Cycle Energy Analysis of a High Strength Steel Heavy Vehicle Component Subjected to Fatigue Loading. *Procedia Structural Integrity*, 38: 538-45.
- [5]. Zhao, X., Jin, N., Liu, X., Shi, Z. 2022. Fatigue failure analysis of steel crane beams with variable-section supports. *Engineering Failure Analysis*, 136: 106217.
- [6]. Feng, R., Chen, P.-Y., Wang, F., Xu, Y., Zhu, J.-H. 2022. Fatigue life of C-FRCM strengthened corroded RC continuous beams under multi-intervention system. *Composite Structures*, 290: 115512.
- [7]. Gao, L., Sun, C., Zhuang, M.-L., Hou, M. 2022. Fatigue life prediction of HTRB630E steel bars based on modified coffin-manson model under pre-strain. *Structures*, 38: 28-39.
- [8]. Oller, S., Salomón, O., Oñate, E. 2005. A continuum mechanics model for mechanical fatigue analysis. *Computational Materials Science*, 32: 175-95.
- [9]. Zalnezhad, E., Sarhan, A.A., Hamdi, M. 2013. Investigating the fretting fatigue life of thin film titanium nitride coated aerospace Al7075-T6 alloy. *Materials Science and Engineering: A*, 559: 436-46.
- [10]. Cheng, G., Plumtree, A. 1998. A fatigue damage accumulation model based on continuum damage mechanics and ductility exhaustion. *International Journal of Fatigue*, 20: 495-501.
- [11]. Shang, D.-G., Yao, W.-X. 1999. A nonlinear damage cumulative model for uniaxial fatigue. *International Journal of Fatigue*, 21: 187-94.
- [12]. Svensson, T. 2002. Cumulative fatigue damage taking the threshold into account. *Fatigue & Fracture of Engineering Materials & Structures*, 25: 871-5.
- [13]. Jono, M. 2005. Fatigue damage and crack growth under variable amplitude loading with reference to the counting methods of stress-strain ranges. *International Journal of Fatigue*, 27: 1006-15.
- [14]. Makkonen, M. 2009. Predicting the total fatigue life in metals. *International Journal of Fatigue*, 31: 1163-75.
- [15]. Zhu, S.P., Huang, H.Z. 2010. A generalized frequency separation-strain energy damage function model for low cycle fatigue-creep life prediction. *Fatigue & Fracture of Engineering Materials & Structures*, 33: 227-37.
- [16]. Majzoobi, G., Hojjati, R., Nematian, M., Zalnejad, E., Ahmadvani, A., Hanifepoor, E. 2010. A new device for fretting fatigue testing. *Transactions of the Indian Institute of Metals*, 63: 493-7.
- [17]. Kulkarni, S.S., Sun, L., Moran, B., Krishnaswamy, S., Achenbach, J. 2006. A probabilistic method to predict fatigue crack initiation. *International Journal of Fracture*, 137: 9-17.
- [18]. Scott-Emuakpor, O.E., Shen, H., George, T., Cross, C. 2008. An energy-based uniaxial fatigue life prediction method for commonly used gas turbine engine materials. *Journal of engineering for gas turbines and power*, 130.
- [19]. Turna, E., Kafkas, F., Şeker, U., Yücesu, H.S. 2018. Kauçuk hava süspansiyon körüklerinin üretim yöntemi ve yorulma ömrünün ürün kalitesi üzerine etkisinin belirlenmesi. *Politeknik Dergisi*, 21: 759-64.
- [20]. Metkar, R., Sunnapwar, V., Hiwase, S. 2011. A fatigue analysis and life estimation of crankshaft-a review. *International Journal of Mechanical and Materials Engineering*, 6: 425-30.
- [21]. Satyanarayana, N., Sambaiah, C. 2012. Fatigue analysis of Aluminum Alloy wheel under radial load. *International Journal of Mechanical and Industrial Engineering (IJMIE)*, ISSN: 1-6.
- [22]. Patel, S., Kumar, V., Nareliya, R. 2013. Fatigue analysis of rail joint using finite element method. *International Journal of Research in Engineering and Technology*, 2: 80-4.
- [23]. Sameer Chakravarthy, N.C., Subbaratnam, B. 2014. Finite element analysis and fatigue analysis of spur gear under random Loading. *International Journal of Mechanical Engineering & Robotics Research*, 3: 533-41.
- [24]. Tulsidas, D., Shantharaja, M., Bharath, V.G. 2014. Life Estimation of a Steam Turbine Blade Using Low Cycle Fatigue Analysis. *Procedia Materials Science*, 5: 2392-401.
- [25]. ANSYS. *Software (ANSYS Inc., Canonsburg, PA, USA) (www.ansys.com)*.
- [26]. Ross, P.J. *Taguchi Techniques for Quality Engineering*, McGraw-Hill International Editions, 2nd Edition, New York, USA, 1996.

# Microwave-Assisted Fabrication of Pd, Co and Ni Nanoparticles Modified-SiO<sub>2</sub>; as Catalysts in the Reduction Reaction of Organic Pollutants

Sevtap Çağlar Yavuz<sup>1\*</sup> , Emre Yavuz<sup>2</sup> , Serkan Dayan<sup>3</sup> 

<sup>1\*</sup> Department of Medical Services and Technicians, Ilic Dursun Yildirim Vocational School, Erzincan Binali Yildirim University, Erzincan, Türkiye

<sup>2</sup> Department of Medical Services and Technicians, Cayirli Vocational School, Erzincan Binali Yildirim University, Erzincan, Türkiye

<sup>3</sup> Drug Application and Research Center, Erciyes University, Kayseri, Türkiye

\* [sevtap.yavuz@erzincan.edu.tr](mailto:sevtap.yavuz@erzincan.edu.tr)

\* Orcid: 0000-0001-6497-2907

Received: 17 July 2023

Accepted: 26 November 2023

DOI: 10.18466/cbayarfbe.1327271

## Abstract

Nanomaterials have been used in catalytic degradation of organic pollutants also act as catalysts in for many years. Due to excellent catalytic performances of metal-based nanoparticles, these materials have been used extensively in various hybrid catalyst synthesis. The main subject of this study, heterogeneous catalysis is a low cost and multi-purpose process for many pollutants. Catalytic degradation of organic pollutants such as; 2-nitrophenol, quinolin yellow and rhodamine B was investigated by using Ni, Co, Pd nanoparticles modified SiO<sub>2</sub> based nanomaterials. The co-doping effect on the prepared nanomaterials has been investigated with different characterization methods in terms of structural and morphological features: scanning electron microscopy, UV/vis absorption spectroscopy, energy-dispersive X-ray spectroscopy and Fourier-transform infrared spectroscopy. The highest catalytic reduction efficiencies (97.6% and 97.5%) for 2-nitrophenol and rhodamine B was obtained by Pd-PEG-AP@SiO<sub>2</sub> respectively. The synthesized Co-PEG-AP@SiO<sub>2</sub> illustrated higher catalytic reduction efficiency for quinolin yellow (70.1%) at the end of 60s. The prepared M-PEG-AP@SiO<sub>2</sub> nanomaterial (M: Pd,Co,Ni) can be able to utilized degradation of organic contaminants effectively.

**Keywords:** Catalysts, Catalytic degradation, Nanoparticles, SiO<sub>2</sub> nanomaterials

## 1. Introduction

Degradation of organic contaminants such as dyes and nitro-aromatic compounds by chemical methods can be performed quickly, simply and with high efficiency. However, removing them with new generation nanomaterials is more environmentally friendly and feasible. It is essential to combine these methods with today's nanomaterials in order to both increase the efficiency and reduce the removal costs, especially in the methods in which reducing agents such as NaBH<sub>4</sub>, which is one of the chemical degradation methods, are used [1,2]. Catalytic degradation is an environmentally friendly technique that has emerged as a promising alternative for the remediation of various organic pollutants [3]. Heterogeneous catalyst applications are the basis of many chemical technologies used today.

The application fields of heterogeneous catalysis include chemical production, environmental technologies, energy storage and conversion [4]. Over the last decades, nanotechnology and nanomaterials have been of great interest, as it is foreseen that it will be an important step for a sustainable future. [5]. These nanoscale composites take part in numerous applications in most heterogeneous catalysis. [6-9]. Due to their high activity noble metals such as Pd, Pt, Rh [10] are often used as co-catalysts in catalytic reactions. However, because noble metals are expensive and scarce, low-cost and high-yield alternatives such as non-noble metals such as Ni and Co are highly preferred [11-16]. In recent years, the release of many toxic and harmful pollutants into the environment has increased gradually due to the rapid progress of modern industry and agriculture.

Organic pollutants in air and water, which are widely noticed among these pollutants, are potentially toxic and carcinogenic [17]. Organic dyes used in textile and food industries are an important source of environmental pollution. Dyes often have carcinogenic effects on humans and are also toxic to aquatic life [18].

Rhodamine B (Rh B) is an important xanthene dye that has many applications in textile, paper, dye and leather production [19,20]. Quinolin yellow (QY), an organic pollutant, is also a food coloring. Adsorption, oxidation, reduction, electrochemical and membrane filtration methods are widely applied to remove these pollutants in domestic and industrial wastewaters [21,22]. 2-Nitrophenol (2-NP), 3-nitrophenol (3-NP), 4-nitrophenol (4-NP) are among the most persistent organic pollutants found in wastewaters by virtue of their high stability and solubility [23]. The degradation of these contaminants have been studied for last years. In order to enhance the photocatalytic degradation performance of metal based nanoparticles (Co, Ag<sub>2</sub>O, Pd, Cu, Ni) they should be well-decorated on templates graphene, SiO<sub>2</sub> etc. [24-27].

The objective of this investigation is synthesis and characterization of Pd/SiO<sub>2</sub>, Co/SiO<sub>2</sub> and Ni/SiO<sub>2</sub> nanomaterials and using for catalytic degradation of aqueous solutions of 2-NP, QY and Rh B dyes.

## 2. Material and Methods

All reagents and solvents were purchased from commercial suppliers and used without further purification. The molecular interactions among the SiO<sub>2</sub> and metallic nanoparticles were affirmed by FT-IR (Fourier-transform infrared spectroscopy) analysis using Perkin Elmer 400 FT-IR/FT-FIR Spectrometer Spotlight 400 Imaging System. The surface morphological characterization was performed by FE-SEM (Field emission scanning electron microscopy), EDX (Energy-dispersive X-ray spectroscopy), and mapping analysis using Zeiss GeminiSEM 500. The immobilization of nanoparticles on SiO<sub>2</sub> was examined by X-ray diffraction (Malvern analytical XRD). The concentration of nitrophenol and dyes were determined by The UV-vis spectrophotometer (Shimadzu UV-2700).

### 2.1. Synthesis of Compounds

#### 2.1.1. General Procedure for the Synthesis of Pd/SiO<sub>2</sub>, Co/SiO<sub>2</sub> and, Ni/SiO<sub>2</sub> Nanomaterials

In order to synthesis Pd/SiO<sub>2</sub> nanomaterial, the previous method in literature was modified [28]. 0.5 g 3-amino functionalized silica gel, 0.025 g PEG P123 and 0.0886 g PdCl<sub>2</sub> were weighted and dissolved in 20 ml ultrapure water. After that this mixture was transferred into 25 ml Teflon-lined stainless steel

hydrothermal unit. The hydrothermal unit was heated in microwave oven at 600 W for 10 minute and then cooled to room temperature. 0.0378 g NaBH<sub>4</sub> was added to this mixture and was heated in microwave oven at 600 W for 10 minutes again. The precipitates were filtered and washed with ultrapure water, ethanol, respectively. The obtained nanomaterial was dried at 60 °C at for 3 hours.

For synthesis of Co/SiO<sub>2</sub> and Ni/SiO<sub>2</sub> nanomaterials, Co(NO<sub>3</sub>)<sub>2</sub>.6H<sub>2</sub>O (0.1455 g) and Ni(NO<sub>3</sub>)<sub>2</sub>.6H<sub>2</sub>O (0.1454 g) was weighted and the similar procedure that described above was performed.

## 2.2. Model Reduction Reaction with Fabricated Catalysts

The catalytic efficiencies of Pd-PEG-AP@SiO<sub>2</sub>, Co-PEG-AP@SiO<sub>2</sub>, and Ni-PEG-AP@SiO<sub>2</sub> nanoparticles were investigated about reduction reaction process and the 2-NP, QY, and Rh B were selected as reduced organic pollutants with BH<sub>4</sub><sup>-</sup> ion (in the optimum concentration) at ambient temperature in water. In brief, firstly, the Pd-PEG-AP@SiO<sub>2</sub>, Co-PEG-AP@SiO<sub>2</sub>, and Ni-PEG-AP@SiO<sub>2</sub> nanoparticles (5 mg) prepared and added to the reaction tube with the organic pollutants solution and NaBH<sub>4</sub> (0.03 M) as a hydrogen source in water (10 ml) at ambient temperature and different times. End of the desired time, the measurement example (approximately 2.5 ml) from the catalytic reaction were filtered through the micro-column with cotton for UV-vis spectrophotometer measurements in different nm range. The catalytic performances of Pd-PEG-AP@SiO<sub>2</sub>, Co-PEG-AP@SiO<sub>2</sub>, and Ni-PEG-AP@SiO<sub>2</sub> nanoparticles were monitored the absorption bands relating organic pollutants and the corresponding peaks were seen appeared and disappeared after reduction process on the UV-vis spectrum.

## 3. Results and Discussion

### 3.1. Synthesis and Characterization

#### FT-IR

The molecular interaction that occurred in the Pd-PEG-AP@SiO<sub>2</sub>, Co-PEG-AP@SiO<sub>2</sub>, and Ni-PEG-AP@SiO<sub>2</sub> nanoparticles were verified by infrared spectroscopy (FT-IR). The spectra of Pd-PEG-AP@SiO<sub>2</sub>, Co-PEG-AP@SiO<sub>2</sub>, and Ni-PEG-AP@SiO<sub>2</sub> nanoparticles are given in Figure 1 and the data of spectrums of nanoparticles are listed as follows;

*For Pd-PEG-AP@SiO<sub>2</sub>, FT-IR (cm<sup>-1</sup>):* 3292, 2980, 2941, 2878, 1709, 1620, 1565, 1549, 1515, 1403, 1338, 1048, 795, 784, 712, 704, 693, 682, 674, 660, 650, 619, 607, 602, 589, 574, 561, 547, 536, 520, 513, 451, 444, 435, 426, 418, 407, 402.



For Co-PEG-AP@SiO<sub>2</sub>, FT-IR (cm<sup>-1</sup>): 3683, 3675, 3664, 2988, 2972, 2901, 1451, 1406, 1394, 1383, 1249, 1241, 1229, 1225, 1074, 1066, 1056, 1050, 1028, 893, 880, 788, 745, 720, 709, 704, 685, 674, 666, 648, 638, 633, 626, 601, 590, 578, 570, 559, 554, 542, 530, 518, 513, 493, 471, 463, 454, 441, 433, 424, 417, 408.

For Ni-PEG-AP@SiO<sub>2</sub>, FT-IR (cm<sup>-1</sup>): 3684, 3675, 3661, 2988, 2972, 2901, 1626, 1451, 1406, 1394, 1382, 1249, 1241, 1226, 1066, 1054, 1028, 893, 880, 799, 789, 753, 744, 675, 668, 626, 602, 578, 570, 554, 539, 532, 526, 520, 471, 464, 449, 441, 430, 419, 412. According to the FT-IR data, the N-H/O-H, C-H (aliphatic) stretching bands were obtained between ≈ 3650-3200 cm<sup>-1</sup>, ≈ 3100-2800 cm<sup>-1</sup>, respectively. Also, the Si-O-Si and Si-O bands were assigned as 1150-1000 cm<sup>-1</sup> and 600-450 cm<sup>-1</sup>, respectively. Thus, the molecular structure of the fabricated nanomaterials is compatible with the FT-IR data (Figure 1).

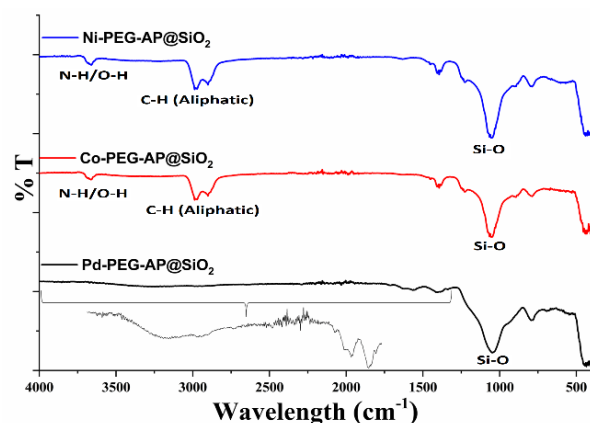


**Figure 1.** FT-IR spectra of the fabricated Pd-PEG-AP@SiO<sub>2</sub>, Co-PEG-AP@SiO<sub>2</sub>, and Ni-PEG-AP@SiO<sub>2</sub> nanoparticles.

### XRD

The X-ray diffraction pattern of the Pd-PEG-AP@SiO<sub>2</sub>, Co-PEG-AP@SiO<sub>2</sub>, and Ni-PEG-AP@SiO<sub>2</sub> are given in Figure 2.

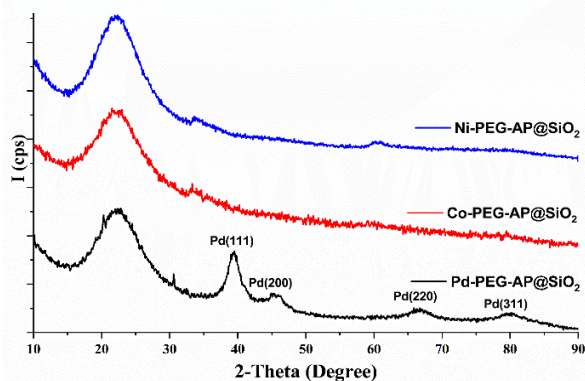


**Figure 2.** XRD pattern of the fabricated Pd-PEG-AP@SiO<sub>2</sub>, Co-PEG-AP@SiO<sub>2</sub>, and Ni-PEG-AP@SiO<sub>2</sub> nanoparticles.

The pattern of Pd-PEG-AP@SiO<sub>2</sub> was matched with JCPDS card: 87-064, but for other materials, the amorphous SiO<sub>2</sub> structure was recorded as the dominant pattern (Figure 2).

### SEM-EDX

The field emission scanning electron microscopy (FE-SEM), EDX, and Pd, Co, and Ni mapping analyses of Pd-PEG-AP@SiO<sub>2</sub>, Co-PEG-AP@SiO<sub>2</sub>, and Ni-PEG-AP@SiO<sub>2</sub> were carried out, and the surface morphologies, EDX, and elemental images are given in Figure 3-5. When the surface morphologies were examined, it was noted that the material containing Pd had a granular structure compared to other materials. It was observed that the materials containing Co and Ni formed a sheet-like morphology as shown in Figure 3. Considering the EDX images, the Si, C, O, N, Pd, Co, and Ni elements were registered as conforming to the structure. The presence of palladium, cobalt, nickel metals (Pd weight: ≈3.7%, Co weight: ≈2.7%, and Ni weight: ≈2.5% with EDX analysis) dispersed on Pd-PEG-AP@SiO<sub>2</sub>, Co-PEG-AP@SiO<sub>2</sub>, and Ni-PEG-AP@SiO<sub>2</sub> were confirmed by the EDX and elemental mapping method (Figure 4-5).

### 3.2. Catalytic Studies

We examined the catalytic performances of Pd-PEG-AP@SiO<sub>2</sub>, Co-PEG-AP@SiO<sub>2</sub>, and Ni-PEG-AP@SiO<sub>2</sub> nanoparticles by using the reduction of 2-NP, QY and Rh B in the presence of sodium borohydride (NaBH<sub>4</sub>) and deionized water at the ambient temperature. The performances of catalysts were monitored by UV-vis spectrophotometer due to the 2-nitrophenolate molecule (λ<sub>max</sub>= 414 nm). In the reduction of 2-NP, the solution of 2-NP (5.00E-04M) has a yellow colour of the absorption band from the 2-nitrophenolate molecule, and the colour gradually vanished due to the reaction product (2-aminophenol).

The catalytic performances were obtained as time-dependent between 10-180 s. The catalytic efficiencies of nanoparticles were achieved as 22.4%, 48.3%, and 97.6% for Pd-PEG-AP@SiO<sub>2</sub>, 11.1%, 22.4%, and 73.1% for Co-PEG-AP@SiO<sub>2</sub>, 11.0%, 11.1%, and 13.5% for Ni-PEG-AP@SiO<sub>2</sub> at the end of 10, 60, and 180 s, respectively (Figure 6).

Similarly, we were worked the reduction of QY (6.60E-05 M) and Rh B (2.09E-05 M) dyes by Pd-PEG-AP@SiO<sub>2</sub>, Co-PEG-AP@SiO<sub>2</sub>, and Ni-PEG-AP@SiO<sub>2</sub> nanoparticles under the same conditions.

For the reduction of QY, the absorption band at 414 nm disappeared as time-dependent between 10-60 s with the catalysts. The catalytic conversions were recorded as 29.2%, 36.0%, and 62.9% for Pd-PEG-AP@SiO<sub>2</sub>, 66.9%, 67.1%, and 70.1% for Co-PEG-



AP@SiO<sub>2</sub>, 58.6%, 59.8%, and 64.7% for Ni-PEG-AP@SiO<sub>2</sub> at the end of 10, 30, and 60 s, respectively (Figure 7).

We have also worked on the reduction of Rh B, the absorption band at 550 nm disappeared during the catalytic reaction. The conversions were founded as 95.1%, 96.6%, and 97.5% for Pd-PEG-AP@SiO<sub>2</sub>, 36.0%, 39.7%, and 40.8% for Co-PEG-AP@SiO<sub>2</sub>, 28.1%, 28.9%, and 34.4% for Ni-PEG-AP@SiO<sub>2</sub> at the end of 10, 30, and 60 s, respectively (Figure 8).

In addition, the kinetic equation for the catalytic reaction of organic pollutants can be represented as  $\ln(C_t/C_0) = -kt$ , where  $t$  is time for the catalytic reaction and,  $k$  is the apparent first-order rate constant ( $s^{-1}$ ) in Table 1. Also, the  $k' = k/M$  parameter ( $M$ : the amount of the catalyst) is introduced for quantitative comparison and the parameter is defined as the ratio of the rate constant  $k$  to the weight of the catalyst added [29].

The reaction rate constant parameters were compared for the fabricated Pd-PEG-AP@SiO<sub>2</sub>, Co-PEG-AP@SiO<sub>2</sub>, and Ni-PEG-AP@SiO<sub>2</sub> nanoparticles and as time-dependend. Our palladium-containing nanomaterial (Pd-PEG-AP@SiO<sub>2</sub>) was found to be highly effective when compared with catalysts made from similar substrates in the literature (Table-1).

According to the obtained data, the Pd-PEG-AP@SiO<sub>2</sub> nanoparticle was recorded as the most effective catalyst overall. However, it was noted that the Co-PEG-AP@SiO<sub>2</sub> nanoparticle performed better in the QY reduction reaction. The development of hybrid materials and their performance in catalytic reactions have gained importance in recent years. Also, the development of low-cost and one-pot materials is attracting more attention. Although the catalytic performance of rare elements (Pd, Ru, Pt etc.) is high, the catalytic performance of other metals is also frequently investigated. In particular, the development of materials containing other metals is supported by researchers.

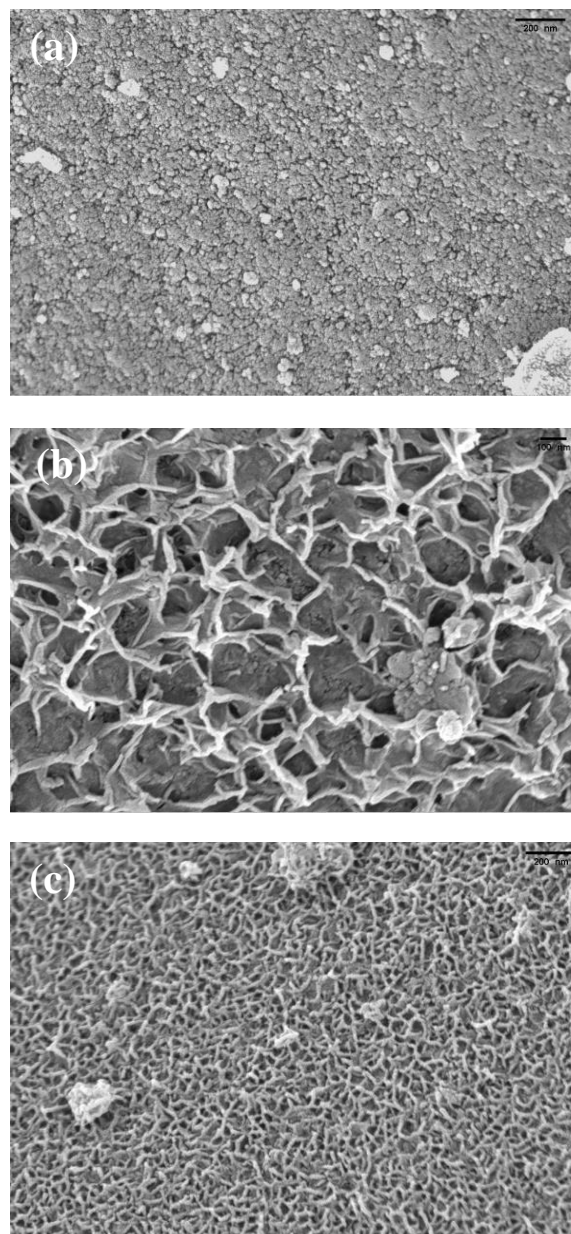


**Figure 3.** SEM images (50.00 KX) of the fabricated Pd-PEG-AP@SiO<sub>2</sub> (a), Co-PEG-AP@SiO<sub>2</sub> (b), and Ni-PEG-AP@SiO<sub>2</sub> (c) nanoparticles, respectively.

Herein, the good performance with the fabricated nanoparticles were achieved in the reduction of some organic pollutants such as 2-NP, QY and Rh B which it is known that the dyes are serious environmental pollutants. The reduction or removal of these type molecules is very important. The hybrid materials can be easily produced to reduce these harmful compounds with high activity.

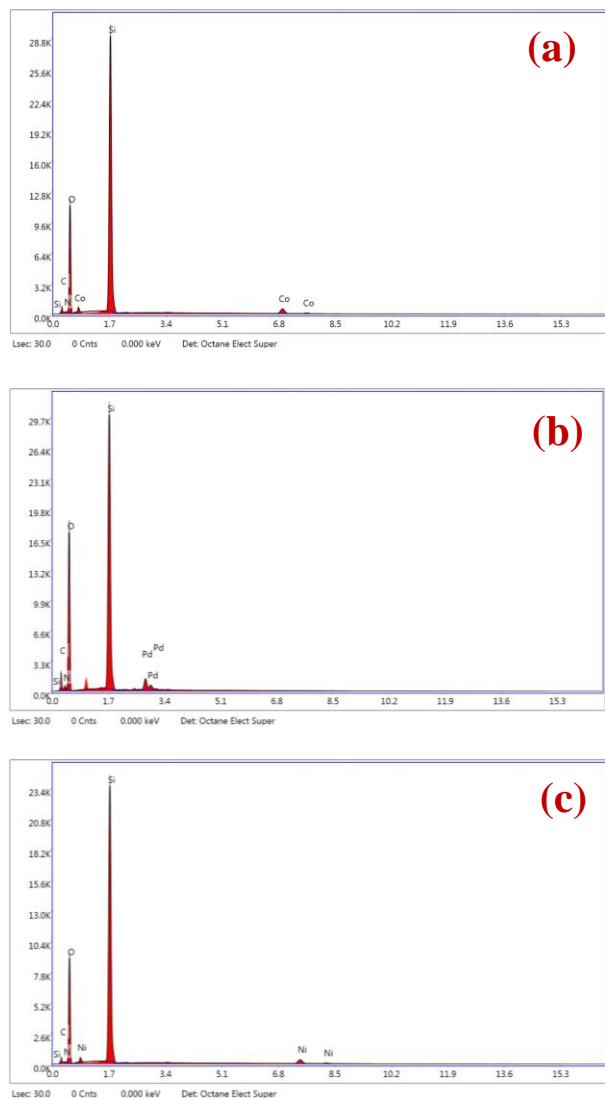


**Figure 4.** EDX images of the fabricated Pd-PEG-AP@SiO<sub>2</sub> (a), Co-PEG-AP@SiO<sub>2</sub> (b), and Ni-PEG-AP@SiO<sub>2</sub> (c) nanoparticles, respectively.

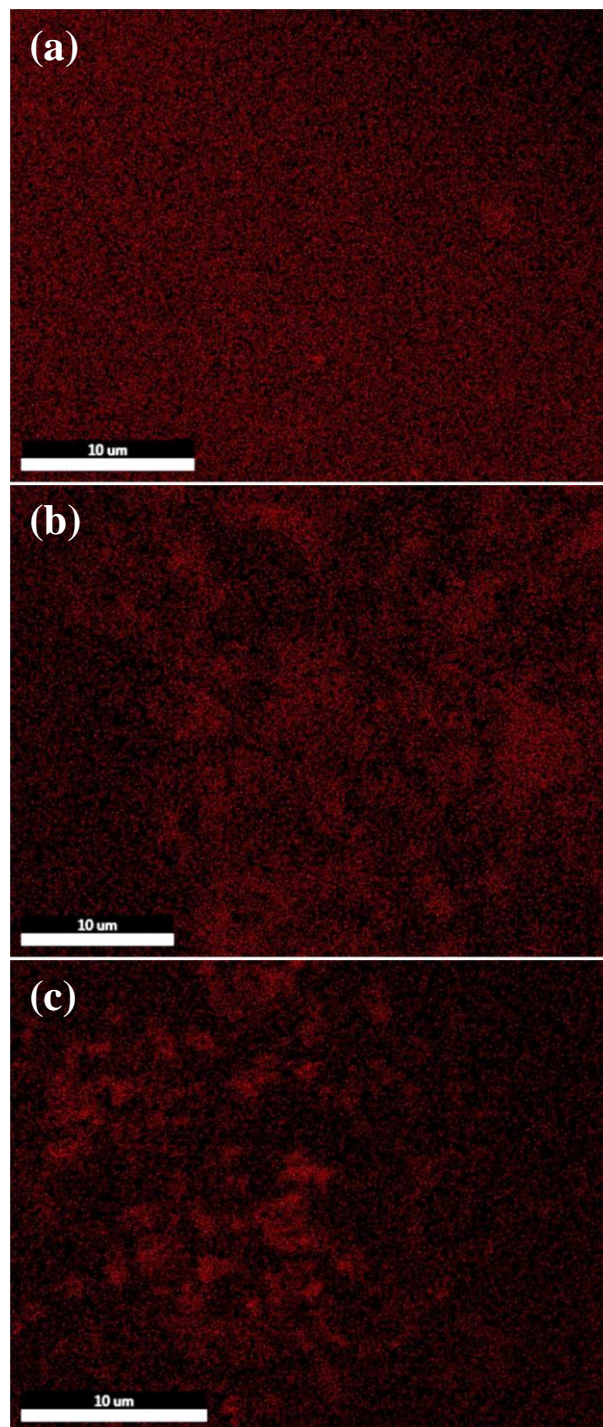


**Figure 5.** EDX-mapping images of the fabricated Pd-PEG-AP@SiO<sub>2</sub> (a) (Pd mapping), Co-PEG-AP@SiO<sub>2</sub> (b) (Co mapping), and Ni-PEG-AP@SiO<sub>2</sub> (c) (Ni mapping) nanoparticles, respectively

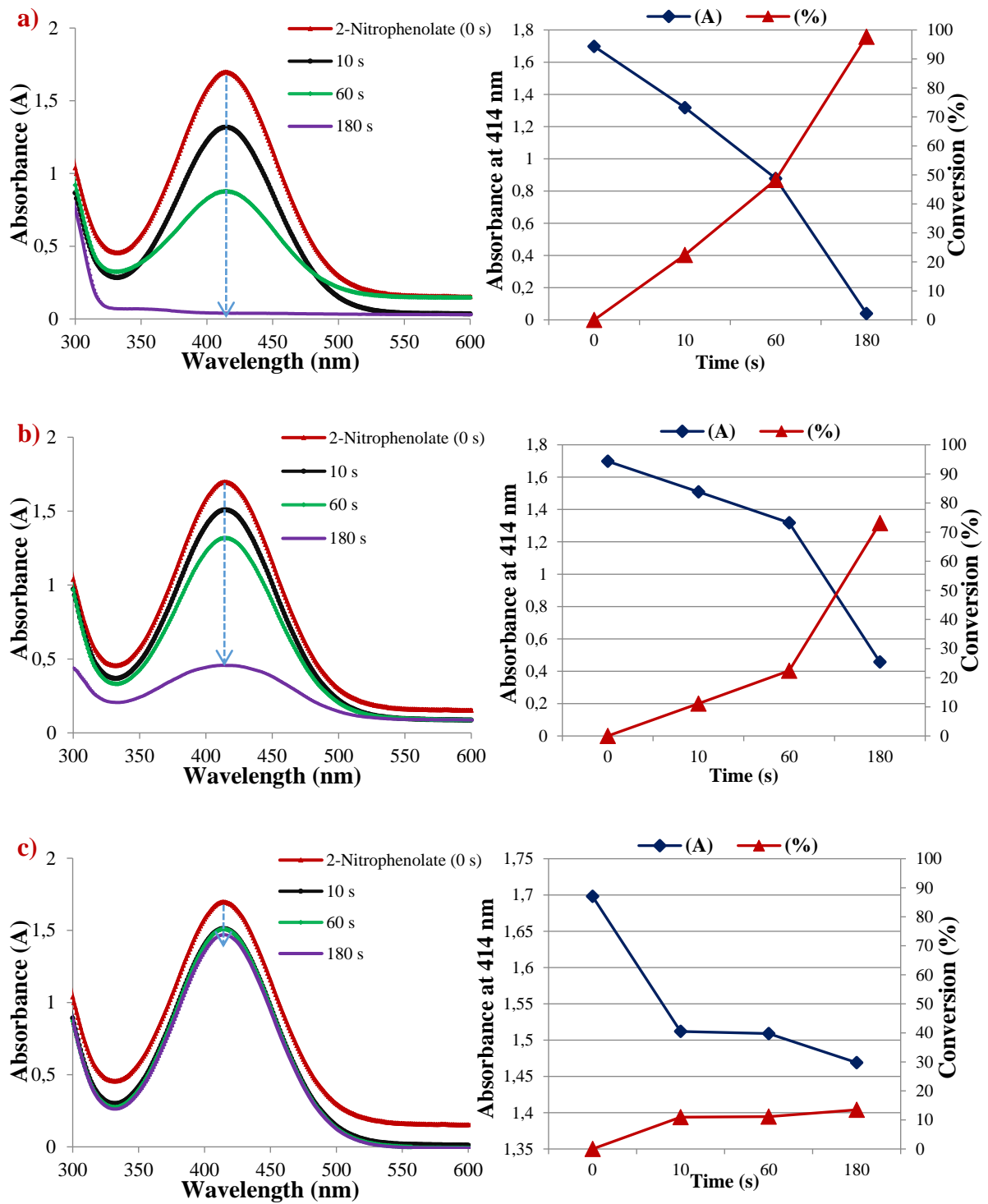


**Figure 6.** Time-dependent UV-vis absorption spectra of the 2-NP ( $5.00E-04$  M) reduced by  $\text{NaBH}_4$  catalyzed by Pd-PEG-AP@SiO<sub>2</sub> (a), Co-PEG-AP@SiO<sub>2</sub> (b), and Ni-PEG-AP@SiO<sub>2</sub> (c) nanoparticles, respectively.



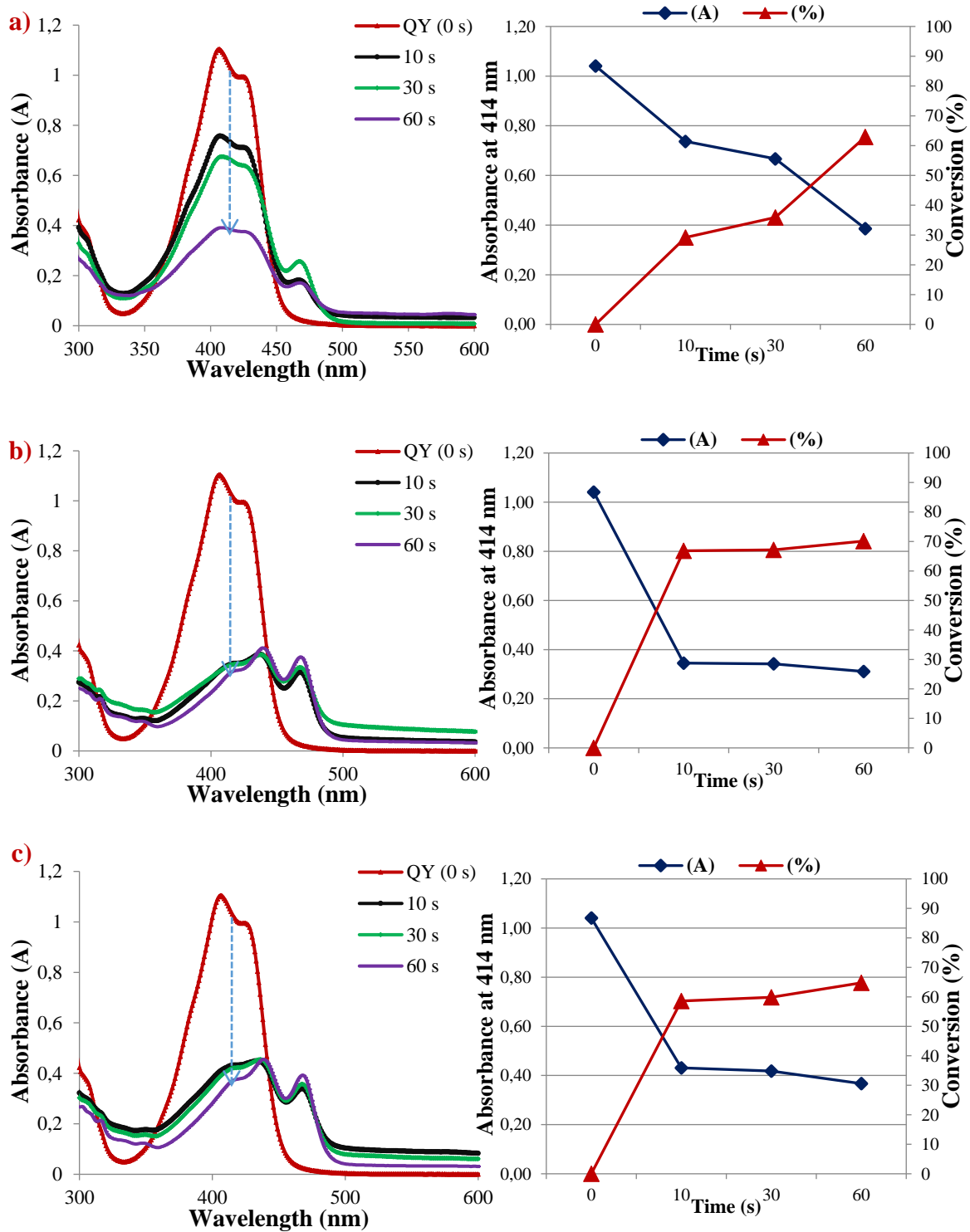


**Figure 7.** Time-dependent UV-vis absorption spectra of the QY ( $6.60\text{E-}05\text{ M}$ ) reduced by  $\text{NaBH}_4$  catalyzed by Pd-PEG-AP@SiO<sub>2</sub> (a), Co-PEG-AP@SiO<sub>2</sub> (b), and Ni-PEG-AP@SiO<sub>2</sub> (c) nanoparticles, respectively.

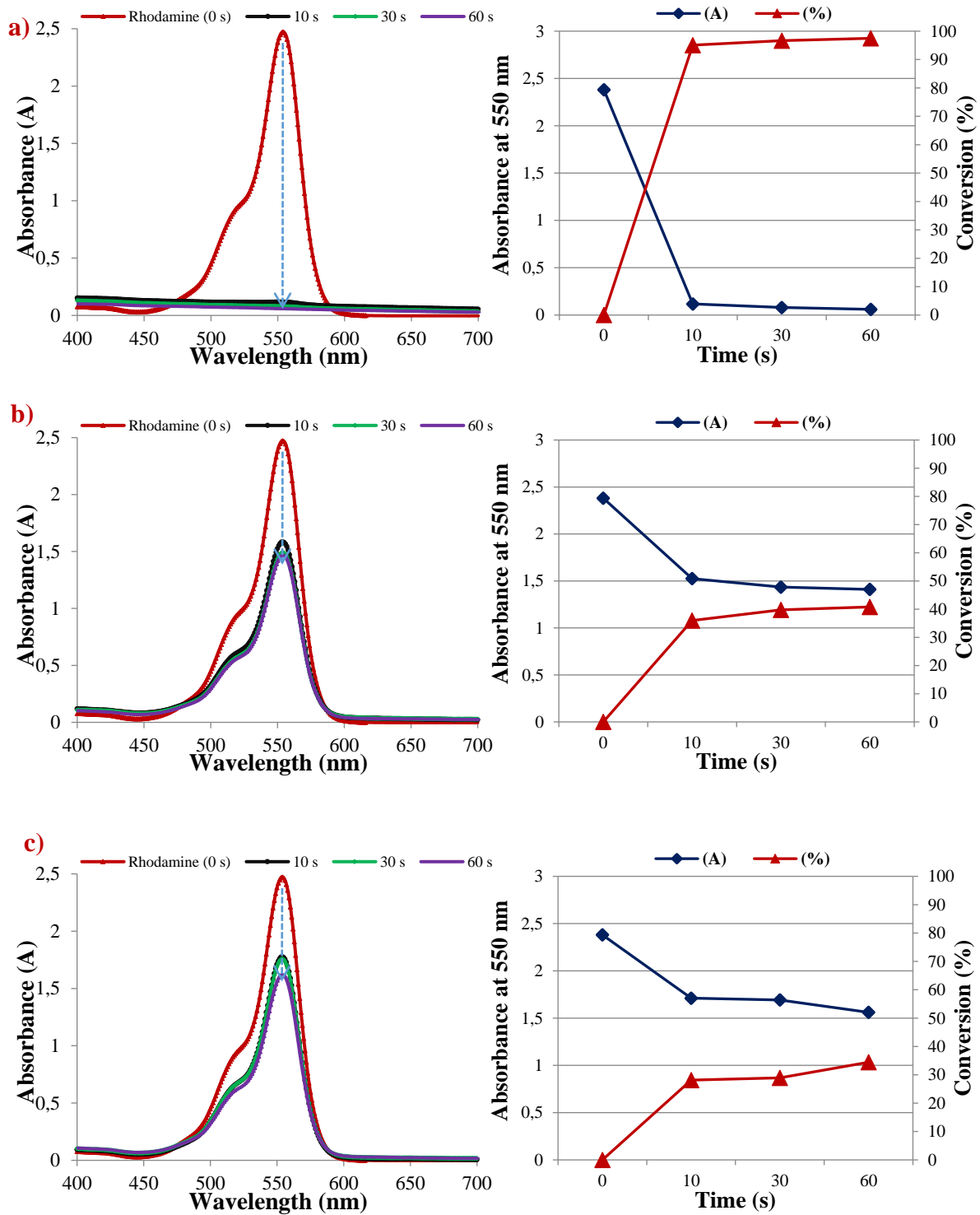


**Figure 8.** Time-dependent UV-vis absorption spectra of the Rh B (10 ppm ( $2.09 \times 10^{-5}$  M)) reduced by  $\text{NaBH}_4$  catalyzed by Pd-PEG-AP@ $\text{SiO}_2$  (a), Co-PEG-AP@ $\text{SiO}_2$  (b), and Ni-PEG-AP@ $\text{SiO}_2$  (c) nanoparticles, respectively.



**Table 1.** The catalytic efficiency rate constant of Pd-PEG-AP@SiO<sub>2</sub>, Co-PEG-AP@SiO<sub>2</sub>, and Ni-PEG-AP@SiO<sub>2</sub> catalysts.

Catalyst	Substrate	k (s <sup>-1</sup> ) <sup>a</sup>			k/M (s <sup>-1</sup> g <sup>-1</sup> ) <sup>b</sup>		
Pd-PEG-AP@SiO <sub>2</sub>	2-NP	2.53E-02 <sup>c</sup>	1.10E-02 <sup>e</sup>	2.08E-02 <sup>f</sup>	5.07E+00 <sup>c</sup>	2.20E+00 <sup>e</sup>	4.16E+00 <sup>f</sup>
Co-PEG-AP@SiO <sub>2</sub>	2-NP	1.18E-02 <sup>c</sup>	4.22E-03 <sup>e</sup>	7.29E-03 <sup>f</sup>	2.36E+00 <sup>c</sup>	8.44E-01 <sup>e</sup>	1.46E+00 <sup>f</sup>
Ni-PEG-AP@SiO <sub>2</sub>	2-NP	1.16E-02	1.97E-03	8.05E-04	2.32E+00	3.93E-01	1.61E-01
Pd-PEG-AP@SiO <sub>2</sub>	QY	3.45E-02 <sup>c</sup>	1.48E-02 <sup>d</sup>	1.65E-02 <sup>e</sup>	6.91E+00 <sup>c</sup>	2.97E+00 <sup>d</sup>	3.31E+00 <sup>e</sup>
Co-PEG-AP@SiO <sub>2</sub>	QY	1.10E-01 <sup>c</sup>	3.71E-02 <sup>d</sup>	2.01E-02 <sup>e</sup>	2.21E+01 <sup>c</sup>	7.42E+00 <sup>d</sup>	4.03E+00 <sup>e</sup>
Ni-PEG-AP@SiO <sub>2</sub>	QY	8.82E-02 <sup>c</sup>	3.04E-02 <sup>d</sup>	1.74E-02 <sup>e</sup>	1.76E+01 <sup>c</sup>	6.08E+00 <sup>d</sup>	3.48E+00 <sup>e</sup>
Pd-PEG-AP@SiO <sub>2</sub>	Rh B	3.01E-01 <sup>c</sup>	1.13E-01 <sup>d</sup>	6.13E-02 <sup>e</sup>	6.03E+01 <sup>c</sup>	2.26E+01 <sup>d</sup>	1.23E+01 <sup>e</sup>
Co-PEG-AP@SiO <sub>2</sub>	Rh B	4.46E-02 <sup>c</sup>	1.69E-02 <sup>d</sup>	8.73E-03 <sup>e</sup>	8.91E+00 <sup>c</sup>	3.38E+00 <sup>d</sup>	1.75E+00 <sup>e</sup>
Ni-PEG-AP@SiO <sub>2</sub>	Rh B	3.30E-02 <sup>c</sup>	1.14E-02 <sup>d</sup>	7.04E-03 <sup>e</sup>	6.61E+00 <sup>c</sup>	2.28E+00 <sup>d</sup>	1.41E+00 <sup>e</sup>
Cu/Ligand@Fullerene [30]	Rh B	9.31E-03 (120 s)	7.52E-03 (240 s)	6.58E-03 (360 s)	3.72E+00 (120 s)	3.01E+00 (240 s)	2.63E+00 (360 s)
Cu/Ligand@Fullerene [30]	2-NP	1.39E-02 (30 s)	1.46E-02 (90 s)	6.78E-03 (300 s)	5.57E+00 (30 s)	5.83E+00 (90 s)	2.71E+00 (300 s)
Co <sub>3</sub> O <sub>4</sub> @nHAP [31]	Rh B	2.74E-03 (90 s)	1.94E-03 (240 s)	2.24E-03 (900 s)	9.13E-01 (90 s)	6.45E-01 (240 s)	7.47E-01 (900 s)
Co <sub>3</sub> O <sub>4</sub> @nHAP [31]	2-NP	4.03E-03 (180 s)	7.31E-03 (360 s)	5.27E-03 (540 s)	1.34E+00 (180 s)	2.44E+00 (360 s)	1.76E+00 (540 s)

<sup>a</sup>The reaction rate constant. <sup>b</sup>The reaction rate constant per total weight of tested catalyst (5 mg). <sup>c</sup> 10 s, <sup>d</sup> 30 s, <sup>e</sup> 60 s, <sup>f</sup> 180 s.

#### 4. Conclusion

The M-PEG-AP@SiO<sub>2</sub> nanomaterial (M: Pd, Co, Ni) was prepared by a facile hydrothermal route in order to degradation of organic contaminants effectively. The obtained nanocatalysts were characterized by XRD, SEM, EDX, FT-IR techniques. The synthesized Pd-PEG@SiO<sub>2</sub> nanomaterial have illustrated outstanding catalytic performance for 2-NP (97.6% conversion) and Rh B (97.5% conversion) degradation. In addition, the Co-PEG-AP@SiO<sub>2</sub> catalysts also showed the best catalytic performance for QY after 60 seconds (70.1% conversion). Owing to the obtained results, the proposed nano catalyst can be able utilized for remediation of contaminated environmental water samples by organic contaminants such as dyes and toxic aromatic compounds.

#### Author's Contributions

**Sevtap Çağlar Yavuz:** Investigation, Data Curation, Methodology, Project administration, Writing - review & editing, Formal analysis, Funding acquisition

**Emre Yavuz:** Investigation, Methodology, Data Curation, Writing-original draft, Project administration

**Serkan Dayan:** Methodology, Data Curation, Project administration, Writing - review & editing, Formal analysis, Funding acquisition

#### Ethics

There are no ethical issues after the publication of this manuscript.

#### 5. References

- Da'na, E., Taha, A., El-Aassar, M. R. 2023. Catalytic reduction of p-nitrophenol on MnO<sub>2</sub>/zeolite-13X prepared with lawsonia inermis extract as a stabilizing and capping agent. *Nanomaterials*, 13(4): 785.
- Kumar, R., Barakat, M., Daza, Y., Woodcock, H., Kuhn, J. 2013. EDTA functionalized silica for removal of Cu (II), Zn (II) and Ni (II) from aqueous solution. *Journal of Colloid and Interface Science*, 408, 200–205.
- Fu, Y., Yin, Z., Qin, L., Huang, D., Yi, H., Liu, X., Liu, S., Zhang, M., Li, B., Li, L., Wang, W., Zhou, X., Li, Y., Zeng, G., Lai, C. 2022. Recent progress of noble metals with tailored features in catalytic oxidation for organic pollutants degradation. *Journal of Hazardous Materials*, 422, 126950.
- Ertl, G., Knözinger, H., Weitkamp, J. (Eds.). 1997. Weinheim: VCH. Handbook of heterogeneous catalysis. 2, 427-440.
- Colmenares, J. C., Luque, R., Campelo, J. M., Colmenares, F., Karpinski, Z., Romero, A. A. 2009. Nanostructured photocatalysts and their applications in the photocatalytic transformation of lignocellulosic biomass: an overview. *Materials*, 2(4): 2228-2258.
- Hurley, K. D., Shapley, J. R. 2007. Efficient heterogeneous catalytic reduction of perchlorate in water. *Environmental Science & Technology*, 41(6): 2044-2049.
- Kim, K. H., Ihm, S. K. 2011. Heterogeneous catalytic wet air oxidation of refractory organic pollutants in industrial wastewaters: a review. *Journal of Hazardous Materials*, 186(1): 16-34.
- Yao, Y., Cai, Y., Lu, F., Wei, F., Wang, X., Wang, S. 2014. Magnetic recoverable MnFe<sub>2</sub>O<sub>4</sub> and MnFe<sub>2</sub>O<sub>4</sub>-graphene hybrid as heterogeneous catalysts of peroxydisulfate activation for efficient degradation of aqueous organic pollutants. *Journal of Hazardous Materials*, 270, 61-70.
- Wang, J., Zhang, J., Song, Y., Xu, X., Cai, M., Li, P., Yuan, W., Xiahou, Y. 2023. Functionalized agarose hydrogel with in situ Ag nanoparticles as highly recyclable heterogeneous catalyst for aromatic organic pollutants. *Environmental Science and Pollution Research*, 30(15): 43950-43961



- [10]. Kim, H. S., Kim, H. J., Kim, J. H., Kim, J. H., Kang, S. H., Ryu, J. H., Park, N. K., Yun, D. S., Bae, J. W. 2022. Noble-metal-based catalytic oxidation technology trends for volatile organic compound (VOC) removal. *Catalysts*, 12(1): 63.
- [11]. Cao, S., Wang, C. J., Lv, X. J., Chen, Y., Fu, W. F. 2015. A highly efficient photocatalytic H<sub>2</sub> evolution system using colloidal CdS nanorods and nickel nanoparticles in water under visible light irradiation. *Applied catalysis B: Environmental*, 162, 381-391.
- [12]. Han, G., Jin, Y. H., Burgess, R. A., Dickenson, N. E., Cao, X. M., Sun, Y. 2017. Visible-light-driven valorization of biomass intermediates integrated with H<sub>2</sub> production catalyzed by ultrathin Ni/CdS nanosheets. *Journal of the American Chemical Society*, 139(44): 15584-15587.
- [13]. Wang, P., Xu, S., Chen, F., Yu, H. 2019. Ni nanoparticles as electron-transfer mediators and NiS<sub>x</sub> as interfacial active sites for coordinative enhancement of H<sub>2</sub>-evolution performance of TiO<sub>2</sub>. *Chinese Journal of Catalysis*, 40(3): 343-351.
- [14]. Zhang, Y., Jin, Z., Yuan, H., Wang, G., Ma, B. 2018. Well-regulated nickel nanoparticles functional modified ZIF-67 (Co) derived Co<sub>3</sub>O<sub>4</sub>/CdS pn heterojunction for efficient photocatalytic hydrogen evolution. *Applied Surface Science*, 462, 213-225.
- [15]. Chai, Z., Zeng, T. T., Li, Q., Lu, L. Q., Xiao, W. J., Xu, D. 2016. Efficient visible light-driven splitting of alcohols into hydrogen and corresponding carbonyl compounds over a Ni-modified CdS photocatalyst. *Journal of the American Chemical Society*, 138(32): 10128-10131.
- [16]. Simon, T., Bouchonville, N., Berr, M. J., Vaneski, A., Adrović, A., Volbers, D., Wyrwich, R., Döblinger, M., Susha, A. S., Rogach, A. L., Jackel, F., Stolarczyk, J. K., Feldmann, J. 2014. Redox shuttle mechanism enhances photocatalytic H<sub>2</sub> generation on Ni-decorated CdS nanorods. *Nature Materials*, 13(11): 1013-1018.
- [17]. Kim, B., Lee, Y. R., Kim, H. Y., Ahn, W. S. 2018. Adsorption of volatile organic compounds over MIL-125-NH<sub>2</sub>. *Polyhedron*, 154, 343-349.
- [18]. Baughman, G. L., Weber, E. J. 1994. Transformation of dyes and related compounds in anoxic sediment: kinetics and products. *Environmental Science & Technology*, 28(2): 267-276.
- [19]. Isari, A. A., Payan, A., Fattahi, M., Jorfi, S., Kakavandi, B. 2018. Photocatalytic degradation of rhodamine B and real textile wastewater using Fe-doped TiO<sub>2</sub> anchored on reduced graphene oxide (Fe-TiO<sub>2</sub>/rGO): Characterization and feasibility, mechanism and pathway studies. *Applied Surface Science*, 462, 549-564.
- [20]. Basturk, E., Karatas, M. 2015. Decolorization of anthraquinone dye Reactive Blue 181 solution by UV/H<sub>2</sub>O<sub>2</sub> process. *Journal of Photochemistry and Photobiology A: Chemistry*, 299, 67-72.
- [21]. Qin, J., Zhang, Q., Chuang, K. T. 2001. Catalytic wet oxidation of p-chlorophenol over supported noble metal catalysts. *Applied Catalysis B: Environmental*, 29(2): 115-123.
- [22]. Fujitani, T., Nakamura, J. 2000. The chemical modification seen in the Cu/ZnO methanol synthesis catalysts. *Applied Catalysis A: General*, 191(1-2): 111-129.
- [23]. Di Paola, A., Augugliaro, V., Palmisano, L., Pantaleo, G., Savinov, E. 2003. Heterogeneous photocatalytic degradation of nitrophenols. *Journal of Photochemistry and Photobiology A: Chemistry*, 155(1-3): 207-214.
- [24]. Naeem, H., Ajmal, M., Khatoun, F., Siddiq, M., Khan, G. S. 2021. Synthesis of graphene oxide-metal nanoparticle nanocomposites for catalytic reduction of nitrocompounds in aqueous medium. *Journal of Taibah University for Science*, 15(1), 493-506.
- [25]. Kamal, T., Asiri, A. M., Ali, N. 2021. Catalytic reduction of 4-nitrophenol and methylene blue pollutants in water by copper and nickel nanoparticles decorated polymer sponges. *Spectrochimica Acta Part A: Molecular and Biomolecular Spectroscopy*, 261, 120019-120028.
- [26]. Veisi, H., Ozturk, T., Karmakar, B., Tamoradi, T., Hemmati, S. 2020. In situ decorated Pd NPs on chitosan-encapsulated Fe<sub>3</sub>O<sub>4</sub>/SiO<sub>2</sub>-NH<sub>2</sub> as magnetic catalyst in Suzuki-Miyaura coupling and 4-nitrophenol reduction. *Carbohydrate polymers*, 235, 115966-115973.
- [27]. Nurwahid, I. H., Dimonti, L. C. C., Dwiatmoko, A. A., Ha, J. M., Yunarti, R. T. 2022. Investigation on SiO<sub>2</sub> derived from sugarcane bagasse ash and pumice stone as a catalyst support for silver metal in the 4-nitrophenol reduction reaction. *Inorganic Chemistry Communications*, 135, 109098-109108.
- [28]. Pal, J., Deb, M. K., Deshmukh, D. K., Sen, B. K. 2014. Microwave-assisted synthesis of platinum nanoparticles and their catalytic degradation of methyl violet in aqueous solution. *Applied Nanoscience*, 4, 61-65.
- [29]. Baghbamidi, S. E., Hassankhani, A., Sanchooli, E., Sadeghzadeh, S.M. 2018. The reduction of 4-nitrophenol and 2-nitroaniline by palladium catalyst based on a KCC-1/IL in aqueous solution. *Applied Organometallic Chemistry*, 32(4): e4251.
- [30]. Dayan, S. Copper Nanoparticles Supported on a Schiff base-Fullerene as Catalyst for Reduction of Nitrophenols and Organic Dyes. *Celal Bayar University Journal of Science*, 16 (3), 285-291.
- [31]. Dayan, S. Performance improvement of Co<sub>3</sub>O<sub>4</sub>@ nHAP hybrid nanomaterial in the UV light-supported degradation of organic pollutants and photovoltaics as counter electrode. *Journal of Molecular Structure*, 1238, 130390.

# Recombinant Adeno-Associated Viral Vector Transduction of Human Prostate Cancer Cell Lines

Muhammet Burak Batır<sup>1\*</sup> 

<sup>1</sup> Department of Biology, Faculty of Engineering and Natural Sciences, Manisa Celal Bayar University, Manisa, Türkiye

\*[buraks1@hotmail.com](mailto:buraks1@hotmail.com)

\*Orcid No: 0000-0002-8722-5055

Received: 1 August 2023

Accepted: 21 September 2023

DOI: 10.18466/cbayarfbe.1336250

## Abstract

At the core of gene therapy lies the use of viral vectors, engineered viruses serving as delivery vehicles to transport restorative genes into target cells. Therefore, the effect of 7 different rAAV serotypes and their different quantities was analyzed here on human prostate cancer cell lines PC-3 and DU-145, which are hard to be transfected. PC-3 and DU-145 cell lines were infected with different multiplicity of infection (MOI) ratios of 7 rAAV serotypes, which were expressing the green fluorescent protein (GFP) transgene driven by the CMV promoter. The transduction efficiency was analyzed by fluorescent microscopy and flow cytometry. In addition, the cell viability of the infected cells was measured by Muse Cell Analyzer at the MOI of 10.000. rAAV 2/2 and rAAV 2/6 have the most significant ability to transduce PC-3 cells. Although rAAV 2/2 and rAAV 2/6 were also the most transducing serotypes in the DU-145 cell line, the transduction rates did not exceed 20% in this cell line. On the other hand, after viral infection, no difference in cell viability was observed in PC-3 cells compared to the mock group, while a significant decrease in viability was observed in DU-145 cells. This study determined the transduction efficiency of 7 different rAAV serotypes on human cancer cell lines. While rAAV 2/2 and rAAV 2/6 serotypes achieved more than 60% transduction efficiency in PC-3 cells, the transduction efficiency could not exceed 20% in DU-145 cells. Overall, this study demonstrated that rAAV 2/2 and rAAV 2/6 could mediate the expression of a transgene with a high transduction efficiency.

**Keywords:** Cancer, Gene therapy, rAAV, Recombinant adeno-associated virus, Transduction

## 1. Introduction

Gene therapy in cancer treatment is a favorable approach that aims to target and modify the genetic features of tumor cells to halt their growth or induce cell death [1]. The direct goal of gene therapy in cancer treatment is to correct or exploit the genetic aberrations that contribute to tumor formation and progression. However, challenges remain, including optimizing delivery methods, minimizing off-target effects, and addressing potential immune responses. Also, as research and technology advance, gene therapy can revolutionize cancer treatment and improve patient outcomes [2,3]. Cancer stays one of the most difficult challenges in modern medicine, with its intricacy and heterogeneity posing noteworthy limitations to efficacious treatment [4].

On the other hand, prostate cancer is a common types of cancer in men worldwide [5]. For this reason, a personalized approach to prostate cancer treatment,

which is resistant to therapy, can be needed. For this reason, gene therapy is a promising outcome for patients resistant to chemotherapy and radiotherapy [6,7].

One of the most significant characteristics directly connected with gene therapy is the effectiveness of the gene transfer method [8,9]. This challenge can be overcome by using AAV (adeno-associated virus) for gene therapy in cancer treatment [10]. AAVs have a broad tissue tropism, indicating they can infect different tissues [11]. The specific tissues infected by AAV rely on the serotype of the AAV used in treatment. Different AAV serotypes have further preferences for targeting distinct tissues, including the neuron, liver, skeletal muscle, heart, and lung [12-16]. Today, there are 11 defined serotypes for human tissues [16-18]. 80-90% of adult individuals are seropositive for AAV2; and no immune response, symptom, or disease associated with AAV has been identified [19,20]. In recent studies, the rep gene and

ITR (inverted terminal repeat) belong to the AAV2 serotype (2/). Still, the capsid morphologies (AAV -/1, -/2, -/3, -/5, -/6, -/7, -/8, -/9, -/11, -/12, -/13) AAV recombinant/hybrid serotypes with different AAV serotypes were found to have higher transduction efficiency [21-23]. However, the optimal amount of virus (multiplicity of infection/MOI) for transduction can vary depending on factors such as the AAV serotype used, the specific target cell type, the therapeutic gene being delivered, and the experimental objectives. Achieving an appropriate MOI is critical to obtaining reliable and consistent results in AAV-mediated gene therapy experiments [24-27].

AAV-mediated gene therapy has great potential to revolutionize cancer therapy by offering personalized, targeted, and potentially remedial approaches. For this reason, this study try to qualify the usability of different recombinant AAV (rAAV) serotypes in gene transfer in different human prostate cancer cell lines. Hence, we compared the transduction efficiency of rAAV 2/1, 2/2, 2/3, 2/5, 2/6, and 2/9 serotypes and MOI rates, by employing green fluorescent protein (GFP) reporter transgene in human prostate cancer cell lines PC-3 and DU-145. The study results provide valuable information for choosing the most relevant rAAV serotype for prostate cancer gene therapy.

## 2. Materials and Methods

### 2.1. Cell Line and Culture Conditions

The human prostate cancer cell lines PC-3 and DU-145 for rAAV-mediated transduction evaluation and HEK293T cell line for rAAV production were gained from ATCC (American Type Cell Culture). PC-3 and DU-145 cells grew as adherent monolayers in a culture flask, maintained in the complete medium of RPMI 1640. The related cells were incubated with 5% CO<sub>2</sub> at 37.0 °C in the humidified incubator (Thermo Fisher Scientific, USA). 5–12 passage numbered PC-3 and DU-145 cells were used for this study. HEK293T cells grew as an adherent monolayer in a culture flask, maintained in the complete medium of DMEM high glucose (Gibco, 11995073) medium. The related cells were incubated with 5% CO<sub>2</sub> at 37.0 °C in the humidified incubator. HEK293T cell with a passage number of 30 was used for this study.

### 2.2. Cell Count And Viability Analysis

After incubation of the cells, number and viability of the cells were defined with Muse Count & Viability reagent (Merck Millipore, USA) according to the manufacturer's instructions using the automated Muse® Cell Analyzer (Merck Millipore, USA), which stains viable and dead cells based on their permeability with the help of the two different dyes.

### 2.3. Production of the rAAV Serotypes

Seven different rAAV serotypes were used for this study. rAAV 2/1, 2/2, 2/4, 2/5, 2/6, 2/8, 2/9 serotypes carried the same GFP transgene driven by cytomegalovirus (CMV) promoter. rAAV serotypes were produced with tripartite transfection of the helper, RepCap and GFP transgene (transfer) plasmids in the HEK293T cell line. Hence, pAdDeltaF6 helper plasmid (112867, Addgene), pAAV2/1 (112862, Addgene), pAAV2/2 (104963, Addgene), pAAV2/4 (VPK-424, Cell Biolabs), pAAV2/5 (104964, Addgene), pAAV2/6 (VPK-426, Cell Biolabs), pAAV2/8 (VPK-428, Cell Biolabs), pAAV2/9 (112865, Addgene) RepCap plasmids and AAV-CMV-GFP plasmid (67634, Addgene) were used to produce rAAV 2/1, 2/2, 2/4, 2/5, 2/6, 2/8, 2/9 serotypes. All rAAV serotypes were purified using the iodixanol gradient ultracentrifugation method. The standard was prepared from a plasmid (Addgene, #59462) stock of  $2 \times 10^9$  molecules/ $\mu$ l to generate a standard curve, and then six different dilutions were made between  $2 \times 10^8$ - $2 \times 10^3$  molecules/ $\mu$ l from plasmid stock. The ITR regions of the plasmid were used as a proxy. Also, the fwd ITR 5'-GGAACCCCTAGTGATGGAGTT-3' and rev ITR 5'-CGGCCTCAGTGAGCGA-3' primer pair was used to amplify the related AAV2 ITR region of the plasmid using SYBR Master Mix 2X in qPCR analysis (GeneMarkBio, Taiwan) [28]. The titers of the rAAV serotypes were determined by qPCR analysis according to the above mentioned standarts. The helper plasmid pAAV2/2 (104963, Addgene) without the GFP transgene and the RepCap plasmid were used to produce Mock AAV viruses.

### 2.4. rAAV-Mediated Transduction Assays

For transduction evaluation,  $10^5$  PC-3 and DU-145 cells were seeded in each well of 24-well plates and incubated at 37.0 °C for 16 hours. Cells were rinsed with PBS, and were then 1 ml full RPMI-1640 media was added to each well of plates. After plating, PC-3 and DU-145 cells were infected with MOI of 10,  $10^2$ ,  $10^3$ , and  $10^4$  rAAV particles/cells for each serotype. Forty-eight hours post-infection, the rAAV serotypes' transduction efficiency was evaluated in fluorescence microscope imaging and flow cytometer analysis. The cells were analyzed under an IX73 microscope (Olympus, Japan) for fluorescence microscope imaging analysis. The rAAV transduction efficiency was evaluated by GFP imaging using images from the different fields of control and infected cells. The images' GFP intensity (total area of green fluorescence) was analyzed by ImageJ analysis software (NIH, MD). The cells were examined by BD Accuri™ C6 (BD Biosciences, USA) for flow cytometer study.

## 2.5. Statistical analysis

The statistical package software (SPSS) was employed to investigate the differences controlled between the groups. The received results were experimented with Tukey post hoc test in conjunction with One-way ANOVA. The p-values less than 0.05 were assumed significant, and all data defined the duplicate experiments. Results were given as a mean  $\pm$  standard deviation (SD).

## 3. Results

### 3.1. Fluorescence Microscopy Analysis of Seven Serotypes rAAV Vectors in PC-3 and DU-145 Prostate Cancer Cell Lines

In our study, to compare the transduction efficiency of 7 different rAAV vectors based on fluorescence microscopy, PC-3 cells were infected with MOI 10,

100, 1.000, and 10.000 of rAAV2/1, rAAV2/2, rAAV2/4, rAAV2/5, rAAV2/6, rAAV2/8, and

rAAV2/9 carrying the GFP transgene driven by cytomegalovirus (CMV) promoter. The transduction efficiency was measured at forty-eight hours post-infection, and the efficiency was increased with the increasing levels of MOI. As shown in Figure 1, an AAV MOI of 10.000 was given the highest GFP transgene expression level for all serotypes.

The transduction rates for MOI 10.000 rAAV2/1, rAAV2/2, rAAV2/4, rAAV2/5, rAAV2/6, rAAV2/8, and rAAV2/9 transduction rates were 52%, 76%, 5%, 11%, 64%, 2%, 3% compared to mock, respectively. Also, the highest transduction efficiency was obtained from AAV2/2 ( $p < 0.0001$ ), AAV2/6 ( $p < 0.0001$ ), and AAV2/1 ( $p < 0.0001$ ) in contrasted with the other AAV serotypes (lower than 50% transduction), respectively.

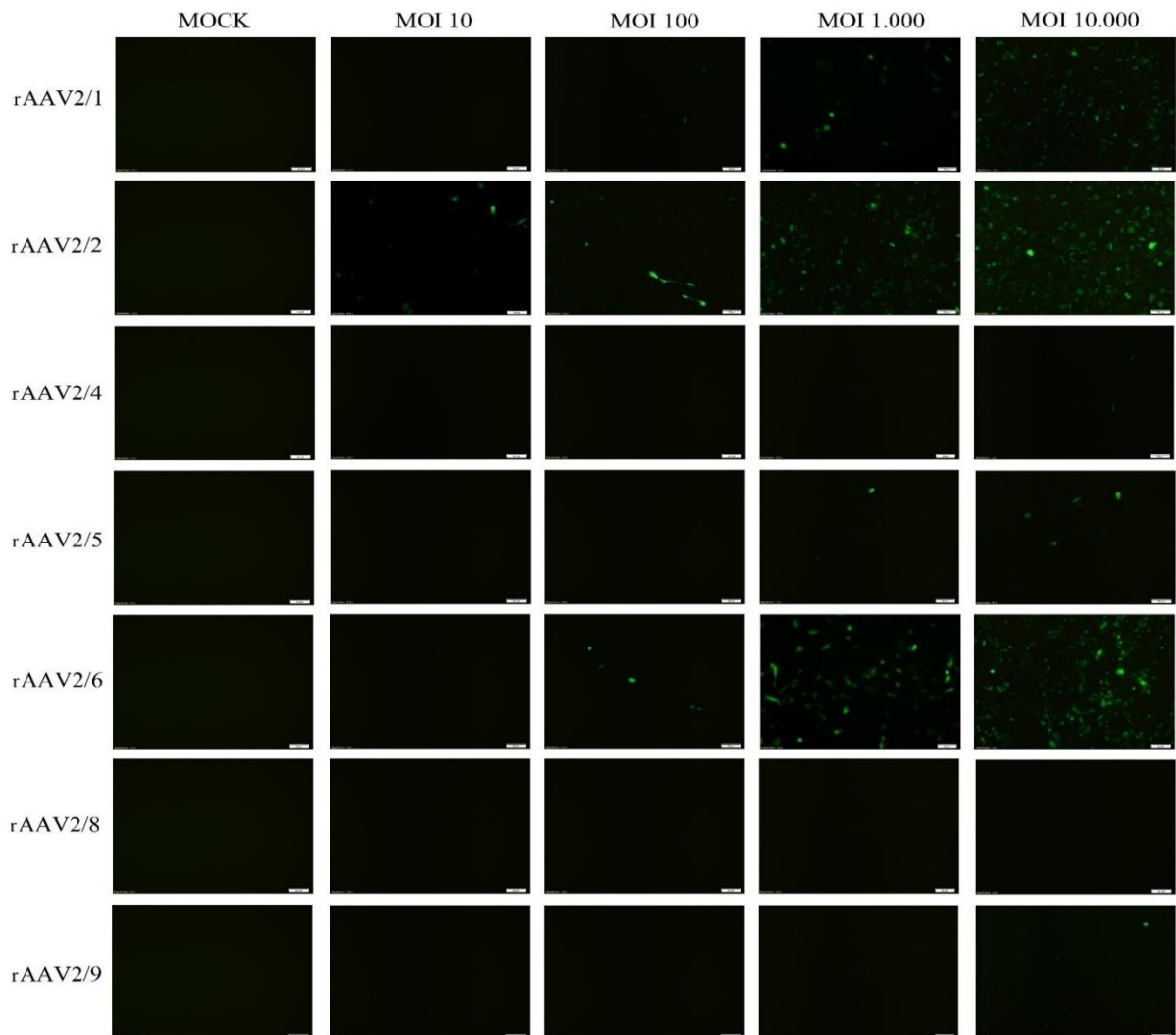


**Figure 1.** Fluorescent microscope image of PC-3 cells transduced with different rAAV serotypes.



On the other hand, these results revealed that the PC-3 cells are highly resistant to rAAV2/4, rAAV2/5, rAAV2/8, and rAAV2/9 infection. The GFP transgene expression could be first detected at forty-eight hours post-infection with fluorescent microscopy, and the signal persisted for 21 days.

DU-145 cells were also infected with MOI 10, 100, 1.000, and 10.000 rAAV2/1, rAAV2/2, rAAV2/4, rAAV2/5, rAAV2/6, rAAV2/8, and rAAV2/9 carrying the GFP transgene driven by the CMV promoter. The transduction efficiency was measured at 48 hours post-infection, and the efficiency was increased with the increasing levels of MOI, the same as PC-3 cells. As displayed in Figure 2, an AAV MOI of 10.000 was given the highest GFP transgene expression level for all serotypes.

The transduction rates for MOI 10.000 of rAAV2/1, rAAV2/2, rAAV2/4, rAAV2/5, rAAV2/6, rAAV2/8, and rAAV2/9 were 9%, 11%, 3%, 1%, 19%, 2%, 1%

(when the dead cells were rinsed away with PBS and the only live adherent cells were counted) compared to mock, respectively (Figure 2). The highest transduction efficiency was obtained from rAAV2/6 ( $p<0.0001$ ), rAAV2/2 ( $p=0.01$ ), and rAAV2/1 ( $p=0.001$ ) serotypes in contrast with the other rAAV serotypes. An increase in dead cell ratios in DU-145 cells was observed with the increasing levels of MOI in contrast to PC-3 cells. Also, the rAAV2/2 infection-related DU-145 cell death ratio was higher than the other rAAV serotypes, which could be noticeable by the microscopic analysis (Figure 2). This situation can be explained by the highest infection rate of rAAV2/2 on DU-145 cells, the same as PC-3 cells, as mentioned above. On the other hand, these results reveal that the DU-145 cells were highly resistant to rAAV2/4, rAAV2/5, rAAV2/8, and rAAV2/9 infection. The GFP transgene expression could be first detected at forty-eight hours post-infection with fluorescent microscopy and the signal persisted for 13 days.

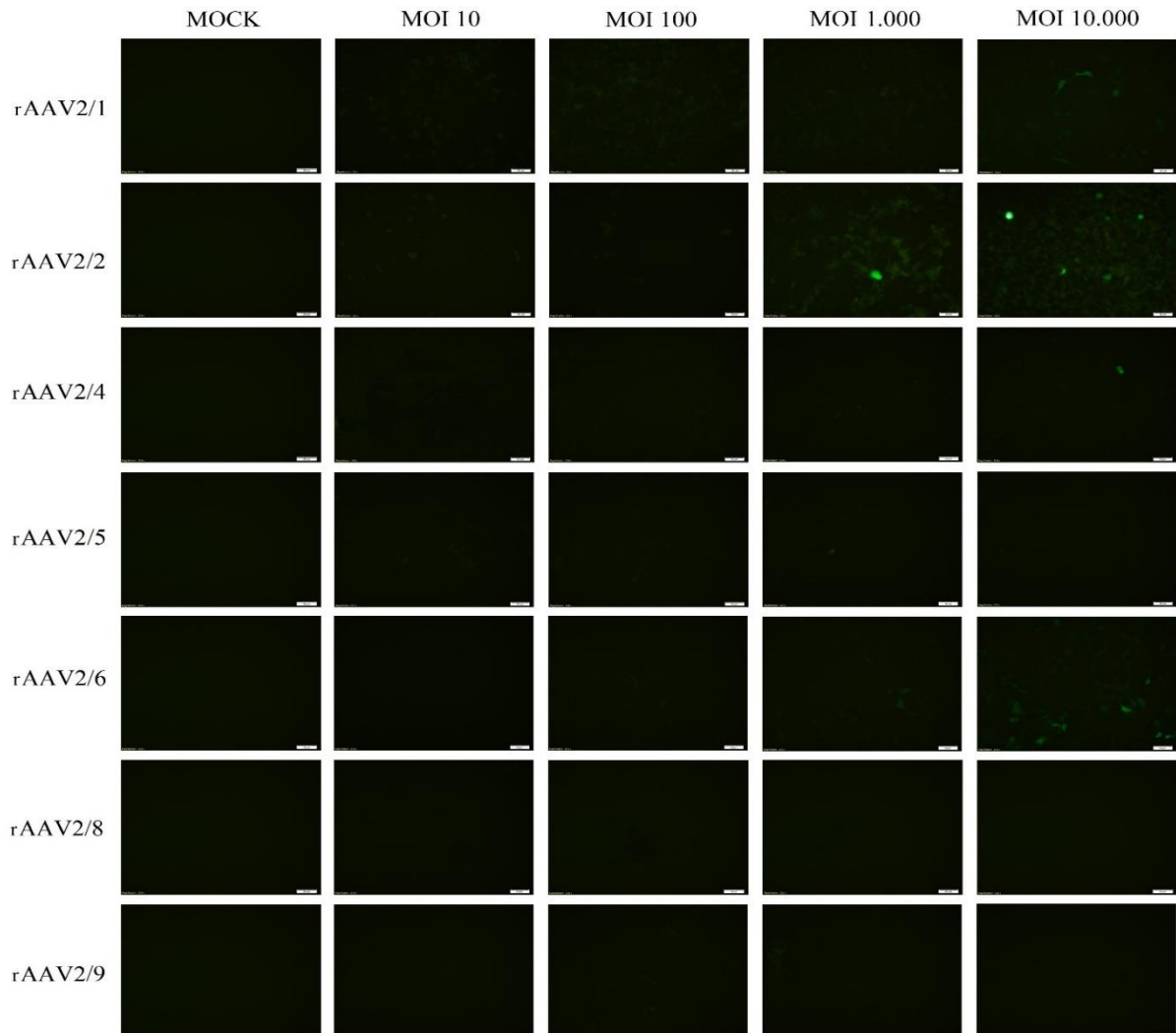


**Figure 2.** Fluorescent microscope image of DU-145 cells transduced with different rAAV serotype.

### 3.2. FACS Analysis of Seven Serotypes rAAV Vectors in PC-3 and DU-145 Prostate Cancer Cell Lines

Fluorescent microscope images showed the highest GFP transgene expression was at 10000 MOI in both PC-3 and DU-145 cell lines (Figure 3 and 4). Therefore, flow cytometry analyzes were performed at 10000 MOI forty-eight hours post-infection in both PC-3 and DU-145 cell lines. From the results displayed in Figure 3, the number of GFP-positive detected cells in the PC-3 cell line was significantly the highest in cells infected with rAAV2/1, rAAV2/2,

and rAAV2/6 serotypes. In particular, the transduction efficiency in cells infected with the AAV2/2 serotype was maximal at 67.1%, while the transduction efficiency in cells infected with rAAV2/1 and rAAV2/6 was 52.3% and 65.1%, according to FACS analysis. As in fluorescent microscope analysis, PC-3 cells were found resistant to rAAV2/4, rAAV2/5, rAAV2/8, and rAAV2/9 infection, and the number of infection-related GFP-positive cells was found to be 3.5%, 8.1%, 0.2%, and 0.2%, respectively. Also, no GFP-expressed cells are detected in mock-infected cells, according to FACS analysis.

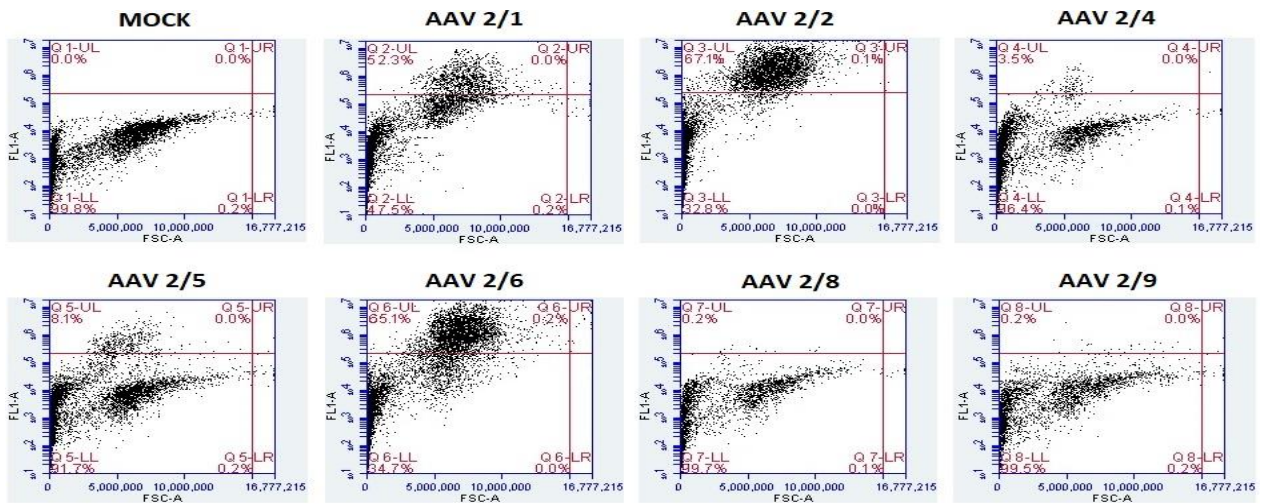


Figure 3. FACS analysis of GFP positive PC-3 cells infected with different serotypes of rAAV.

From the results shown in Figure 4, the DU-145 cell groups infected with rAAV2/1, rAAV2/2, and rAAV2/6 serotypes had a significantly higher transduction efficiency compared to all other rAAV serotypes. In particular, the transduction efficiency

in cells infected with the rAAV2/2 serotype was maximal at 11.5%, while the transduction efficiency in cells infected with rAAV2/1 and rAAV2/6 was 7.6% and 17.6%, according to FACS analysis.

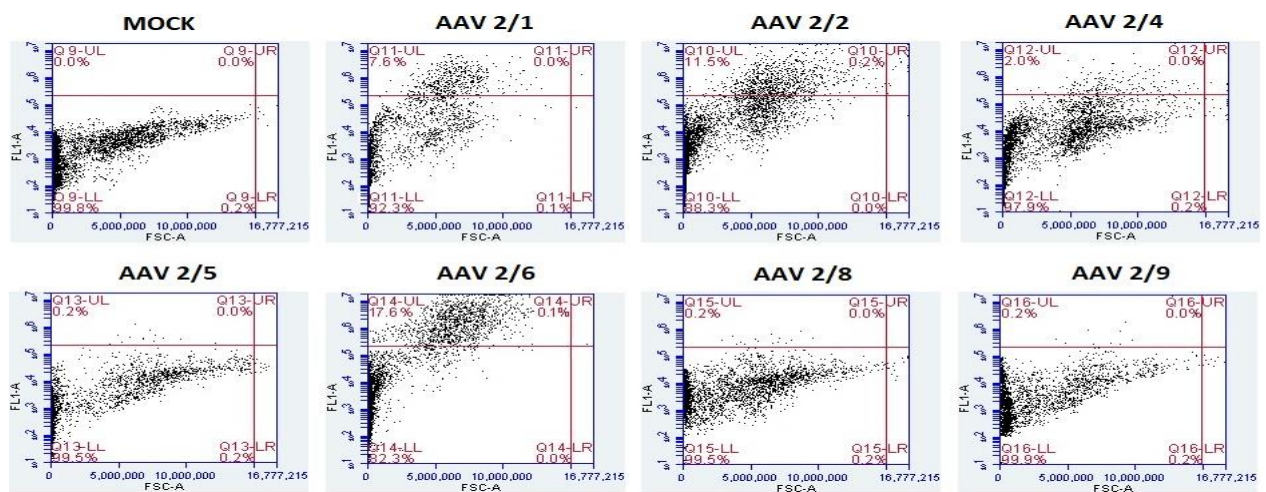


Figure 4. FACS analysis of GFP positive DU-145 cells infected with different serotypes of rAAV.

As in fluorescent microscope analysis, DU-145 cells were found resistant to rAAV2/4, rAAV2/5, rAAV2/8, and rAAV2/9 infection, and the number of infection-related GFP-positive cells was found to be 2.0%, 0.2%, 0.2%, and 0.0%, respectively (Figure 4).

Also, no GFP-expressing cells were detected in mock-infected cells, according to FACS analysis. In particular, according to the results obtained from the FACS analysis, it was observed that the transduction efficiency does not exceed 20% in DU-145 cells in contrast with the PC-3 cells. However, the number of viable cells passing through the device for analysis was less than that of PC-3 cells.

### 3.3. Cell Viability Assay of PC-3 and DU-145 Prostate Cancer Cell Lines Infected with Seven Serotypes rAAV Vectors

Cell viability was measured by flow cytometry after transduction of the GFP gene in PC-3 and DU-145 cell lines with rAAV vectors (Figure 5 and 6). Our results showed that infection of PC-3 cells with rAAV2/1, rAAV2/2, rAAV2/4, rAAV2/5, rAAV2/6, and rAAV2/8 at MOI of 10000 did not create a significant difference ( $p>0.05$ ) between the groups. The cell viability rate exceeded 95% in all groups infected with different rAAV serotypes (Figure 5). Mean value of the cell viability rate for mock, rAAV2/1, rAAV2/2, rAAV2/4, rAAV2/5, rAAV2/6, rAAV2/8, and rAAV2/9 serotype infected cells were, 97.4%, 97.0%, 97.6%, 98.4%, 97.8%, 98.0%, 98.0% and 98.6%, respectively.

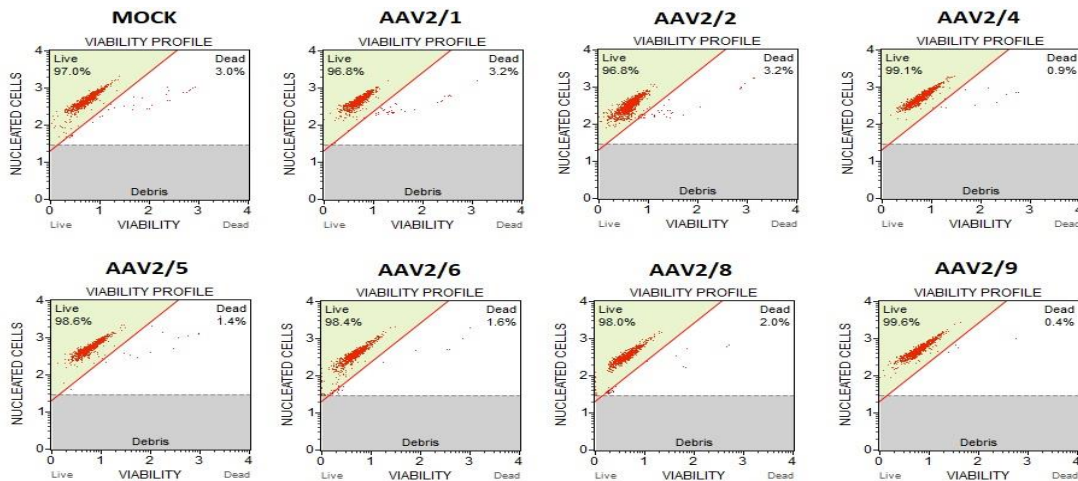


Figure 5. Cell viability of PC-3 cells infected with different serotypes of rAAV.

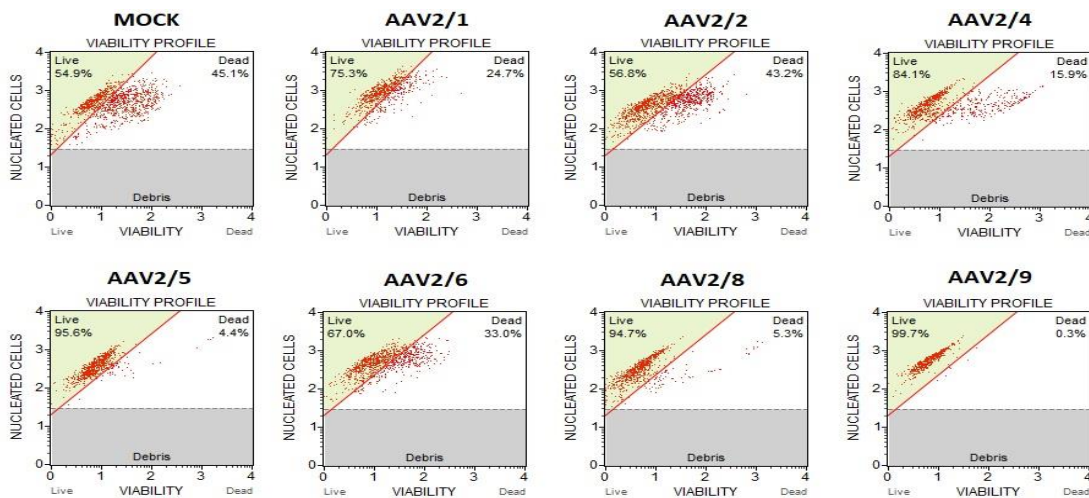


Figure 6. Cell viability assay of DU-145 cells infected with different serotypes of rAAV.



Unlike PC-3 cells, DU-145 cells infected with rAAV2/1, rAAV2/2, rAAV2/4, rAAV2/5, rAAV2/6, and rAAV2/8 serotypes at MOI of 10000 showed decreases in cell viability for some groups. These decreases in cell viability were determined for rAAV2/1, rAAV2/2, and rAAV2/6 serotypes, where the infection rates were the highest. Mean value of the cell viability rate for mock, rAAV2/1, rAAV2/2, rAAV2/4, rAAV2/5, rAAV2/6, rAAV2/8, and rAAV2/9 serotype infected cells were, 55.2%, 76.6%, 57.4%, 84.6%, 97.2, 68.0%, 94.2% and 99.0%, respectively.

#### 4. Discussion

Gene therapy is a recent and alternative remedy for cancer types that cannot be quickly cleared by surgery and are invulnerable to radiotherapy and chemotherapy. For this reason, researchers take advantage of the viral vector-mediated gene transfer for cancer therapy. Hence, the increased transduction efficiency of the preferred viral vector recreates a crucial function in the maximum success rate of gene therapy [29]. Adeno-associated viruses are now vastly investigated and utilized for gene therapy. Also, AAV vectors are fast evolving as one of the prevailing gene delivery approaches due to their prolonged-expression and numerous serotypes qualified for transducing different cell classes. Considerable AAV serotypes have been defined, and individual serotypes have specific cell tropisms based on distinct capsid proteins [30,31].

Another possible use of transduction with AAV vectors is in ex vivo investigations. Here, via rAAV vectors, the genome of mutant cells of the patient can be corrected by homologous recombination to be altered. This modification directly induces a site-specific DNA double-strand break [32-34]. These site-specific double-strand breaks can be produced by nucleases found in the rAAV genome, such as a zinc finger nuclease, transcription activator-like effector nuclease (TALEN), or clustered Regularly Interspaced Short Palindromic Repeats/Cas9 (CRISPR/Cas9) [35-38]. Hence, a wild-type gene can be added instead of the mutant gene in the patient's cell. The most crucial point in using rAAV vectors in this way is to determine the tissue type-specific serotype.

In this study, we revealed the transduction efficiency of seven different rAAV serotypes (rAAV2/1, rAAV2/2, rAAV2/4, rAAV2/5, rAAV2/6, rAAV2/8, rAAV2/9) which induce cell expression of the fluorescent gene GFP in PC-3 and DU-145 prostate cancer cells. In other studies, it has been shown that the rAAV2/2 and rAAV2/5 serotypes' transduction efficiency is higher in respiratory epithelial cells and lung cancer cell lines [40]. In addition, the serotype of

rAAV2/4 in muscle tissue, rAAV2/5 serotype in brain tissue, rAAV2/2 serotype in kidney tissue, rAAV2/8 serotype in pancreatic tissue, and rAAV2/1, rAAV2/8 and rAAV2/9 serotypes in heart tissue were reported to have higher transduction efficiencies [40-44]. Our study revealed that the transduction efficiency of especially rAAV2/2 and rAAV2/6 viruses was superior to other virus serotypes tested. Transduction efficiency in cell line PC-3 was found as rAAV2/2>rAAV2/6>rAAV2/1>rAAV2/5>rAAV2/4 >rAAV2/9>rAAV2/8 and in cell line DU-145 was found as rAAV2/6>rAAV2/2>rAAV2/1>rAAV2/4>rAAV2/5=rAAV2/8 =rAAV2/9. In particular, the increased MOI rates were effective in the transduction of rAAV serotypes; the increase in the number of GFP-positive cells with the increase in the number of viruses entering the cell medium is evident in fluorescence microscopy analyses. For this reason, starting with a high MOI rate in future studies will increase the effectiveness of gene therapy.

Differences in cell viability were found after infection in PC-3 cells and DU-145 cells infected with rAAV serotypes. Cell viability below 95% was not observed in any group of PC-3 cells after infection with seven different rAAV serotypes, whereas cell viability decreased below 80% in cell groups infected with rAAV2/2, rAAV2/6, and rAAV2/1 serotypes. Furthermore, it was observed that the viability decreased below 60%, especially in DU-145 cells infected with rAAV2/2. Indeed, this result indicates that the serotypes with the highest tropism towards DU-145 cells are rAAV2/2, rAAV2/6, and rAAV2/1. Several reasons can explain this situation. Differently from PC-3 cells, a different receptor mediating the binding of viruses on the membrane surface of DU-145 cells may cause the cells to enter the apoptotic process, or there may be differences in the expression of genes associated with the DNA repair mechanism or apoptosis pathway in the cells. Our knowledge of the cellular receptors utilized by different serotypes of rAAV for cell attachment is limited [40]. In order to understand the difference in cell viability, we may reveal the gene expression levels by performing transcriptome analyses of PC-3 and DU-145 cells after rAAV infections and thus elucidate the mechanism of action of AAV-triggered differential cell death.

All taken together, these results indicate helpful knowledge on selecting the most relevant rAAV serotype for forthcoming viral vector-mediated analyses, which target human prostate cancer cells. rAAV2/2 and rAAV2/6 can readily infect a human prostate cancer cell. Therefore, using serotypes rAAV2/2 and rAAV2/6 equipped with a restorative gene would be the most appropriate option for administering different kinds of human prostate cancer as an alternative therapy choice.

## Acknowledgement

The author did not receive any specific grant for this research from any funding agency in the public, commercial, or not-for-profit sectors.

## Author's Contributions

**Muhammet Burak Batır:** Conceptualized the related study, performed the experiments and analyses of the result, drafted and wrote the manuscript.

## Ethics

There are no ethical issues after the publication of the related manuscript.

## References

- [1]. Sekhoacha, M., Riet, K., Motloung, P., Gumenku, L., Adegoke, A., & Mashele, S. (2022). Prostate Cancer Review: Genetics, Diagnosis, Treatment Options, and Alternative Approaches. *Molecules* (Basel, Switzerland), 27(17), 5730. <https://doi.org/10.3390/molecules27175730>
- [2]. Dastjerd, N. T., Valibeik, A., Rahimi Monfared, S., Goodarzi, G., Moradi Sarabi, M., Hajabdollahi, F., Maniati, M., Amri, J., & Samavarchi Tehrani, S. (2022). Gene therapy: A promising approach for breast cancer treatment. *Cell biochemistry and function*, 40(1), 28–48. <https://doi.org/10.1002/cbf.3676>
- [3]. Xue, J., Chen, K., Hu, H., & Gopinath, S. C. B. (2022). Progress in gene therapy treatments for prostate cancer. *Biotechnology and applied biochemistry*, 69(3), 1166–1175. <https://doi.org/10.1002/bab.2193>
- [4]. Oztatlici, H., Oztatlici, M., Daglı, S. N., & Karadeniz Saygili, S. (2022). Bir sefalosporin olan sefepim, nb2a nöroblastoma hücrelerinde apoptozu ve oksidatif stresini indükler. *Euroasia Journal of Mathematics, Engineering, Natural & Medical Sciences*, 9(21), 79–86. <https://doi.org/10.38065/euroasiaorg.962>
- [5]. Achard, V., Putora, P. M., Omlin, A., Zilli, T., & Fischer, S. (2022). Metastatic Prostate Cancer: Treatment Options. *Oncology*, 100(1), 48–59. <https://doi.org/10.1159/000519861>
- [6]. Huang, J., Zhuang, C., Chen, J., Chen, X., Li, X., Zhang, T., Wang, B., Feng, Q., Zheng, X., Gong, M., Gong, Q., Xiao, K., Luo, K., & Li, W. (2022). Targeted Drug/Gene/Photodynamic Therapy via a Stimuli-Responsive Dendritic-Polymer-Based Nanococktail for Treatment of EGFR-TKI-Resistant Non-Small-Cell Lung Cancer. *Advanced materials* (Deerfield Beach, Fla.), 34(27), e2201516. <https://doi.org/10.1002/adma.202201516>
- [7]. Lundstrom K. (2003). Latest development in viral vectors for gene therapy. *Trends in biotechnology*, 21(3), 117–122. [https://doi.org/10.1016/S0167-7799\(02\)00042-2](https://doi.org/10.1016/S0167-7799(02)00042-2)
- [8]. Chen, M., Mao, A., Xu, M., Weng, Q., Mao, J., & Ji, J. (2019). CRISPR-Cas9 for cancer therapy: Opportunities and challenges. *Cancer letters*, 447, 48–55. <https://doi.org/10.1016/j.canlet.2019.01.017>
- [9]. Sun, W., Shi, Q., Zhang, H., Yang, K., Ke, Y., Wang, Y., & Qiao, L. (2019). Advances in the techniques and methodologies of cancer gene therapy. *Discovery medicine*, 27(146), 45–55.
- [10]. Strecker, M. I., Wlotzka, K., Strassheimer, F., Roller, B., Ludmirski, G., König, S., Röder, J., Opitz, C., Alekseeva, T., Reul, J., Sevenich, L., Tonn, T., Wels, W. S., Steinbach, J. P., Buchholz, C. J., & Burger, M. C. (2022). AAV-mediated gene transfer of a checkpoint inhibitor in combination with HER2-targeted CAR-NK cells as experimental therapy for glioblastoma. *Oncoimmunology*, 11(1), 2127508. <https://doi.org/10.1080/2162402X.2022.2127508>
- [11]. Mulcrone, P. L., Zhang, J., Pride, P. M., Lam, A. K., Frabutt, D. A., Ball-Kell, S. M., & Xiao, W. (2022). Genomic Designs of rAAVs Contribute to Pathological Changes in the Livers and Spleens of Mice. *Advances in cell and gene therapy*, 2022, 6807904. <https://doi.org/10.1155/2022/6807904>
- [12]. Banskota, S., Raguram, A., Suh, S., Du, S. W., Davis, J. R., Choi, E. H., Wang, X., Nielsen, S. C., Newby, G. A., Randolph, P. B., Osborn, M. J., Musunuru, K., Palczewski, K., & Liu, D. R. (2022). Engineered virus-like particles for efficient in vivo delivery of therapeutic proteins. *Cell*, 185(2), 250–265.e16. <https://doi.org/10.1016/j.cell.2021.12.021>
- [13]. Pillay, S., Meyer, N. L., Puschnik, A. S., Davulcu, O., Diep, J., Ishikawa, Y., Jae, L. T., Wosen, J. E., Nagamine, C. M., Chapman, M. S., & Carette, J. E. (2016). An essential receptor for adeno-associated virus infection. *Nature*, 530(7588), 108–112. <https://doi.org/10.1038/nature16465>
- [14]. Pupo, A., Fernández, A., Low, S. H., François, A., Suárez-Amarán, L., & Samulski, R. J. (2022). AAV vectors: The Rubik's cube of human gene therapy. *Molecular therapy : the journal of the American Society of Gene Therapy*, 30(12), 3515–3541. <https://doi.org/10.1016/j.ymthe.2022.09.015>
- [15]. Rode, L., Bär, C., Groß, S., Rossi, A., Meumann, N., Viereck, J., Abbas, N., Xiao, K., Riedel, I., Gietz, A., Zimmer, K., Odenthal, M., Büning, H., & Thum, T. (2022). AAV capsid engineering identified two novel variants with improved in vivo tropism for cardiomyocytes. *Molecular therapy : the journal of the American Society of Gene Therapy*, 30(12), 3601–3618. <https://doi.org/10.1016/j.ymthe.2022.07.003>
- [16]. Zincarelli, C., Soltys, S., Rengo, G., & Rabinowitz, J. E. (2008). Analysis of AAV serotypes 1–9 mediated gene expression and tropism in mice after systemic injection. *Molecular therapy : the journal of the American Society of Gene Therapy*, 16(6), 1073–1080. <https://doi.org/10.1038/mt.2008.76>
- [17]. Tabebordbar, M., Lagerborg, K. A., Stanton, A., King, E. M., Ye, S., Tellez, L., Krunnfüsz, A., Tavakoli, S., Widrick, J. J., Messmer, K. A., Troiano, E. C., Moghadaszadeh, B., Peacker, B. L., Leacock, K. A., Horwitz, N., Beggs, A. H., Wagers, A. J., & Sabeti, P. C. (2021). Directed evolution of a family of AAV capsid variants enabling potent muscle-directed gene delivery across species. *Cell*, 184(19), 4919–4938.e22. <https://doi.org/10.1016/j.cell.2021.08.028>
- [18]. Tan, F., Chu, C., Qi, J., Li, W., You, D., Li, K., Chen, X., Zhao, W., Cheng, C., Liu, X., Qiao, Y., Su, B., He, S., Zhong, C., Li, H., Chai, R., & Zhong, G. (2019). AAV-*ie* enables safe and efficient gene transfer to inner ear cells. *Nature communications*, 10(1), 3733. <https://doi.org/10.1038/s41467-019-11687-8>
- [19]. Grieger, J. C., & Samulski, R. J. (2005). Adeno-associated virus as a gene therapy vector: vector development, production and clinical applications. *Advances in biochemical engineering/biotechnology*, 99, 119–145.
- [20]. Verdera, H. C., Kuranda, K., & Mingozzi, F. (2020). AAV Vector Immunogenicity in Humans: A Long Journey to Successful Gene Transfer. *Molecular therapy : the journal of the American Society of Gene Therapy*, 28(3), 723–746. <https://doi.org/10.1016/j.ymthe.2019.12.010>





- [21]. Choi, V. W., McCarty, D. M., & Samulski, R. J. (2005). AAV hybrid serotypes: improved vectors for gene delivery. *Current gene therapy*, 5(3), 299–310. <https://doi.org/10.2174/1566523054064968>
- [22]. Kochergin-Nikitsky, K., Belova, L., Lavrov, A., & Smirnikhina, S. (2021). Tissue and cell-type-specific transduction using rAAV vectors in lung diseases. *Journal of molecular medicine* (Berlin, Germany), 99(8), 1057–1071. <https://doi.org/10.1007/s00109-021-02086-y>
- [23]. Mietzsch, M., Jose, A., Chipman, P., Bhattacharya, N., Daneshparvar, N., McKenna, R., & Agbandje-McKenna, M. (2021). Completion of the AAV Structural Atlas: Serotype Capsid Structures Reveals Clade-Specific Features. *Viruses*, 13(1), 101. <https://doi.org/10.3390/v13010101>
- [24]. Gray, S. J., Choi, V. W., Asokan, A., Haberman, R. A., McCown, T. J., & Samulski, R. J. (2011). Production of recombinant adeno-associated viral vectors and use in vitro and in vivo administration. *Current protocols in neuroscience*, Chapter 4, Unit4.17–4.17. <https://doi.org/10.1002/0471142301.ns0417s57>
- [25]. Liu, Y., Kim, Y. J., Ji, M., Fang, J., Siriwon, N., Zhang, L. I., & Wang, P. (2014). Enhancing gene delivery of adeno-associated viruses by cell-permeable peptides. *Molecular therapy. Methods & clinical development*, 1, 12. <https://doi.org/10.1038/mtm.2013.12>
- [26]. Yao, S., Rong, W., & Yuan, Y. (2023). Optimization of adeno-associated virus (AAV) gene delivery into human bone marrow stem cells (hBMSCs). *Stem cell investigation*, 10, 3. <https://doi.org/10.21037/sci-2022-042>
- [27]. Zheng, Z., Ye, J., Leng, M., Gan, C., Tang, N., Li, W., Valencia, C. A., Dong, B., & Chow, H. Y. (2023). Enhanced sensitivity of neutralizing antibody detection for different AAV serotypes using HeLa cells with overexpressed AAVR. *Frontiers in pharmacology*, 14, 1188290. <https://doi.org/10.3389/fphar.2023.1188290>
- [28]. Aurnhammer, C., Haase, M., Muether, N., Hausl, M., Rauschhuber, C., Huber, I., Nitschko, H., Busch, U., Sing, A., Ehrhardt, A., & Baiker, A. (2012). Universal real-time PCR for the detection and quantification of adeno-associated virus serotype 2-derived inverted terminal repeat sequences. *Human gene therapy methods*, 23(1), 18–28. <https://doi.org/10.1089/hgtb.2011.034>
- [29]. Muraine, L., Bensalah, M., Dhiab, J., Cordova, G., Arandel, L., Marhic, A., Chapart, M., Vasseur, S., Benkhelifa-Ziyyat, S., Bigot, A., Butler-Browne, G., Mouly, V., Negroni, E., & Trollet, C. (2020). Transduction Efficiency of Adeno-Associated Virus Serotypes After Local Injection in Mouse and Human Skeletal Muscle. *Human gene therapy*, 31(3-4), 233–240. <https://doi.org/10.1089/hum.2019.173>
- [30]. Berns, K. I., & Srivastava, A. (2019). Next Generation of Adeno-Associated Virus Vectors for Gene Therapy for Human Liver Diseases. *Gastroenterology clinics of North America*, 48(2), 319–330. <https://doi.org/10.1016/j.gtc.2019.02.005>
- [31]. Zengel, J., & Carette, J. E. (2020). Structural and cellular biology of adeno-associated virus attachment and entry. *Advances in virus research*, 106, 39–84. <https://doi.org/10.1016/bs.aivir.2020.01.002>
- [32]. Chow, R. D., Guzman, C. D., Wang, G., Schmidt, F., Youngblood, M. W., Ye, L., Errami, Y., Dong, M. B., Martinez, M. A., Zhang, S., Renauer, P., Bilguvar, K., Gunel, M., Sharp, P. A., Zhang, F., Platt, R. J., & Chen, S. (2017). AAV-mediated direct in vivo CRISPR screen identifies functional suppressors in glioblastoma. *Nature neuroscience*, 20(10), 1329–1341. <https://doi.org/10.1038/nn.4620>
- [33]. Hung, S. S., Chrysostomou, V., Li, F., Lim, J. K., Wang, J. H., Powell, J. E., Tu, L., Daniszewski, M., Lo, C., Wong, R. C., Crowston, J. G., Pébay, A., King, A. E., Bui, B. V., Liu, G. S., & Hewitt, A. W. (2016). AAV-Mediated CRISPR/Cas Gene Editing of Retinal Cells In Vivo. *Investigative ophthalmology & visual science*, 57(7), 3470–3476. <https://doi.org/10.1167/iovs.16-19316>
- [34]. Miller, D. G., Petek, L. M., & Russell, D. W. (2003). Human gene targeting by adeno-associated virus vectors is enhanced by DNA double-strand breaks. *Molecular and cellular biology*, 23(10), 3550–3557. <https://doi.org/10.1128/MCB.23.10.3550-3557.2003>
- [35]. Batır, M. B., Şahin, E., & Çam, F. S. (2019). Evaluation of the CRISPR/Cas9 directed mutant TP53 gene repairing effect in human prostate cancer cell line PC-3. *Molecular biology reports*, 46(6), 6471–6484. <https://doi.org/10.1007/s11033-019-05093-y>
- [36]. Ernst, M. P. T., Broeders, M., Herrero-Hernandez, P., Oussoren, E., van der Ploeg, A. T., & Pijnappel, W. W. M. P. (2020). Ready for Repair? Gene Editing Enters the Clinic for the Treatment of Human Disease. *Molecular therapy. Methods & clinical development*, 18, 532–557. <https://doi.org/10.1016/j.omtm.2020.06.022>
- [37]. Lino, C. A., Harper, J. C., Carney, J. P., & Timlin, J. A. (2018). Delivering CRISPR: a review of the challenges and approaches. *Drug delivery*, 25(1), 1234–1257. <https://doi.org/10.1080/10717544.2018.1474964>
- [38]. Maestro, S., Weber, N. D., Zabaleta, N., Aldabe, R., & Gonzalez-Aseguinolaza, G. (2021). Novel vectors and approaches for gene therapy in liver diseases. *JHEP reports : innovation in hepatology*, 3(4), 100300. <https://doi.org/10.1016/j.jhepr.2021.100300>
- [39]. Chen, C., Akerstrom, V., Baus, J., Lan, M. S., & Breslin, M. B. (2013). Comparative analysis of the transduction efficiency of five adeno associated virus serotypes and VSV-G pseudotype lentiviral vector in lung cancer cells. *Virology journal*, 10, 86. <https://doi.org/10.1186/1743-422X-10-86>
- [40]. Alves, S., Bode, J., Bemelmans, A. P., von Kalle, C., Cartier, N., & Tews, B. (2016). Ultramicroscopy as a novel tool to unravel the tropism of AAV gene therapy vectors in the brain. *Scientific reports*, 6, 28272. <https://doi.org/10.1038/srep28272>
- [41]. Chen, X., He, Y., Tian, Y., Wang, Y., Wu, Z., Lan, T., Wang, H., Cheng, K., & Xie, P. (2020). Different Serotypes of Adeno-Associated Virus Vector- and Lentivirus-Mediated Tropism in Choroid Plexus by Intracerebroventricular Delivery. *Human gene therapy*, 31(7-8), 440–447. <https://doi.org/10.1089/hum.2019.300>
- [42]. Korneyenkov, M. A., & Zamyatnin, A. A., Jr (2021). Next Step in Gene Delivery: Modern Approaches and Further Perspectives of AAV Tropism Modification. *Pharmaceutics*, 13(5), 750. <https://doi.org/10.3390/pharmaceutics13050750>
- [43]. Van Vliet, K. M., Blouin, V., Brument, N., Agbandje-McKenna, M., & Snyder, R. O. (2008). The role of the adeno-associated virus capsid in gene transfer. *Methods in molecular biology* (Clifton, N.J.), 437, 51–91. [https://doi.org/10.1007/978-1-59745-210-6\\_2](https://doi.org/10.1007/978-1-59745-210-6_2)
- [44]. Wu, Z., Asokan, A., & Samulski, R. J. (2006). Adeno-associated virus serotypes: vector toolkit for human gene therapy. *Molecular therapy : the journal of the American Society of Gene Therapy*, 14(3), 316–327. <https://doi.org/10.1016/j.ymthe.2006.05.009>

# On 7-Dimensional Nilpotent Leibniz Algebras with 1-Dimensional Leib Ideal

İsmail Demir<sup>1\*</sup> 

<sup>1</sup> Usak University, Faculty of Engineering and Natural Sciences Department of Mathematics, Uşak, Türkiye

\*[ismail.demir@usak.edu.tr](mailto:ismail.demir@usak.edu.tr)

\*Orcid: 0000-0002-8070-6489

Received: 8 August 2023

Accepted: 18 December 2023

DOI: 10.18466/cbayarfbe.1339702

## Abstract

Leibniz algebras are nonanticommutative versions of Lie algebras. Lie algebras have many applications in many scientific areas as well as mathematical areas. Scientists from different disciplines have used specific examples of Lie algebras according to their needs. However, we mathematicians are more interested in generality than in obtaining a few examples. The classification problem for Leibniz algebras has an intrinsically wild nature as in Lie algebras. In this article, the approach of congruence classes of bilinear forms is extended to classify certain subclasses of seven-dimensional nilpotent Leibniz algebras over complex numbers. Certain cases of seven-dimensional complex nilpotent Leibniz algebras of those with one-dimensional Leib ideal and derived algebra of codimension two are classified.

**Keywords:** Bilinear forms, Classification, Leibniz algebra, Nilpotency.

## 1. Introduction

Although first considered by Bloh in 1965 [1], Leibniz algebras as nonantisymmetric (nonanticommutative) generalization of Lie algebras were presented by Loday [2]. A vector space  $L$  over  $\mathbb{C}$  with a bilinear product  $[\cdot, \cdot] : L \times L \rightarrow L$  satisfying the Leibniz identity

$$[a, [b, c]] = [[a, b], c] + [b, [a, c]]$$

for all  $a, b, c \in L$  is said to be a Leibniz algebra. The lower central series of a Leibniz algebra  $L$  can be defined as  $L \supseteq L^2 \supseteq L^3 \supseteq \dots$  where  $L^1 = L$  and  $L^k = [L, L^{k-1}]$  for integers  $k \geq 2$ . If  $L^{c+1} = 0$  whenever  $L^c \neq 0$  for some  $c > 0$ , then  $L$  is a nilpotent Leibniz algebra of class  $c$ .  $L$  is called odd-nilpotent if its all nontrivial ideals of the lower central series are odd-dimensional. Leibniz algebra  $L$  of dimension  $n$  is called filiform Leibniz algebra if  $\dim(L^j) = n - j$  for  $2 \leq j \leq n$ .  $Leib(L)$  generated by the squares,  $[a, a]$ , for all  $a \in L$  is an ideal of  $L$ , is of the utmost importance while studying structure theory of Leibniz algebras. The center of a Leibniz algebra  $L$  can be defined by  $Z(L) = \{b \in L \mid [a, b] = 0 = [b, a] \text{ for all } a \in L\}$ . Non-split Leibniz algebras are those that cannot be expressed as the direct sum of nontrivial ideals. Throughout this paper, we assume Leibniz algebras are non-split non-Lie vector spaces over  $\mathbb{C}$ .

It is an important but nontrivial task to classify any kind of nonassociative algebras. Because the classification of

nilpotent Lie algebras is regarded as wild, the classification of nilpotent Leibniz algebras is also wild. In fact, the problem is more complicated for Leibniz algebras due to a lack of anticommutativity. Many researchers have provided numerous results on the classification of nilpotent Leibniz algebras over  $\mathbb{C}$  until now (see [2-14]); however, the problem has still not been completed. Seven-dimensional odd-nilpotent Leibniz algebras have been classified in [14] with the congruence classes of the bilinear forms approach. The main aim of this paper is to apply the same technique to give the classification of some subcases seven dimensional nilpotent Leibniz algebras with one-dimensional Leib ideal. The isomorphism test between the classes can be done by using Algorithm 2.6 proposed in [5].

## 2. Preliminaries

We include the following useful Lemmas from [12].

**Lemma 2.1.**  $L^c \subseteq Z(L)$  if  $L$  is a class  $c$  nilpotent Leibniz algebra.

**Lemma 2.2.** Let  $L$  be a non-split Leibniz algebra. Then,  $Z(L) \subseteq L^2$ .

**Lemma 2.3.** Any nilpotent Leibniz algebra  $L$  satisfies  $Leib(L) \subseteq Z(L)$ .

**Lemma 2.4.** For any  $n$ -dimensional nilpotent Leibniz algebra  $L$ ;  $\dim(Z(L)) = n - i$  and  $\dim(\text{Leib}(L)) = 1$  imply  $\dim(L^2) \leq \frac{i^2-i+2}{2}$ .

**Lemma 2.5.** For any  $n$ -dimensional nilpotent Leibniz algebra  $L$ ;  $\dim(L^2) = n - i$ ,  $\dim(\text{Leib}(L)) = 1$ , and  $\dim(L^3) = j$  imply the inequality  $n \leq j + \frac{i^2+i+2}{2}$ . Furthermore, if  $\text{Leib}(L) \subseteq L^3$ , then  $n \leq j + \frac{i^2+i}{2}$ .

**Lemma 2.6.** For any  $n$ -dimensional nilpotent Leibniz algebra  $L$ ;  $\dim(L^2) = n - i$  and  $L^4 \neq 0$  imply  $\dim(Z(L)) < n - i - 1$ .

The following matrices are the canonical forms for the congruence classes of matrices associated with a bilinear form on a complex vector space. Denoting

$$X \setminus Y := \begin{pmatrix} 0 & Y \\ X & 0 \end{pmatrix}$$

**Theorem 2.1.** [15] Any complex square matrix is congruent to a direct sum of the following canonical forms of matrices:

$$A_{2n+1} = \begin{bmatrix} 0 & 1 & 0 & 0 \\ 0 & \ddots & \ddots & 0 \\ 0 & 0 & 0 & 1 \end{bmatrix} \setminus \begin{bmatrix} 1 & 0 & 0 \\ 0 & \ddots & 0 \\ 0 & \ddots & 1 \\ 0 & 0 & 0 \end{bmatrix}$$

$$B_{2n}(\alpha) = \begin{bmatrix} 0 & 0 & 0 & \alpha \\ 0 & 0 & \alpha & 1 \\ 0 & \ddots & \ddots & 0 \\ \alpha & 1 & 0 & 0 \end{bmatrix} \setminus \begin{bmatrix} 0 & 0 & 0 & 1 \\ 0 & 0 & 1 & \alpha \\ 0 & \ddots & \ddots & 0 \\ 1 & \alpha & 0 & 0 \end{bmatrix}, \alpha \neq \pm 1$$

$$C_{2n+1} = \begin{pmatrix} 0 & 0 & 0 & 0 & 0 & 0 & 1 \\ 0 & 0 & 0 & 0 & 0 & 1 & 1 \\ 0 & 0 & 0 & 0 & \ddots & \ddots & 0 \\ 0 & 0 & 0 & 1 & 1 & 0 & 0 \\ 0 & 0 & 1 & -1 & 0 & 0 & 0 \\ 0 & \ddots & \ddots & 0 & 0 & 0 & 0 \\ 1 & -1 & 0 & 0 & 0 & 0 & 0 \end{pmatrix}$$

$$D_{2n} = \begin{bmatrix} 0 & 0 & 0 & 1 \\ 0 & 0 & 1 & -1 \\ 0 & \ddots & \ddots & 0 \\ 1 & -1 & 0 & 0 \end{bmatrix} \setminus \begin{bmatrix} 0 & 0 & 0 & 1 \\ 0 & 0 & 1 & 1 \\ 0 & \ddots & \ddots & 0 \\ 1 & 1 & 0 & 0 \end{bmatrix}, (n \text{ even})$$

$$E_{2n} = \begin{pmatrix} 0 & 0 & 0 & 0 & 0 & 0 & 1 \\ 0 & 0 & 0 & 0 & 0 & 1 & 1 \\ 0 & 0 & 0 & 0 & \ddots & \ddots & 0 \\ 0 & 0 & 0 & 1 & 1 & 0 & 0 \\ 0 & 0 & -1 & 1 & 0 & 0 & 0 \\ 0 & \ddots & \ddots & 0 & 0 & 0 & 0 \\ -1 & 1 & 0 & 0 & 0 & 0 & 0 \end{pmatrix}$$

$$F_{2n} = \begin{bmatrix} 0 & 0 & 0 & -1 \\ 0 & 0 & -1 & 1 \\ 0 & \ddots & \ddots & 0 \\ -1 & 1 & 0 & 0 \end{bmatrix} \setminus \begin{bmatrix} 0 & 0 & 0 & 1 \\ 0 & 0 & 1 & 1 \\ 0 & \ddots & \ddots & 0 \\ 1 & 1 & 0 & 0 \end{bmatrix}, (n \text{ odd})$$

### 3. Classification

Let  $L$  be 7-dimensional nilpotent Leibniz algebra with 1-dimensional Leib ideal. Some subclasses of 7-dimensional odd-nilpotent Leibniz algebras have been classified in [14]. For the sake of simplicity, we will consider Leibniz algebras with the derived algebra of codimension two, because employing the congruence classes of bilinear forms technique is easier in that situation.

Choose  $\dim(L^2) = n - 2$  and  $\text{Leib}(L) = \text{span}\{v_n\}$ . Extending it to a basis  $\{v_3, v_4, \dots, v_{n-1}, v_n\}$  for  $L^2$  and take a subspace  $V$  in  $L$  so that  $L = L^2 \oplus V$ . Therefore,  $[u, v] = \beta_3 v_3 + \beta_4 v_4 + \beta_{n-1} v_{n-1} + \beta_n v_n$  for  $3 \leq k \leq n, \beta_k \in \mathbb{C}$ , for each  $u, v \in V$ . The bilinear form  $f(\cdot, \cdot): V \times V \rightarrow \mathbb{C}$  provided by  $f(u, v) = \beta_n$  for each  $u, v \in V$ . Let  $\{v_1, v_2\}$  be a basis for  $V$ , and using Theorem 2.1, we can easily determine that the possible matrices of the bilinear form above are the following:

$$F_2 = \begin{pmatrix} 0 & 1 \\ -1 & 0 \end{pmatrix}, \quad A_1 \oplus C_1 = \begin{pmatrix} 1 & 0 \\ 0 & 0 \end{pmatrix},$$

$$C_1 \oplus C_1 = \begin{pmatrix} 1 & 0 \\ 0 & 1 \end{pmatrix}, \quad E_2 = \begin{pmatrix} 0 & 1 \\ -1 & 1 \end{pmatrix}, \quad B_2 = \begin{pmatrix} 0 & 1 \\ \alpha & 0 \end{pmatrix}$$

where  $\alpha \neq \pm 1$ . We only consider non-Lie Leibniz algebras so that we can eliminate the matrix  $F_2$ . In addition, it is sufficient to focus only the matrices  $A_1 \oplus C_1$  and  $C_1 \oplus C_1$  since the other two matrices yield algebras that are always isomorphic to algebras obtained by these two matrices, as proved in Lemma 2.1 in [10].

Denote the following invariant  $\chi(L) = (\dim(L), \dim(L^2), \dim(L^3), \dots, \dim(L^c))$  where  $c$  is the class of nilpotency. Then, take a 7-dimensional nilpotent Leibniz algebra  $L$  with  $\dim(\text{Leib}(L)) = 1$  where  $\dim(L^2) = 5$ . Notice that there is no Leibniz algebra for the cases  $\dim(L^3) = 0, 1, 2$ , as Lemma 2.5 suggests. Hence, we have  $\dim(L^3) = 3$ . Odd-nilpotent subclasses of this case are already classified in [14]. The remaining cases are listed below:

- i.  $\chi(L) = (7, 5, 3, 2)$
- ii.  $\chi(L) = (7, 5, 3, 2, 1)$

**Theorem 3.1.** There does not exist any Leibniz algebra with Leib ideal of dimension one in the case  $\chi(L) = (7, 5, 3, 2)$ .

**Proof.** Take a nilpotent Leibniz algebra  $L$  with  $\chi(L) = (7, 5, 3, 2)$  and  $\dim(\text{Leib}(L)) = 1$ . We see that  $\text{Leib}(L) \subseteq Z(L)$  by using Lemma 2.3. Besides, from Lemma 2.5, we obtain  $\text{Leib}(L) \not\subseteq L^3$ . Lemma 2.2 implies  $L^4 \subseteq Z(L) \subset L^2$ . Then, by using Lemma 2.6, we deduce  $1 < \dim(Z(L)) < 4$ . But  $\dim(Z(L))$  cannot be 2, because otherwise  $L^4 = Z(L)$  implies that  $\text{Leib}(L) \subseteq L^4 \subset L^3$  which contradicts with  $\text{Leib}(L) \not\subseteq L^3$ . Hence,

suppose  $\dim(Z(L)) = 3$ . Taking a complementary subspace  $W$  to  $L^3$  in  $L^2$ . Since  $L^4 \neq 0$ , we have  $L^3 \neq Z(L)$ . Moreover, from  $L^4 \subseteq Z(L)$ , we can see that the only possibility is  $\dim(L^3 \cap Z(L)) = 2$ . Using  $Leib(L) \not\subseteq L^3, L^4$ , choose  $Leib(L) = span\{w_7\}, L^4 = span\{w_5, w_6\}$  and,  $L^3 = span\{w_4, w_5, w_6\}$ . Then,  $Z(L) = span\{w_5, w_6, w_7\}$  and  $L^2 = span\{w_3, w_4, w_5, w_6, w_7\}$ . Later, take  $A = span\{w_1, w_2, w_3, w_4, w_5, w_6, w_7\}$ . Then, the nonzero products in  $L$  are given as follows:

$$\begin{aligned} [w_1, w_1] &= \alpha_1 w_7, [w_2, w_2] = \alpha_2 w_7, [w_1, w_2] = \alpha_3 w_3 + \alpha_4 w_4 + \alpha_5 w_5 + \alpha_6 w_6 + \alpha_7 w_7, [w_2, w_1] = -\alpha_3 w_3 - \alpha_4 w_4 - \alpha_5 w_5 - \alpha_6 w_6 + \alpha_8 w_7, [w_1, w_3] = \beta_1 w_4 + \beta_2 w_5 + \beta_3 w_6 = -[w_3, w_1], [w_2, w_3] = \beta_4 w_4 + \beta_5 w_5 + \beta_6 w_6 = -[w_3, w_2], [w_1, w_4] = \gamma_1 w_5 + \gamma_2 w_6 = -[w_4, w_1], [w_2, w_4] = \gamma_3 w_5 + \gamma_4 w_6 = -[w_4, w_2], [w_3, w_4] = \gamma_5 w_5 + \gamma_6 w_6 = -[w_4, w_3]. \end{aligned}$$

We obtain the following equations using Leibniz identity:

$$\begin{aligned} \gamma_5 &= 0 = \gamma_6 \\ \beta_4 \gamma_1 - \beta_1 \gamma_3 &= 0 & (3.1) \\ \beta_4 \gamma_2 - \beta_1 \gamma_4 &= 0 & (3.2) \end{aligned}$$

Assume  $\gamma_3 = 0$ . Then,  $\gamma_1 \neq 0$  and from Equation 3.1, we have  $\beta_4 = 0$ . But  $\dim(L^3) = 3$  with Equation 3.2 implies  $\gamma_4 = 0$  which contradicts with the fact that  $\dim(L^4) = 2$ . Suppose  $\gamma_3 \neq 0$ . Later, with the change-of-basis  $x_1 = \gamma_3 w_1 - \gamma_1 w_2, x_2 = w_2, x_3 = w_3, x_4 = w_4, x_5 = w_5, x_6 = w_6, x_7 = w_7$ , we can force  $\gamma_1 = 0$ . Additionally, from Equation 3.1, we get  $\beta_1 = 0$ . But  $\dim(L^3) = 3$  with Equation 3.2 implies  $\gamma_2 = 0$  which contradicts with the fact that  $\dim(L^4) = 2$ . Therefore, there is no Leibniz algebra in the case  $\chi(L) = (7, 5, 3, 2)$  and  $\dim(Leib(L)) = 1$ . The proof is completed. ■

Suppose  $\chi(L) = (7, 5, 3, 2, 1)$  and  $\dim(Leib(L)) = 1$ . We have  $Leib(L) \subseteq Z(L)$  due to Lemma 2.3. Besides, from Lemma 2.5, we obtain  $Leib(L) \not\subseteq L^3$ . Lemma 2.2 implies  $L^5 \subseteq Z(L) \subset L^2$ . Then, by using Lemma 2.6, we deduce  $1 \leq \dim(Z(L)) < 4$ . If  $\dim(Z(L)) = 1$ , then  $Leib(L) = Z(L) = L^5 \subset L^3$ , we arrive a contradiction. Hence,  $\dim(Z(L)) = 2$  or  $\dim(Z(L)) = 3$ . We will first consider the case  $\dim(Z(L)) = 3$ .

**Theorem 3.2.** Let  $\chi(L) = (7, 5, 3, 2, 1)$ ,  $\dim(Leib(L)) = 1$  and  $\dim(Z(L)) = 3$ . Then,  $L$  is isomorphic to one of the following algebras with nontrivial multiplications ( $i^2 = -1$ ):

$$L1 \quad [\zeta_1, \zeta_1] = \zeta_7, [\zeta_1, \zeta_2] = \zeta_3 = -[\zeta_2, \zeta_1], [\zeta_1, \zeta_3] = \zeta_5 = -[\zeta_3, \zeta_1], [\zeta_1, \zeta_5] = \zeta_6 = -[\zeta_5, \zeta_1], [\zeta_2, \zeta_3] = \zeta_4 = -[\zeta_3, \zeta_2]$$

$$\begin{aligned} L2 \quad & [\zeta_1, \zeta_1] = \zeta_7, [\zeta_1, \zeta_2] = \zeta_3 = -[\zeta_2, \zeta_1], [\zeta_1, \zeta_3] = \zeta_4 = -[\zeta_3, \zeta_1], [\zeta_2, \zeta_3] = \zeta_5 = -[\zeta_3, \zeta_2], [\zeta_2, \zeta_5] = \zeta_6 = -[\zeta_5, \zeta_2] \\ L3 \quad & [\zeta_1, \zeta_1] = \zeta_7, [\zeta_1, \zeta_2] = \zeta_3 = -[\zeta_2, \zeta_1], [\zeta_1, \zeta_3] = \zeta_5 = -[\zeta_3, \zeta_1], [\zeta_1, \zeta_5] = \zeta_6 = -[\zeta_5, \zeta_1], [\zeta_2, \zeta_2] = \zeta_7, [\zeta_2, \zeta_3] = \zeta_4 = -[\zeta_3, \zeta_2] \\ L4 \quad & [\zeta_1, \zeta_1] = \zeta_7, [\zeta_1, \zeta_2] = \zeta_3 = -[\zeta_2, \zeta_1], [\zeta_1, \zeta_3] = \zeta_5 = -[\zeta_3, \zeta_1], [\zeta_1, \zeta_5] = i\zeta_6 = -[\zeta_5, \zeta_1], [\zeta_2, \zeta_2] = \zeta_7, [\zeta_2, \zeta_3] = \zeta_4 = -[\zeta_3, \zeta_2], [\zeta_2, \zeta_5] = \zeta_6 = -[\zeta_5, \zeta_2] \end{aligned}$$

**Proof.** Take a complementary subspace  $W$  to  $L^3$  in  $L^2$ . Since  $L^4 \neq 0$ , we have  $L^3 \neq Z(L)$ . We have  $L^3 \cap Z(L) \neq \emptyset$ , since  $L^5 \subseteq Z(L)$ . Furthermore,  $\dim(L^3 \cap Z(L)) = 1$  implies  $W \subseteq Z(L)$  and since  $L^3 = [L, L^2] = [L, L^3 \oplus W] = L^4$  we arrive at a contradiction. Therefore,  $\dim(L^3 \cap Z(L)) = 2$ . Using  $Leib(L) \not\subseteq L^3, L^4, L^5$ , choose  $Leib(L) = span\{w_7\}, L^5 = span\{w_6\}, L^4 = span\{w_5, w_6\}$ , and  $L^3 = span\{w_4, w_5, w_6\}$ . Then,  $Z(L) = span\{w_4, w_6, w_7\}$  and  $L^2 = span\{w_3, w_4, w_5, w_6, w_7\}$ . Later, take  $V = span\{w_1, w_2\}$ .

**Case 1.** If the bilinear form matrix is  $A_1 \oplus C_1$ , then the nonzero products in  $L$  can be given as:

$$\begin{aligned} [w_1, w_1] &= w_7, [w_1, w_2] = \alpha_1 w_3 + \alpha_2 w_4 + \alpha_3 w_5 + \alpha_4 w_6 = -[w_2, w_1], [w_1, w_3] = \beta_1 w_4 + \beta_2 w_5 + \beta_3 w_6 = -[w_3, w_1], [w_2, w_3] = \beta_4 w_4 + \beta_5 w_5 + \beta_6 w_6 = -[w_3, w_2], [w_1, w_5] = \gamma_1 w_6 = -[w_5, w_1], [w_2, w_5] = \gamma_2 w_6 = -[w_5, w_2], [w_3, w_5] = \gamma_3 w_6 = -[w_5, w_3]. \end{aligned}$$

From Leibniz identity, we get the following equations:

$$\begin{aligned} \gamma_3 &= 0 \\ \beta_5 \gamma_1 - \beta_2 \gamma_2 &= 0 & (3.3) \end{aligned}$$

First, suppose  $\gamma_2 = 0$ . Then,  $\gamma_1 \neq 0$  and from Equation 3.3, we have  $\beta_5 = 0$ . Using  $\dim(L^3) = 3$ , we can see that  $\beta_2, \beta_4 \neq 0$ . Then, the change of basis  $\zeta_1 = w_1, \zeta_2 = w_2, \zeta_3 = \alpha_1 w_3 + \alpha_2 w_4 + \alpha_3 w_5 + \alpha_4 w_6, \zeta_4 = \alpha_1(\beta_4 w_4 + \beta_6 w_6), \zeta_5 = \alpha_1(\beta_1 w_4 + \beta_2 w_5 + \beta_3 w_6) + \alpha_3 \gamma_1 w_6, \zeta_6 = \alpha_1 \beta_2 \gamma_1 w_6, \zeta_7 = w_7$  shows  $L$  is isomorphic to  $L1$ . Next, suppose  $\gamma_2 \neq 0$ . Applying the change of basis  $x_1 = \gamma_2 w_1 - \gamma_1 w_2, x_2 = w_2, x_3 = w_3, x_4 = w_4, x_5 = w_5, x_6 = w_6, x_7 = \gamma_2^2 w_7$ , we can force  $\gamma_1 = 0$ . Then, from Equation 3.3, we get  $\beta_2 = 0$ . Therefore,  $\beta_1, \beta_5 \neq 0$  since  $\dim(L^3) = 3$ . The change of basis  $\zeta_1 = w_1, \zeta_2 = w_2, \zeta_3 = \alpha_1 w_3 + \alpha_2 w_4 + \alpha_3 w_5 + \alpha_4 w_6, \zeta_4 = \alpha_1(\beta_1 w_4 + \beta_3 w_6), \zeta_5 = \alpha_1(\beta_4 w_4 + \beta_5 w_5 + \beta_6 w_6) + \alpha_3 \gamma_2 w_6, \zeta_6 = \alpha_1 \beta_5 \gamma_2 w_6, \zeta_7 = w_7$  shows  $L$  is isomorphic to  $L2$ .

**Case 2.** If the bilinear form matrix is  $C_1 \oplus C_1$ , then the nonzero products in  $L$  can be given as:

$$[w_1, w_1] = w_7, [w_1, w_2] = \alpha_1 w_3 + \alpha_2 w_4 + \alpha_3 w_5 + \alpha_4 w_6 = -[w_2, w_1], [w_2, w_2] = w_7, [w_1, w_3] = \beta_1 w_4 + \beta_2 w_5 + \beta_3 w_6 = -[w_3, w_1], [w_2, w_3] = \beta_4 w_4 + \beta_5 w_5 + \beta_6 w_6 = -[w_3, w_2], [w_1, w_5] = \gamma_1 w_6 =$$

Again, Leibniz identity yields same equations as in Case 1. Let  $\gamma_2 = 0$ . Then,  $\gamma_1 \neq 0$  since  $\dim(Z(L)) = 3$ . From Equation 3.3, we have  $\beta_5 = 0$ . Using  $\dim(L^3) = 3$ , we obtain  $\beta_2, \beta_4 \neq 0$ . Then, the change of basis  $\zeta_1 = w_1, \zeta_2 = w_2, \zeta_3 = \alpha_1 w_3 + \alpha_2 w_4 + \alpha_3 w_5 + \alpha_4 w_6, \zeta_4 = \alpha_1(\beta_4 w_4 + \beta_6 w_6), \zeta_5 = \alpha_1(\beta_1 w_4 + \beta_2 w_5 + \beta_3 w_6) + \alpha_3 \gamma_1 w_6, \zeta_6 = \alpha_1 \beta_2 \gamma_1 w_6, \zeta_7 = w_7$  shows  $L$  is isomorphic to  $L3$ . Further, take  $\gamma_2 \neq 0$ . If  $\gamma_1 = 0$ , then  $x_1 = w_2, x_2 = w_1, x_3 = w_3, x_4 = w_4, x_5 = w_5, x_6 = w_6, x_7 = w_7$  is the change of basis forces  $\gamma_2 = 0$ . Therefore,  $L$  is isomorphic to  $L3$ . Let  $\gamma_1 \neq 0$ . Assume that  $\gamma_1^2 + \gamma_2^2 \neq 0$ . Then  $x_1 = \gamma_1 w_1 + \gamma_2 w_2, x_2 = \gamma_2 w_1 - \gamma_1 w_2, x_3 = w_3, x_4 = w_4, x_5 = w_5, x_6 = w_6, x_7 = (\gamma_1^2 + \gamma_2^2)w_7$  is the change of basis that forces  $\gamma_2 = 0$  and consequently  $L$  is isomorphic to  $L3$ . Take  $\gamma_1^2 + \gamma_2^2 = 0$ . Then, from Equation 3.3, we obtain  $\beta_2^2 + \beta_5^2 = 0$ . Notice that  $\beta_1^2 + \beta_4^2 \neq 0$  due to  $\dim(L^3) = 3$ . When  $\beta_1^2 + \beta_4^2 \neq 0$ , applying the change of basis  $x_1 = \beta_4 w_1 - \beta_1 w_2, x_2 = \beta_1 w_1 + \beta_4 w_2, x_3 = w_3, x_4 = w_4, x_5 = w_5, x_6 = w_6, x_7 = (\beta_1^2 + \beta_4^2)w_7$  forces  $\beta_1 = 0$ . Thus, without loss of generality, we can take  $\beta_1 = 0$ . Finally, the change of basis  $\zeta_1 = w_1, \zeta_2 = w_2, \zeta_3 = \alpha_1 w_3 + \alpha_2 w_4 + \alpha_3 w_5 + \alpha_4 w_6, \zeta_4 = \alpha_1(\beta_4 w_4 + \beta_5 w_5 + \beta_6 w_6) + \alpha_3 \gamma_2 w_6, \zeta_5 = \alpha_1 \beta_2 w_5 + (\alpha_1 \beta_3 + \alpha_3 \gamma_1)w_6, \zeta_6 = \alpha_1 \beta_2 \gamma_2 w_6, \zeta_7 = w_7$  shows  $L$  is isomorphic to  $L4$ . ■

We obtain 4 single algebras. Similarly, the classification of the case  $\chi(L) = (7, 5, 3, 2, 1), \dim(Leib(L)) = 1$  and  $\dim(Z(L)) = 2$  can be obtained by applying the aforementioned technique above.

**Theorem 3.3.** Let  $\chi(L) = (7, 5, 3, 2, 1), \dim(Leib(L)) = 1$  and  $\dim(Z(L)) = 2$ . Then,  $L$  is isomorphic to one of the following algebras with nontrivial multiplications (here  $i^2 = -1$ ):

- L1  $[\zeta_1, \zeta_1] = \zeta_7, [\zeta_1, \zeta_2] = \zeta_3 = -[\zeta_2, \zeta_1], [\zeta_1, \zeta_3] = \zeta_4 = -[\zeta_3, \zeta_1], [\zeta_1, \zeta_4] = \zeta_5 = -[\zeta_4, \zeta_1], [\zeta_1, \zeta_5] = \zeta_6 = -[\zeta_5, \zeta_1]$
- L2  $[\zeta_1, \zeta_1] = \zeta_7, [\zeta_1, \zeta_2] = \zeta_3 = -[\zeta_2, \zeta_1], [\zeta_1, \zeta_3] = \zeta_4 = -[\zeta_3, \zeta_1], [\zeta_1, \zeta_4] = \zeta_5 = -[\zeta_4, \zeta_1], [\zeta_1, \zeta_5] = \zeta_6 = -[\zeta_5, \zeta_1], [\zeta_2, \zeta_3] = \zeta_6 = -[\zeta_3, \zeta_2]$
- L3  $[\zeta_1, \zeta_1] = \zeta_7, [\zeta_1, \zeta_2] = \zeta_3 = -[\zeta_2, \zeta_1], [\zeta_1, \zeta_3] = \zeta_4 = -[\zeta_3, \zeta_1], [\zeta_1, \zeta_4] = \zeta_5 = -[\zeta_4, \zeta_1], [\zeta_1, \zeta_5] = \zeta_6 = -[\zeta_5, \zeta_1], [\zeta_2, \zeta_3] = \zeta_5 = -[\zeta_3, \zeta_2], [\zeta_2, \zeta_4] = \zeta_6 = -[\zeta_4, \zeta_2]$
- L4  $[\zeta_1, \zeta_1] = \zeta_7, [\zeta_1, \zeta_2] = \zeta_3 = -[\zeta_2, \zeta_1], [\zeta_1, \zeta_3] = \zeta_4 = -[\zeta_3, \zeta_1], [\zeta_1, \zeta_4] = \zeta_5 =$

$$-[\zeta_5, w_1], [\zeta_2, w_5] = \gamma_2 w_6 = -[\zeta_5, w_2], [\zeta_3, w_5] = \gamma_3 w_6 = -[\zeta_5, w_3].$$

- $-\zeta_4, \zeta_1], [\zeta_1, \zeta_5] = \zeta_6 = -[\zeta_5, \zeta_1], [\zeta_2, \zeta_3] = \zeta_5 + \zeta_6 = -[\zeta_3, \zeta_2], [\zeta_2, \zeta_4] = \zeta_6 = -[\zeta_4, \zeta_2]$
- L5  $[\zeta_1, \zeta_1] = \zeta_7, [\zeta_1, \zeta_2] = \zeta_3 = -[\zeta_2, \zeta_1], [\zeta_1, \zeta_3] = \zeta_4 = -[\zeta_3, \zeta_1], [\zeta_1, \zeta_4] = \zeta_5 = -[\zeta_4, \zeta_1], [\zeta_2, \zeta_3] = \zeta_5 = -[\zeta_3, \zeta_2], [\zeta_2, \zeta_5] = \zeta_6 = -[\zeta_5, \zeta_2], [\zeta_3, \zeta_4] = -\zeta_6 = -[\zeta_4, \zeta_3]$
- L6  $[\zeta_1, \zeta_1] = \zeta_7, [\zeta_1, \zeta_2] = \zeta_3 = -[\zeta_2, \zeta_1], [\zeta_1, \zeta_3] = \zeta_4 = -[\zeta_3, \zeta_1], [\zeta_1, \zeta_4] = \zeta_5 = -[\zeta_4, \zeta_1], [\zeta_2, \zeta_3] = \zeta_5 + \zeta_6 = -[\zeta_3, \zeta_2], [\zeta_2, \zeta_5] = \zeta_6 = -[\zeta_5, \zeta_2], [\zeta_3, \zeta_4] = -\zeta_6 = -[\zeta_4, \zeta_3]$
- L7  $[\zeta_1, \zeta_1] = \zeta_7, [\zeta_1, \zeta_2] = \zeta_3 = -[\zeta_2, \zeta_1], [\zeta_1, \zeta_3] = \zeta_5 + \zeta_6 = -[\zeta_3, \zeta_1], [\zeta_1, \zeta_4] = \zeta_6 = -[\zeta_4, \zeta_1], [\zeta_2, \zeta_3] = \zeta_4 = -[\zeta_3, \zeta_2], [\zeta_2, \zeta_4] = \zeta_5 = -[\zeta_4, \zeta_2], [\zeta_2, \zeta_5] = \zeta_6 = -[\zeta_5, \zeta_2]$
- L8  $[\zeta_1, \zeta_1] = \zeta_7, [\zeta_1, \zeta_2] = \zeta_3 = -[\zeta_2, \zeta_1], [\zeta_1, \zeta_3] = \zeta_5 + \zeta_6 = -[\zeta_3, \zeta_1], [\zeta_1, \zeta_5] = \zeta_6 = -[\zeta_5, \zeta_1], [\zeta_2, \zeta_3] = \zeta_4 = -[\zeta_3, \zeta_2], [\zeta_2, \zeta_4] = \zeta_5 = -[\zeta_4, \zeta_2], [\zeta_3, \zeta_4] = \zeta_6 = -[\zeta_4, \zeta_3]$
- L9  $[\zeta_1, \zeta_1] = \zeta_7, [\zeta_1, \zeta_2] = \zeta_3 = -[\zeta_2, \zeta_1], [\zeta_1, \zeta_3] = \zeta_5 + \alpha \zeta_6 = -[\zeta_3, \zeta_1], [\zeta_1, \zeta_5] = \zeta_6 = -[\zeta_5, \zeta_1], [\zeta_2, \zeta_3] = \zeta_4 = -[\zeta_3, \zeta_2], [\zeta_2, \zeta_4] = \zeta_5 = -[\zeta_4, \zeta_2], [\zeta_2, \zeta_5] = \zeta_6 = -[\zeta_5, \zeta_2], [\zeta_3, \zeta_4] = \zeta_6 = -[\zeta_4, \zeta_3]$
- L10  $[\zeta_1, \zeta_1] = \zeta_7, [\zeta_1, \zeta_2] = \zeta_3 = -[\zeta_2, \zeta_1], [\zeta_1, \zeta_3] = \zeta_4 = -[\zeta_3, \zeta_1], [\zeta_1, \zeta_4] = \zeta_5 = -[\zeta_4, \zeta_1], [\zeta_1, \zeta_5] = \zeta_6 = -[\zeta_5, \zeta_1], [\zeta_2, \zeta_2] = \zeta_7$
- L11  $[\zeta_1, \zeta_1] = \zeta_7, [\zeta_1, \zeta_2] = \zeta_3 = -[\zeta_2, \zeta_1], [\zeta_1, \zeta_3] = \zeta_4 = -[\zeta_3, \zeta_1], [\zeta_1, \zeta_4] = \zeta_5 = -[\zeta_4, \zeta_1], [\zeta_1, \zeta_5] = \zeta_6 = -[\zeta_5, \zeta_1], [\zeta_2, \zeta_2] = \zeta_7, [\zeta_2, \zeta_3] = \zeta_6 = -[\zeta_3, \zeta_2]$
- L12  $[\zeta_1, \zeta_1] = \zeta_7, [\zeta_1, \zeta_2] = \zeta_3 = -[\zeta_2, \zeta_1], [\zeta_1, \zeta_3] = \zeta_4 = -[\zeta_3, \zeta_1], [\zeta_1, \zeta_4] = \zeta_5 = -[\zeta_4, \zeta_1], [\zeta_1, \zeta_5] = \zeta_6 = -[\zeta_5, \zeta_1], [\zeta_2, \zeta_2] = \zeta_7, [\zeta_2, \zeta_3] = \zeta_5 + \alpha \zeta_6 = -[\zeta_3, \zeta_2], [\zeta_2, \zeta_4] = \zeta_6 = -[\zeta_4, \zeta_2]$
- L13  $[\zeta_1, \zeta_1] = \zeta_7, [\zeta_1, \zeta_2] = \zeta_3 = -[\zeta_2, \zeta_1], [\zeta_1, \zeta_3] = \zeta_4 = -[\zeta_3, \zeta_1], [\zeta_1, \zeta_4] = \zeta_5 = -[\zeta_4, \zeta_1], [\zeta_1, \zeta_5] = \beta \zeta_6 = -[\zeta_5, \zeta_1], [\zeta_2, \zeta_2] = \zeta_7, [\zeta_2, \zeta_3] = \zeta_5 + \alpha \zeta_6 = -[\zeta_3, \zeta_2], [\zeta_2, \zeta_5] = \zeta_6 = -[\zeta_5, \zeta_2], [\zeta_3, \zeta_4] = -\zeta_6 = -[\zeta_4, \zeta_3]$
- L14  $[\zeta_1, \zeta_1] = \zeta_7, [\zeta_1, \zeta_2] = \zeta_3 = -[\zeta_2, \zeta_1], [\zeta_1, \zeta_3] = \zeta_4 = -[\zeta_3, \zeta_1], [\zeta_1, \zeta_4] = \zeta_5 = -[\zeta_4, \zeta_1], [\zeta_1, \zeta_5] = \zeta_6 = -[\zeta_5, \zeta_1], [\zeta_2, \zeta_2] = \zeta_7, [\zeta_2, \zeta_3] = i \zeta_4 + \alpha \zeta_5 + \beta \zeta_6 = -[\zeta_3, \zeta_2], [\zeta_2, \zeta_4] = i \zeta_5 + \gamma \zeta_6 = -[\zeta_4, \zeta_2], [\zeta_2, \zeta_5] = i \zeta_6 = -[\zeta_5, \zeta_2]$
- L15  $[\zeta_1, \zeta_1] = \zeta_7, [\zeta_1, \zeta_2] = \zeta_3 = -[\zeta_2, \zeta_1], [\zeta_1, \zeta_3] = \zeta_4 = -[\zeta_3, \zeta_1], [\zeta_1, \zeta_4] = \zeta_5 = -[\zeta_4, \zeta_1], [\zeta_1, \zeta_5] = \zeta_6 = -[\zeta_5, \zeta_1], [\zeta_2, \zeta_2] = \zeta_7, [\zeta_2, \zeta_3] = i \zeta_4 + \alpha \zeta_5 + \beta \zeta_6 = -[\zeta_3, \zeta_2], [\zeta_2, \zeta_4] = i \zeta_5 + \gamma \zeta_6 = -[\zeta_4, \zeta_2], [\zeta_2, \zeta_5] = \theta \zeta_6 = -[\zeta_5, \zeta_2], [\zeta_3, \zeta_4] = \delta \zeta_6 = -[\zeta_4, \zeta_3]$







#### 4. Conclusion

We reached the complete classification of nilpotent Leibniz algebras of dimension seven, whose derived algebra is of dimension five, while the Leib ideal is one dimensional with the restriction  $\dim(L^3) < 4$ . The classifications given in this paper and in [14] achieve that result. There exist 19 single algebras, 4 one-parameter continuous families, 2 two-parameter continuous families, 1 three-parameter continuous family, and 1 one-parameter continuous family. It is left to look at the case  $\dim(L^3) = 4$  in order to complete the classification of nilpotent Leibniz algebra of dimension seven, whose derived algebra is of dimension five while Leib ideal is one dimensional. Notice that  $\chi(L) = (7, 5, 4, 3, 2, 1)$  is filiform Leibniz algebra, and the classification of this subclass with one-dimensional Leib ideal can be obtained by Theorem 2.2 in [4].  $TLb_7$  in that Theorem will produce desired algebras. In fact, the classification of the subclass  $TLb_7$  is given in [6]. According to that classification, there are 13 single algebras and 9 one-parameter continuous families of filiform non-Lie Leibniz algebras of dimension seven. Furthermore, there is no Leibniz algebra for the case  $\chi(L) = (7, 5, 4)$ , because here  $L^3 = Z(L)$  with the Lemma 2.4 give  $\dim(L^2) \leq 4$ , which contradicts  $L^2$  being a 5-dimensional ideal. Hence, we have the following six cases to classify:

- i.  $\chi(L) = (7, 5, 4, 3, 2)$
- ii.  $\chi(L) = (7, 5, 4, 3, 1)$
- iii.  $\chi(L) = (7, 5, 4, 3)$
- iv.  $\chi(L) = (7, 5, 4, 2, 1)$
- v.  $\chi(L) = (7, 5, 4, 2)$
- vi.  $\chi(L) = (7, 5, 4, 1)$

Our approach of bilinear forms can also be utilized to classify these cases. It is known that there are 119 single algebras and six one-parameter continuous families of Lie algebra of dimension seven over an algebraically closed field [16]. Even though, we restrict our attention to seven-dimensional nilpotent Leibniz algebras whose Leib ideal is one dimensional and derived algebra is of dimension five, we get 32 single algebras, 13 one-parameter continuous families, two two-parameter continuous families, one three-parameter continuous family, and one one-parameter continuous family so far and there are still some cases to cover. As a future work, classification of higher dimensional nilpotent Leibniz algebras with one dimensional Leib ideal and/or classification of nilpotent Leibniz algebras of higher dimensions with the derived algebra of codimension two can be obtained by the congruence classes of bilinear forms method.

#### Author's Contributions

**İsmail Demir:** Drafted and wrote the manuscript, performed the experiment and result analysis.

#### Ethics

There are no ethical issues after the publication of this manuscript.

#### References

- [1]. Bloh, A. 1965. On a Generalization of Lie Algebra Notion. *Mathematics in USSR Doklady*; 165(3): 471-473.
- [2]. Loday, JL. 1993. Une Version Non-Commutative des Algebres de Lie: Les Algebres de Leibniz. *L'Enseignement Mathematique*; 39(3-4): 269-293.
- [3]. Albeverio, S, Omirov, BA, Rakhimov, IS. 2006. Classification of 4-Dimensional Nilpotent Complex Leibniz Algebra. *Extracta Mathematicae*; 21(3): 197-210.
- [4]. Rakhimov, IS, Bekbaev, UD. 2010. On Isomorphisms and Invariants of Finite Dimensional Complex Filiform Leibniz algebras. *Communications in Algebra*; 38: 4705-4738.
- [5]. Casas, JM, Insua, MA, Ladra, M, Ladra, S. 2012. An Algorithm for the Classification of 3-Dimensional Complex Leibniz Algebras. *Linear Algebra and its Applications*; 9: 3747-3756.
- [6]. Abdulkareem, AO, Rakhimov, IS, Husain, SK. On Seven-Dimensional Filiform Leibniz Algebras, In: Kilicman, A., Leong, W., Eshkuvatov, Z. (eds) International Conference on Mathematical Sciences and Statistics, 2014, pp 1-11.
- [7]. Gomez, JR, Omirov, BA. 2015. On Classification of Filiform Leibniz Algebras. *Algebra Colloquium*; 22: 757-774.
- [8]. Demir, I, Misra, KC, Stitzinger, E. 2017. On Classification of Four-Dimensional Nilpotent Leibniz Algebras. *Communications in Algebra*; 45(3): 1012-1018.
- [9]. Rakhimov, IS, Khudoyberdiyev, AK, Omirov, BA. 2017. On Isomorphism Criterion for a Subclass of Complex Filiform Leibniz Algebras. *International Journal of Algebra and Computation*; 27(7): 953-972.
- [10]. Demir, I. Classification of 5-Dimensional Complex Nilpotent Leibniz Algebras, In: N. Jing, K. C. Misra (Eds.), Representations of Lie Algebras, Quantum Groups and Related Topics, Contemporary Mathematics, Volume 713, American Mathematical Society, 2018, pp. 95-120.
- [11]. Mohamed, NS, Husain, SK, Rakhimov, IS. 2019. Classification of a Subclass of 10-Dimensional Complex Filiform Leibniz Algebras. *Malaysian Journal of Mathematical Sciences*; 13(3): 465-485.
- [12]. Demir, I. 2020. Classification of Some Subclasses of 6-Dimensional Nilpotent Leibniz Algebras. *Turkish Journal of Mathematics*; 44: 1925-1940.
- [13]. Farris, L. Finite Dimensional Nilpotent Leibniz Algebras with Isomorphic Maximal Algebras, Doctoral Dissertation, North Carolina State University, 2022.
- [14]. Demir, I. On Classification of 7-Dimensional Odd-Nilpotent Leibniz Algebras. *Hacettepe Journal of Mathematics and Statistics*, (in press).
- [15]. Teran, F. 2016. Canonical Forms for Congruence of Matrices and T-palindromic Matrix Pencils: a Tribute to H. W. Turnbull and A. C. Aitken. *SeMA Journal: Bulletin of the Spanish Society of Applied Mathematics*; 73: 7-16.
- [16]. Gong, MP. Classification of Nilpotent Lie Algebras of Dimension 7 (over Algebraically Closed Field  $\mathbb{F}$  and  $\mathbb{R}$ ), Doctoral Dissertation, University of Waterloo, 1998.

# Green Biosynthesis of Silver Nanoparticles were Obtained from the Extract of Pomegranate (*Punica granatum* L.) Leaves by Supercritical Extraction Using Microwave Method

Gönül Serdar <sup>1\*</sup> 

<sup>1</sup> Karadeniz Technical University, Central Research Laboratory, Trabzon, Türkiye

\*[gonulserdar@ktu.edu.tr](mailto:gonulserdar@ktu.edu.tr)

\*Orcid No: 0000-0002-3589-2323

Received: 9 August 2023

Accepted: 21 October 2023

DOI: 10.18466/cbayarfb.1338606

## Abstract

In this study, pomegranate (*Punica granatum* L.) leaf extract and 2% (w/v) aqueous solutions isolated by SFE extraction and microwave extraction were used to create silver nanoparticles (AgNPs). The pomegranate was grown in Turkey's Eastern Black Sea region. AgNO<sub>3</sub> solution (0.25, 0.5, and 1 mM) received separate additions of 0.1 and 0.2 mL extract before being microwave-irradiated. Ag nanoparticles made using green chemical techniques were characterized by UV-Visible, XRD, TEM, Zetasizer and FT-IR. By analyzing the plasmon resonance absorption (SPR) spectra by the UV-Visible technique, the ideal circumstances were identified. The face-centered cubic crystalline silver nanostructures' lattice planes (111), (200), (220), and (311) show that the different Bragg reflection peaks occurred at 2 values of 38.1°, 44.3°, 64.6°, and 77.6°. The average particle size of Ag nanoparticles produced by microwave extraction in an aqueous medium was 86.02 ± 0.579 nm, the zeta potential was -14 ± 0.777 mV, and the polydispersity index was 0.257 ± 0.004, according to the results of zeta-Sizer study. The UV-vis absorption spectra of the AgNP solutions, which were kept in a refrigerator, barely altered and remained constant for roughly 4-5 months.

**Keywords:** AgNPs, FTIR, Pomegranate (*Punica granatum* L.) leaf, Supercritical Fluid Extraction (SFE), TEM, XRD

## 1. Introduction

Nanotechnology is primarily concerned with materials with diameters ranging from 1 to 100 nm and possessing properties distinct from bulk materials. This update expands the possibilities for nanomaterials in healthcare and environmental remediation [1-3]. Nanotechnology is a combination of technology with science that involves the production or production, design, which is and analysis of nanometer-scale materials [4,5] The ability to manipulate the atoms or molecules in a structure of substances at the nanoscale level allows us to modify their properties various materials for specialized uses [6]. That is why nanotechnology has piqued the interest of numerous scientists and researchers throughout the world and has grown in popularity in both scientific studies and industry [4,7,8]. Currently, nanotechnology involving the environmentally friendly production of nanoparticles that has become an attractive idea that has gained much significance and importance in the past few years because of its excellent facility, clean processing, use of non-toxic chemicals, cost-effectiveness, and environmental and sustainability [4].

Nanomaterials are increasingly being used in combination with anticancer medications, and these molecules have numerous medical applications [9-12]. One of the practical applications of nanomaterials is combining them with anticancer medications so that the medicinal product can be administered to the cell more efficiently while reducing toxicity and adverse effects on healthy cells [9,13-15]. Because of the rising cancer death rate and flaws in radiotherapy and chemotherapy procedures in advanced stages of cancer, it is critical to develop modern cancer control and treatment strategies [16-19]. Nanoparticles with a measurement of 100 nm or less are often used in cancer medical research to target cancer cells when used with anticancer medications [20-22]. The nanomaterials were created using a variety of organisms, for example bacteria, fungi, yeast, and various others, resulting in an environmentally benign and clean process of synthesis [1].

In the biosynthesis process, various plants and components of plants are employed to produce nanoparticles that act as reducing and capping agents.

The synthesis of particles using plant extracts is a type of "green chemistry" that is safe, harmless, and environmentally friendly. Nanoparticles are produced biologically by employing extract-based production and chemicals with reductive action to transform metal ions into the element metal [1]. *Punica granatum* L. has been utilized for treating a variety of ailments for thousands of years throughout various cultures and civilizations [23]. Pomegranate is a well-known fruit in Asian culture. In folkloric medicine, pomegranate has numerous medicinal purposes [9]. Pomegranate is a well-known medicinal plant with many uses in traditional medicine. *Punica granatum* leaves are used to treat stomach ailments, diarrhea, dysentery, hemorrhages, and conjunctivitis, etc. The production of nanoparticles through plant leaf extracts for therapeutic reasons has recently gained traction [23]. According to prior research, the most significant secondary metabolites in Pomegranate are phenolic compounds such as glycosides, the sterols steroids, resins, flavonoids, alkaloids, lipids, coumarins that and vitamins. Indeed, the variety of chemicals found in Pomegranate are accountable for the plant's extensive range of pharmacological applications [9,24-27]. Silver nanoparticles are one of the most prevalent nanoparticles in this field, and they are thought to be potential anticancer agents. Plants provide a variety of components and biochemicals that can act as stabilizing and reducing agents in the synthesis of green nanoparticles. When compared to alternative biological, physical, and chemical approaches, green synthesis technologies are more environmentally friendly, non-toxic, cost-effective, and stable [28,29]. The production of nanoparticles from plant extract is a low-cost procedure that produces higher yields because to the large amount of phytochemical components in the extract, which can also act as reducing and stabilizing agents, transforming metal ions into metal nanoparticles [28]. Silver nanoparticles (AgNPs) are a type of substance with diameters ranging from 1 to 100 nm and is widely studied [4,28]. Because of their distinctive and appealing chemical, physical, and biological features, there has recently been an increase in devotion to the study of AgNPs and their diverse behaviors [4,30-32]. The silver nanoparticle is primarily used for enhancing biomedical applications such as medication administration, wound healing, tissue scaffolding, and protective covering. Furthermore, nanosilver has a large accessible surface area, which permits any ligand to connect to it. Silver nitrate is often used as an antibacterial agent. A silver nanoparticle is a novel and emerging antibacterial agent [28]. The physical, chemical, and biological features of such a nanoparticle are significant. Silver nanoparticles have significantly more favorable effects, such as broad-spectrum antibacterial response, non-toxicity, anticancer characteristics, and other therapeutic reasons, as well as the ability to generate distinct, diversified nanostructures and low-cost manufacture [28]. Alternative and sustainable extraction processes have been developed in

recent years. These environmentally friendly and efficient approaches yield high-yielding oils, resolving the issues that existing technologies present [33,34]. Some of these technologies include supercritical fluid extraction, aqueous extraction, enzymatic pre-treatment, and extraction aided by ultrasound, microwaves, or electrical pulses [33,35]. Microwave-assisted synthesis is seen as an option to the aforementioned issues due to its multiple advantages over the other synthesis methods, such as low cost, shorter time for processing, increased yield, high purity, and tiny particle size distribution, among others. It also has a high degree of influence over the end product shape and particle size [36]. In this respect, pomegranate leaves extract-mediated synthesis supported by microwave irradiation may serve as a quick and easy way to produce Ag nanoparticles because NP formation and development take place within just a short amount period in the reaction medium, leaves extracts raise NP capping rate, stabilization process is sped up, and AgNP aggregates increase. A supercritical fluid is used as a solvent in supercritical fluid extraction. Carbon dioxide is the most commonly used because of its apolar characteristics. Because the solvent is environmentally friendly, inert, and safe, and it is quickly eliminated after extraction with decompression, it is gaining appeal as a green technology. In comparison to other approaches, SFE solvent has a modifiable dissolved potential that can be adjusted by varying the pressure and temperature. Furthermore, supercritical fluids have a larger diffusion coefficient as well as less viscosity and surface tension than liquid solvents, which favors mass transfer [37]. Accordingly, in this study, pomegranate leaves were extracted using the SFE method, which is one of the modern extraction techniques. The method was optimized by performing biosynthesis of silver nanoparticles using microwave method in different volumes of the extract obtained with different concentrations of AgNO<sub>3</sub> solution. The current study aimed to produce a low-cost green synthesis of AgNPs utilizing *P. granatum* leaf extract (PGE). With this study, silver nanoparticles were produced from pomegranate leaves collected in the province of Turkey-Trabzon, which can be used as a basic source for the science and medicine industries, including pharmacology, food, and medicine. The goal of this study was to produce Ag nanoparticles, which has become the focus, according with the fundamentals of green chemistry. The synthesis and characterisation of Ag nanoparticles from pomegranate (*Punica granatum* L.) leaves extracted with SFE by microwave techniques have not been investigated in the literature. Therefore, the objective of this study was to produce and characterize Ag nanoparticles for the first time from pomegranate (*Punica granatum* L.) leaf extract obtained by the supercritical extraction method and from Turkey's Trabzon province using microwave-assisted technology. Uv-Vis, FTIR, TEM, XRD, and DLS techniques were then utilized to characterize the silver nanoparticles produced in accordance with green chemistry principles.



## 2. Materials and Methods

### 2.1. Chemicals

Silver nitrate ( $\text{AgNO}_3$  purity 99% Sigma Aldrich) salt was employed as the starting material in this study. The solvent used was deionized water. All compounds used were of analytical quality and were utilized without purification.

### 2.2. Preparation of Pomegranate Leaf Extract

Pomegranate (*Punica granatum* L.) leaves were gathered in the Eastern Black Sea region (Trabzon, Turkey), dried in an air-conditioned space, and then transported in little pieces under suitable conditions. 20 g of the sample was placed in a high pressure steel container fitted with an Applied Separation supercritical extractor (Spe-ed SFE, USA), a modifier (with co-solvent) pump (Applied Separation Series 1500), a chiller (Applied Separation Polyscience), and a pressure pump (Atlas Copco GX-4FF). The sample is enclosed between the glass wool's bottom and the container's top. The extraction was carried out at a pressure of 200 bar and a temperature of 50°C for 2.5 hours, with an ethanol modifier flow rate of 0.5 mL/min.

### 2.3. The green fabrication of Ag nanoparticles

In this synthesis, 0.1, 0.2 mL of pomegranate leaf extract solution, 20 mL, 0.25 mM, 0.5 mM and 1 Mm aqueous  $\text{AgNO}_3$  were added, and with a power of 90 W, 1–31 minutes, combined in a microwave extraction equipment (Figure 1). The color of the combination changed rapidly from colorless to light brown. The stability of the produced AgNPs was measured for up to 4-5 months. UV-vis measurements revealed a shift in the SPR of AgNPs. Centrifugation is at 10,000 rpm for 15 minutes (Hermle Z326K) separated the produced AgNPs. The pellets acquired were re-distributed and three times in sterile deionized water to remove any free biomass residue. The cleaned pellets were oven-dried at 50 C for 14 hours before being cleaned off for further character analysis.

### 2.4. Characterization of AgNPs

UV-visible spectrum analysis, Zeta-sizer, FT-IR, TEM, XRD analysis were used to analyze silver nanoparticles. UV-Vis absorption spectroscopy is used to identify nanoparticles with wavelengths that extend from 300 to 800 nm. Metallic nanoparticles produced under specific salt conditions have significant absorption, resulting in a point spectrum in the visible range [38]. UV-visible spectrum analysis was carried out using a Perkin Elmer Lambda 25 UV-visible spectrophotometer. The UV spectral peaks of nanoparticles of silver were reported to be between 400 and 480 nm in the literature [39-41]. The spectrum characterizes the sample

substances by providing absorption or transmittance as a function of wavelength [42]. FTIR analysis is a viable, cost-effective, easy, and non-invasive method for identifying the role of biomolecules in the reduction of nanoparticles (silver nitrate to silver) [43]. The produced nanoparticles were analyzed using the FTIR SHIMADZU instrument in the wavelength range of 4000 to 550  $\text{cm}^{-1}$ . At the nanoscale level, transmission electron microscopy (TEM) classified and confirmed the crystal structure of material [44,45]. The crystalline AgNPs were studied using a TEM (Hitachi HT -7700). XRD can be used to examine the atomic structures of materials. This technique is useful for determining the both qualitative and quantitative levels of materials. XRD (XRD, Panalytical X'Pert3 Powder) experiments was used to identify and are able to from the size and structure of crystalline nanoparticles [44,45]. XRD charts were measured using Cu-K radiation ( $\lambda=1.54059$ ) at 45 kV and 40 mA in the 10°-80° range. The Debye-Scherrer formula was used to estimate the particle dimension of nanomaterials from XRD data. By using dynamic light scattering (DLS) (Malvern Zetasizer Nano ZSP Analyzer, Malvern, UK), it was possible to determine the size distribution and zeta potential of AgNPs in aqueous suspension.

## 3. Results and Discussion

The UV-visible absorption spectrophotometer is the most widely used instrument for studying the SPR. The UV-visible spectroscopy analysis was utilized to observe the sharp and intense SPR peaks, and the aqueous pomegranate extract was employed to synthesis AgNPs. The absorption band's intensity was found to be promising as the consequence of the formation of highly distributed nanoparticles. A correlation between the generation of silver nanoparticles and the manipulation of their size and distribution, as well as their production, was demonstrated to be dependent on the solvent employed for extract synthesis [46]. The biological metabolites included in the extract have a big impact on the size, shape, and optical properties of silver nanoparticles [46]. The reaction solution's color changed from yellowish-brown to reddish-brown in less than 31 minutes, clearly demonstrating the biological reduction of  $\text{AgNO}_3$  into AgNPs. (Fig. 1a). The color of pomogranate leaf extract went dark once the aqueous  $\text{AgNO}_3$  solution was added, indicating the reaction had begun. The characterisation of silver nanoparticles based on the SPR (surface plasmon resonance) peak found at 430 nm provided proof that AgNPs had been successfully synthesized. Furthermore, the biosynthesised PLE-AgNPs showed stability for a longer time (4-5 months). It is well known that the silver metal nanoparticle SPR phenomenon makes AgNPs appear dark brown in water [47].

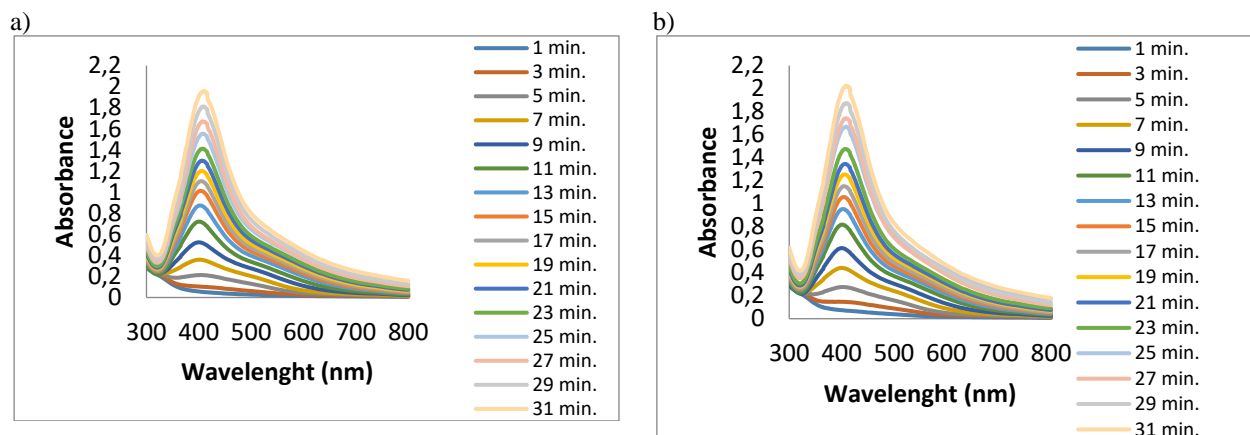


**Figure 1.** UV-vis spectra of Ag nanoparticles produced by microwave extraction with 0.25 mM AgNO<sub>3</sub> and in different amounts of Pomegranate leaves extract [a) 0.1 mL,b)0.2 mL]

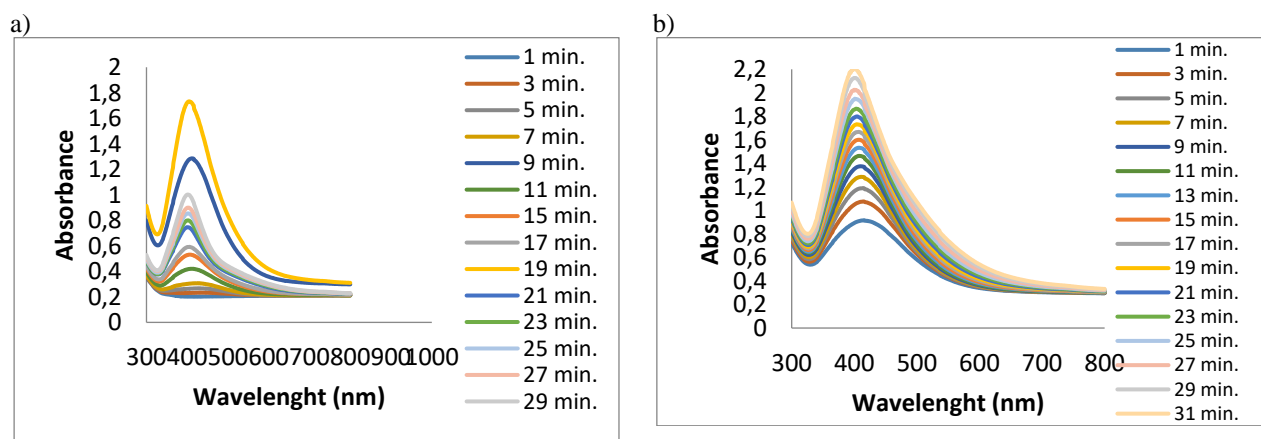


**Figure 2.** UV-vis spectra of Ag nanoparticles produced by microwave extraction with 0.5 mM AgNO<sub>3</sub> and in different amounts of Pomegranate leaves extract [a) 0.1 mL,b)0.2 mL]

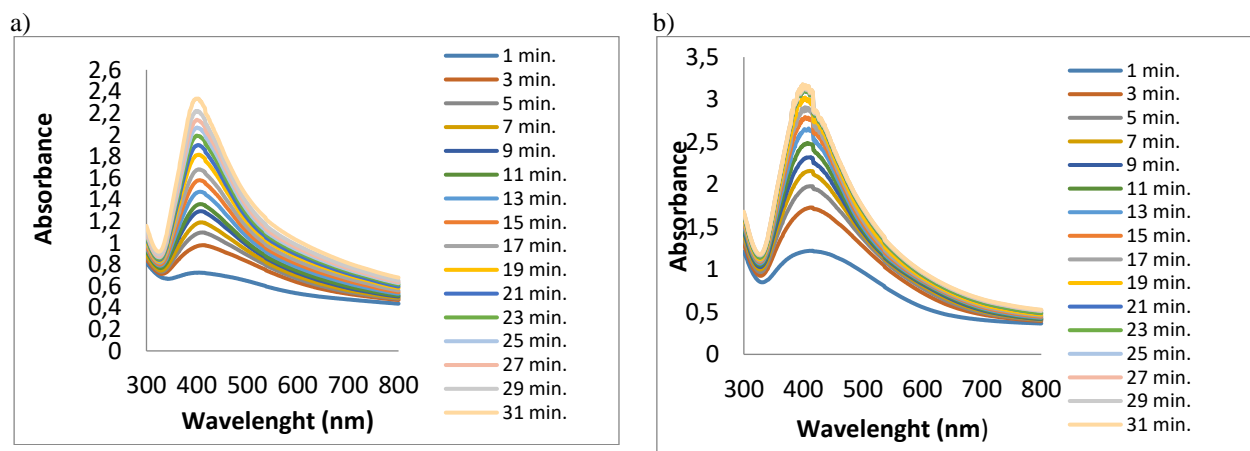


**Figure 3.** UV-vis spectra of Ag nanoparticles produced by microwave extraction with 1 mM AgNO<sub>3</sub> and in different amounts of Pomegranate leaves extract [a) 0.1 mL,b)0.2 mL]

It demonstrates that reducing  $\text{Ag}^+$  to  $\text{Ag}^0$  by adding PLE to an  $\text{AgNO}_3$  solution results in the production of silver nanoparticles. A particularly noticeable deepening of color which indicates the reaction's saturation within 31 min, is consistent with little agglomeration and good particle dispersion in the media synthesis process [48]. Size, shape of the metal nanoparticles as well as those of the surrounding medium affect the breadth and frequency of the surface plasmon absorption. The stable position of the absorbance peak at the appropriate wavelength revealed that the generated PLE-AgNPs were not aggregates, which is in line with earlier reports of [47,49,50]. The PLE contains a variety of biological organic molecules that are responsible for the reduction and stabilization of AgNPs.

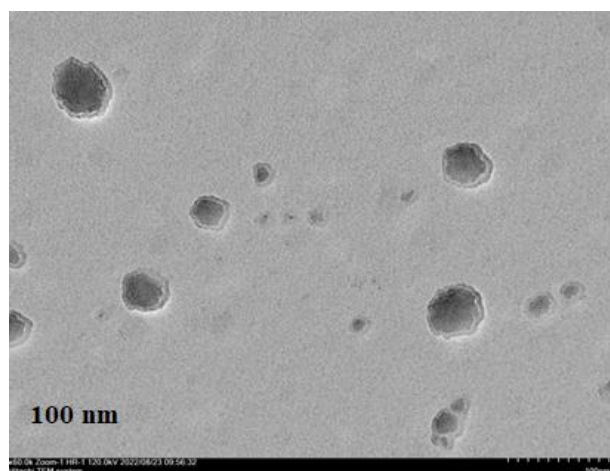


**Figure 4.** TEM images of Ag nanoparticles synthesized by microwave extraction method with 0.25 mM  $\text{AgNO}_3$  and 0.1 mL Pomegranate leaves extract (100 nm)

The sample TEM image of the Figure 4 shows a representative TEM picture of the silver nanoparticles that have been found. The monodisperse character of the PLE-AgNPs was shown by the TEM Picture(Fig. 4).

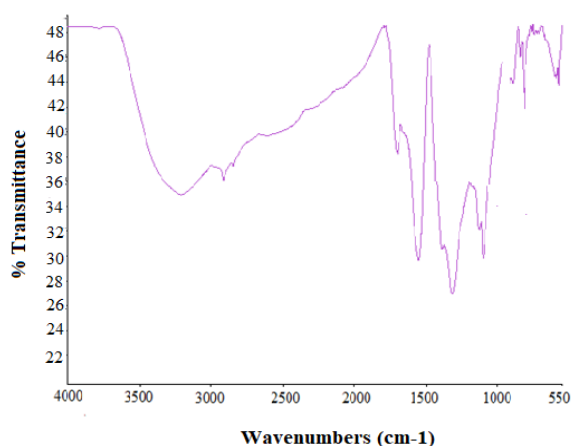


**Figure 5.** FT-IR spectrum of PLE-AgNPs.

The functional groups involved in the Pomegranate leaves extract reduction of silver into the different AgNPs were identified using FTIR analysis. Strong absorption peaks were visible in the FTIR spectra of the produced AgNPs and the aqueous Pomegranate leaves extract, respectively, at  $3210\text{ cm}^{-1}$ ,  $2935\text{ cm}^{-1}$ ,  $1552\text{ cm}^{-1}$ ,  $1299\text{ cm}^{-1}$  and  $1041\text{ cm}^{-1}$ . Different functional groups of the Pomegranate leaves extract were likely involved in the formation of the AgNPs, and they play a crucial role in the process of capping and stabilization, which allows for the AgNPs from agglomerating (Figure 5).

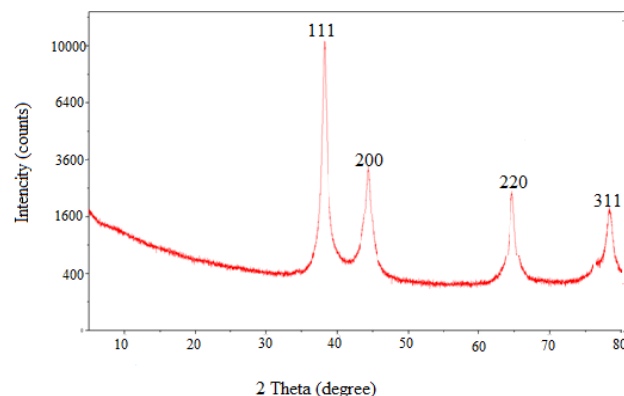


**Figure 6.** XRD analysis result of Ag nanoparticles synthesized by microwave extraction method with 0.25 mM  $\text{AgNO}_3$  and 0.1 mL Pomegranate leaves extract (diffraction peaks  $2\theta=38.1^\circ$ ,  $44.3^\circ$ ,  $64.6^\circ$ ,  $77.6^\circ$  respectively)

Figure 6 displays the XRD pattern of the produced AgNPs. The diffraction peaks at 2 theta were assigned to the corresponding diffraction signals at  $38.1^\circ$ ,  $44.3^\circ$ ,  $64.6^\circ$ ,  $77.6^\circ$  were provided to the corresponding diffraction signals at 111, 200, 220 and 311 respectively, which show the face-centered cubic crystalline AgNPs (Joint Committee on Powder Diffraction Standards; JCPDS no. 04-0783). Since these peaks are primarily oriented along the (111) plane, the reflection (111) in Figure 6 has a high intensity compared to the other reflections, which shows the presence of silver nanocrystals [51]. Silver's crystalline nature was established by X-ray diffraction (XRD). The findings agree with earlier research revealing comparable AgNP diffraction peaks [51,52].

Over a period of 4-5 months, the stability of the produced PLE-AgNPs revealed no aggregation or significant SPR change. Additionally, in order to determine the charge and stability of the produced PLE-AgNPs, examined the DLS and zeta potential. The zeta potential, which depicts the surface charge of NPs and predicts interactions between NPs, is a significant characteristic that can be used to estimate the long-term stability of NPs in suspension [51]. The zeta potential of dispersion produced PLE-AgNPs in deionized water was  $-14\pm 0.777\text{ mV}$  and the polydispersity index for gold nanoparticles is  $0,257\pm 0.004$  (Figure 7(b)). Figure 7(b) shows that PLE-AgNPs have a negative charge.

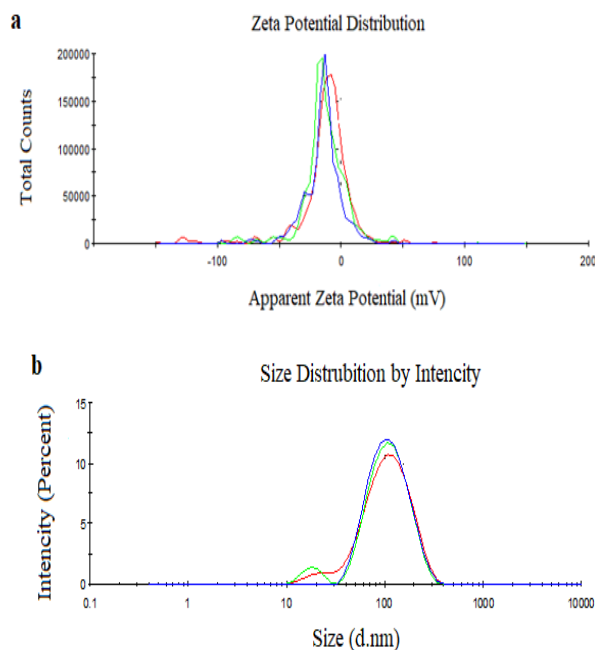


**Figure 7.** Stability of synthesized PLE-AgNPs up to 3.5-4 months and their (a) zeta potential and (b) particle size distribution determined by DLS.

The repulsion between the particles, which is confirmed by the negative charge on PLE-AgNPs, prevents coalescence and agglomeration, supporting the long-term stability of synthesized AgNPs.

Figure 7(b) shows the DLS size distribution image of PLE-AgNPs. The produced AgNPs are poly-dispersed in nature, as shown by the particle size distribution curve. AgNPs have an estimated  $86.02 \pm 0.5788$  nm average particle size distribution (Figure 7(b)).

#### 4. Conclusion

Silver nitrate ( $\text{AgNO}_3$ ) was used as a source of  $\text{Ag}^+$  ion for the synthesis of Ag nanoparticles. The color change of the solution from yellow to dark brown showed the formation of Ag nanoparticles. Optimum conditions were determined by measuring plasmon resonance (SPR) absorption spectra. Silver nanoparticles were successfully produced with 0.1 mL (0.25 mM) extract volume. After 7 minutes of microwave application, in the specific resonance band range of 90 W and around 400-460 nm, 0.1 ml pomegranate leaf extract and silver nanoparticles were successfully produced in Figure 1. Pomegranate leaves extract under typical conditions allowed for the quick, simple, economical and successful synthesis of AgNPs in under seven minutes. The pomegranate leaves extract polyphenol molecules worked as stabilizing and reducing agents, respectively. The potential use of synthesized PLE-AgNPs was increased because they were discovered to be stable and showed no symptoms of aggregation during storage for up to 4-5 months. By acting and demonstrating a

combined function as a reducing and capping agent for the PLE-AgNPs, the organic phytochemicals present in the leaf extract prevented the use of any hazardous chemicals.

#### Acknowledgements

The Central Research Laboratories of Karadeniz Technical University and Atatürk University are gratefully acknowledged by the author.

#### Author's Contributions

**Gönül Serdar:** Drafted and wrote the manuscript, performed the experiment and result analysis.

#### Ethics

There are no declared conflicts of interest for the author. Research ethics and publication requirements are fulfilled by the study.

#### References

- [1]. Shinde, BH, Shinde, PB, Inamdar, AK, Patole, SP, Inamdar, SN, Chaudhari, SB. 2023. Recent trends in biosynthesis of metal nanoparticles for the environmental applications. *Materials Today: Proceedings*; <https://doi.org/10.1016/j.matpr.2023.03.747>(accessed at 11.04.2023).
- [2]. Mahmoud,AED, Al-Qahtani, KM, Alflaj, SO, Al-Qahtani, SF, Alsamhan,FA. 2021. Green copper oxide nanoparticles for lead, nickel, and cadmium removal from contaminated water, *Scientific Reports*; 11 (1): 12547.
- [3]. Varghese, BA, Nair,RVR, Jude, S, Varma, K, Amalraj,A, Kuttappan, S. 2021. Green synthesis of gold nanoparticles using *Kaempferia parviflora* rhizome extract and their characterization and application as an antimicrobial, antioxidant and catalytic degradation agent. *Journal Taiwan Institute Chemical Engineering*;126: 166–172.
- [4]. Amina, A.2022. Green synthesis of plant mediated silver nanoparticles and their anticancer potentials: review of contemporary literature. *Spored. international journal (s.i.j)*;1(2): 2971-6373.
- [5]. Zhang, XF, Liu, ZG, Shen, W, Gurunathan, S. 2016.Silver Nanoparticles: Synthesis, Characterization, Properties, Applications, and Therapeutic Approaches. *Int J Mol Sci*; 17(9):1534.
- [6]. Burduşel, AC, Gherasim, O, Grumezescu, AM, Mogoantă, L, Ficai, A, Andronescu, E.2018. Biomedical Applications of Silver Nanoparticles: An Up-to-Date Overview. *Nanomaterials (Basel)*; 8(9):681.
- [7]. Katas, H, Moden, NZ, Lim, CS, Celesistinus, Chan, JY, Ganasan P, Abdalla, SSI. 2018. Biosynthesis and Potential Applications of Silver and Gold Nanoparticles and Their Chitosan-Based Nanocomposites in Nanomedicine. *Journal of Nanotechnology*, <https://doi.org/10.1155/2018/4290705>
- [8]. Abdel-Fattah, WI, Ali, GW. 2018.On the anti-cancer activities of silver nanoparticles. *Journal Applied technology Bioengineering*; 5(1):43-46.
- [9]. Fu, Y, Li J, Almasi, M.2023.Pomegranate Peel Extract-Mediated Green Synthesis of Silver Nanoparticles: Evaluation of Cytotoxicity, Antioxidant, and Anti-esophageal Cancer Effects. *ChemistrySelect*, [doi.org/10.1002/slct.202204841](https://doi.org/10.1002/slct.202204841)





- [10]. Singh, P, Kim, YJ, Singh, H, Mathiyalagan, R, Wang, C, Yang, DC. 2015. *Journal Nanomaterial*; 234741.
- [11]. Aldewachi, H, Chalati, T, Woodroffe, MN, Bricklebank, N, Sharrack, B, Gardiner, P. 2017. *Nanoscale*; 10:18–33.
- [12]. Kumar, D, Saini, N, Jain, N, Sareen, R, Pandit, V. 2013. *Drug Delivery*; 10: 397– 409.
- [13]. Goppert, TM, Muller, RH. 2005. *International Journal Pharmacy*; 302:172–186.
- [14]. Ogawara, K, Furumoto, K, Nagayama, S, Minato, K, Higaki, K, Kai, T, Kimura, T. 2004. *J. Controlled Release*; 100: 451–455.
- [15]. Bahrami, B, Hojjat-Farsangi, M, Mohammadi, H, Anvari, E, Ghalamfars, G, Yousefi, M, Jadidi-Niaragh, F. 2017. *Immunology Letters*; 190: 64– 83.
- [16]. Ajnai, G, Chiu, A, Kan, T, Cheng, CC, Sai THT, Chang J. 2014. *Journal Experimental Clinical Medicine*; 6:172–178.
- [17]. Kong, FY, Zhang, JW, Li, RF, Wang, ZX, Wang, WJ, Wang, W. 2017. *Molecules*; 22:1445.
- [18]. Singh, H, Du, J, Yi, TH. 2017. *Artificial Cells, Nanomedicine, and Biotechnology*; 45(7):1310–1316.
- [19]. Singh, P, Kim, YJ, Singh, H, Wang, C, Hwang, KH, FarhMel, A, Yang, DC. 2015. *International Journal Nanomedicine*; 10:2567–2577.
- [20]. Singh, P, Kim, YJ, Yang, DC. 2016. *Artificial Cells, Nanomedicine, and Biotechnology*; 44: 1949–1957.
- [21]. Singh, H, Du, J, Singh, P, Yi, TH. 2018. *Artificial Cells, Nanomedicine, and Biotechnology*; 46:1163–1170.
- [22]. Sanvicens, N, Marco, MP. 2008. *Trends Biotechnology*; 26:425–433.
- [23]. Kumar, M, Dandapat, S, Ranjan, R, Kumar, A, Sinha, MP. 2018. Plant mediated synthesis of silver nanoparticles using *Punica granatum* aqueous leaf extract. *Journal Microbiology Expirementation*; 6(4):175-178.
- [24]. Jha, AK, Prasad, K. A green low-cost biosynthesis of Sb2O3 nanoparticles. 2009. *Biochemical Engineering Journal*; 43(3):303–306.
- [25]. Kathiresan, K, Manivannan, S, Nabeel, AM, et al. 2009. Studies on silver nanoparticles synthesized by a marine fungus *Penicillium fellutanum* isolated from coastal mangrove sediment. *Bioenterfaces*; 71(1):133–137.
- [26]. Ahmad, A, Senapati, S, Khan, MI, Kumar, R, et al. 2003. Extracellular biosynthesis of monodisperse gold nanoparticles by a novel extreme ophillic actinomycete. *Thermonospora sp. Langmuir*; 19(8):3550–3553.
- [27]. Dujardin, E, Peet, C, Stubbs, G, et al. 2003. Organization of metallic nanoparticles using tobacco mosaic virus templates. *NanoLetturer*, 3(3):413–417.
- [28]. Vijayaram, S, Razafndralambo, H, Sun, YZ, Vasantharaj S, Ghafarifarsani H, Hoseinifar HS, Raeszadeh M. 2023. Applications of Green Synthesized Metal Nanoparticles. *Biological Trace Element Research*; 13 : 1–27.
- [29]. Mustapha, T, Misni, N, Ithnin, NR, Daskum, AM, Unyah, NZ. 2022. A review on plants and microorganisms mediated synthesis of silver nanoparticles, role of plants metabolites and applications. *International Journal of Enviromental Research Public Health*; 19(2):674.
- [30]. Liddle, JA, Gallatin, GM. 2016. *Nanomanufacturing: A Perspective. ACS Nano*; 10(3): 2995-3014.
- [31]. Heinz, H, Pramanik, C, Heinz, O, Ding, Y, Mishra, RK, Marchon, D, et al. 2017. Nanoparticle decoration with surfactants: Molecular interactions, assembly, and applications. *Surface Science Reports*, 72(1): 1-58.
- [32]. Mohammed Fayaz, A, Balaji, K, Girilal, M, Yadav, R, Kalaichelvan, PT, et al. 2016. Biogenic synthesis of silver nanoparticles and their synergistic effect with antibiotics: a study against gram-positive and gram-negative bacteria. *Nanomedicine: Nanotechnology, Biology and Medicine*; 6(1): 103-109.
- [33]. Bañares, C, Chabni, A, Donlebún, BP, Reglero, G, Torres, CF. 2023. Chemical characterization of pomegranate and alfalfa seed oils obtained by a two-step sequential extraction procedure of expeller and supercritical CO2 technologies. *Journal of Food Composition and Analysis*; 115: 105040.
- [34]. El-Shamy S, Farag MA. 2021. Novel trends in extraction and optimization methods of bioactives recovery from pomegranate fruit biowastes: Valorization purposes for industrial applications. *Food chemistry*; 365,:130465.
- [35]. Paul, A, Radhakrishnan, M. 2020. Pomegranate seed oil in food industry: Extraction, 802 characterization, and applications. *Trends in Food Science & Technology*; 105: 273-283.
- [36]. Shitu, G, Katibi, KK, Taura, LS, Muhammad, A, Chiromawa IM, Adamu, SB, Iya, SGD. 2023. X-ray diffraction (XRD) profile analysis and optical properties of Klockmannite copper selenide nanoparticles synthesized via microwave assisted technique. *Ceramics International*; 49(8):12309-12326.
- [37]. Gasparini, A, Ferrentino, G, Angeli, L, Morozova, K, Zatelli, D, Scampicchio, M. 2023. Ultrasound assisted extraction of oils from apple seeds: A comparative study with supercritical fluid and conventional solvent extraction. *Innovative Food Science and Emerging Technologies*; 86:103370.
- [38]. Khan, Y, Sadia, H, Shah, SZA, Khan, MN, Shah, AA, Ullah, N, Ullah, MF, Bibi, H, Bafakeeh, OT, Khedher, NB, Eldin, SM, Fadhli, BM, Khan, MJ. 2022. Classification, Synthetic, and Characterization Approaches to Nanoparticles, and Their Applications in Various Fields of Nanotechnology. *Catalysts*; 12(11):1386.
- [39]. Serdar, G, Albay, C, Sökmen, M. 2019. Biosynthesis and Characterization of Silver Nanoparticles from the Lemon Leaves Extract. *Cumhuriyet Science Journal*; 40(1):170-172
- [40]. Serdar, G. 2021. Biosynthesis of Silver Nanoparticles Using Extract of Fig (*Ficus carica*) Leaf by Microwave Extraction. *Bulletin of Biotechnology*; 2 (2):44-5.
- [41]. Sökmen, M, Alomar, S, Albay, C, Serdar, G. 2017. Microwave assisted production of silver nanoparticles using green tea extracts. *Journal of Alloys and Compounds*; 725:190-198.
- [42]. Rozali, NL, Azizan, KA, Singh, R, Jaafar, SNS, Othman, A, Weckwerth, W, Ramli, US. 2023. Fourier transform infrared (FTIR) spectroscopy approach combined with discriminant analysis and prediction model for crude palm oil authentication of diferent geographical and temporal origins. *Food Control*; 146:109509.
- [43]. Naganthran, A, Verasoundarapandian, G, Khalid, FE, Masarudin, MJ, Zulkharnain, A, Nawawi, NM, Ahmad, SA. 2022. Synthesis, characterization and biomedical application of silver nanoparticles. *Materials*; 15(2):427.
- [44]. Habeeb Rahuman, HB, Dhandapani, R, Narayanan, S, Palanivel, V, Paramasivam, R, Subbarayalu, R, Muthupandian, S. 2022. Medicinal plants mediated the green synthesis of silver nanoparticles and their biomedical applications. *IET Nanobiotechnol*; 16(4):115–144.



- [45]. Seerengaraj, V, Razafndralambo, H, Sun, YZ, Vasantharaj S, Ghafarifarsani, H, Hoseinifar, SH, Raeeszadeh, M. 2023. Applications of Green Synthesized Metal Nanoparticles. *Biological Trace Element Research*; <https://doi.org/10.1007/s12011-023-03645-9>.
- [46]. Panda, MK, Dhal, NK, Kumar, M, Mishra PM, Behara RK. 2021. Green synthesis of silver nanoparticles and its potential effect on phytopathogens, *Material Today Processin*; 35 (2):233–238.
- [47]. Bhuyar P, Rahim, MH, Sundararaju, S, Ramaraj, R, Maniam, GP, Govindan, N. 2020. Synthesis of silver nanoparticles using marine macroalgae *Padina* sp. and its antibacterial activity towards pathogenic bacteria. *Beni-Suef University Journal of Basic and Applied Sciences*; 9 (3):1-15.
- [48]. Nabikhan A, Kandasamy, K, Raj, A, Alikunhi, NM. 2010. Synthesis of antimicrobial silver nanoparticles by callus and leaf extracts from saltmarsh plant, *Sesuvium portulacastrum* L. *Colloids Surf. B Biointerfaces*; 79 (2):488–493.
- [49]. Resmi, CR, Sreejamol, P, Pillai, P. 2014. Green synthesis of silver nanoparticles using *Azadirachta indica* leaves extract and evaluation of antibacterial activities. *International of Journal Advances Biol Research*; 4: 300-303.
- [50]. Seekonda, S, Rani, R. 2022. Eco-friendly synthesis, characterization, catalytic, antibacterial, antidiabetic, and antioxidant activities of *Embelia robusta* seeds extract stabilized AgNPs. *Journal of Science: Advanced Materials and Devices*; 7(4): 100480.
- [51]. Saratale, RG, Shin, HS, Kumar, G, Benelli, G, Kim, DS, Saratale, GD. 2018. Exploiting antidiabetic activity of silver nanoparticles synthesized using *Punica granatum* leaves and anticancer potential against human liver cancer cells (HepG2). *Artificial cells, nanomedicine, and biotechnology*; 46(1):211–222.
- [52]. Sarkar, S, Kotteeswaran, V. 2018. Green synthesis of silver nanoparticles from aqueous leaf extract of Pomegranate (*Punica granatum*) and their anticancer activity on human cervical cancer cells. *Advances in Natural Sciences: Nanoscience and Nanotechnology*; 9:025014

## ***Helianthus Annuus L. Comparison of The Properties of Fibers Obtained From The Plant By Methods of Decortication and Retting***

Nilsu Ataman<sup>1\*</sup> , Levent Şık<sup>1</sup> 

<sup>1</sup>Manisa Celal Bayar University, Faculty of Engineering and Natural Sciences, Biology Department, Manisa, Türkiye

\*[nilsu.atamann@gmail.com](mailto:nilsu.atamann@gmail.com)

\* Orcid No: 0000-0002-1279-0260

Received: 26 September 2023

Accepted: 24 December 2023

DOI: 10.18466/cbayarfbe.1366612

### **Abstract**

A large amount of sunflower production is carried out in our country. The 2,500,000 tons of sunflower stalks that appeared after production pose a problem for our farmer. In order to clean up this environmental problem from the field, sunflower stalks are destroyed by burning to warm up in winter, broken down and mixed into the soil, or burned after harvesting. It is thought that by obtaining qualified, ecological and naturally decomposing sunflower fiber from the stem of the sunflower plant, which is an agricultural waste, it can increase the added value of agricultural products and contribute to the protection of the environment. In this study, the anatomical characteristics of the stem of the sunflower plant were determined, and natural lignocellulosic fibers were obtained from the sunflower stem by retting and decortication methods (fresh stem, dried stem). Various physical, chemical and mechanical properties of these fibers have been measured. For this purpose, FTIR (Fourier Transform Infrared Spectroscopy) analysis, XRD (X-Ray Diffractometer) analysis and SEM (Scanning Electron Microscope) analysis were applied to the fibers obtained by different methods. Thermal analyses were performed by TG-DTA (Thermogravimetric) analysis. In addition, fiber strength, fiber fineness, fiber length and color measurements were made. The chemical content of the obtained fibers (pectin, lignin, cellulose, hemicellulose) was determined. The properties of the fibers were compared using the obtained data. As a result of the study, it has been seen that the characteristic properties of the sunflower fibers obtained by the retting method are better. It has been determined that the elemental, thermal and crystal structures of the fibers obtained by different methods are similar. It was concluded that sunflower fiber will not be spun as a yarn, but can be used as a natural polymeric composite reinforcement material.

**Keywords:** *Helianthus annuus L.*, Sunflower stem, Bast fibers, Retting, Decortication, Fiber qualities

### **1. Introduction**

A large amount of waste is generated in the post-harvest production area of most cultivated plants. The wastes of plants such as flax, hemp, ramie and jute contained in cellulosic bast fibers are an important source of raw materials for the textile, composite and paper sector. By evaluating these wastes, it is thought that by obtaining qualified, ecological and naturally decomposing sunflower fiber from the stem of the sunflower plant, which is an agricultural waste, it can increase the added value of agricultural products and contribute to the protection of the environment. With the increase in population in our world, natural cellulosic raw material resources are gradually decreasing due to the fact that agricultural areas are used more for the food sector [1].

The sunflower plant (*H. annuus L.*), which belongs to the Asteraceae family, is an annual plant belonging to the Helianthus genus in the Asterales order [2]. 136 genera and 1345 species from the Asteraceae family grow in our country. The largest number of endemic species are in the Asteraceae family. It is one of the richest families in terms of species and genera [3]. The sunflower plant, which belongs to the Asteraceae family, is an annual plant belonging to the Asterales order, *Helianthus* genus and *annuus* species. The genus *Helianthus* has 51 species and 19 subspecies in the world. 14 of these species are annual and 37 are perennial [2]. There are two important species of the Helianthus genus (*Helianthus tuberosus L.*, *Helianthus annuus L.*) in our country. In our country, it is known as gündöndü, günebakan and günciçeği [4].

Sunflower grows in subtropical and temperate climate conditions in July-August. It is a plant species that loves light and sun. It grows in moist, organic matter-rich, well-drained, neutral pH (6.5-7.5) soils with high water holding capacity and mostly in arid and semi-arid climates [2,5]. Sunflower, which has single and large-headed capitula, contains a large number of achene. Sunflower does not consist of a single flower, but consists of 1,000 to 2,000 individual flowers connected to the table base. It has a strong tap root structure that spreads deep and wide. It can use water from 3 meters deep with its root structure [2,6]. Although the sunflower plant has many uses, it is an important raw material source especially for animal feed, fertilizer, soap, chemistry, cosmetics, paint, biodiesel, plastic and food industries. Large amounts of oil sunflower are produced in our country [6]. Sunflower stalks left in the field after the sunflower plants produced in our country are collected cause problems. The stems are collected from the field and destroyed by burning to warm up in the winter months, they are mixed into the soil by breaking up or they are burned after harvesting [7].

In the current study, it is aimed to determine the morphological properties of the sunflower stem and to obtain natural lignocellulosic fiber from the sunflower stem. In addition, examining the chemical, physical and mechanical properties of the obtained fibers and the details obtained has become another target. Two different methods were used to obtain sunflower fiber: retting and decortication of fresh and dried stems. The usability of previously broken sunflower fiber as a polymeric composite reinforcement material, its rights were obtained, and the usability of these fibers in textiles was emphasized. In addition, we will attach great importance to increasing the recognition of fibers and disseminating plant fibers obtained from management waste for the future of many industries, especially textile. It is believed that the research outputs will contribute to the literature on reducing environmental pollution produced by plant waste and producing soluble fiber that meets the need for natural cellulose from the stems of the sunflower plant, which are agricultural residues.

## 2. Materials and Methods

To obtain fiber from the stem of the sunflower plant, 75 kg of sunflower plants were collected from the Altınova district of Balıkesir province in August 2022. Since the sunflower is harvested in August, this month was chosen as the harvest time. 75 kg of plants were collected in 1 hour. Samples to be used in anatomical studies were stored in 70% ethanol during fieldwork.

### 2.1. Anatomical Properties

The stem of the sunflower plant examined in the study was kept in glycerin for 15 days to soften. Transverse and longitudinal sections were taken as thin layers from the

stored sunflower stem with the help of a razor blade. The obtained sections were examined and photographed using a LEICA DM 750 camera microscope.

### 2.2. Obtaining Fibers

In order for the fibers to be used for different purposes after the harvest of the sunflower plant, first of all, the fibers must be separated from the stems. The process of separating the fibers from the stems was done by retting, decortication (fresh stem, dried stem) methods. The purpose of retting and decortication (dried stem, fresh stem) methods is to easily separate the woody parts of the stems and to expose the fibers [8].

### 2.3. Combing of Fibers

The resulting sunflower stems were combed to separate the woody parts. Three different combs were used in the study. First, the stems were passed through an 8 cm wide, 2-row, 36-tooth comb. Thus, the fiber was separated from the woody regions (lignin). Afterwards, the fibers were cleaned by combing again with two different combs with finer and denser teeth (79 teeth and 124 teeth), thus achieving a homogeneous and parallel appearance.

### 2.4. Characterization Analyzes

Various measurements were made to determine the physical, chemical and mechanical properties of the fiber obtained by different methods. The breaking strength, breaking elongation, color properties, fiber fineness and fiber length of the obtained fibers were examined. Fourier transform infrared spectroscopy (FTIR), X-ray diffraction (XRD) and Scanning Electron Microscope (SEM) analyzes were applied for structural characterization. Thermal analyzes were carried out with TG-DTA (Thermogravimetric) analysis. The breaking strength, elongation at break, color properties, fiber fineness and fiber length of the fibers kept for at least 24 hours in the laboratory under standard atmospheric conditions ( $20\text{ }^{\circ}\text{C} \pm 2\text{ }^{\circ}\text{C}$  temperature and  $65\% \pm 4\%$  relative humidity) were examined.

#### 2.4.1. Chemical Content of Fiber

The determination of the chemical structure of sunflower fibers was based on the "Chinese Textile Industry Standard" in the study of Zhang et al. (2013) [9]. Sunflower fibers were dried in an oven at  $100\text{ }^{\circ}\text{C}$  for 4 hours to reach constant weight (W0), then washed with 70% ethanol solution and dried. To determine the pectin content, it was mixed with 0.5% EDTA (ethylene diamine tetra acetic acid) solution in a magnetic heater for 30 minutes. After being rinsed with pure water and filtered, it was brought to a constant weight in the oven at  $100\text{ }^{\circ}\text{C}$  for 4 hours and measured (W1). Pectin content (%) was calculated using the formula below.



$$\% \text{ Pektin} = \frac{W_0 - W_1}{W_0} * 100 \quad (2.1)$$

To determine the hemicellulose content of the fibers, in the next step, the pectin-free samples were washed with acetone, rinsed with pure water, dried and mixed with 0.5 M HCl at boiling point with a magnetic heater for 60 minutes. After being rinsed with pure water and filtered, it was dried in an oven at 100 °C for 4 hours and its weight was measured (W2). Hemicellulose content (%) was calculated using the formula below.

$$\% \text{ Hemişelüloz} = \frac{W_1 - W_2}{W_0} * 100 \quad (2.2)$$

The fibers, which were kept in 72% sulfuric acid solution for 24 hours at room temperature to determine their cellulose content, were then vacuum filtered and rinsed using a sintered glass filter funnel (por 3). The fibers were dried in the oven and their weight was measured (W3). The amount of Klason lignin was also calculated by sulfuric acid treatment. Calculations (% Cellulose, % Lignin) were made using the formulas below.

$$\% \text{ Selüloz} = \frac{W_2 - W_3}{W_0} * 100 \quad (2.3)$$

$$\% \text{ Lignin} = \frac{W_3}{W_0} * 100 \quad (2.4)$$

#### 2.4.2. Fiber Length

Sunflower fibers were combed and cleaned, and after making them homogeneous and parallel, the length of the resulting fibers was measured with the help of a ruler.

#### 2.4.3. Fiber Fineness

The Metric System (Nm) was used to determine the fiber fineness. It was calculated by finding the length value in meters of a textile material weighing 1 gram. Since the thickness of the upper and lower parts of the plant's stem are different, the weight of 5 fibers, 8 cm long, was measured from both the lower and upper parts. This measurement was made twice and the weight average was taken.

#### 2.4.4. Color Measurement

“Hunter Lab UltraScan PRO” brand color measurement device was used to determine the color changes in the fiber. L\*, a\* and b\* color values of sunflower fibers obtained by three different methods were obtained. The L\* value is in the range of 0-100 and 0 indicates black and 100 indicates white. In addition, a\* and b\* color values are used for the determination of darkness [10].

#### 2.4.5. Fiber Strength

Strength measurement was carried out with testXpert II software on the “Zwick Roell Z010” device. Jaw gap was 100 mm/min, head speed was 100 mm/min and no pre-tension was applied. By making 10 measurements from each production method, the breaking strength (cN/dtex) of sunflower fiber and the standard deviation and coefficients of variation (%CV) of these values were obtained.

#### 2.4.6. XRD (X-Ray Diffractometer) Analysis

XRD analysis was performed to determine the crystal structure of fibers obtained from sunflower stalks by different methods. The fibers are ground and ground into powder. Approximately 2 g of sample was performed on a Panalytical/ Epyrean model (Ni filtered CuK $\alpha$  beam source) X-ray diffraction device that can operate at 40 kV and 40 mA. Scanning was performed between angles of 10°-80° at a speed of 2°/sec.

#### 2.4.7. FTIR (Fourier Transform Infrared Spectroscopy) Analysis

FTIR analysis was performed to determine the molecular structure of sunflower fibers. It was carried out with a Perkin Elmer Spectrum1400 brand spectrometer in the scanning range of 4000-650 cm<sup>-1</sup> and at room temperature. The test was performed at 4 cm<sup>-1</sup> resolution.

#### 2.4.8. TG-DTA (Thermogravimetric) Analysis

TGA analysis was performed to determine thermal and gravimetric changes of sunflower fibers. It was carried out on EXSTAR TG/DTA7300 brand thermo gravimetric analyzer in nitrogen environment between 25-600°C temperatures at a heating rate of 10°C/min. The analysis result was calculated by taking as reference the curve of change of mass against time and temperature.

#### 2.4.9. SEM (Scanning Electron Microscope) Analysis

In the SEM analysis, the fibers obtained by different methods and the transverse and longitudinal sections of the sunflower plant stem were placed appropriately on double-sided adhesive carbon tapes.

### 3. Results and Discussion

#### 3.1. Anatomical Properties

The fibers in dicotyledonous sunflower plant stems, which have a secondary structure, are divided into three groups: primary and secondary bast fibers and xylem fibers [11]. The development of these three structures is independent of each other. Primary fibers are longer and of higher quality than secondary fibers and xylem fibers [12]. When viewed in cross section, it consists of protective tissue, cortex and central cylinder parts. The cortex is divided into two: primary cortex and secondary cortex. The primary cortex consists of primary phloem. There are sclerenchyma fibers in this part and these fibers

are also called primary bast fibers. Secondary cortex consists of secondary phloem. There are phloem sclerenchyma cells in the secondary phloem. The fibers formed in the phloem sclerenchyma are called secondary bast fibers. These fibers provide support to the phloem [13].

It consists of the central cylinder, secondary xylem and soft core. The soft core consists of spongy parenchymatic cells. There are sclerenchyma cells in the secondary xylem and therefore they are called xylem fibers [13].

Anatomical findings of the sunflower fibers examined in this study are given in Figures 1. and Figure 2. Transverse and longitudinal microscopic images of the sunflower stem.

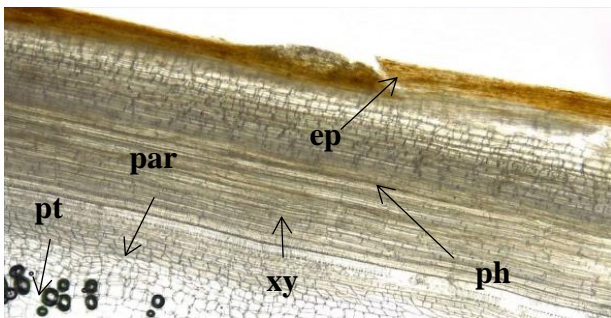


**Figure 1.** *Helianthus annuus* L. 10x magnified longitudinal sections of the stem of the plant (ep: epidermis, xy: xylem, ph: phloem, par: parenchyma, pt: pith)

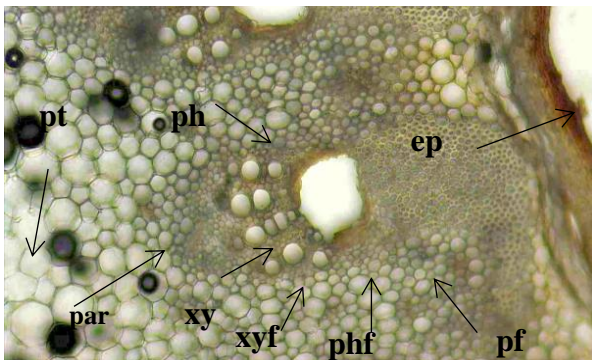


**Figure 2.** *Helianthus annuus* L. 10x magnified cross-section of the stem of the plant (ep: epidermis, xy: xylem, xyf: xylem fibers, ph: phloem, phf: phloem fibers, pf: primary fibers, par: parenchyma, pt: pith)

### 3.2. Obtaining Fibers

Since the fibers are very fragile, few and short fibers were obtained during the scans performed in the decortication (dried stem) method. In the retting method, less brittle and longer fibers were obtained compared to the decortication method (fresh stem, dried stem).

In this study, since the retting method produces less brittle and longer fibers than other methods, fiber was obtained by the retting method twice to calculate the fiber yield. As a result, 92 grams of fiber was obtained from 832 grams of sunflower stalks, yielding 11.6% efficiency.

### 3.3. Chemical Content of Fiber

In experimental studies conducted to determine the chemical content of sunflower fiber;

In the fibers obtained by the retting method, the cellulose rate was found to be 47.7%, the hemicellulose rate was 13.1%, the lignin rate was 31.1%, and the pectin rate was 12%. In the fibers obtained by the decortication (fresh stem) method, the cellulose rate was found to be 48.8%, the hemicellulose rate was 16.4%, the lignin rate was 21.7%, and the pectin rate was 13.7%. With the method obtained by decortication (dried stem), the cellulose rate in the fibers was found to be 55.5%, the hemicellulose rate was 19%, the lignin rate was 19.8%, and the pectin rate was 10.5%.

Fibers obtained from sun-dried stems were found to have a higher cellulose content than fibers obtained by other methods. Fibers obtained by retting method were found to have higher lignin content than fibers obtained by other methods. In addition, the cellulose ratio was low because the lignin was not removed sufficiently in the retting method. Chemical structure; Harvest time may vary depending on the climatic conditions in which the plant is grown, soil structure and the methods in which the fibers are obtained.

### 3.4. Fiber Length

The longest fibers were obtained by the retting method (16-37 cm). During scanning, it was determined that the shortest fibers were obtained by the decortication (dried stem) method (6-15 cm) since the fibers were fragile.

### 3.5. Fiber Fineness

According to the findings, the thickest fibers were obtained by the retting method and the thinnest fibers were obtained by the decortication (dried stem) method (Table 1.). It has been determined that it consists of thinner fibers than the upper part of the stem and thicker fibers than the lower part of the stem.

**Table 1.** Fiber fineness results according to the fiber obtaining method

Method	Upper part of the stem (Nm)	Lower part of the stem (Nm)
Retting	~ 4,2	~ 3,7
Decortication (fresh stem)	~ 10,5	~ 4.5
Decortication (dried stem)	~ 14,8	~ 5,9

### 3.6. Color Measurement

In this study, the  $a^*$  value in the color system is between 4 and 7; It was determined that the  $b^*$  value varied between 19 and 30 and all  $a^*$  and  $b^*$  values obtained as a result of the measurement were positive (Table 2). Accordingly, the fibers obtained by decortication (dried stem) method are closer to red tones than the fibers obtained by retting and decortication (fresh stem); It is concluded that the fibers obtained by decortication (fresh stem) are closer to yellow tones than the fibers obtained by retting and decortication (dried stem). It is seen that the illuminance value ( $L^*$ ), which varies between 0 and 100, varies between 56 and 67 according to this study. According to the  $L^*$  values determined as a result of the measurements of the fibers obtained by all three methods, the fibers obtained by the retting method were lighter in color than the fibers obtained by the decortication (fresh stem) and decortication (dried stem) methods. It was observed that it was darker in color than the fibers obtained by decortication (fresh stem) methods.

**Table 2.** Color measurement results of sunflower fibers according to the method of obtaining the fiber

Method	$L^*$	$a^*$	$b^*$
Retting	67,11	4,15	19,18
Decortication (fresh stem)	64,55	7,07	30,24
Decortication (dried stem)	56,88	7,95	23,08

### 3.7. Strength Property

It is observed that the variation of the values obtained for the breaking strength is high. The reason for its high variation is that the thickness of the upper and lower parts of the sunflower plant's stem is different and the fibers are not uniform and homogeneous along their length. Fibers obtained by retting method have higher breaking strength values. Fibers obtained by decortication (dried stem) method were found to have the lowest breaking strength.

**Table 3.** Strength results of sunflower fibers

Method	Breaking strength (cN/tex)		
	Average	Standard deviation	% CV
Retting	6048	1715,68	28,37
Decortication (fresh stem)	2699,90	814,81	30,18
Decortication (dried stem)	811,70	339,98	41,88

### 3.8. XRD (X-ray diffractometer) Analysis

XRD analysis curves applied to examine and compare the effect of the internal structure of fibers obtained from sunflower stems by 3 different methods are shown in Figure 3. The intensities of the peaks showing (110) and (002) crystal structures varied between methods. When the peak intensities of sunflower fibers were examined, it was determined that the highest intensity was in the fibers obtained by the retting method, and the lowest intensity was in the fibers obtained by the decortication (dried stem) method. XRD measurements showed that sunflower fibers have similar crystal structures between the production methods.

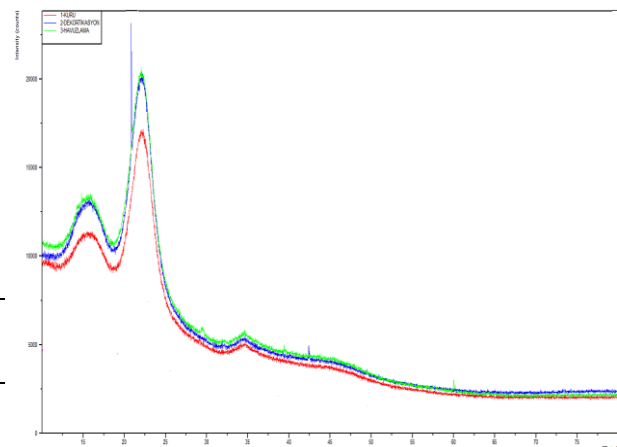


**Figure 3.** XRD curves according to the methods of obtaining sunflower fibers (Red- Retting, Blue- Decortication (fresh stem), Green- Decortication (dried stem))

### 3.9. FTIR (Fourier Transform Infrared Spectroscopy) Analysis

FTIR spectra of sunflower fibers obtained by 3 different methods are seen in Figure 4. The peaks in the FTIR spectrum show the functional groups of the basic components of cellulosic fibers such as cellulose, hemicellulose, lignin and pectin [14].

The peaks formed in the absorption bands between  $3287.3\text{-}3319.5\text{ cm}^{-1}$  in the FTIR spectra show O-H voltage Decibels and alcohol groups. The presence of C-H group tension or  $\text{CH}_2$  and  $\text{CH}_3$  vibrations [15]. in cellulose and hemicellulose components was observed to occur in the absorption band of  $2898.8; 2876.6\text{-}2953.1; 2852.5\text{-}2912.9$ . There has been a change in the fibers obtained by decortication (dried stem) method in these bonds. This is because weight loss occurs due to the removal of water. The absorption between  $1729$  and  $1733.1\text{ cm}^{-1}$  belongs to the ester group in hemicellulose or the carbonyl (C=O) group of the bond vibration of carboxyl acid (R-COOH) in lignin [16]. This bond was broken down by the effect of microorganisms during the retting method. The peaks seen in the other absorption band showed that they had similar elemental properties according to different production methods.

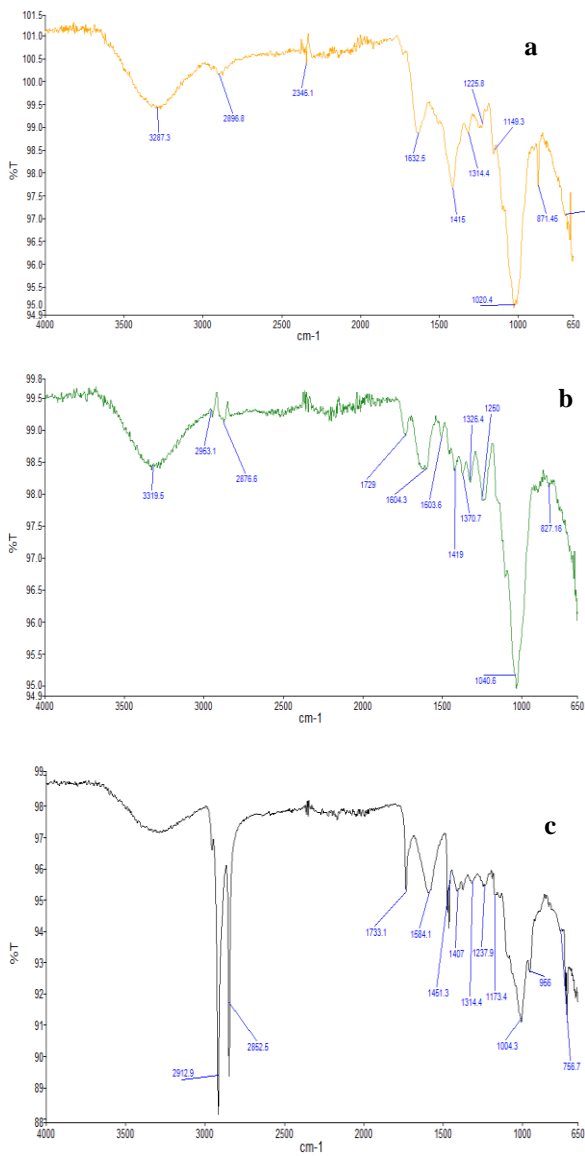


**Figure 4.** FTIR spectra according to the methods of obtaining sunflower fibers (a-Retting b- Decortication (fresh stem) c-Decortication (dried stem))

### 3.10. TG-DTA Analysis

The graphs obtained as a result of TG-DTG analyzes performed to determine the temperature resistance of fibers are given in Figure 5. The weight loss of fibers obtained by 3 different methods occurs as a result of multi-step reactions. Differences in the number of deteriorations are due to dehydration, decomposition events and material removal in the fibers. It is understood that this weight loss continues continuously with increasing heating rate and this process continues until the final temperature of 600°C.

When the basic decomposition temperature was compared, it was seen that it started and ended at approximately the same temperatures for all fibers.

The greatest weight loss is very slow up to 200°C, the slope between 250°C and 350°C indicates very rapid weight loss. However, as a result of the analysis, it is seen that the weight losses in the fibers are approximately the same. As a result, it was found that the thermal behavior and stability of fibers obtained by 3 different methods were similar.

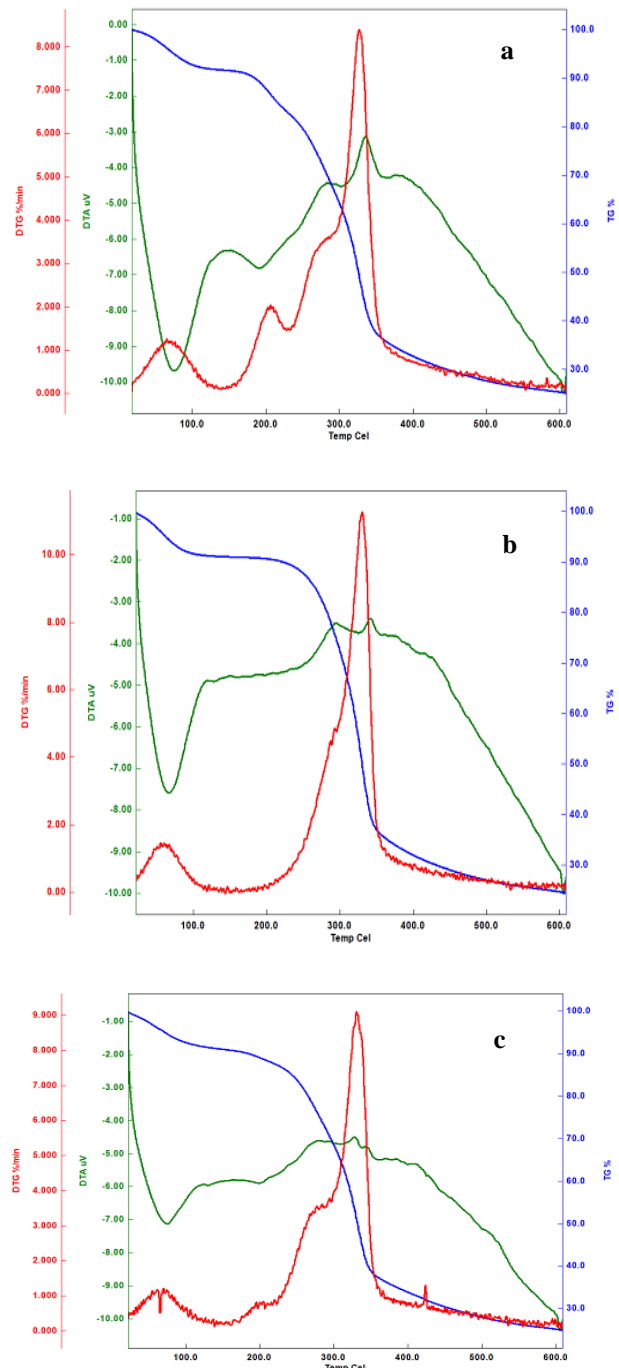


**Figure 5.** TG graphs according to the methods of obtaining sunflower fibers (a- Retting b- Decortication (fresh stem) c -Decortication (dried stem))



### 3.11. SEM (Scanning Electron Microscope) Analysis

SEM microscopic images of transverse and longitudinal sections of the fibers are shown in Figure 6-7-8-9. Accordingly, the fiber thickness of sunflower fibers varies along the fiber. It contains many fibrils in the fiber and it is seen that the fibers are arranged in a parallel way and there is no space between them. The fiber is in the shape of a polygonal cavity (lumen) in the cell center. It was determined that there are many spherical pits on the surface of the fibers. Looking at the sunflower fiber, it is seen that the rough fiber surface and its surface are covered with impurities. Since the surface of the sunflower fibers obtained by retting method is covered with more substances compared to the fibers obtained by decortication (dried stem) and decortication (fresh stem) methods, the visibility of the pores has decreased.

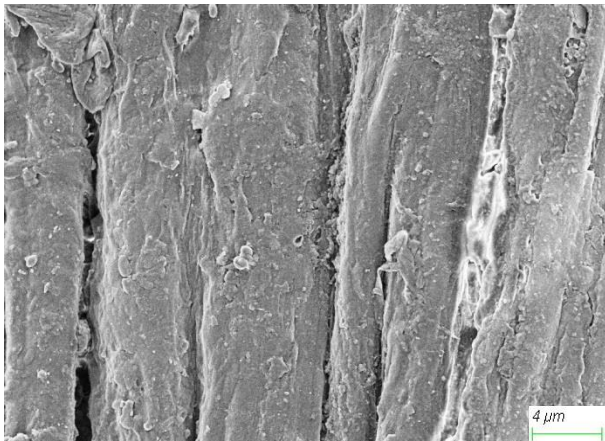


**Figure 6.** Longitudinal section SEM images of the fiber obtained by retting method from the stem of *Helianthus annuus* L. plant

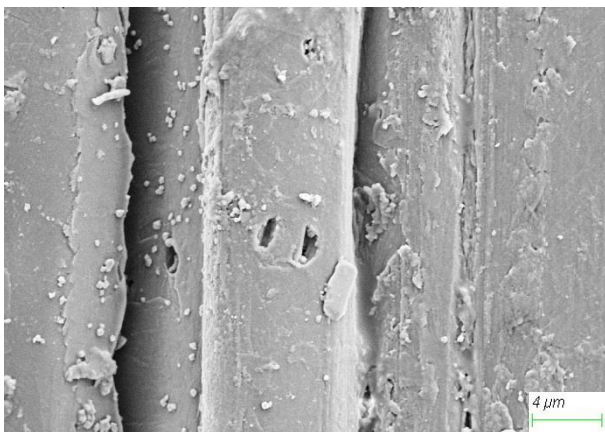


**Figure 7.** Longitudinal section SEM images of the fiber obtained by decortication (fresh stem) method from the stem of the *Helianthus annuus* L. plant

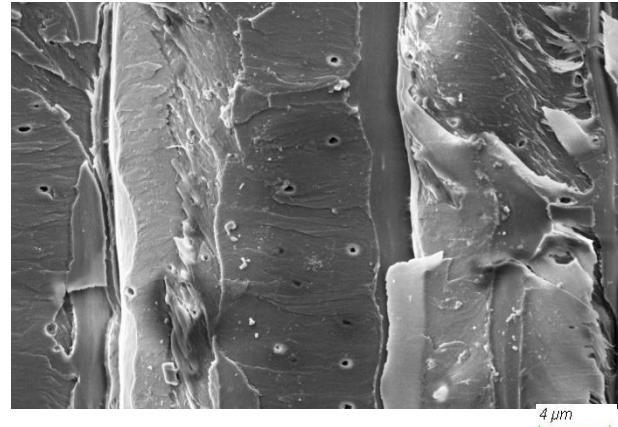


**Figure 8.** Longitudinal section SEM images of the fiber obtained by the decortication (dried stem) method from the stem of *Helianthus annuus* L.

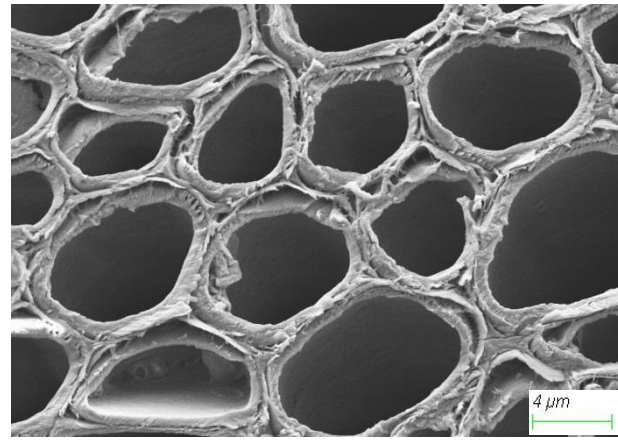


**Figure 9.** Cross-sectional SEM images of the fiber obtained from the stem of the *Helianthus annuus* L. plant

### 4. Conclusion

As a result of the study, when the properties of natural lignocellulosic sunflower fiber were compared, it was seen that the characteristic properties of the fibers obtained by the retting method were better. It has been determined that the elemental, thermal and crystalline structures of the fibers obtained by different methods are similar.

The purpose of cultivation of plants such as flax, hemp and jute is important. Farmers cultivate for their intended use. Sunflower is not used as a fiber plant, it is generally cultivated for oil production. The primary aim of farmers is to ensure oil yield. If fiber production is targeted, the added value of the fiber must be revealed and its economic study must be carried out. Additionally, farmers should be informed about the main and secondary uses of the fibre.

Planting and harvesting times should be planned according to the intended use. At harvest time, the fibers obtained from the stems of the sunflower plant are thick and hard due to the high amount of lignin. It is thought that when sunflower stalks are collected earlier than the harvest time, thinner, spinnable fibers can be obtained and these fibers can be used in the textile industry. Since the sunflower fiber obtained at harvest time will not be spun into yarn, it can be used as a natural polymeric composite reinforcement material. Nowadays, the use of natural fibers of plant origin in composite materials is increasing. The use and superior properties of composite materials in many areas come to the fore. The qualified, ecological and biodegradable properties of sunflower fiber will contribute to increasing the added value of agricultural products and protecting the environment.

### Acknowledgement

Manisa Celal Bayar University Scientific Research Projects supported this study with the project code 2022-103.

### Author's Contributions

**Nilsu Ataman:** Performed the experiments and results analysis.

**Levent Şık:** Prepared experimental method, supervised the experiment's progress, result in interpretation and helped in manuscript preparation.

### Ethics

There are no ethical issues after the publication of this manuscript.

### References

- [1]. Yılmaz, N. D. Effects of enzymatic treatments on the mechanical properties of corn husk fibers. *Journal of the Textile Institute*, 2013,104(4), 396-406.
- [2]. Seiler, G. J., Gulya, T. J., Fredrick, M. L. Exploration for Wild Helianthus Species from the Desert Southwestern USA for Potential Drought Tolerance/Recolección De Las Especies Silvestres Del Género Helianthus En Las Partes Desiertas Del Suroeste De Los Ee. Uu. Como Fuentes De Tolerancia a Sequía Potenciales/Collecte D'espèces Sauvages D'helianthus Dans Les Régions Désertiques Du Sud-Ouest Des Étatsunis En Tant Que Sources Potentielles De Tolérance À La Sécheresse. *Helia*, 2006, 29(45), 1-10.
- [3]. Güner, A. Türkiye Bitkileri Listesi. Nezahat Gökyiğit Botanik Bahçesi Yayını, İstanbul, 2013.
- [4]. Tüfekçi, Ş. Ayçiçeği (*Helianthus Annuus* L.) Bitkisi. Ereğli Ticaret Borsası, 2019, 14.
- [5]. Kaya, Y. Ayçiçeği Tarımı. Trakya Tarımsal Araştırma Enstitüsü Müdürlüğü <https://arastirma.tarimorman.gov.tr/ttae/Sayfalar/Detay.aspx?SayfaId=54> (accessed at 16.03.2023).
- [6]. Kaya, Y. Ayçiçeği Tarımı. *Edirne Tarım ve Hayvancılık Dergisi*, 2018, 10-11.

[7]. Korucu, S, Soy, G. 2019. An Investigation on the Effects of Tungsten Carbide and Grafen Reinforcements to Mechanical Properties in the Aluminium Matrix Composites. *Düzce University Journal of Science and Technology*; 7(3): 1466–1487.

[8]. Gedik, G., Avıncı, O. O., Yavaş, A. Kenevir lifinin özellikleri ve tekstil endüstrisinde kullanımıyla sağladığı avantajlar. *Tekstil Teknolojileri Elektronik Dergisi*, 2010, 4(3), 39-48.

[9]. Zhang ,J., Zhang, H., Zhang, J. "Evaluation of liquid ammonia treatment on surface characteristics of hemp fiber", *Cellulose*, 2013, (21), 569–579.

[10]. Özcan, A. (2008). Kağıt yüzey pürüzlülüğünün L\* a\* b\* değerleri üzerine etkisinin belirlenmesi. *İstanbul Ticaret Üniversitesi Fen Bilimleri Dergisi*, 7(14), 53-61.

[11]. Toker, M.C. Bitki morfolojisi, Ankara Üniversitesi Fen Fakültesi, Biyoloji Bölümü, II. Baskı, Ankara, 2004, 140.

[12]. Mert, M. *Lif Bitkileri*( 3. Baskı). Nobel Yayın Dağıtım, Ankara, 2020, 448.

[13]. Algan, G., Toker, M.C. Bitki Hücresi ve Morfolojisi Laboratuvar Kitabı. A.Ü. Fen Fakültesi Biyoloji Bölümü A.Ü. Fen Fakültesi Döner Sermaye İşletmesi Yayınları, Ankara, 2004, 143.

[14]. Sudha, S., Thilagavathi, G. Effect of alkali treatment on mechanical properties of woven jute composites, *The Journal of The Textile Institute*, 2016, 107(6), 691-701.

[15]. Bulut, Y. and Aksit, A. A comparative study on chemical treatment of jute fiber: potassium dichromate, potassium permanganate and sodium perborate trihydrate. *Cellulose*, 2013, 20 (6), 3155–3164.

[16]. De Rosa, I. M., Kenny, J. M., Puglia, D., Santulli, C., Sarasini, F. Morphological, thermal and mechanical characterization of okra (*Abelmoschus esculentus*) fibres as potential reinforcement in polymer composites, *Composites Science and Technology*, 2010, 70(1), 116-122.

# A New Record of Genus *Parastigmaeus* (Acariformes: Stigmaeidae) from Türkiye

Mustafa Akyol<sup>1\*</sup> 

<sup>1</sup> Department of Biology, Faculty of Engineering and Natural Sciences, Manisa Celal Bayar University, Manisa, Türkiye

\*[makyol77@gmail.com](mailto:makyol77@gmail.com)

\*Orcid No: 0000-0002-3466-7618

Received: 27 September 2023

Accepted: 7 November 2023

DOI: 10.18466/cbayarfbe.1367147

## Abstract

*Parastigmaeus urmiaensis* Mohammad Doustaresharaf and Bagheri, 2019 is founded for the first time from Türkiye and new report to genus *Parastigmaeus* the mite fauna of Türkiye. One female specimen of the species is collected from soil and litter under *Spartium junceum* (Fabaceae) in Manisa province, Türkiye. *P. urmiaensis* is redescribed and illustrated based on the adult female.

**Keywords:** Acari, New report, *Parastigmaeus*, Raphignathoidea, Türkiye.

## 1. Introduction

Members of the family Stigmaeidae are known predators and found in all biogeographical regions though most of them were discovered in the Palearctic, Nearctic, Afrotropical, Australian, Oriental regions [1].

The family Stigmaeidae is known has got in large quantities genus and species in the superfamily Raphignathoidea and includes about 636 species in 34 valid genera [2-5], of which 11 genera and 131 species are recorded from Türkiye, namely *Agistemus* Summers, 1960 (3 species), *Cheyllostigmaeus* Willmann, 1951 (9 species), *Eryngiopus* Summers, 1964 (4 species), *Eustigmaeus* Berlese, 1910 (28 species), *Ledermuelleriopsis* Willmann, 1953 (14 species), *Mediolata* Canestrini, 1889 (9 species), *Prostigmaeus* Kuznetsov, 1984 (3 species), *Stigmaeus* Koch, 1836 (50 species), *Storchia* Oudemans, 1923 (5 species), *Villersia* Oudemans, 1927 (1 species) and *Zetzellia* Oudemans, 1927 (5 species) [3-13].

*Parastigmaeus* is a small genus, in family Stigmaeida, with three described species in the world [14-17], namely *Parastigmaeus capensis* Meyer, 1969 (South Africa), *P. andreae* Khanjani and Ueckermann, 2002 (Iran) and *P. urmiaensis* Mohammad Doustaresharaf and Bagheri, 2019 (Iran). In this study, new report to genus *Parastigmaeus* Kuznetsov, 1984 the mite fauna of Türkiye.

A new record of Turkish fauna *Parastigmaeus urmiaensis* Mohammad Doustaresharaf and Bagheri is illustrated and redescribed based on the adult female. Similarities and differences were discussed by comparing them with the type locality (Iran) of the species.

## 2. Materials and Methods

The specimens were collected from soil and litter under *Spartium junceum*, Manisa province, Türkiye, and taken to the laboratory in plastic bags and extracted by Berlese-Tullgren funnels for 7 days. Mites were collected in 70% ethanol and mounted on slides in modified Hoyer's medium. The mite specimens were measured and drawn by means of a research microscope (Nikon Eclipse E 400). The setal nomenclature follows those of Kethley (1990) and Grandjean (1944) [18, 19]. All measurements were given in micrometers ( $\mu\text{m}$ ). Measurements of legs were taken from base of coxa to tips of tarsal claws. The specimens are deposited as slide mounted in the (CBZM), Manisa, Türkiye. See Zhang (2018) for abbreviations [20].

## 3. Results and Discussion

### Genus *Parastigmaeus* Kuznetsov, 1984

*Parastigmaeus* Kuznetsov, 1984: 1105; Ueckermann and Meyer, 1987: 50; Fan, Flechtmann and De Moraes, 2016: 106 [15, 21].

Type species: *Pseudostigmaeus capensis* Meyer, 1969



## ***Parastigmaeus urmiaensis* Mohammad Doustasharaf and Bagheri, 2019**

**Diagnosis:** Subcapitular setae *n* very long, prodorsal shield divided, with three pairs of aggenital setae, tarsus III with 7 setae, tarsus IV with a small solenidion [17].

**Description:** Female (*n* = 1) (Figs 1, 2).  
Length of body (excluding gnathosoma) 414, width 216.

Gnathosoma (Figs 1A, B, 2E). Chelicerae 99, fixed digit 78, moveable digit 83. Ventral subcapitulum smooth, with two pairs of subcapitular setae, *m* 26 and *n* 65 and two pairs of adoral setae, *or*1 10 and *or*2 10. Palp 104, trochanter without seta, femur with three setae, genu with one seta, palp tibia with well-developed claw + one seta-like accessory claw and two setae, palp tarsus with one terminal tridentate eupathidium + one subterminal simple eupathidium + one solenidion + four simple setae.

Dorsum of idiosoma (Fig. 1A). Prodorsum with three pairs of setae (*vi*, *ve* and *sci*); prodorsal shield divided to two large shields, each shield with an eye; setae *vi* and *ve* located on prodorsal shields but setae *sci* on small shield contiguous prodorsal shield; hysterosoma without shields except suranal shield of which is smooth, entire and bearing two pairs of setae (*h*1 and *h*2), seta *h*2 the longest of dorsal setae. Rest of hysterosomal setae on very small platelets. Lengths and distances of dorsal idiosomal setae as follows: *vi* 23, *ve* 42, *sci* 34, *c*1 23, *c*2 36, *d*1 18, *d*2 17, *e*1 18, *e*2 17, *f*26, *h*1 36, *h*2 44, *vi-vi* 47, *vi-ve* 21, *ve-ve* 81, *ve-sci* 65, *sci-sci* 161, *sci-c*1 47, *c*1-*c*1 55, *c*1-*c*2 70, *c*2-*c*2 169, *c*2-*d*1 78, *d*1-*d*1 91, *d*1-*e*1 65, *e*1-*e*1 44, *e*1-*e*2 62, *e*2-*e*2 138, *e*1-*f*29, *f-f* 75, *f-h*1 42, *h*1-*h*1 36, *h*1-*h*2 23, *h*2-*h*2 83.

Venter of idiosoma (Fig. 1B). Endopodal shield absent; ventral setae includes *1a* 13, *3a* 16 and *4a* 16; one pair of long genital setae *g*1 21 present; anogenital area striated, with three pairs of aggenital setae *ag*1 13, *ag*2 13, *ag*3 31 and pseudanal setae *ps*1 26, *ps*2 26, *ps*3 29.

Legs (Figs 2 A-D). Length of legs (from base of coxa to tip of tarsal claw) leg I 195, leg II 169, leg III 156, leg IV 164. Chaetotaxy of leg segments: coxae 2-1-2-2, trochanters 1-1-1-1, femora 4-4-2-2, genua 3(+1 $\kappa$ )-1-0-0, tibiae 5(+1 $\phi\phi$ )-5(+1 $\phi\phi$ )-5(+1 $\phi\phi$ )-5(+1 $\phi\phi$ ), tarsi 13(+1 $\omega$ )-9(+1 $\omega$ )-7(+1 $\omega$ )-7(+1 $\omega$ ). Length of solenidia:  $\omega$ I 8,  $\omega$ II 7,  $\omega$ III 4,  $\omega$ IV 2.

Male: Unknown.

Material examined. One female collected from litter and soil under the *Spartium junceum*, 94 m a.s.l., 38° 54' 09"N 27° 48' 23"E, Akhisar district, Manisa province, 09 November 2020, Türkiye, coll. M. Akyol.

### **Discussion**

*Parastigmaeus urmiaensis* Mohammad Doustasharaf and Bagheri, 2019 was described for the first time from Iran and collected from soil, (altitude 1775 m a.s.l.) Urmia, West Azerbaijan province, Iran [17]. In this study, the samples collected from soil and litter under *Spartium junceum* (altitude 94 m a.s.l.) in Akhisar district, Manisa province, Türkiye.

The body size of 385 (356–370) long and 195 (164–172) wide in the Iranian specimens; 414 long and 216 wide in the Turkish specimens. Body size of the Turkish specimen is bigger than the Iranian specimens.

The Turkish specimen resembles the Iranian specimens, but some measurements of body setae (*ve* 42, *sci* 34, *c*1 23, *c*2 36, *e*2 17, *f*26, *1a* 13, *3a* 16, *4a* 16, *g*1 21, *ag*1 13, *ag*2 13, *ag*3 31, *ps*3 29 in the Turkish specimens) are different from the type specimens (*ve* 38 (32–34), *sci* 25 (21–22), *c*1 19 (16–20), *c*2 26 (25–28), *e*2 12 (12–13), *f* 20 (18–20), *1a* 23 (21–25), *3a* 25 (22–23), *4a* 19 (17–20), *g*1 38 (37–40), *ag*1 15 (16–18), *ag*2 17 (15–18), *ag*3 25 (22–23), *ps*3 23 (24–25) in the Iranian specimens). Also, setae *sci* on small shield contiguous prodorsal shield in the Turkish specimen whereas setae *sci* on integument in the Iranian specimens.

*P. urmiaensis* was found from the type locality (Iran) [17]. This is the second report of this species and a new record for the Turkish fauna.

### **Ethics**

There are no ethical issues after the publication of this manuscript.

### **Author's Contributions**

**Mustafa Akyol:** Drafted and wrote the manuscript, performed the experiment and result analysis

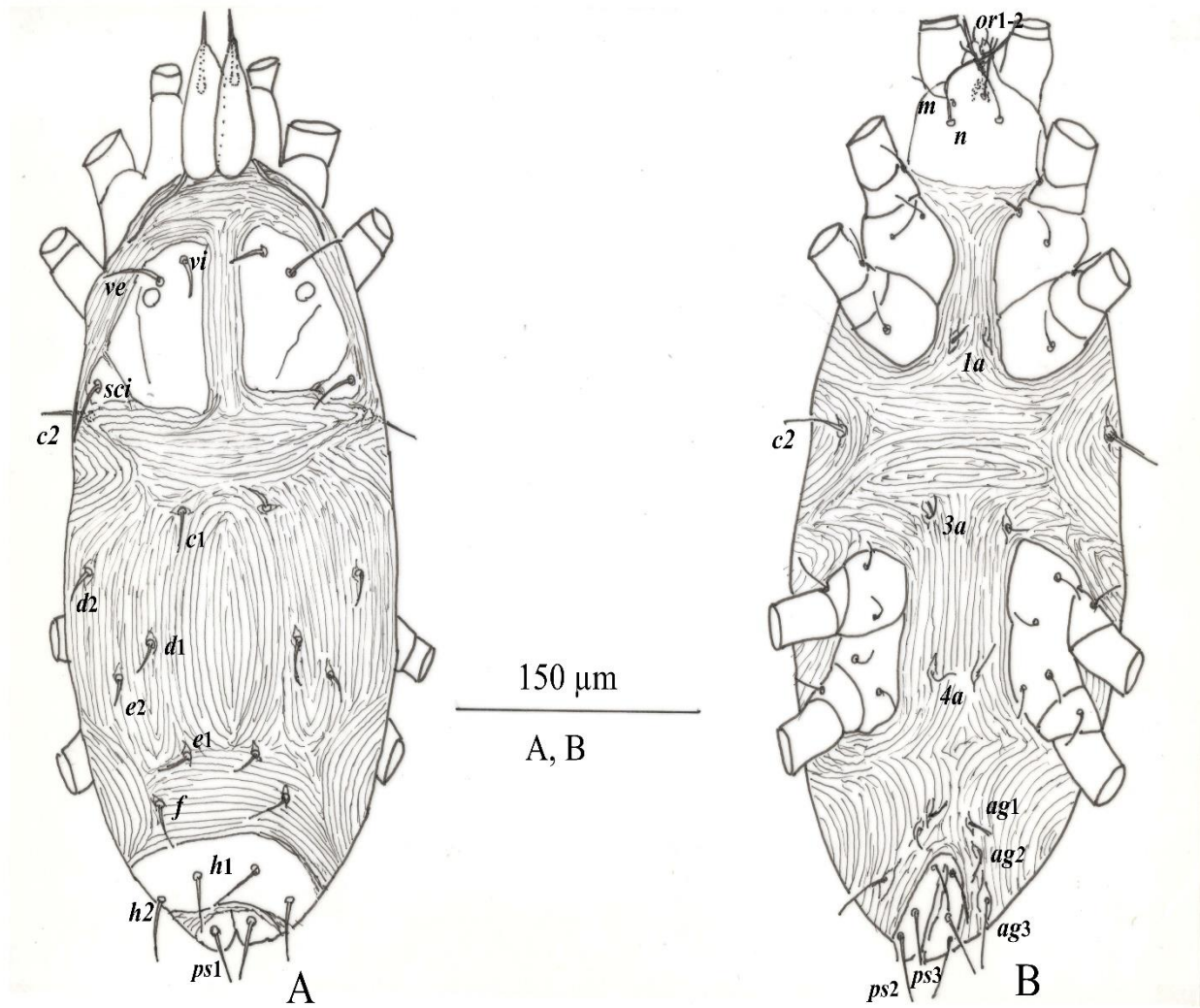


**Figure 1.** *Parastigmaeus urmiaensis* Mohammad Doustaresharaf and Bagheri (female): A. Dorsal view of idiosoma; B. Ventral view of idiosoma.



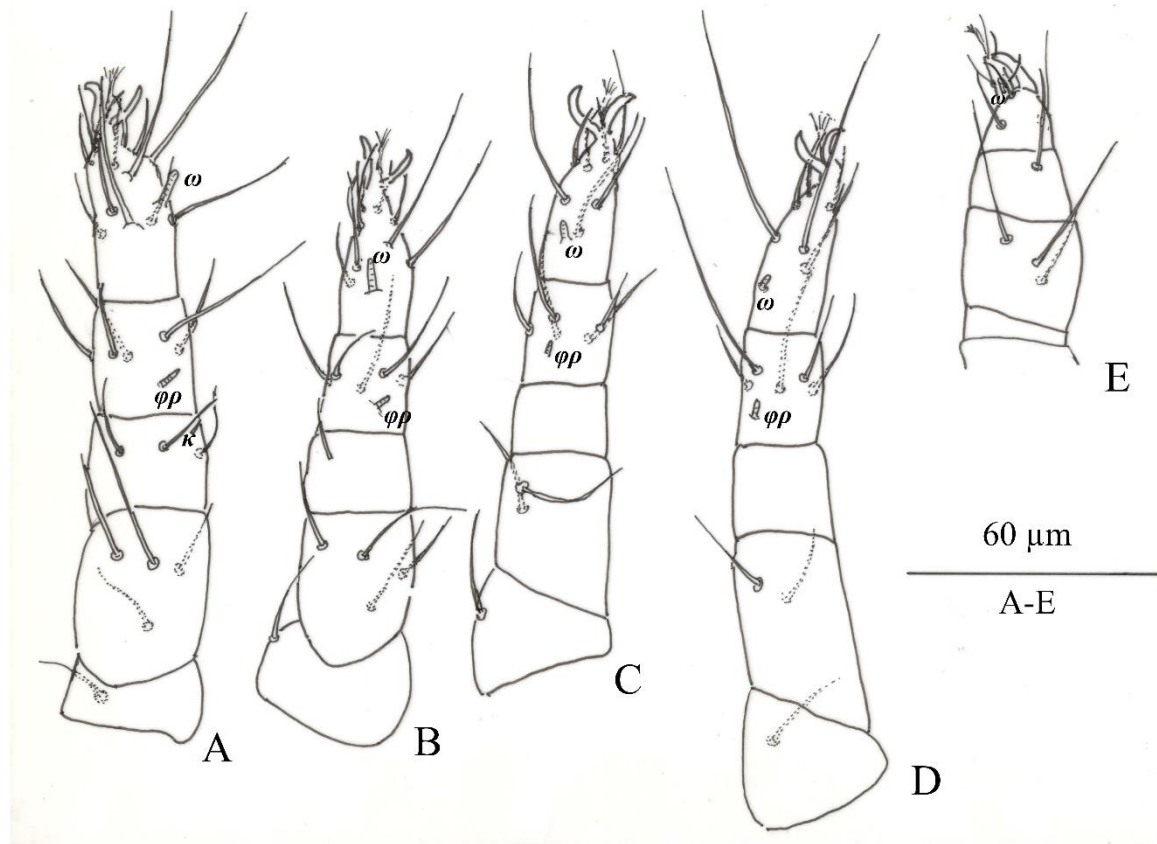


**Figure 2.** *Parastigmaeus urmiaensis* Mohammad Doustaresharaf and Bagheri (female): A. Leg I; B. Leg II; C. Leg III; D. Leg IV; E. Palp.

## References

- [1]. Fan, Q-H, Zhang, Z-Q. Raphignathoidea (Acari: Prostigmata). Fauna of New Zealand 52. Manaaki Whenua Press, 2005; 400 pp.
- [2]. Fan, Q-H, Flechtmann, CHW, De Moraes, DJ. 2016. Annotated catalogue of Stigmaeidae (Acari: Prostigmata), with a pictorial key to genera. *Zootaxa*, 4176: 1–199.
- [3]. Doğan, S. 2019. Raphignathoidea (Acari: Trombidiformes) of Turkey: A review of progress on the systematics, with an updated checklist. *Acarological Studies*, 1 (2): 129–151.
- [4]. Beron, P. Acarorum Catalogus VII: Trombidiformes, Prostigmata, Raphignathoidea (Fam. Barbutiidae, Caligonellidae, Camerobiidae, Cryptognathidae, Dasythyreidae, Dytiscacaridae, Eupalopsellidae, Homocaligidae, Mecognathidae, Raphignathidae, Stigmaeidae, Xenocaligonellidae). Pensoft, National Museum of Natural History, Sofia, Bulgarian Academy of Sciences, Sofia, 2020, 306 pp.
- [5]. Akyol, M. 2023. *Stigmaeus quercus* (Acari: Stigmaeidae), a new species from Manisa province, Türkiye. *Systematic and Applied Acarology*, 28 (2), 167–172.
- [6]. Yeşilayer, A, Çobanoğlu, S. 2013. Determination of Raphignathoid mites (Acari: Prostigmata: Raphignathoidea) ornamental plants of İstanbul (Turkey). *Turkish Journal of Entomology*, 37: 93–03. [In Turkish]
- [7]. Akyol, M. 2017. Fauna of the coastal Aegean raphignathoid mites (Acari: Prostigmata: Raphignathoidea). *Plant Protection Bulletin*, 57: 205–229. [In Turkish]
- [8]. Akyazı, R, Ueckermann, EA, Akyol, D, Soysal, M. 2017. Distribution of mite species (Acari) on persimmon trees in Turkey (Ordu), with one newly recorded mite species and one re-described species. *International Journal of Acarology*, 43: 563–581.
- [9]. Akyol, M, Gül, MP. 2018. A new species of *Zetzellia* Oudemans (Acari, Stigmaeidae) from Turkey. *Systematic and Applied Acarology*, 23 (3): 463–467.
- [10]. Doğan, S, Doğan, S. 2020. Türkiye faunası için yeni stigmaeid akarlar (Acariformes: Raphignathoidea: Stigmaeidae). *Acarological Studies*, 2 (2): 94–118.

- [11]. Akyol, M. 2021. Two New Records of Stigmaeid Mites (Acari: Stigmaeidae) for the Turkish Fauna. *KSÜ Tarım ve Doğa Dergisi*, 24 (2): 430-434.
- [12]. Doğan, S, Doğan, S, Khanjani. 2021. On some species of the genus *Ledermuelleriopsis* Willmann (Acariformes: Stigmaeidae) in Turkey. *Systematic and Applied Acarology*, 26(2): 455–463.
- [13]. Doğan, S, Doğan, S. 2022. A new species of the genus *Cheylostigmaeus* Willmann (Acari: Trombidiformes: Stigmaeidae) from Turkey. *Systematic and Applied Acarology*, 27(10): 2062–2075.
- [14]. Meyer, MKPS. 1969. Some stigmaeid mites from South Africa (Acari: Trombidiformes). *Acarologia*, 11(2): 227–271.
- [15]. Ueckermann, E.A, Meyer, MKPS. 1987. Afrotropical Stigmaeidae (Acari: Prostigmata). *Phytophylactica*, 19: 371–397.
- [16]. Khanjani, M., Ueckermann, EA. 2002. The stigmaeid mites of Iran (Acari: Stigmaeidae). *International Journal of Acarology*, 28: 317–339.
- [17]. Mohammad Doustaresharaf, M, Bagheri, M, Saber, M. 2019. Two species of stigmaeid mites (Acari: Stigmaeidae) from Iran: *Eryngiopus rezaiyeiensis* sp. nov. and *Parastigmaeus urmiaensis* sp. nov. *Systematic and Applied Acarology*, 24(2): 259–270.
- [18]. Kethley, J. Acarina: Prostigmata (Actinedida). In: Soil Biology Guide. Dindal, D.L. (Ed.). Wiley, New York, 1990, 667–756.
- [19]. Grandjean, F. 1944. Observations sur les acarions de la famille des Stigmaeidae. *Archives des Sciences physiques et naturelles*, 26: 103–131.
- [20]. Zhang, Z-Q. 2018. Repositories for mite and tick specimens: acronyms and their nomenclature. *Systematic and Applied Acarology*, 23(12): 2432–2446.
- [21]. Fan, Q-H, Flechtmann, CHW, De Moraes, DJ. 2016. Annotated catalogue of Stigmaeidae (Acari: Prostigmata), with a pictorial key to genera. *Zootaxa*, 4176: 1–199.

# Investigation of the Relationship Between the Structural Properties and Air, Water Drop and Particle Permeability of Different Masks Available in the Market

Candan Akca<sup>1\*</sup> , Mehmet İsmail Katı<sup>1,2</sup> 

<sup>1</sup> DEFAM (Applied Science Research Center), Manisa Celal Bayar University, Manisa, Türkiye

<sup>2</sup> Department of Medical Imaging Techniques, Vocational School of Health Sciences, Manisa Celal Bayar University, Manisa, Türkiye

\*[candan.akca@cbu.edu.tr](mailto:candan.akca@cbu.edu.tr)

\* Orcid No: 0000-0001-5305-0296

Received: 5 October 2023

Accepted: 18 December 2023

DOI: 10.18466/cbayarfbe.1371598

## Abstract

This study was performed on the masks which started to have vital importance after the Covid-19 which were first seen in China at the end of 2019 and spread all over the world in a short time and became a global epidemic. By examining the structural and morphological properties (number of layers, fabric properties used in different layers, average fiber diameter, fiber distribution, average porosity diameter, etc.) of different masks procured from local producers, air permeability, water drop and particle permeability were investigated. Structural and morphological properties of different layers of masks were observed through SEM analysis. The air permeability analysis of the masks was performed at 100 pascals pressure, in an area of 5 cm<sup>2</sup> in 4 repetitions using Textest-Fx 3300 Air Permeability Device. The water drop permeability analysis was carried out with 0.3 µM NaCl solution under standard atmospheric conditions in a non-pressurized environment. A crocrometer was used for particle permeability analysis. And it was tested whether the fine particulate dust passed to the back of the mask. It has been determined that the air permeability, water drop and particle permeability behavior of the masks with different structural and morphological properties are very different.

**Keywords:** Areal density, Air permeability, Fiber diameter, Mask, Meltblown nonwoven, Spunbond nonwoven, Water drop permeability

## 1. Introduction

Surgical masks have been used since the early 1900s to minimize the risk of infection and to keep the current epidemic under control [1-3]. Health scientist Carl Friedrich Flügge (1847-1923) and his team who were working on tuberculosis and droplet infection in Breslau first suggested in 1897 the use of mouth bandages to prevent droplets scattered around [2]. This mouth bandage recommended had a single layer and is made of cotton gauze [2].

The first use of surgical masks started in the operating rooms in Germany and America in the 1920s. Following World War, research were carried out on face masks. These studies generally focused on the thickness of face masks made of gauze and fabric. In the 1940s, washable and sterilizable masks consisting of different number of layers were accepted and widespread in Germany. In the

mid-1960s, disposable paper masks were first produced in America and spread all over the world [2,4]. Again in the 1960s, disposable synthetic nonwoven masks were produced in America and their use became widespread [5, 6].

As is known, Covid-19, which was first seen in China, and spread and turned into a global epidemic in a short time, affected all humanity and caused the death of nearly 7 million people [7-9]. Due to the Covid-19 pandemic surgical masks came into our life and became one of our most effective weapons in order to protect against the virus and keep its spread under control [10]. It is reported in the studies performed that virus protection can reach over 90% if all people in the society wear masks properly. When an infected person does not wear a mask and a normal person wears a mask, the transmission rate reaches 70 percent, and in cases where only the infected person wears a mask, the transmission rate reaches 5

percent [11]. However, since it is not known who is infected and who is not, everyone needs to wear a mask. The mask prevents getting sick by preventing the virus from entering the body. Or, it causes the person to encounter less virus and thus overcome the disease more mildly [12, 13].

The rapid spread of the Covid-19 pandemic all over the world and the fact that the world was caught unprepared caused in the first instance the need for masks to be not met all over the world. Later, after mask manufacturers and even local apparel manufacturers had started to manufacture, the need for masks was able to be met [14, 15]. The need for a large amount of masks in a short time due to the pandemic has caused a large amount of uncertified masks to be produced and put on the market [16, 17].

Masks are produced with different certifications in different countries. These certificates guarantee and standardize the filtration efficiency at certain levels. These masks are divided into different mask classes according to their filtering efficiency. [16-18]. One of the certificates widely used in certified mask production is the European Union standards [18]. Certified face masks are subject to the European Union EN 14683 Standard. And according to filtration efficiency, there are classes such as Type I, Type II (Medical face masks) and Type IIR (Fluid resistant surgical face masks). Type I and Type II are suitable for medical use, but are not suitable and sufficient for clinical environments. For clinical settings, Type IIR is the appropriate class [18, 19].

Masks with higher filtration efficiency are masks that fall into the Personal Protective Equipment class (FFP) and are subject to the European Union EN 149-A1 Standard. These masks have three classes according to their filtration efficiency: FFP1, FFP2 and FFP3 [18, 19]. These masks provide protection against biological aerosols (including bacteria and viruses) suspended in the air. FFP3 mask has fluid resistant feature like Type IIR mask. Masks, which are classified as Personal Protective Equipment (FFP), are produced mostly for healthcare professionals [18, 19].

Spunbond and meltblown nonwoven surfaces are used in the production of disposable multilayer nonwoven masks. Techniques for obtaining spunbond nonwoven surface and meltblown nonwoven surface are different techniques. The most obvious differences between these two processes are:

- Temperature and speed of air used in thinning the filaments
- It is where the filaments are pulled and the thinning force is applied.

Due to these technical differences; meltblown nonwoven production technique is more ideal for microfiber production. However, it does not provide the necessary polymer orientation to create good physical properties. Spunbond nonwoven production technique is not ideal for microfiber production. However, it provides the necessary conditions for improving polymer orientation and physical properties. Although the initial investment cost of the meltblown nonwoven production technique is much lower than the spunbond nonwoven production technique, the meltblown nonwoven production cost increases several times the spunbond nonwoven production cost due to the effect of the energy cost used during production [20, 21].

The middle layer of the three-layer mask must have a filtering feature. The outer and inner layers should be made of spunbond nonwoven surface, and the middle layer should be made of meltblown nonwoven surface, which performs the main filtering function [22-25]. Masks that use a spunbond nonwoven surface in all layers without a meltblown nonwoven layer provide less protection against the virus. Again, fabric masks provide limited protection [26, 27]. The filtration performance of masks is closely related to parameters such as areal densities of the meltblown and spunbond layers used, fiber diameter, fiber distribution, and porosity size [28].

## 2. Materials and Methods

### 2.1. Materials

1 unit single-layer fabric mask produced from 100 % cotton (Mask 10) and 9 different surgical face masks were purchased from local vendors.

### 2.2. Methods

The areal density is to determine the mass per unit area. The areal density of nonwoven was calculated according to the following Equation (1),

$$D_A = m / A \quad (1)$$

where  $D_A$  is areal density ( $\text{g}/\text{m}^2$ ),  $m$  is mass (g) measured by an electronic balance, and  $A$  is area ( $\text{m}^2$ ). Five measurements were taken and the average value was calculated [29].

Surface morphologies of spunbond nonwoven, meltblown nonwoven and cotton fabrics in the layers forming surgical masks were observed with SEM (scanning electron microscope). In addition, the average fiber diameter was calculated by taking 4 different measurements. While examining the different layers of the surgical masks, 4 different measurements were taken from the maximum porous areas and the average porosity diameter was calculated.



The air permeability analysis of the masks was performed at 100 pascals pressure, in an area of 5 cm<sup>2</sup> in 4 repetitions using Textest-Fx 3300 Air Permeability Device.

The water drop permeability analysis was carried out with 0.3 µM NaCl solution under standard atmospheric conditions in a non-pressurized environment. The movement of the water droplet on the mask surface was observed for 4 hours in nonwoven surgical masks and until it is absorbed from the surface and disappears completely in the cotton single layer mask.

A fine powder was used as the particle in the particle permeability analysis. The analysis was carried out using an equal amount of powder for each mask using a crocmeter (Figure 1). The purpose of using the crocmeter device is to provide a pressurized environment in particle permeability analysis.



**Figure 1.** Crocmeter

### 3. Results and Discussion

#### 3.1. Surface Analysis with SEM (The Relationship Between Average Fiber Diameter, Fiber Diversity, Fabric Feature and Porosity)

9 of the 10 masks examined are made of nonwoven fabric, each of which is 3-layer surgical face masks. And the layers of each mask (outer / middle / inner layers) show different properties (in terms of weight, average fiber thickness and fiber distribution, porosity). In some masks, spunbond polypropylene nonwoven fabric is used in all three layers, while in others, meltblown polypropylene nonwoven fabric is used, which performs the main filtration function, in the middle layer.

One of the masks is a single layer mask made of 100% cotton fabric (166 g/m<sup>2</sup>) fabric. In the SEM analysis performed, it was found out that two different fiber groups (with different average fiber diameters) had been used in different layers of some masks (mask no 1,2,3,4,5 and 9) in which spunbond polypropylene nonwoven fabric had been used. In some masks, nonwoven surfaces were obtained by using a single fiber group (masks no 6,7,8,10). When the relationship between the pore size and the properties of the fiber used (such as fiber diameter, using more than one fiber group with different diameters together in fabric production) is examined, it has been observed that the spunbond nonwoven fabrics manufactured using coarser fibers (with higher fiber diameters) have higher porosity size.

Again, much smaller porosity was observed in spunbond nonwoven fabrics where two different fiber groups with different fiber diameters were used. In these fabrics where two different fiber groups are used, the porosity decreases to much more lower degree, as the pores formed at the intersection points of the fibers with higher fiber diameter are covered with other fibers with much smaller fiber diameter. This can clearly be seen in Figure 2 and Figure 3.

The critical factor here is the amount of difference between the fiber diameters of the two different fiber groups. The smaller the diameter of the fiber (nano size or 1-2 µm size) used in the production of spunbond nonwoven fabric, the lower the porosity is.

It is observed in SEM analysis that in the masks where meltblown nonwoven fabric is used in the middle layer, fibers with much smaller fiber diameter (between 0.6 nm and 1-2 µm) are used, so the porosity is much lower. Such that, it is seen that the porosity level of some meltblown layers is so low that cannot be detected or measured (Figure 4). This confirms that masks with a meltblown nonwoven middle layer are more protective.

According to the results of SEM analysis, the average fiber diameter in a single layer mask made of 100% cotton fabric is 14.12 µm. And the average porosity diameter is 119.7 µm (Figure 5).

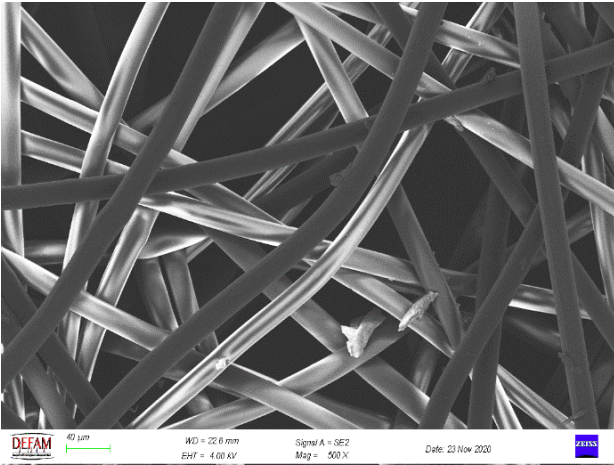


Figure 2. Spunbond surface with single fiber group

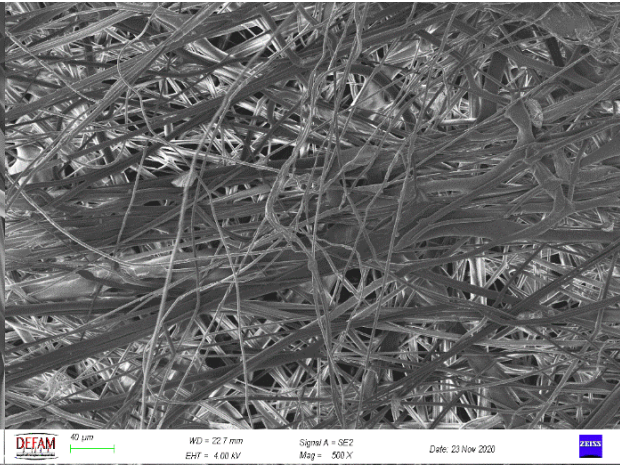


Figure 3. Spunbond surface with two fiber groups

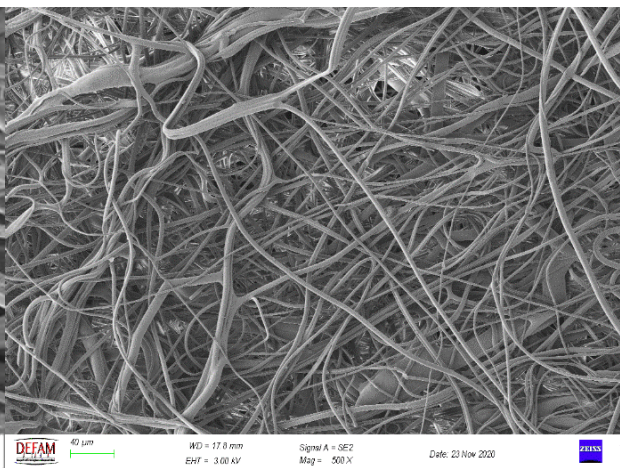
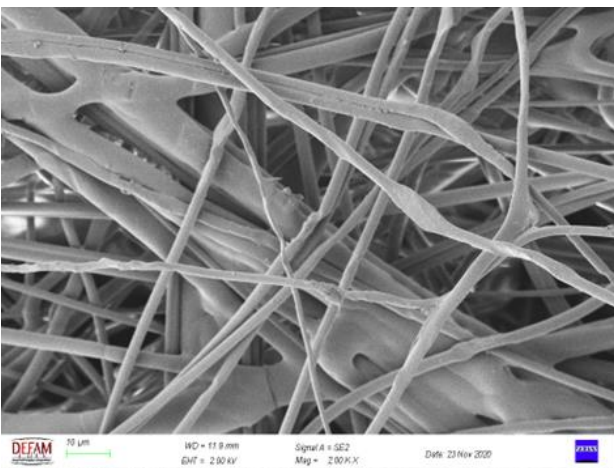


Figure 4. Meltblown surface

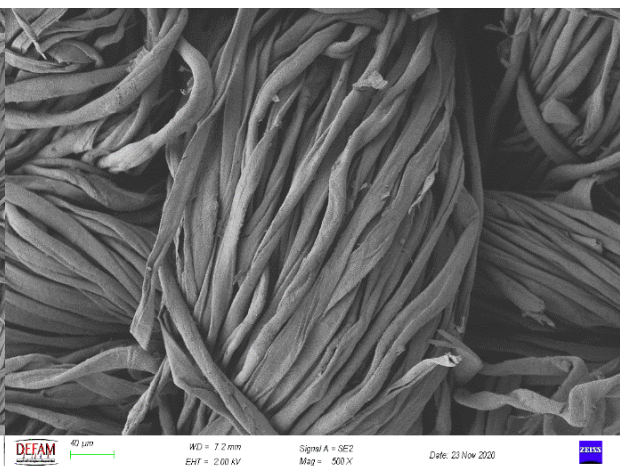
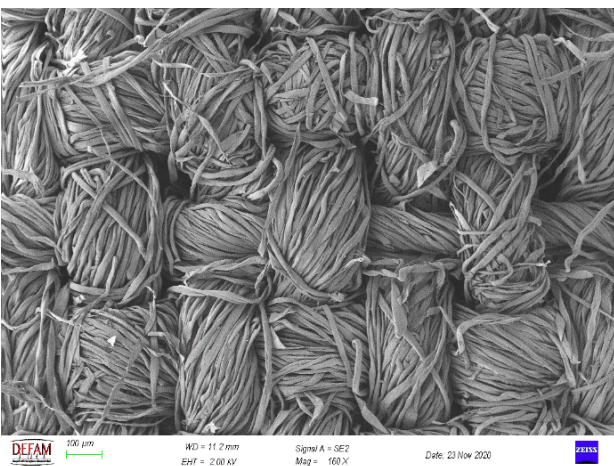


Figure 5. Image of 100% cotton fabric mask surface



### 3.2. Air Permeability Analysis

The air permeability analysis of the masks was performed at 100 pascals pressure, in an area of 5 cm<sup>2</sup> in 4 repetitions using Textest-Fx 3300 Air Permeability Device.

According to results of air permeability analysis, the permeability of the surgical face mask with meltblown nonwoven layer (85.5-189.25 l/m<sup>2</sup>/sec) are much lower than that of the masks without metlblown layer and all three layers of which are made of spunbond nonwoven fabric (360.25-950.25 l/m<sup>2</sup>/sec). Considering their air permeability, it can be said that surgical masks with meltblown nonwoven layers are more protective than surgical masks without meltblown nonwoven layers and 3 layers of which are made of spunbond nonwoven fabrics.

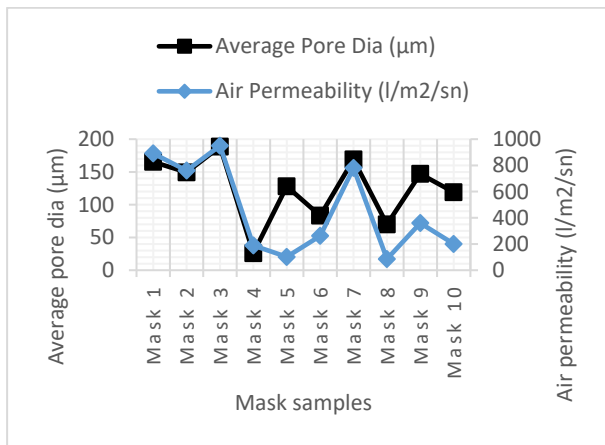


**Figure 6.** Relationship between mean pore diameter and air permeability

According to the results of the air permeability analysis, air permeability of single layer mask made of 100% cotton is 201 l/m<sup>2</sup>/sec. Its air permeability is much lower compared to surgical masks 3 layers of which are made of spunbond nonwoven fabric. This fact can be seen in Figure 6.

#### 3.2.1. The Relationship Between Areal Density and Air Permeability

The field densities of spunbond and meltblown nonwoven layers are not related to air permeability alone, but parameters such as field density, fiber diameter, fiber group number, fiber density have a combined effect on air permeability. This fact can be seen in Figure 7.

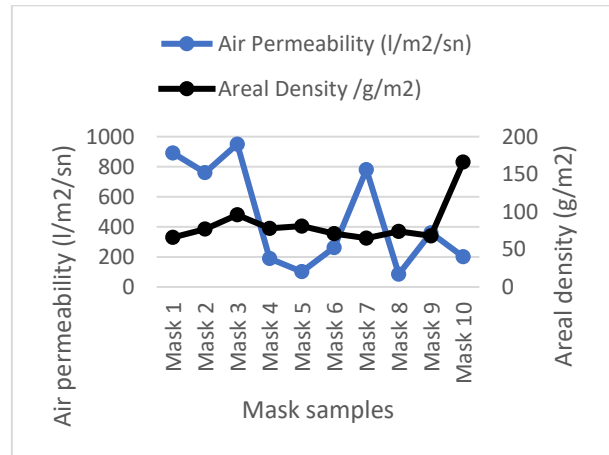


**Figure 7.** Relationship between field density and air permeability

### 3.3. Water Drop Permeability

The Water Drop Permeability Test is based on the principle of leaving water drops containing 0.3 µM NaCl on the masks and checking the amount of drops passed to the other side. The test was carried out in an unpressurised environment. And it was calculated with the formulation below.

$$P = C_0 - C_1 / C_0 \times 100 \quad (2)$$

Where, P is the filtration efficiency (%), C<sub>0</sub> is the mass concentration of NaCl in the upstream, and C<sub>1</sub> is the mass concentration of NaCl in the downstream [29].

According to the results of the water drop permeability test performed in a non-pressurized environment, the duration during which water drop stays on the surface is more than 4 hours in all surgical face masks and no transition to the back surface of the fabric has been detected. The single layer mask made of 100% cotton fabric absorbs the water drop in less than 120 seconds. During this time, 58.032 % of the water drop passes to the second layer. Structural properties and air, water drop permeability of masks were given in Table 1 below.

### 3.4. Particulate Permeability

A crocmeter was used for particle permeability analysis. An equal amount of fine particulate powder was used for each mask. And as a result of tidal movements of the crocmeter, it was tested whether the fine particulate dust passed to the back of the mask.

**Table 1.** Number of Layers, Layer Properties, Area Density, Average Fiber Diameter, Average Porosity Diameter, Air Permeability, Water Drop Permeability Values of Different Masks available in the Market

Masks	Number of Layers	Layer Origin Outer/middle/inner	Areal Density(g/m <sup>2</sup> ) Outer/middle/inner	Average Fiber Dia. (µm) Outer/middle/inner	AveragePore Dia. (µm)	Water Permeability	Air Permeability (l/m <sup>2</sup> /sn)
1	3	SB/SB/SB	29/18/19	20.55-19.03 16.76-15.70 16.76-15.70	106.5 195.3 195.3	> 4 hours	891.25
2	3	SB/SB/SB	32/19/26	22.38-18.86 19.78-18.96 22.38-18.86	116.5 216.2 116.5	> 4 hours	760.5
3	3	SB/SB/SB	32/34/30	33.02-28.25 28.96-23.84 33.02-28.25	195.6 176.5 195.6	> 4 hours	950.25
4	3	MB+SB	26/25/27	15.02-1.44 16.32-1.86 16.32-1.86	NA 39.38 39.38	> 4 hours	189.25
5	3	SB/MB/SB	34/23/24	22.34-20.36 1.915 22.40	145.8 7.603 233.8	> 4 hours	102
6	3	SB/MB/SB	19/27/25	15.86 2.02 18.75	83.92 NA 167.6	> 4 hours	262.25
7	3	SB/SB/SB	30/15/20	15.53 25.95 25.60	108.1 291.9 108.9	> 4 hours	780.5
8	3	SB/MB/SB	30/21/23	30.22 2.39 22.57	80.55 8.845 123	> 4 hours	85.5
9	3	SB/SB/SB	30/18/20	19.67-1.235 23.69 23.69	NA 221.4 221.4	> 4 hours	360.25
10	1	Cotton 100%	166	14.12	119.7	<120 seconds/% 58.032	201

SB: Spunbond polipropilen nonwoven, MB: Meltblown polipropilen nonwoven, NA: Not available

The particle size analysis of the fine particulate powder used in the analysis was performed on the Mastersizer 3000 device. Analysis parameters were here:

**Dispersant Name:** Water  
**Dispersant Refractive Index:** 1,330  
**Particle Refractive Index:** 1,550

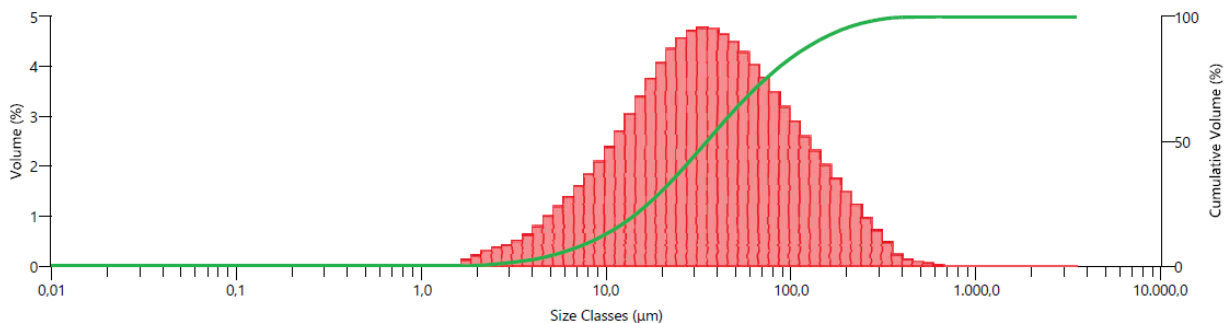


**Figure 8.** Particulate Size Histogram of the Fine Particulate Powder

Volume In Range (0,1;10) µm 12,78 %  
Volume In Range (10;100) µm 70,58 %  
Volume Below (2) µm 0,23 %  
Volume Below (45) µm 59,18 %



According to the results of the particle size analysis of the powder used in the particle permeability analysis, the volumetric ratio of the particles in the range of 0.1-10  $\mu\text{m}$  is 12.78%. The volume fraction of particles in the 10-100  $\mu\text{m}$  range is 70.58%. The volume fraction of particles below 2  $\mu\text{m}$  is 0.23%. The volume fraction of particles below 45  $\mu\text{m}$  is 59.18% (Figure 8).

Particle permeability analysis was applied to all masks. None of the multi-layered nonwoven disposable masks had any back-to-face particle transfer. However, a small amount of particle migration was observed on the back side of the 100% cotton single-ply fabric mask. However, it could not be analyzed due to the small amount passed.

#### 4. Conclusion

When the relationship between number of layers, fiber diameter, field density and porosity size of masks and their air permeability, water droplet permeability and particle permeability performance is examined; the following results have been reached:

- An increase in air permeability was observed in the masks in which spunbond nonwoven fabric was used in all three layers compared to the mask the middle layer of which was made of meltblown nonwoven fabric. The air permeability of single layer mask made of 100% cotton fabric is higher than that of the masks with middle layer made of meltblown nonwoven, but it is quite better than masks 3 layers spunbond nonwoven.

- In the layers using spunbond nonwoven fabrics, an increase in the porosity size was observed on the surfaces where single fiber group was used compared to the surfaces where two separate fiber groups were used. Since much thinner fibers are used on the surfaces where meltblown nonwoven fabric is used, the porosity is quite less than the surfaces where spunbond nonwoven fabric is used, and even the porosity size cannot be determined in some layers.

- According to the results of the water drop permeability test performed in a non-pressurized environment, the duration during which water drop stays on the surface is more than 4 hours in all surgical masks and no transition to the back surface of the fabric has been detected. The single layer mask made of 100% cotton fabric absorbs the water drop in less than 120 seconds. And during this time, 58,032 % of the water drop passes to the second layer.

- According to particle permeability analysis none of the multi-layered nonwoven disposable masks had any back-to-face particle transfer. However, a small amount of particle migration was observed on the back side of the 100% cotton single-ply fabric mask. However, it could not be analyzed due to the small amount passed.

#### Acknowledgement

The experiments in this paper were partially performed at Manisa Celal Bayar University (Turkey) Applied Science and Research Center (DEFAM).

#### Author's Contributions

**Candan Akça:** Assisted in characterization of the structure, supervised the experiments' progress, result interpretation and helped in manuscript preparation.

**Mehmet İsmail Katı:** Assisted in analytical analysis on the structure, supervised the experiment's progress, result interpretation and helped in manuscript preparation.

#### Ethics

There are no ethical issues after the publication of this manuscript.

#### References

- [1]. Matuschek, C, et al. 2020. The History and Value of Face Masks. *European Journal of Medical Research*. 25(23).
- [2]. Strasser, B, Schlich, T. 2020. A History of Medical Mask and The Rise of Throwaway Culture. *The Art of Medicine*. 396(10243): 19-20.
- [3]. Oberg, T, Brosseau, L. 2007. Surgical Mask Filter and Fit Performance. *American Journal of Infection Control*; 36(4): 276-282.
- [4]. Belkin, N. L. 1996. A century after their introduction, are surgical masks necessary? *AORN Journal*, 64(4), 602-607. doi:10.1016/s0001-2092(06)63628-4
- [5]. Tesfaldet, Y, Ndeh, N. 2022. Assessing face masks in the environment by means of the DPSIR framework. *Science of The Total Environment*. 814(152859). <https://doi.org/10.1016/j.scitotenv.2021.152859>
- [6]. Pullangott, G., Kannan, U., S., G., et al. 2021. A comprehensive review on antimicrobial face masks: an emerging weapon in fighting pandemics. *RSC Advances*, 11(12), 6544-6576. doi:10.1039/d0ra10009a
- [7]. Coronavirus: the first three months as it happened <https://www.nature.com/articles/d41586-020-00154-w>. (accessed at 12.06.2023).
- [8]. Covid-19 Coronavirus Pandemic <https://www.worldometers.info/coronavirus/> (accessed at 12.06.2023).
- [9]. WHO Coronavirus (COVID-19) Dashboard <https://covid19.who.int/> (accessed at 12.06.2023).
- [10]. Martinelli L, Kopilaš V., et al. Face Masks During the COVID-19 Pandemic: A Simple Protection Tool With Many Meanings. *Front Public Health*. 2021 Jan 13;8:606635. doi: 10.3389/fpubh.2020.606635.
- [11]. Maske aşı gibidir virüsü engeller <https://www.sozcu.com.tr/2020/saglik/maske-asi-gibidir-virusu-engeller-6053491/> (accessed at 12.06.2023).
- [12]. One More Reason to Wear a Mask: You'll Get Less Sick From COVID-19 <https://www.ucsf.edu/news/2020/07/418181/one-more-reason-wear-mask-youll-get-less-sick-covid-19> (accessed at 12.06.2023).

- [13]. Wearing a Mask Could Keep You from Getting Seriously Sick <https://publichealth.jhu.edu/2020/wearing-a-mask-could-keep-you-from-getting-seriously-sick> (accessed at 12.06.2023).
- [14]. Chua, M. H. Cheng, W. Goh, S. S. Kong, J. Li, B. Lim, J. Y. C. 2020. Face Masks in the New COVID-19 Normal: Materials, Testing, and Perspectives. *Research*, 1–40. doi:10.34133/2020/7286735
- [15]. Van Straten, B, de Man, P, van den Dobbelseen, J, Koeleman, H, van der Eijk, A, Horeman, T. 2020. Sterilization of disposable face masks by means of standardized dry and steam sterilization processes; an alternative in the fight against mask shortages due to COVID-19. *Journal of Hospital Infection*. doi:10.1016/j.jhin.2020.04.001
- [16]. Blad, T, Nijssen, J, Broeren, F, Boogaard, B, Lampaert, S, van den Toorn, S, van den Dobbelseen, J. 2020. A Rapidly Deployable Test Suite for Respiratory Protective Devices in the COVID-19 Pandemic. *Applied Biosafety*. 25(3), 161–168. doi:10.1177/1535676020947284
- [17]. Carlos Rubio-Romero, J, del Carmen Pardo-Ferreira, M, Antonio Torrecilla García, J, Calero-Castro, S. 2020. Disposable masks: Disinfection and sterilization for reuse, and non-certified manufacturing, in the face of shortages during the COVID-19 pandemic. *Safety Science*, 104830. doi:10.1016/j.ssci.2020.104830
- [18]. Begg, S, Emekwuru, N, Miché, N, Whitney, B, Ejohwomu, O. 2020. Can we use these masks? Rapid assessment of the inhalation resistance performance of uncertified medical face masks in the context of restricted resources imposed during a public health emergency. *medRxiv*, 2020-05.
- [19]. Puro, V, Magnavita, N, Ippolito, G. 2004. SARS and masks. *Journal of Hospital Infection*, 56(1), 73–74. doi:10.1016/j.jhin.2003.09.010
- [20]. Bhat, G. S, Malkan, S. R, Islam, S. Spunbond and meltblown web formation. In *Handbook of Nonwovens*, Woodhead Publishing, 2022, pp 217-278.
- [21]. Wilson, A. 2010. The formation of dry, wet, spunlaid and other types of nonwovens. *Applications of Nonwovens in Technical Textiles*, 3–17. doi:10.1533/9781845699741.1.3
- [22]. Özer, A, Hacimustafaoğlu, M. 2020. What Should be the Mask Types, Features and Standards Recommended for Health Institutions and for the General Population During the COVID-19 Pandemic? *J Pediatr Inf*, 14(3), 150-154. DOI: 10.5578/ced.202054
- [23]. Zhang, J, Wang, H, Chen, C, Gui, A, Zhang, X, Wang, Y, Zeng, W. 2022. Analysis of microstructure and protective performance of melt-blown materials for medical protective masks. In *Journal of Physics: Conference Series* Vol. 2194, No. 1, p. 012010. IOP Publishing.
- [24]. Lee, B. O, Ko, J. A, Han, S. W. 2010. Characteristics of PP/PET bicomponent melt blown nonwovens as sound absorbing material. In *Advanced Materials Research*, Vol. 123, pp. 935-938). Trans Tech Publications Ltd.
- [25]. Moradi, , Ahmadi, M. S, Mashroteh, H. 2019. Development of tri-layer breathable fluid barrier nonwoven fabrics for surgical gown applications. *The Journal of The Textile Institute*.
- [26]. Xu, J, Xio, X, Zhang, W, Xu, R, Kim, S. C, Cui, Y, Wu, E. 2020. Air-filtering masks for respiratory protection from PM2. 5 and pandemic pathogens. *One Earth*, 3(5), 574-589.
- [27]. Shi, Y, Zhang, X, Xu, K, Jin, X, Zhao, Y, Huang, C. 2023. How will actual wearing time influence the protective effect of surgical masks?. *Textile Research Journal*, 93(7-8), 1641-1650.
- [28]. Xu, Y, Zhang, X, Teng, D. *et al.* 2022. Multi-layered micro/nanofibrous nonwovens for functional face mask filter. *Nano Res.* 15, 7549–7558. <https://doi.org/10.1007/s12274-022-4350-2>
- [29]. Xiao, Y, et al. 2019. Study on the Relationship Between Structure Parameters and Filtration Performance of Polypropylene Meltblown Nonwovens. *Autex Research Journal*. 20(4): 1-6.

## Dose Determination of Fluvial Sediments in Manisa

Müjde Durukan Gültepe<sup>1\*</sup> , Arzu Ege<sup>1</sup> 

<sup>1</sup> Manisa Celal Bayar University, Faculty of Engineering and Natural Sciences, Department of Physics, Manisa - Türkiye

\*[mujde.durukan@cbu.edu.tr](mailto:mujde.durukan@cbu.edu.tr)

\* Orcid No:0000-0003-3401-3515

Received: 26 October 2023

Accepted: 21 December 2023

DOI: 10.18466/cbayarfbe.1381567

### Abstract

Quartz, which is one of the most abundant minerals in nature, can be found in magmatic and metamorphic forms, as well as the usual components of granite and sedimentary formations. Quartz minerals, which are also known as the main component of quartzites, are also known as gangue minerals in many mineralizations. Quartz samples from two different sampling levels, namely the Kaletepe lower and the Kaletepe upper region, used in the study were prepared. Thermoluminescence (TL) glow curves of the samples exposed to radiation with a  $^{90}\text{Sr}/^{90}\text{Y}$   $\beta$  source were recorded with a TLD reader. While peaks were obtained at approximately 270 °C from the glow curves of the Kaletepe lower samples irradiated with  $\beta$  source, peaks were obtained at approximately 270 °C and 350 °C from the Kaletepe upper samples. When the annual average dose and age values of the lower and upper Kaletepe samples are examined, it can be said that it was formed in a time period of ~8000 years between two areas with a height difference of 130m.

**Keywords:** Equivalent Dose, Fluvial Sediments, Thermoluminescence dating, Quartz.

### 1. Introduction

The increasing importance of radiation research due to technological advancements and the need to determine radiation exposure levels in various fields, including physics and medicine. Luminescence is the emission of light because of the energy absorption of some semiconductor and insulator materials. When a material is exposed to radiation, according to Stoke's law, some of the energy of the incident radiation is absorbed in the material and is released as a longer wavelength light is emitted [1] which describes the relationship between the energy of the absorbed radiation and the wavelength of the emitted light. Luminescence can be used to determine the dose of radiation exposure, as the intensity of the emitted light is proportional to the amount of energy absorbed by the material. Therefore, by measuring the luminescence intensity of a material exposed to radiation, it is possible to determine the amount of radiation to which it was exposed.

The luminescence technique is useful in detecting radiation exposure to humans, using it as a radiation dosimeter, and dating geological artifacts. Some materials having luminescent properties glow when heated after exposure to radiation; this physical phenomenon is called thermoluminescence (TL) [2].

The history of TL research is described, beginning with Robert Boyle's observations in the 17th century on minerals like diamond and feldspar, which exhibit TL properties. The 18th and 19th centuries saw further studies on TL, including the first systematic studies by Wiedemann and Schmidt on materials exposed to cathode rays, and the discovery of the relationship between TL signals and radioactivity, which opened the door to dosimetric studies. The usability of phosphor materials in dose measurement and the TL properties of these materials are among the subjects that have been studied with interest [3]. The band structure of a solid, as well as impurities and lattice irregularities, are factors that affect TL. The wavelength of the emitted photon is a property of the radiating material, rather than the incident radiation [4-6].

Quartz, which is one of the most common minerals in nature, is the usual component of magmatic, metamorphic, especially granite, and sedimentary formations. Quartz minerals, which are also known as the main component of quartzites, are also known as gangue minerals. Many natural materials, such as quartz minerals, have been examined as TL materials, and many materials have been studied in the literature.

The main components of sediments are quartz and feldspar minerals, and these minerals are constantly exposed to ionizing radiation. The luminescence obtained from quartz is widely used in dosimetry [7, 8] especially in dating geological materials and rocks [9]. Thermoluminescence dose measurements has been used to date various geological materials such as sediments, soils, and archaeological [9].

Thermoluminescence dose measurements of sediments is useful in determining the depositional age and history of sedimentary basins, which can provide important information about the evolution of landscapes and climate [10]. These measurements have also been used to determine the age of archaeological artifacts, such as pottery and burnt stones, providing important insights into the history of human civilization [11].

Quartz grains, which are highly resilient and widely available minerals found on the Earth's surface, have been extensively employed in the process of optically stimulated luminescence (OSL) dating. This dating method is commonly applied to Quaternary sediments spanning various types of depositional environments [11,12]. Recent studies have shown that the luminescence characteristics of quartz can serve as a valuable tool for analyzing the origin and source of sediments. This innovative application of quartz luminescence properties enables researchers to gain insights into sediment provenance, allowing them to determine the geographical origin and transport history of sediments [13, 14].

Thermoluminescence (TL) is also used in archeology and geology to determine the age of sediments and materials. TL dating is based on the principle that some minerals, such as quartz or feldspar, accumulate electrons trapped in their crystal lattice when exposed to ionizing radiation in the medium. Over time, these trapped electrons are released when the mineral is heated, resulting in a measurable thermoluminescence signal. The amount of light released is proportional to the amount of radiation the mineral has been exposed to since the last warming event. They can estimate the age of the sample by measuring the intensity of the emitted light. TL signals from quartz saturate more slowly than signals from other techniques, allowing older sediments to be dated. However, the saturation behavior depends on several factors, such as the specific mineral, the type and intensity of radiation exposure, and the date of burial of the sample. TL dating is typically appropriate for specimens several thousand to several hundred thousand years old. TL dating is often employed for dating older sediments due to the slower saturation of its signal compared to OSL dating. However, the specific age range that can be accurately determined depends on several factors and the limitations of each dating method [15, 16].

In this study, the thermoluminescence (TL) properties of quartz samples obtained from sedimentary formations in the Kaletepe region of the Salihli district of Manisa province were investigated. The quartz samples obtained in the study were prepared from two different elevation levels, namely the lower Kaletepe region and the upper Kaletepe region, with four of each. TL glow curves of the samples exposed to radiation at different times with a  $^{90}\text{Sr}/^{90}\text{Y}$   $\beta$  source were recorded with the Harshaw 3500 TLD reader - analyzer system. While peaks were obtained at approximately 270 °C from the glow curves of the lower Kaletepe samples irradiated with  $\beta$  source, peaks were obtained at approximately 270 °C and 350 °C from the upper Kaletepe samples. The equivalent dose measurements of the lower and upper Kaletepe region fluvial sediment samples are examined and found as  $278.409 \pm 13.762$  and  $182.320 \pm 25.293$  mGy, respectively. If the ages of the lower and upper Kaletepe region fluvial sediment samples are examined, it can be said that they were formed in a time period of ~8000 years between two areas with a height difference of 130m. The study area is located in the eastern part of the Aegean extensional zone, which is widely known as the active continental expansion zone. For example, there are various studies on the fault system in this field [17, 18, 19, 20]. For this reason, the dose measurement of fluvial sediments in the region is very important in dating previous earthquakes.

## 2. Material and Method

In this study, it was aimed to investigate the TL properties of sedimentary samples obtained from the Kaletepe area of the Salihli district of Manisa province. Kaletepe locality (Fig.1), which is 10 km away from Salihli district of Manisa province, is located at 38°29' north latitude and 28°01' east longitude.

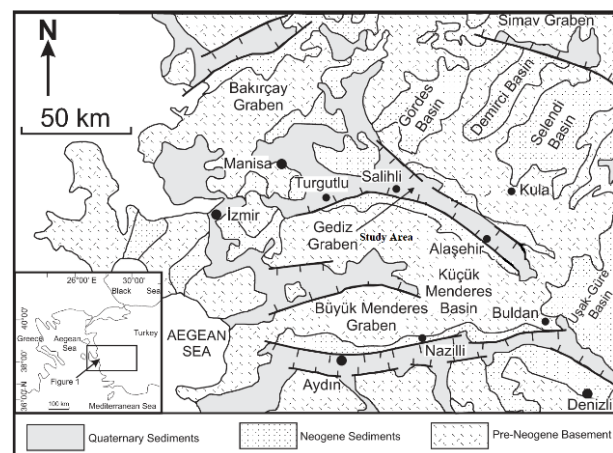


**Figure 1.** Geological map of the study area showing the Neogene and Quaternary basins of Western Türkiye [17].



The reason why these samples are preferred is that they are close to the last geological age (the Quaternary) and yield efficient results in radiation techniques and dating. This indicates that the samples that were chosen extremely rich minerals like quartz and feldspar. Sedimentary quartz samples suitable for the study were determined in terms of both mineral contents and luminescence techniques in the field studies carried out in the Kaletepe area of Salihli district. Two separate areas were determined in the sampling area at two different heights, the lower (292nm) and upper (434 m) of the Kaletepe area [17].

When collecting and transporting the samples, care was taken to avoid exposing the sediments to light. As a result of an X-ray diffraction analysis (XRD) of the sediment samples, the quartz minerals were used for dose measurements since the sample contains quartz and is suitable for the system's quartz analysis measurement. The X-ray diffraction analysis (XRD) of sediment samples was performed. As a result of these analyses, the coarse grain method was used to determine the equivalent dose in sediments because the minerals are rich in quartz. Quartz samples with a grain size of 100  $\mu\text{m}$  and above were preferred. Certain chemical procedures have been applied to separate the minerals of the desired grain size from the sediment. In the coarse grain method, sediment samples were first sifted. The samples were then kept in %10 HCl and %30  $\text{H}_2\text{O}_2$  solutions, then washed with distilled water until they were completely cleaned. After these processes, the samples were dried in an oven at 60°C. Following these procedures, the samples were washed with distilled water again and checked with a pH meter to see if they had become completely neutral. The neutralized samples were passed through a 140 $\mu$  sieve with wet sieving and left to dry in the oven again. Quartz was separated from these elements by using a sodium polytungstate ( $3\text{Na}_2\text{WO}_4 \cdot 9\text{WO}_3 \cdot \text{H}_2\text{O}$ ) solution with a density of 2.82 g/cm in order not to encounter any metal in the samples that were subjected to chemical processes. Quartz minerals of the desired coarse grain size were obtained by passing the samples through distilled water again. A single sample of 4–10 mg is sufficient to determine the equivalent dose, but the measurements were repeated with four samples to reduce statistical error. Experimental Studies were carried out at Manisa Celal Bayar University and Ege University Nuclear Sciences Institute.

Four discs of sedimentary samples exposed to radiation at different times with a  $^{90}\text{Sr}/^{90}\text{Y}$   $\beta$  source were prepared, and TL glow curves of these samples were obtained. Harshaw 3500 TLD reader - analyzer system was used for all TL measurements during the study. This system is a computer-connected hand-operated reader that allows manual reading of TL chips, sticks, and powders in a wide variety of sizes.

This reader system is suitable for all applications that require TLD detectors. The Harshaw TLD Model 3500 reader-analyzer system includes a sample drawer for the single-element TL detector, a linear, programmable heating system, and a cooled photomultiplier tube with associated electronics for measuring TL light output. Planchet heating includes a welded thermocouple for the best temperature repeatability. Operating software, WinREMS, running on a separate computer, provides the user interface, reader control, and application software. With this system, samples can be heated up to 600 °C. Owing to the PM tube, the incoming signals are amplified, and the data is processed and recorded by the computer to which the WinREMS program is connected.

### 3. Results and Discussion

In this study, the luminescence curves of the samples obtained from the lower and upper Kaletepe areas were irradiated at different times using the  $^{90}\text{Sr}/^{90}\text{Y}$   $\beta$  source with a half-life of 28 years and an activity of 650 MBq and having dose rate  $5.30 \pm 0.60$  mGy/s were recorded with a TLD reader.

In the study, after measuring the natural signal of the samples, the glow curves were recorded by applying preheat temperatures of 230, 240, 250, and 260 °C for the lower Kaletepe region (Fig. 2) and 220, 230, 240, and 250 °C for the upper Kaletepe region (Fig. 2), respectively. After the preheating temperature was determined, the dose response curve of the sample was determined. When the glow curves obtained are examined, it is seen that they were obtained with preheating of 250 °C for the Kaletepe lower sample and 230 °C for the Kaletepe upper sample. Therefore, at the stage of determining the equivalent dose, it was decided to apply these determined preheats to the TL measurements.

First, the natural signal of the prepared samples was taken, and then the doses of 19, 57, 114, and 280 Gy were given to the samples of the Sr- $^{90}\beta$  source and the Kaletepe lower region, and doses of 19, 57, 114, 153, and 280 Gy to the samples of the Kaletepe upper region (Fig. 3). After each irradiation, glow curves from 50 °C to 450 °C and background measurements were obtained with a Harshaw TLD reader at a heating rate of  $2^\circ\text{C}\cdot\text{s}^{-1}$ . Using these measurements, clear glow curves were recorded. When TL luminescence curves of the Kaletepe upper quartz sample were examined, TL luminescence signals were observed at approximately 270 °C and 370 °C (Fig. 3.). As a result of the exposure of the Kaletepe upper quartz sample to the beta source for a long time, it was observed that the TL intensity increased with increasing dose (Fig. 3).

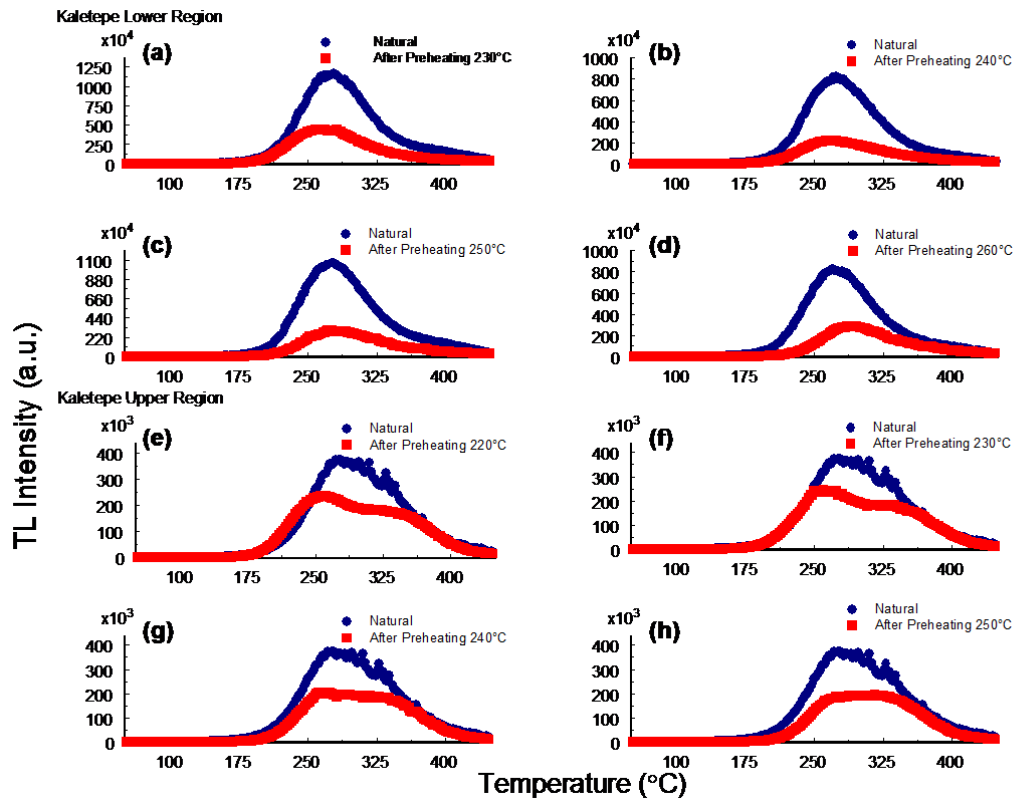


**Figure 2.** Glow curves of Kaletepe lower and upper region samples obtained because of natural and preheating at (a) 230 °C, (b) 240 °C, (c) 250 °C, (d) 260 °C, (e) 220 °C, (f) 230 °C, (g) 240 °C and (h) 250 °C respectively.

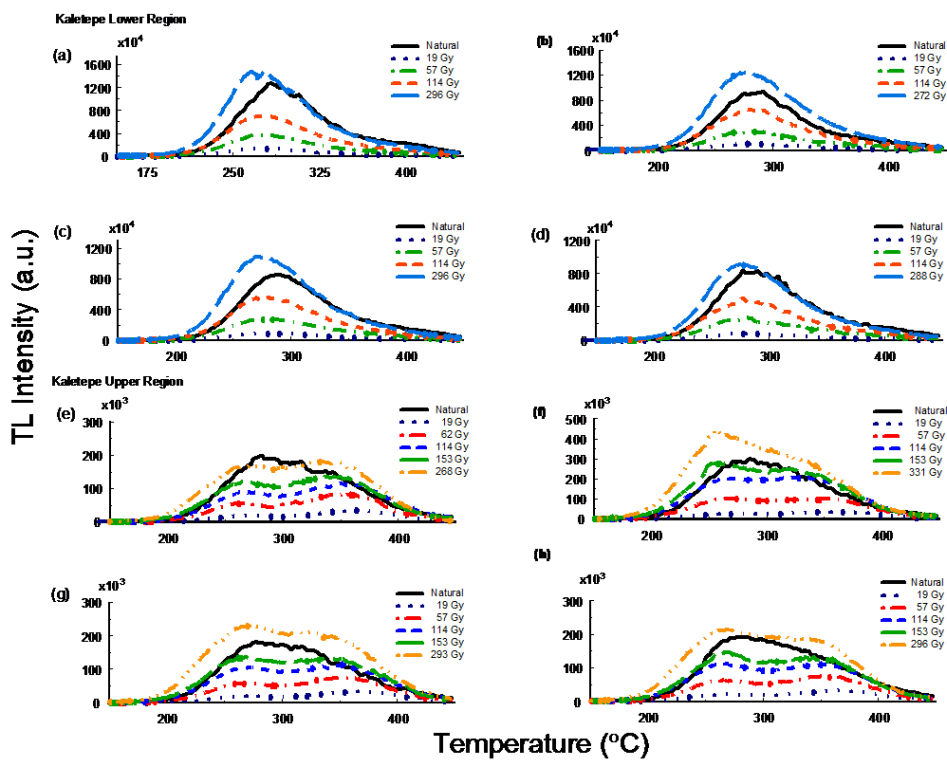


**Figure 3.** TL glow curves of the Kaletepe lower and upper region quartz sample after irradiation at different doses with Sr-<sup>90</sup>β source and natural dose.

Peaks were obtained at approximately 270°C from the glow curves of the Kaletepe lower samples irradiated with a dose of 296 Gy. It can be said that the TL intensity of the samples exposed to the  $^{90}\text{Sr}/^{90}\text{Y}$  beta source for a longer time is higher. As can be seen from the TL glow curves of sediment samples obtained from two different altitudes, Kaletepe lower and Kaletepe upper, the samples taken were found to be suitable for thermoluminescence studies. When planning such studies, supplying materials from different locations of

the sedimentary areas will be very productive for the study. In addition, with the results of these studies, studies related to the age determination of sedimental samples in this region were carried out, and useful results were obtained [21]. From the ratio of the glow curves to each other, it was observed that there was a plateau between 300 and 316 °C for the lower samples of Kaletepe (Fig. 4) and between 250 and 265 °C for the upper samples of Kaletepe (Fig. 4).

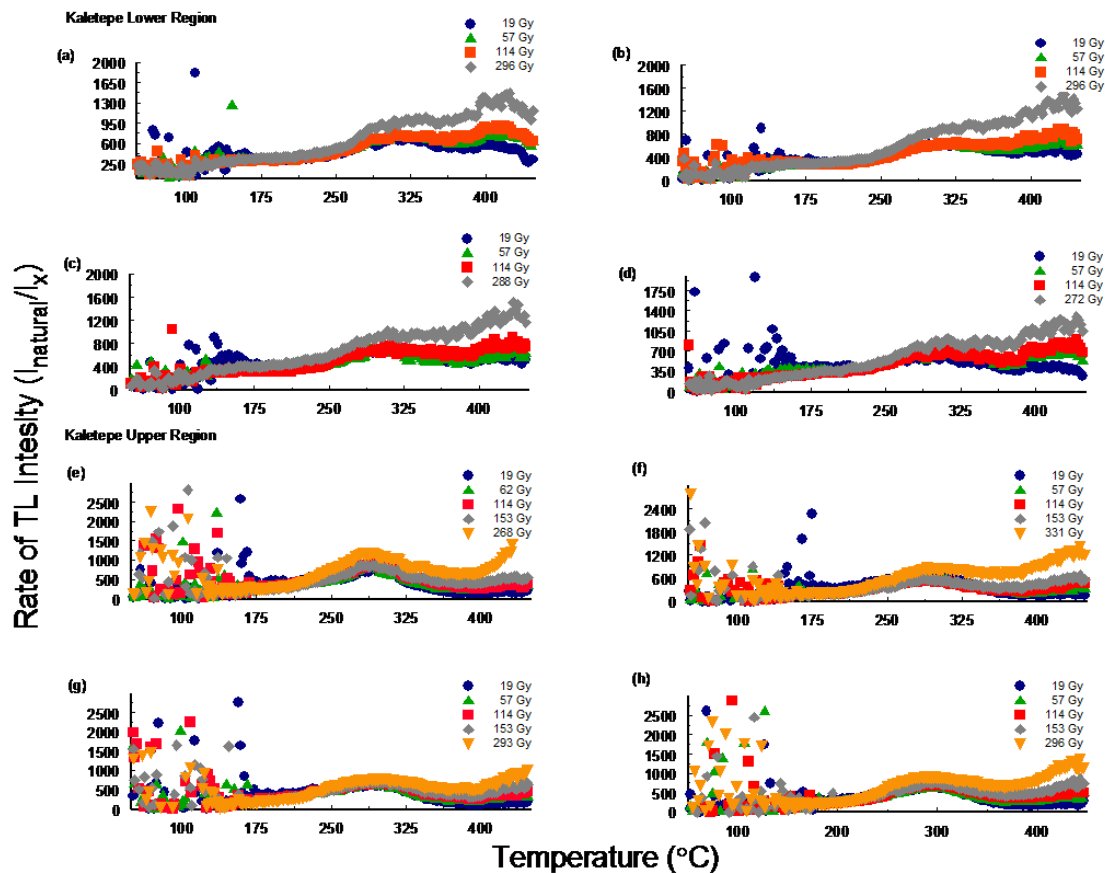


**Figure 4.** Plateau test results of Kaletepe lower and upper region samples ( $I_{\text{natural}}$ : Natural signal intensity,  $I_x$ : x dose-related intensity).

Growth curves were drawn for both areas using the integrations in this temperature range. The dose value corresponding to the natural signal on these curves gives the equivalent dose of the samples. The ages of the samples were determined from the ratio of the equivalent dose values to the annual dose values calculated for the selected areas. The annual dose rates of the samples were taken as stated in the study [21].

The line equation obtained from the growth curves was used to determine the point where the natural signal intersects the x-axis. Equivalent dose values were calculated from these quartz samples. According to these

results, the Kaletepe lower sample equivalent dose was calculated  $278 \pm 14$  Gy (Fig. 5), and the Kaletepe upper sample was calculated  $182 \pm 25$  Gy (Fig. 6).

By determining the annual dose rate and equivalent dose values in both areas, the date on which the quartz particles obtained chemically from the sediment samples transported by the river saw the last light was determined. Considering the average annual dose values, the age of the sediment sample belonging to the lower area of Kaletepe was  $91.282 \pm 24.649$  and the age of the sediment sample belonging to the upper area of Kaletepe was calculated as  $83.062 \pm 28.253$  (Table 1).

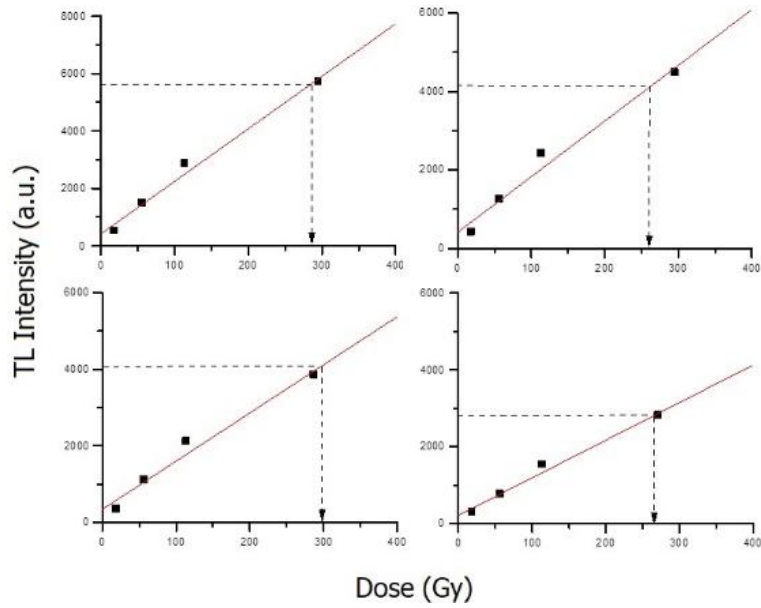


**Figure 5.** Growth curves of Kaletepe lower samples.

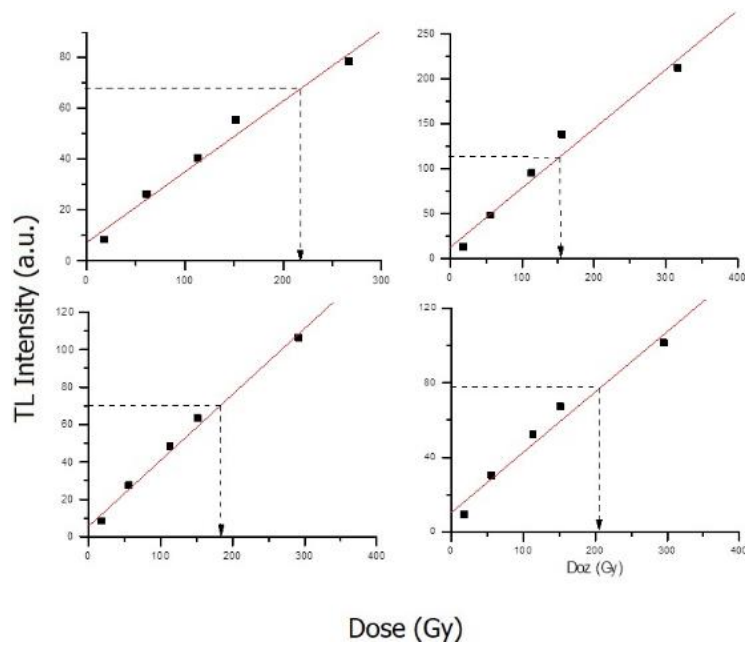


**Figure 6.** Growth curves of Kaletepe upper samples.

**Table 1.** The equivalent dose calculated for the lower and upper Kaletepe samples, the annual dose and age values [21].

$$Age = [Equivalent\ Dose\ (mGy)] / [Annual\ Dose\ (mGy/y)]$$

	Kaletepe (lower)	Kaletepe (upper)
Equivalent Dose (mGy)	278.409±13.762	182.320±25.293
Annual Dose (mGy.y <sup>-1</sup> )	3.05±0.82	2.20±0.69
Age (y)	91.282±24.649	83.062±28.253

According to the annual mean dose values, the age of the Kaletepe lower area was calculated  $91,282 \pm 24,649$  years and the age of the Kaletepe upper area was calculated  $83,062 \pm 28,253$  years. Considering the average annual dose and age values obtained, it can be said that it was formed in a time period of ~8000 years between the upper and lower areas of Kaletepe with a height difference of ~130 m. According to these results, it can be thought that the events that enabled the transport of fluvial sediments occurred in the Salihli - Kaletepe region of Manisa Province about 90 thousand years ago [22].

#### 4. Conclusion

In this study, Salihli-Kaletepe region fluvial sediment samples were dated by thermoluminescence (TL) techniques. A coarse-grained technique was used for dating studies. Annual dose rate and equivalent dose values for both regions (lower and upper Kaletepe) were determined from sediment samples carried by the river. Thus, the ages of the fluvial sediments obtained by chemical means were determined.

#### Acknowledgements

This research is supported by grants from the Scientific and Technological Research Council of Turkey (TÜBİTAK) Contract No. TBAG 104T139, and the Ege University Science and Technology Research Center (EBİLTEM Contract No. 2007/BIL/020).

#### Data availability

The graphs created with the data obtained during the study are presented. Data generated and/or analyzed during the current study are available from the corresponding author upon reasonable request.

#### Author's Contributions

**Müjde Durukan Gültepe:** Designed the research and created the article and then critically reviewed the article and unanimously approved the final draft.

**Arzu Ege:** Collected samples from the Kaletepe location in accordance with the processes and took measurements after chemically processing them and making them suitable. Guided and supervised the whole process. M. Durukan Gültepe, A. Ege revised the manuscript; and all authors read and approved the final manuscript.

#### Ethics Declarations

There are no ethical issues after the publication of this manuscript.

#### References


- [1]. Stokes, S. (1999). Luminescence dating applications in geomorphological research. *Environmental Science, Geomorphology*, vol. 29, 153-171.
- [2]. Shannon, M. A., Rittenour, T. M., Nelson, M.S., Atae, N., Brown, N., DeWitt, R., Durcan, J., Evans, M., Feathers, J., Frouin, M., Guérin, G., Heydari, M., Huot, S., Jain, M., Keen-Zebert, A., Li, B., López, G. I., Neudorf, C., Porat, N., Rodrigues, K., Sawakuchi, A. O., Spencer J. Q. G. K (2022). Thomsen; Guide for interpreting and reporting luminescence dating results, *GSA Bulletin*, 135 (5-6): 1480–1502.
- [3]. Satılmış, U. S., Ege, A. (2019). Thermoluminescence response of UV irradiated cerium doped Sr<sub>3</sub>Y<sub>2</sub>(BO<sub>3</sub>)<sub>4</sub> phosphor, *Journal of the Institute of Science and Technology*, 9(1): 169-176.
- [4]. McKeever, S.W.S. (1985). Thermoluminescence of solids. *Cambridge University Press*.
- [5]. McKeever, S.W.S., Moscovitch, M., Townsend, P. D. (1995). Thermoluminescence dosimetry materials: properties and uses. *Nuclear Technology Publishing*.
- [6]. Vij, D. R. (1998). Luminescence of Solids. *Plenum Press*, New York.
- [7]. Souza, D. N., de Lima, J.F., Valerio, M.E.G., Fantini, C., Pimenta, M.A., Moreira, R.L., Caldas, L.V.C. (2002). Influence of thermal treatment on the Raman, Infrared and TL responses of natural topaz, *Nuclear Inst. And Methods in Physics B*, 230-235.
- [8]. Hashimoto, T., Yasuda, K., Sato, K., Sakaue, H., Katayama, H. (1998). Radiation-induced luminescence images and TL-property changes with thermal annealing treatment on Japanese twin quartz. *Radiation Measurements*, vol. 29, Issue 5, 493-502.
- [9]. Huntley, D.J., Godfrey-Smith, D.I., Thewalt, M.L.W., Berger, G.W. (1988) Thermoluminescence spectra of some mineral samples relevant to thermoluminescence dating. *Journal of Luminescence*, vol. 39, Issue 3, 123-136.
- [10]. Wintle, A.G., Murray, (2006). A. S. A review of quartz optically stimulated luminescence characteristics and their relevance in single-aliquot regeneration dating protocols, *Radiation Measurements*, 41: 369-391.
- [11]. Wintle, A. G. (2008). Luminescence dating: where it has been and where it is going. *Boreas*, 37: 471-482.
- [12]. Wintle, A.G., Adamiec, G. (2017). Optically stimulated signals from quartz: A review, *Radiation Measurements*, vol. 98, 10-33pp.
- [13]. Capaldi, T. N., Rittenour, T. M., Nelson, M. S. (2022). Downstream changes in quartz OSL sensitivity in modern river sand reflects sediment source variability: Case studies from Rocky Mountain and Andean rivers, *Quaternary Geochronology*, vol. 71, 101317.
- [14]. Gray, H. J., Jain, M., Sawakuchi, A. O., Mahan, S. A., Tucker, G. E. (2019). Luminescence as a sediment tracer and provenance tool, *Reviews of Geophysics*, 57, 987– 1017pp.
- [15]. Pacompia, Y., Supo-Ramos, J. G., Gonzales-Lorenzo, C. D., Callo-Escobar, D. J., Rocca, R. R., Pastrana, E. C., Gomes, M. B., Silva-Carrera, B. N., Watanabe, S., Ayca-Gallegos, O., Ayala-Arenas, J.S. (2023). Luminescence dating and firing temperature determination of ancient ceramics fragments from the Tunata-hill site in the Churajon archaeological complex in Arequipa, Peru, *Radiation Physics and Chemistry*, vol. 204, 110725.





- [16]. Al-Khasawneh, S. (2023). Optically Stimulated Luminescence Dating (OSL): Procedures and Applications to Archaeology Research in Jordan, *Cultural Heritage: At the Intersection of the Humanities and the Sciences*, 357.
- [17]. Sözbilir, H. (2002). Geometry and origin of folding in the neogenesediments of the Gediz Graben, Western Anatolia, Turkey, *Geodinamica Acta*, 15: 277-288pp.
- [18]. Bozkurt, E., Sözbilir, H. (2004). Tectonic evolution of the Gediz graben: field evidence for an episodic, two-stage extension in western Turkey, *Geological Magazine*, 141, 63–79.
- [19]. Bozkurt, E., Sözbilir, H. (2006). Evolution of the large-scale active Manisa fault, southwest Turkey: implications on fault development and regional tectonics, *Geodinamica Acta*, 19, 427-453.
- [20]. Zhu, L., Mitchell B. J., Akyol N., Cemen, I., Kekovalı K. (2006). Crustal thickness variations in the Aegean region and implications for the extension of continental crust, *J. Geophys. Res.*, 111, B01301.
- [21]. Ege, A., Ekdal, E., Karali, T., Can, N. (2009). Annual dose measurement for luminescence dating in Salihli, Turkey. *Turkish J. Eng. Env. Sci.*, 33, 21- 29.
- [22]. Ege A., (2008). Dating Geological Samples Using Radiation Techniques, Ege University, Graduate School of Natural and Applied Sciences, Department of Nuclear Sciences, (PhD Thesis), İzmir.

## Investigation of Effect of Air Gap between Surface and Bolus on Dose Distribution for 6 MV Photon Beam

Osman Vefa Gül<sup>1\*</sup> 

<sup>1</sup>Department of Radiation Oncology, Faculty of Medicine, Selcuk University, Konya, Türkiye

\*[vefagul@selcuk.edu.tr](mailto:vefagul@selcuk.edu.tr)

\* Orcid No: 0000-0002-6773-3132

Received: 16 November 2023

Accepted: 28 December 2023

DOI: 10.18466/cbayarfbe.1391876

### Abstract

In radiotherapy, tissue equivalent boluses are frequently used in the treatment of superficially located tumors. The air gap between the patient's skin and the bolus may cause dosimetric uncertainties. This study aims to dosimetrically investigate the effect of the air gap between the surface and the bolus on dose distribution. Computed tomography (CT) images of the phantom were obtained and transferred to the treatment planning system (TPS). In the TPS, a bolus was placed on the phantom surface and then air gaps were created between the bolus and the surface. The effect of the air gaps between the surface and the 5 mm thick bolus on the dose distribution was analyzed with the point doses obtained from the TPS. For the 6 MV X-ray, it was observed that the air gap negatively affected the surface doses calculated by TPS. Accordingly, an inverse correlation was found between air gap and surface dose. It is recommended that bolus use, especially in curved anatomical regions, should be applied before CT scanning as much as possible. When using bolus material in radiotherapy, it is recommended to be careful not to leave an air gap between the surface and the bolus.

**Keywords:** Air-gap effect, Bolus, Radiotherapy, Skin dose

### 1. Introduction

The main goal of radiotherapy is to deliver the necessary dose to the target volume while ensuring that the surrounding critical organs are protected in the best possible way [1, 2]. In this way, the tumor is destroyed and the patient's quality of life is improved. Treatment planning systems (TPS) are used for dose calculation in radiotherapy. Dosimetric measurement data obtained for each treatment device are uploaded to the TPS. Using this data, TPSs provide dose calculation to the user through different algorithms. High-energy photon energy is used in radiotherapy and the lowest X-ray energy used is usually 6 MV [3, 4]. The maximum dose values of these rays occur at different depths depending on the energy. For 6 MV X-rays, the maximum dose depth is approximately 1.5 cm [5]. As the size of the energy used increases, the depth of the maximum point also increases.

The dose accumulated at the point where the beam of radiation comes into contact with the patient's surface is not the maximum dose and this is called the skin-sparing effect in radiotherapy. Therefore, the skin is protected by the nature of high-energy photon beams

[6]. While this is an advantage in radiotherapy of deep-seated tumors, it can be a disadvantage in superficial tumors. In the radiotherapy of superficially located tumors, a tissue-equivalent material called bolus is used to overcome the skin-protective properties of high-energy photon beams [7, 8].

Bolus is a tissue-equivalent material in contact with the skin in the area to be irradiated and is used to increase the surface dose in photon and electron treatments [9]. The bolus must have an electron density, physical density and atomic number equivalent to that of tissue or water, as well as being flexible and malleable to easily take the shape of the skin contour. It is also important for clinical use that it is transparent to facilitate the adjustment of the irradiated area, is not affected by high dose levels, is durable, non-toxic, non-flammable, does not allow the growth of bacteria and fungi and has an acceptable cost [10]. Boluses made from tissue equivalent materials are divided into two groups, Super-Flab or Super Stuff. Super-Flab boluses are specific thicknesses and are prepared in advance and irradiated in gel layers in the irradiation area. they can land on it. Super-stuff boluses form in the transporter field are boluses that can solidify.

Usually, the most commonly used bolus type is Super-flab are boluses. Super-flab boluses have a mass of  $1.02\text{g/cm}^3$  and the raw material is vinyl. The thickness of the bolus material to be used varies depending on the distance, thickness and location of the tumor to the skin. Contact of the bolus material with the skin surface is extremely important. There is usually no problem with bolus use in anatomically flat areas. However, in anatomically irregular areas, the air gap between the patient's skin and the bolus may cause dosimetric uncertainties [11, 12].

This study aims to dosimetrically investigate the effect of the air gap between the surface and the bolus on dose distribution.

## 2. Materials and Methods

### 2.1. Phantom design

Since the current study was not performed on patients, solid water phantoms consisting of water-equivalent plates were used to provide the required depth. Solid phantoms are a water-equivalent material used for dosimetry procedures in calibration and quality control protocols of high-energy X-ray and electron beams in radiotherapy. In this study, PTW FREIBURG brand RW3 model  $30\times 30\times 1$  cm solid water phantoms (PTW, Freiburg, Germany) were used. For irradiation of RW3 solid phantoms in treatment planning system (TPS), images of the phantom were obtained on a Toshiba Aquilion S4 Computed tomography (CT) device (Toshiba Medical Systems, Japan). The obtained CT images were TPS.

### 2.2. Bolus material

The high-energy photons used in radiotherapy have skin protective properties. In this study, a tissue equivalent bolus material was used to ensure that the phantom surface received enough dose. The bolus was created virtually in TPS. The phantom created in the TPS was tissue equivalent and had a density of  $1\text{g/cm}^3$ . Air gaps were created to examine the effect of the air gap between the bolus and the surface on dose distribution. The air gaps between the bolus and phantom surface were 0, 1, 3, 5 and 10 mm, respectively. The bolus thickness created via TPS was 5 mm.

### 2.3. Dose calculation

In Eclipse TPS, dose calculations were performed using the AAA algorithm. An area of  $10\times 10\text{cm}^2$  was determined for the beam area. To evaluate the effect of source surface distance (SSD) on dose distribution, plans were created at 3 different SSDs. These SSDs were 95,

97.5 and 100 cm, respectively. For all plans, the gantry angle was 0 degrees and the prescription dose was 200 cGy. X-ray energy for all plans was 6 MV. For each SSD, beam plans were created for 0, 1, 3, 5 and 10 mm air gaps between the bolus and phantom surface. The plan created for a 5 mm air gap and SSD= 97.5 cm is shown in Fig 1. Surface doses for each plan were obtained by point dose reading with the same standards.

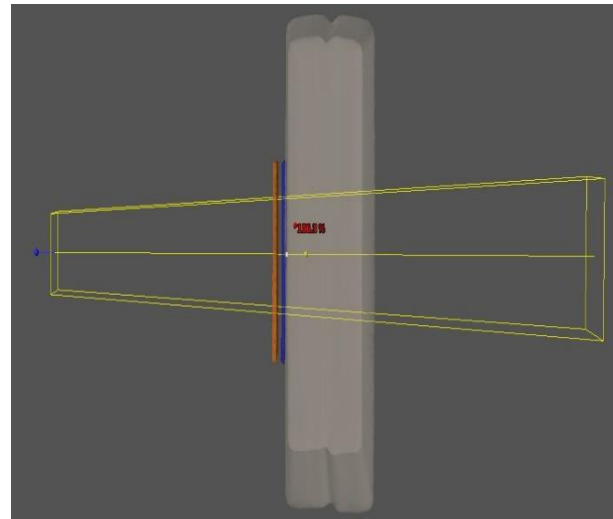


**Figure 1.** Beam field without air gap (blue) and with 5 mm air gap (orange) for SSD=97.5

## 3. Results and Discussion

A change in surface doses was expected according to the change in SSD'. As a result of the calculations made in TPS, the surface doses were 199.6, 175.2 and 199.7 cGy for SSD= 95 cm, SSD= 97.5 cm and SSD= 100 cm, respectively, when there was no air gap between the bolus and the surface. When there was a 10 mm air gap between the bolus and the surface, the surface doses were 106.2, 70.6 and 193 cGy, respectively. The dose distributions on the phantom due to three different SSD variations are shown in Fig 2.

For SSD=95, the surface doses for air gap 0, 1, 3, 5 and 10 mm were 199.6, 156.9, 108.4, 106.2 and 104.4 cGy, respectively. For SSD=97.5, the surface doses for air gap 0, 1, 3, 5 and 10 mm were 175.2, 135.2, 96.7, 85.4 and 70.6 cGy, respectively. Point dose measurements showed that surface doses decreased significantly as the gap between the phantom surface and the bolus increased. The effects of the air gap between the phantom surface and the bolus on the dose distribution at different depths are shown in Fig 3, Fig 4 and Fig 5 for SSD= 95, SSD= 97.5 and SSD= 100 cm, respectively.

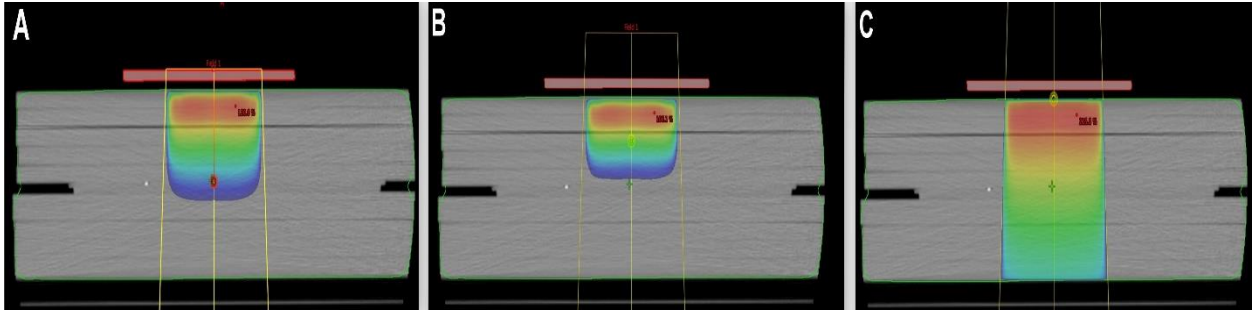


**Figure 2.** Dose distributions for different SSDs with 5mm air gap between bolus and phantom surface. A: SSD=95cm, B: SSD= 97.5cm and C: SSD= 100cm

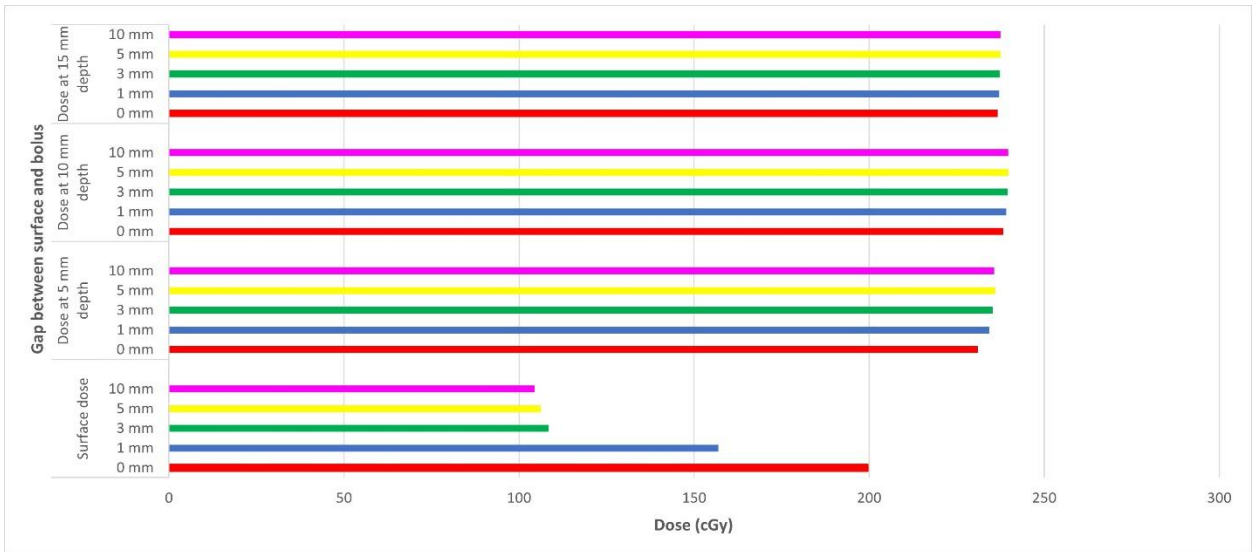


**Figure 3.** The effect of the air gap on the dose distribution at different depths for SSD= 95 cm as a result of calculations made on TPS.

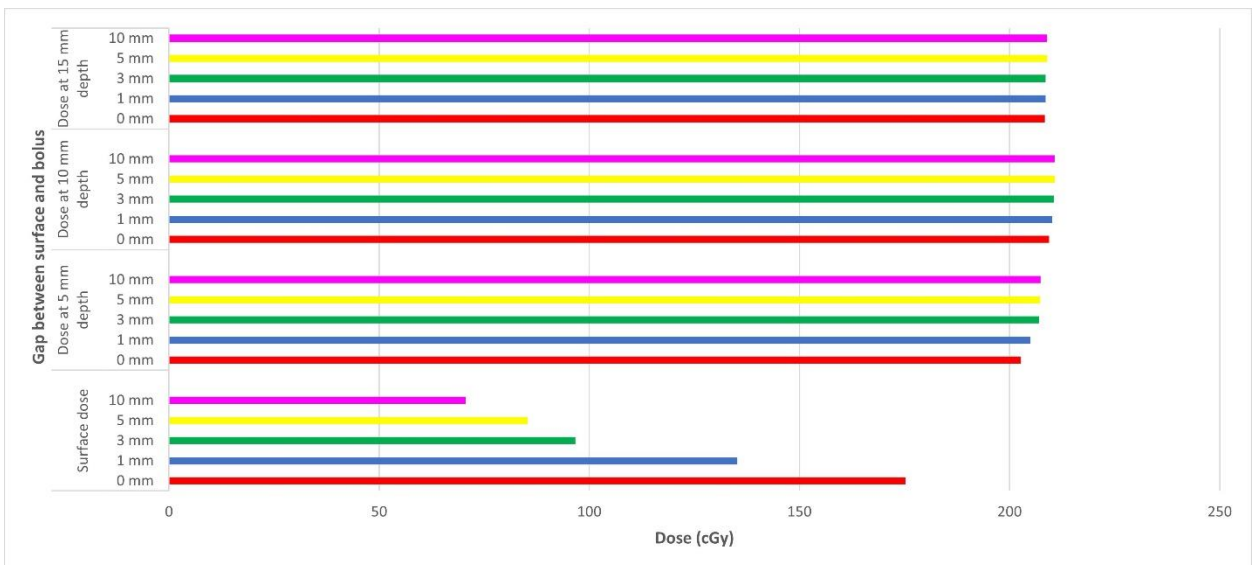


**Figure 4.** The effect of the air gap on the dose distribution at different depths for SSD=97.5 cm as a result of calculations made on TPS.



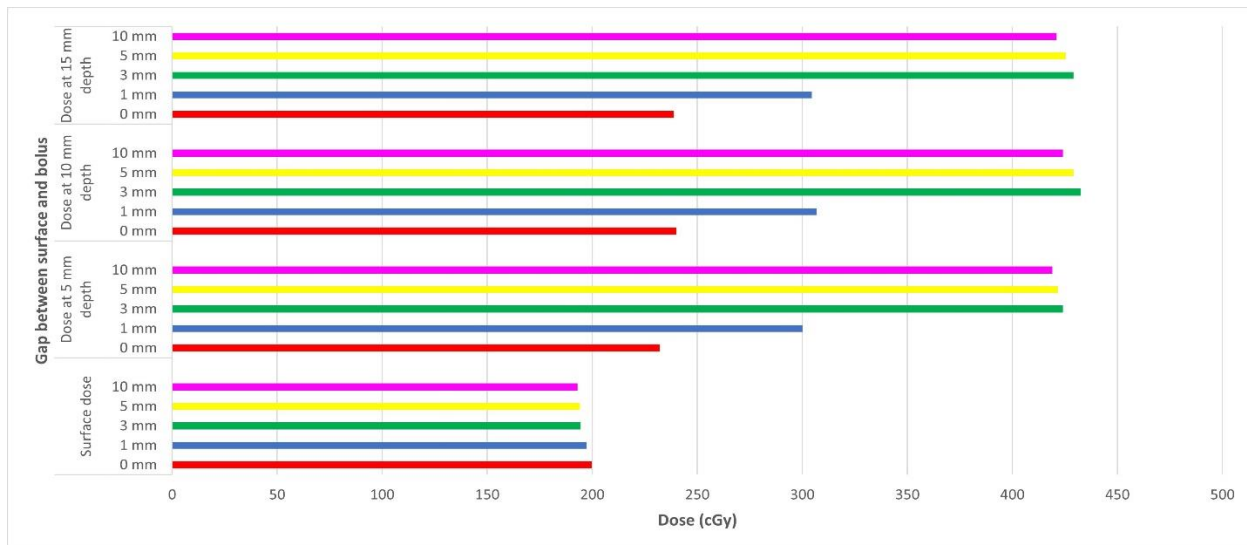


**Figure 5.** The effect of the air gap on the dose distribution at different depths for SSD=100 cm as a result of calculations made on TPS.

Khan et al. using a 1.0 cm super-flab bolus, investigated the effects of various scenarios of air gaps between the surface and the bolus on dose distribution. They showed that as the distance between the bolus and the surface increases, the relative dose decreases [13].

In the current study, dose distributions were investigated at different depths and different SSDs. For SSD= 95 and SSD= 97.5 cm, it was observed that the surface dose decreased as the distance of the gap between the bolus and the surface increased. There was no significant difference between the dose distributions for build-up depth. For SSD=100 cm, the surface dose decreased as the air gap increased, but fluctuations were observed in the calculations by TPS at other depths. Srinivas et al. evaluated dosimetric parameters such as depth dose along the central axis using a 6 MV clinical photon beam in the presence of air gaps between the gel bolus and the treatment surface. They reported that the surface dose decreased as the air gap increased in the presence of a 0.5 cm bolus and a 10x10 cm<sup>2</sup> beam field [14].

In this TPS study, it was found that especially the surface dose decreased with increasing air gap in parallel with Srinivas et al. In a study by Butson et al. using a parallel plate ionization chamber and radiochromic film with 6MV photon beams and 1cm bolus, it was observed that small air spaces between the bolus and the skin reduced the skin dose [15].

In the current study, it was observed that increasing the gap between the surface and bolus decreased the surface dose for different SSDs.

#### 4. Conclusion

In dosimetric literature studies and current research, it has been observed that the air gap between the surface and the bolus reduces the surface dose. The limitation of the study is that it is a TPS-based study. It is recommended that bolus use, especially in curved anatomical regions, should be applied before CT scanning as much as possible. When using bolus material in radiotherapy, it is recommended to be careful not to leave an air gap between the surface and the bolus.

#### Acknowledgement

There are no financial declarations. This work not grant funded.

#### Author's Contributions

**Osman Vefa Gül:** Drafted and wrote the manuscript, supervised the progress of the experiment, and performed the experiment and results analysis.

#### Ethics

There are no ethical issues after the publication of this manuscript.

#### References

- [1]. Burnet, N. G. (2004). Defining the tumour and target volumes for radiotherapy. *Cancer Imaging*, 4(2), 153-161.
- [2]. Mukherji, A. (2018). *Basics of planning and management of patients during radiation therapy : a guide for students and practitioners*. New York, NY: Springer Berlin Heidelberg.
- [3]. Park, J. M., Kim, J.-i., Heon Choi, C., Chie, E. K., Kim, I. H., & Ye, S.-J. (2012). Photon energy-modulated radiotherapy: Monte Carlo simulation and treatment planning study. *Medical Physics*, 39(3), 1265-1277.

- [4]. Fadzil, M. S. A., Noor, N. M., Tamchek, N., Ung, N. M., Abdullah, N., Dolah, M. T., & Bradley, D. A. (2022). A cross-validation study of Ge-doped silica optical fibres and TLD-100 systems for high energy photon dosimetry audit under non-reference conditions. *Radiation Physics and Chemistry*, 200.
- [5]. Dogan, N., & Glasgow, G. P. (2003). Surface and build-up region dosimetry for obliquely incident intensity modulated radiotherapy 6 MV x rays. *Medical Physics*, 30(12), 3091-3096.
- [6]. Zhang, C., Lewin, W., Cullen, A., Thommen, D., & Hill, R. (2023). Evaluation of 3D-printed bolus for radiotherapy using megavoltage X-ray beams. *Radiological Physics and Technology*, 16(3), 414-421.
- [7]. Wang, X., Wang, X., Xiang, Z., Zeng, Y., Liu, F., Shao, B., . . . Liu, L. (2021). The Clinical Application of 3D-Printed Boluses in Superficial Tumor Radiotherapy. *Frontiers in Oncology*, 11.
- [8]. Wang, K. M., Rickards, A. J., Bingham, T., Tward, J. D., & Price, R. G. (2022). Technical note: Evaluation of a silicone-based custom bolus for radiation therapy of a superficial pelvic tumor. *Journal of Applied Clinical Medical Physics*, 23(4).
- [9]. Endarko, E. (2021). Evaluation of Dosimetric Properties of Handmade Bolus for Megavoltage Electron and Photon Radiation Therapy. *Journal of Biomedical Physics and Engineering*, 11(06).
- [10]. Lu, Y., Song, J., Yao, X., An, M., Shi, Q., & Huang, X. (2021). 3D Printing Polymer-based Bolus Used for Radiotherapy. *Int J Bioprint*, 7(4), 414.
- [11]. Dyer, B. A., Campos, D. D., Hernandez, D. D., Wright, C. L., Perks, J. R., Lucero, S. A., . . . Rao, S. S. (2020). Characterization and clinical validation of patient-specific three-dimensional printed tissue-equivalent bolus for radiotherapy of head and neck malignancies involving skin. *Physica Medica*, 77, 138-145.
- [12]. Aras, S., Tanzer, I. O., & Ikizceli, T. (2020). Dosimetric Comparison of Superflab and Specially Prepared Bolus Materials Used in Radiotherapy Practice. *European Journal of Breast Health*, 16(3), 167-170
- [13]. Khan, Y., Villarreal-Barajas, J. E., Udowicz, M., Sinha, R., Muhammad, W., Abbasi, A. N., & Hussain, A. (2013). Clinical and Dosimetric Implications of Air Gaps between Bolus and Skin Surface during Radiation Therapy. *Journal of Cancer Therapy*, 04(07), 1251-1255.
- [14]. Srinivas, C., Lobo, D., Banerjee, S., Ravichandran, R., Putha, S., Prakash Saxena, P. U., Sunny, J. (2020). Influence of air gap under bolus in the dosimetry of a clinical 6 MV photon beam. *Journal of Medical Physics*, 45(3).
- [15]. Butson, M. J., Cheung, T., Yu, P., & Metcalfe, P. (2000). Effects on skin dose from unwanted air gaps under bolus in photon beam radiotherapy. *Radiation Measurements*, 32(3), 201-204.